CR-164,953

NUMERICAL SIMULATION OF A COMPRESSIBLE, HOMOGENEOUS, TURBULENT SHEAR FLOW

by

W. J. Feiereisen,

W. C. Reynolds,

and

J. H. Ferziger

Report No. TF-13

Thermosciences Division
Department of Mechanical Engineering
Stanford University
Stanford, California

March 1981

Page

12   Eq. (2.1.6) – second term should be $\partial/\partial x'_k$.

17   Brackets missing in last integrand of Eq. (2.2.8) and in both integrands in Eq. (2.2.9).

18   Eq. (2.3.3) (ρu_i) should be $(\rho u_i)_{,i}$.

56   First line, remove space in "has."

58   Third line of Eq. (4.7.1) should be $-2\mu < u_{1,2} u''_{1,2} >$.

74   First equation (unnumbered), last P should be $\mathcal{P}$.

80   Line 4 – period missing after values.

81   Next to last line, "component" misspelled.

85   Table 4.5 – Exponent of Re_λ should be c.

      Table 4.6 – Equation number should be (4.11.6).

160   Fig. 4.20 – Inset should read $D = 1.6182$.

166   c in definition of M should have subscript "o".

NUMERICAL SIMULATION OF A COMPRESSIBLE, HOMOGENEOUS, TURBULENT SHEAR FLOW

by

W. J. Feiereisen

W. C. Reynolds

and

J. H. Ferziger

Report No. TF-13

Thermosciences Division
Department of Mechanical Engineering
Stanford University
Stanford, California 94305

March 1981

This Page Intentionally Left Blank

Acknowledgments

To earn a Ph.D. is more than just to do research and write a thesis. I wish to acknowledge many people who helped me during my graduate study.

NUMERICAL SIMULATION OF A COMPRESSIBLE, HOMOGENEOUS, TURBULENT SHEAR FLOW

Abstract

A direct, low Reynolds number, numerical simulation has been performed on a homogeneous turbulent shear flow. The full compressible Navier-Stokes equations were used in a simulation on the ILLIAC IV computer with a 64^3 mesh.

The flow fields generated by the code were used as an experimental data base, to examine the behavior of the Reynolds stresses in this simple, compressible flow. Emphasis was placed on determining the variation of the structure of the stresses and their dynamic equations as the character of the flow changed.

The objectives of this work center round the modeling of these stresses in a compressible turbulent flow. It has been found that the structure of the stress tensor is more heavily dependent on the shear number and less on the fluctuating Mach number than was originally thought.

The pressure-strain correlation tensor in the dynamic stress equations can be directly calculated in this simulation. It is found that these correlations can be decomposed into several parts, as contrasted with the traditional incompressible decomposition into two parts. The performance of existing models for the conventional terms is examined, and a new model is proposed for the "mean-fluctuating" part.

The additional terms in the pressure-strain tensor relate to the compressibility of the fluid. They are found to be of the same order of magnitude as the conventional terms. The modeling, therefore, becomes quite important in an averaged simulation of the Navier-Stokes equations. The behavior of these terms is examined and suggestions made for their modeling. A new class of models based on a structural similarity concept is examined. This type of model is used for the entire pressure strain tensor and looks promising.

In these simulations the computer is used as a numerical wind tunnel, a capability only recently available with the advent of large,

fast, "vector" machines like the ILLIAC IV. The ability to measure quantities that were previously inaccessible from these simulations should prove to be a great boon to turbulence research. Further direct and large eddy simulations in "building block" flows, such as the homogeneous shear flow, are therefore highly recommended. They can lead to a fuller understanding of the physics of turbulence, while at the same time providing information to the conventional turbulence modeler who is interested in technologically useful flows.

Table of Contents

List of Tables

List of Illustrations

ix

Nomenclature

Note: In Chapters I and II all quantities have dimensions. In Chapters III and IV all quantities have been nondimensionalized on ρ_o, C_o, L_b, μ, κ, and C_p.

Symbol

A	Coefficient in Taylor-Green solution. Constant in Lumley-Newman function.
A_1	Constant in fourth-rank tensor model.
A_{ij}	Mean velocity gradient tensor.
a	Convective speed. Constant in least-squares fitting function.
B_{ij}	Coordinate transformation tensor.
b	Constant in least-squares fitting function.
b_{ij}	Reynolds stress anisotropy tensor.
C	Fourier-space Courant number. Shear-stress correlation coefficient. Constant in solution (2.5.3).
C', C''	Fourier-space-modified Courant numbers.
C_p	Constant pressure specific heat.
c	Speed of sound. Constant in least-squares fitting function.
c_o	Constant sound speed.
c_1	Rotta constant.
c_2, c_3	Constants in extended fourth-rank tensor model.
D	Computational domain.
D_{ij}, D_{ij}^H	Homogeneous dissipation.
D_{ij}^D	Dilatation dissipation.
d	Constant in least-squares fitting function.
d_{ij}	Dissipation anisotropy tensor.

E_j	Mean density gradient.
$E(k)$	3-D energy spectrum.
$E_{ii}(k_\ell)$	1-D energy spectrum.
$E_{ij}^S(k)$	3-D spectra of the solenoidal turbulent stresses.
$E_{ij}^D(k)$	3-D spectra of the dilatation turbulent stresses.
e	Total energy per unit mass. Constant in least-squares fitting function.
F_j	Mean pressure gradient.
f	Constant in least-squares fitting function.
$G_{ijk\ell}$	Tensor in fourth-rank tensor model.
g_i	Inhomogeneous terms in Poisson and wave equations.
h	Time step.
i	$\sqrt{-1}$.
$\underline{J}$	Jacobian matrix for Euler equations.
$\underline{J}_o$	Constant Jacobian matrix.
k	Wave number magnitude.
k',k''	Modified wave number magnitudes.
k_i	Wave number vector.
L	Integral length scale.
L_b	Computational box size.
M	Fluctuating Mach number.
N	Number of mesh points in one direction.
n	Iteration number.
P	Pressure.
P'	Fluctuating pressure.
P_o	Constant mean pressure.
$\underline{P}$	Eigenvectors of $\underline{J}$.
P	Turbulent kinetic energy production.

P_{ij}	Turbulent stress production tensor.
P_i	Decomposed pressure field.
p_{ij}	Production anisotropy tensor.
$\vec{Q}$	Solution vector for Euler equations.
$\vec{Q}_o$	Initial solution vector for Euler equations.
q	Turbulent velocity.
q^2	Turbulent intensity.
q_j	Heat flux.
$\vec{R}$	Solution for the Euler equations in eigenvector space.
R_{ij}	Reynolds stress tensor.
R_{ij}^S	Incompressible (solenoidal) part of the Reynolds stress tensor.
R_{ij}^D	Compressible (dilatation) part of the Reynolds stress tensor.
$R_{ij}(r_1,r_2,r_3)$	General two-point velocity correlation.
Re_L	Integral scale turbulent Reynolds number.
	Lumley's Reynolds number $\dfrac{\rho q^4}{\varepsilon \nu}$.
Re_λ	Taylor microscale Reynolds number.
r_1,r_2,r_3	Two-point correlation separations.
S	Shear rate dU/dy.
Sk_i	Velocity derivative skewnesses.
St	Nondimensional time. Mesh metric
(SL/q)	Shear number.
(SL/c)	Shear Mach number.
T	Temperature
t	Time.
U_j	Mean velocity.
$\overline{u}_i$	Reynolds-averaged velocity vector.

$\tilde{u}_i$	Favre-averaged velocity vector.
u_i'	Reynolds fluctuating velocity vector.
u_i''	Favre fluctuating velocity fector.
u_i^S	Solenoidal velocity vector.
u_i^D	Dilatation velocity fector.
u_i^R	Initial random velocity vector.
V	Viscous stability number.
V'	Modified viscous stability number.
x	Downstream direction.
x_j	Cartesian coordinates.
x_j'	Transformed coordinates.
y	Gradient direction.
z	Spanwise direction.

Greek Letters

α	Computational root. Angle between Cartesian and principal axis coordinates.
Δx	Mesh spacing.
δ_{ij}	Kroenecker delta.
ε	Homogeneous dissipation.
Φ	1/2 trace of pressure-strain tensor.
ϕ_{ij}	Pressure-strain tensor.
$_k\phi_{ij}$	Decomposed pressure-strain tensor.
ϕ	Velocity potential
γ	Ratio of specific heats.
κ	Coefficient of heat conductivity.
$\underline{\Lambda}$	Eigenvalue matrix for the Jacobian $\underline{J}$.
λ	Complex stability number.

μ Molecular viscosity.

ν Kinematic viscosity.

θ Argument of complex computational root α.

ρ Density.

ρ' Fluctuating density.

ρ_o Average density (constant).

$\sigma_{a,b}$ Principal Reynolds stresses in the $x-y$ plane.

τ_{ij} Viscous stress tensor.

Ω_{ij} Mean-velocity rotation tensor.

ξ Internal energy per unit mass.

Roman Numerals

I   First invariant of the Reynolds stress anisotropy tensor b_{ij}.

II   Second invariant of the Reynolds stress anisotropy tensor b_{ij}.

III   Third invariant of the Reynolds stress anisotropy tensor b_{ij}.

Chapter I

MOTIVATION AND LITERATURE

1.1 Introduction

Modeling of turbulent fluid flows is a subject of great scientific and technological interest. Turbulent flows by their nature contain a large range of sizes of motion (length scales) and an equivalent range of time scales. This range of scales causes problems for the flow simulator because the smallest and largest scales of motion in his flow cannot be represented at the same time on a relatively coarse mesh. The required mesh systems are beyond the capability of modern computers.

We believe that the Navier-Stokes equations describe the flow of a Newtonian fluid. Reynolds (1883) applied an averaging operator to the Navier-Stokes equations in the hope that the resulting equations would be easier to solve. Because these equations are nonlinear, averaging introduces unknown correlations that prevent the system of equations from being complete (closed), unless assumptions are introduced about how these correlations behave. The unknown correlations in the momentum equations are the Reynolds stresses and assumptions about their behavior are turbulence models.

Turbulence modeling has received much attention over the years. Most of the fundamental work in this area has been based on the imcompressible Navier-Stokes equations. However, most flows of technological interest are compressible. For many years, models developed from the incompressible equations have been applied to compressible flows, in many cases with great success. At higher Mach numbers, existing turbulence models become increasingly inadequate. As it is very difficult to make experimental measurements in these flows we do not know the reason for this failure.

It is the purpose of this work to study what happens to the Reynolds stresses at high Mach number and investigate how they can be modeled. We use direct simulation of the full, unaveraged, Navier-Stokes equations to study this problem. Even with the power of a modern vector computer we are limited to simple geometries and low Reynolds numbers. By simulating the full Navier-Stokes equations we have no

1

closure problem. We can introduce an averaging process on the simulated results and directly calculate the various turbulence terms. Simulations such as these give us insight and guidance for constructing turbulence models that will be of use in more complicated flows.

In this work we perform simulations of compressible homogeneous turbulent shear flows on the ILLIAC IV computer and use the resulting flow fields as data bases.

Our objectives are:
1. To develop techniques for direct simulation of compressible homogeneous turbulent flows.
2. To apply these techniques to a shear flow simulation on the ILLIAC IV.
3. To develop a data base from these simulations.
4. To study the Reynolds stresses and terms in the Reynolds stress equations searching for the effects of compressibility.
5. To test turbulence models by comparing them with exact results computed from the data base.

In the remainder of this chapter we discuss the origion of the Reynolds stress, the various types of averaging and the complications that arise in compressible flows. We describe previous attempts to understand compressible turbulence and further discuss the reasons that led us to a direct simulation.

In chapter II we present the mathematical foundations of these simulations and select numerical method.

In chapter III we show how the equations and the numerical methods are implemented in a computer code on a vector computer. We describe the testing of the computer codes and the time development of a typical simulation.

In chapter IV we present results. We first describe characterization of these simulations. Then we present the data base. We discuss the structure of the Reynolds stresses and then some of the terms in their dynamic equations. We evaluate several turbulence models and propose some improvements.

Chapter V contains the conclusions.

2

1.2 Averaging and the Origin of the Reynolds Stresses

Solutions of the Navier-Stokes equations represent the flow of a Newtonian fluid. They are the governing equations for laminar and turbulent flows at all speeds. As alluded to earlier, structures in turbulent flows, at technologically interesting Reynolds numbers, contain too large a range of sizes for representation with current computers,

Hirt (1969) has shown that the number of mesh points in a simple, complete (no turbulence model), three-dimensional simulation scales on a Reynolds number formed from the turbulence quantities,

$$N^3 \propto (Re_L)^{9/4} = \left(\frac{qL}{\nu}\right)^{9/4} \tag{1.2.1}$$

where q is a turbulent vleocity scale, L is a turbulent length scale, and ν is the kinematic viscosity. N is the requred number of mesh points in one direction. For large Re_L, N^3 is beyond current storage capacity. This necessitates that a smoothing or averaging be applied to reduce this range in length scales so that we may stay within the resolution capacity of modern computers. This averaging is normally applied directly to the Navier-Stokes equations. Consequently, an averaged form of these equations, including a turbulence model, is usually solved.

We write the full Navier-Stokes equations using tensor notation:

Conservation of Mass

$$\rho_{,t} + (\rho u_i)_{,i} = 0 \tag{1.2.2}$$

Conservation of Momentum

$$(\rho u_i)_{,t} + (\rho u_i u_j)_{,j} + P_{,j} = \tau_{ij,j} \tag{1.2.3}$$

Conservation of Energy

$$(\rho e)_{,t} + (u_i(\rho e + P))_{,j} = (u_i \tau_{ij})_{,j} - q_{j,j} \tag{1.2.4}$$

3

where

$$\rho e \;=\; \frac{P}{(\gamma-1)} + \rho\,\frac{u_i u_i}{2} \;=\; \rho\xi + \frac{\rho u_i u_i}{2} \qquad (1.2.5)$$

is the sum of the internal and kinetic energies per unit volume. We have used ξ for the internal energy per unit mass because the standard symbol u is used for velocity.

$$\tau_{ij} \;=\; \mu(u_{i,j} + u_{j,i} - \tfrac{2}{3}\,\delta_{ij}u_{k,k}) \qquad (1.2.6)$$

is the viscous stress tensor, and

$$q_{j,j} \;=\; -\kappa T_{,jj} \qquad (1.2.7)$$

is the heat flux vector. The pressure P is related to ξ and ρ through an equation of state, $P = f(\xi,\rho)$, in our case the perfect gas law with constant specific heats. We divide the variables into mean and fluctuating components,

$$\rho = \bar{\rho} + \rho'\;;\quad u_i = \bar{u}_i + u_i'\;;\quad e = \bar{e} + e'\;;\quad P = \bar{P} + P' \qquad (1.2.8)$$

and apply Reynolds averaging to equations (1.2.2)-(1.2.7). The averaging operator is as yet unspecified, but has the property that $\overline{u_i'} = 0$. Writing the momentum equation only and indicating the average with a bar,

$$(\bar{\rho}\,\bar{u}_i)_{,t} + (\overline{\rho'u_i'})_{,t} + (\bar{\rho}\,\bar{u}_i\bar{u}_j)_{,j} + \bar{P}_{,t}$$

$$(1.2.9)$$

$$= \bar{\tau}_{im,j} - \underbrace{\left[\bar{\rho}(\overline{u_i'u_j'}) + \bar{u}_i(\overline{\rho'u_j'}) + \bar{u}_j\overline{\rho_i'u_j'}\right]}_{\text{Reynolds Stress}}{}_{,j}$$

we see the appearance of additional terms, the Reynolds stresses. These terms increase the number of variables in the problem and require additional equations if we are to have a complete set. The term with the time-derivative now appears as two terms; the second term must also be

4

modeled. Seeking additional equations, we can form equations for the Reynolds stresses, but unfortunately we find the appearance of yet higher-order correlations in these equations. This process of forming equations for these higher-order correlations is hopeless, because we can never complete the set. We must introduce a model for the Reynolds stresses that relates them to the mean-flow variables.

A standard simplification is to assume that the flow has constant density and is therefore incompressible $(\overline{u}_{i,i} = 0)$. The Reynolds stresses in Eq. (1.2.9) then reduce to $\overline{u'_i u'_j}$, and the second time-derivative term disappears. Favre (1965) introduced a variation of the averaging procedure that simplified the appearance of the Reynolds stresses in the compressible flow. He multiplied the velocity and energy by the density and averaged this product to form "mass-weighted" variables.

$$\tilde{u}_i = \frac{\overline{\rho u_i}}{\overline{\rho}}, \qquad u''_i = u_i - \tilde{u}_i \qquad (1.2.10)$$

This averaging has the property $\overline{\rho u''_i} = 0$. Applying this definition to Eqs. (1.2.2) through (1.2.7), we find that the appearance of the Reynolds stresses has been simplified and looks quite similar to the incompressible stress.

$$\overline{\rho}\;\overline{u'_i u'_j} + \overline{u_j \rho' u'_i} + \overline{u_i \rho' u'_j} - \overline{\rho' u'_i u'_j} \;\rightarrow\; \overline{\rho u''_i u''_j} \qquad (1.2.11)$$

$$\text{Reynolds-averaged} \qquad\qquad \text{Favre-averaged}$$

The simplification is in appearance alone and has nothing to do with the physics. It is the form that most modern compressible flow simulations use. We shall show that Reynolds- and Favre-averaging are identical in the homogeneous flows that we simulate, and that our conclusions apply to either type.

Favre-averaging of the Navier-Stokes equations is thoroughly treated in Rubesin and Rose (1973), to which the reader is referred for a complete discussion.

1.3 A Short History

Early studies of compressible turbulence applied decompositions to the flow variables and studied their interaction. Kovasznay (1953) and Chu and Kovasznay (1958) proposed the idea of "modes." They derived equations for the vorticity mode, corresponding to convective and vortical motions, and for the pressure (acoustic) and entropy (temperature) modes. They analytically studied interactions among these modes, but were limited to low turbulence levels by their analytic techniques. They concluded that these interactions were second-order and therefore quite small at low turbulence levels. Moyal (1952) concluded the same in his analysis. He divided the kinetic energy spectra into "eddy turbulence" and "random noise" parts. He did this by Fourier-transforming the velocity vector and decomposing it into vectors that are, respectively, perpendicular and parallel to the wave-number vector. His analysis, like that of Chu and Kovasznay, was limited to low turbulence levels and therefore not applicable in technologically useful flows.

We recall this work because we are now able to perform these decompositions numerically, without the restriction to low turbulence levels. We shall use Moyal's decomposition in the presentation of some results in Chapter IV.

Because measurements in high-speed flows are so difficult, little is known about the structure of the Reynolds stresses and their equations. Historically, simulators have used models derived from the incompressible Navier-Stokes equations. Morkovin (1962) used the limited data available at the time to show that the Reynolds stresses in supersonic boundary layers were structurally similar to incompressible flow. Laufer (1969) used Favre averages to come to the same conclusion. Over the years, application of incompressible models has met with great success in boundary layers. However, limits on this applicability began to be recognized. Bradshaw (1977) quantified Morkovin's hypothesis. He agreed with Morkovin that incompressible models should not be applied in boundary layers with external Mach numbers greater than five, nor in boundary layers with large pressure gradients (shock-boundary layer interaction). Bradshaw also concluded that these models are inappropriate

in free-stream layers with Mach numbers greater than 1.5; however, no physical reason is given. A general conclusion of the Free Shear Layers Conference (Morkovin et al. (1972)) was that existing turbulence models were inadequate for these flows. None was able to predict the well-known decrease in mixing-layer spreading rate with increased Mach number without introducing empirical data.

These failures have variously been attributed to variations in density or some unspecified "compressibility effect." Brown and Roshko (1974) performed a low-speed, variable density, mixing layer experiment. Their flow was virtually incompressible, but they controlled the density ratio of the two streams by using gases of different molecular weights. They found no evidence of spreading rate variation with density ratios appropriate for single-component, high-speed mixing layers and concluded that spreading-rate variation must be a "compressibility effect." Oh (1974) simulated a two-dimensional, high-speed mixing layer. He proposed a kinetic-energy equation model that provided for a nonzero pressure-dilatation interaction. He was able to correctly predict the trend of the spreading, leading us to suspect that there are unrecognized physical phenomena that must be modeled. The questions that remain unanswered for lack of experimental data are, "What changes occur in the Reynolds stresses and their equations in a compressible flow, and how should they be modeled?" In the next section, we discuss how we approached these questions.

1.4 The Approach of This Work

Much progress in turbulence research has come from the study of homogeneous flows. These are flows that extend to infinity in all directions and are statistically similar everywhere in space. Presumably a homogeneous flow is an approximation to a piece of an inhomogeneous flow. It allows us to separate and distinguish competing processes in the development of the turbulence and is also amenable to analytic treatment (Batchelor, 1953).

Several homogeneous turbulent-flow experiments have been performed (box-turbulence: Comte-Bellot and Corrsin, 1971, and Bennett, 1976; shear flow: Rose, 1966, Champagne et al., 1970, and Harris et al.,

7

1977); plane strain: Tucker and Reynolds, 1975) to obtain experimental measurements of turbulence quantities. All of these experiments were performed in steady-flow wind tunnels and substituted spatial (downstream) development for time development. Consequently, they are approximations to homogeneous flow and are slightly inhomogeneous in the downstream direction. Analysis by Harris (1977) showed that this shear flow has about the maximum mean-velocity gradient possible while still maintaining an approximation to homogeneity. The downstream distance in which a significant change in turbulence quantities occurs must be larger than the largest turbulent length scales in the flow. This cannot be satisfied at high speeds with large velocity gradients. Therefore, there are no high Mach number homogeneous flow experiments. However, we would still like to study a compressible homogeneous flow. This is where the work must start if we are to understand turbulence in a compressible flow.

In the last few years, the advent of very large computers has provided the capability of doing three-dimensional simulations of flows with simple geometries (Deardorff, 1970; Orszag, 1971; Clark, 1977; Mansour, 1978; Moin, 1978; and Pulliam, 1979). The majority of turbulent flow simulations have solved averaged or filtered equations and incorporated a turbulence model.

Because of the absence of experimental measurements of compressible turbulence, we use a large vector computer as a numerical wind tunnel and perform numerical experiments. This approach was pioneered by Clark (1977). He simulated box turbulence with the unaveraged, incompressible Navier-Stokes equations and therefore did not need a model to close his equations. In contrast to experiment, his simulations (and all homogeneous flow simulations) developed in time and was therefore a closer approximation to the ideal. He compared the performance of turbulence models against the "exact" terms as calculated from his simulated flow fields.

In this work, we simulate a compressible, homogeneous, turbulent shear flow by solving a transformed version of the full Navier-Stokes equations ((1.2.2) through (1.2.7)). A shear flow is the simplest turbulent flow with a continuous source of turbulent kinetic-energy

production. At low Mach number we may also compare with the shear flow experiments listed above.

The mean flow is pictured in Fig. 1.1. Geometrically, it is like a deck of playing cards, with each card sliding on top of the one below it.

1.5 Numerical Requirements

We cannot simulate a homogeneous flow with an infinite domain. Like an experimentalist, we choose a portion of the flow and impose boundary conditions. We must choose a large enough portion of the flow that the turbulent length scales are much smaller than our domain, or the boundary conditions will interfere. Ideally, we would like to impose periodic boundary conditions, i.e., one side of our computational mesh is identical to the opposite side. These boundary conditions are essentially transparent to the simulation, if the turbulent length scales are small enough. However, inspection of Fig. 1.1 shows that the shear flow is not periodic. The mean velocity varies across a computational mesh. In Chapter II we shall introduce an analytic coordinate transformation on the Navier-Stokes equations that allows the equations to have periodic solutions.

If we are to use the simulated flow fields as a data base, we must be sure of their accuracy. We require a highly accurate numerical method in both space and time. This requirement is also addressed in Chapter II, where we discuss the equations and the numerical method.

Chapter II

EQUATIONS AND NUMERICAL METHOD

In this chapter we discuss the coordinate transformation that we apply to the Navier-Stokes equations. We describe an alternate way of writing the momentum equations that ensures the numerical conservation of quantitie that are analytically conserved, and we justify the choice of a numerical method.

2.1 The Linear Coordinate Transformation

We apply a coordinate transformation to the Navier-Stokes equations that allows them to have periodic solutions. We then impose Periodic Boundary Conditions (PBCs) on the transformed equations and use Fourier methods for the spatial derivatives.

Homogeneous flows extend to infinity in space. Obviously we cannot simulate the entire flow, nor is it necessary. We choose a portion of the flow field and impose boundary conditions on the edge of this domain. Boundary conditions are a source of numerical uncertainty in any simulation. In simulations of a homogeneous flow, we may reduce this uncertainty by applying PBCs after a suitable coordinate transformation. PBCs enforce all variables to be periodic on the domain. They are essentially transparent to the simulation if the domain is significantly larger than the largest turbulent length scales that naturally develop inside it. PBCs are desirable because they do not introduce unknown effects into the flow. They are the least intrusive boundary conditions available for this geometry, and we would like to use them.

Most homogeneous flows are not periodic (except isotropic flows), because the mean velocity is not periodic. This can be seen by dividing the variables into mean and fluctuating components. We do this in general for all homogeneous flows with linear mean-velocity gradients, and then show how the derivation is made specific for homogeneous shear flows. We write:

$$\rho = \rho' + \rho_o + E_j x_j \; ; \quad u_i = u_i' + A_{ij} x_j \; ; \quad P = P' + P_o + F_j x_j$$

$$(2.1.1)$$

where the mean parts of the density and pressure have both constant and linear gradient parts. Tensor A_{ij} and vectors E_j and F_j represent the linear gradients of each variable. They are constants for our case but may be generalized to vary with time. For example, in the shear flow,

$$A_{ij} = \frac{\partial U_i}{\partial x_j} = \begin{bmatrix} 0 & S & 0 \\ 0 & 0 & 0 \\ 0 & 0 & 0 \end{bmatrix} \qquad (2.1.2)$$

where S is the "shear rate," $\partial U/\partial y$. We shall show that E_j and F_j must be zero when we introduce the coordinate transformation.

If we introduce the definitions (2.1.1) into the conservation of mass equation (2.1.2), we immediately produce an equation with the coordinates as coefficients.

$$\frac{\partial}{\partial t} \rho' + (\rho' u_i')_{,i} + A_{ij} x_j (\rho'_{,i} + E_i)$$

$$(2.1.3)$$

$$+ u_{i,i}' (\rho_o + E_j x_j) + A_{ii} (\rho' + \rho_o + E_j x_j) + E_j u_j' = 0$$

Equation 2.1.3 will not allow periodic solutions, because the coordinate, x_j, appears explicitly in the coefficients. Hence we are led to apply a coordinate transformation in order to eliminate these coefficients and to derive equations for the fluctuating (primed) quantities only.

We define this transformation for the general case as

$$x_i' = B_{ij} x_j, \quad t' = t \qquad (2.1.4)$$

where B_{ij} relates the transformed corodinates to the Cartesian coordinate. This idea originated with Rogallo (1979), who first applied it to the solution of an incompressible homogeneous shear flow. He substituted the decomposed field (2.1.1) and the transformation (2.1.4) into

the incompressible momentum equations and derived the conditions that allow the equations to have periodic solutions. We follow the same reasoning for the full Navier-Stokes equations. The same procedure is followed for all the equations. We illustrate this for the mass equation only because the algebra is very messy.

Inserting (2.1.1) and (2.1.4) into the Navier-Stokes equations (1.1.2)-(1.1.7) and writing the mass equation, the derivatives become

$$\frac{\partial}{\partial x_j} \rightarrow B_{kj} \frac{\partial}{\partial x_b'}$$

$$\frac{\partial}{\partial t} \rightarrow \frac{\partial}{\partial t'} + \dot{B}_{jk} C_{k\ell} x_\ell' \frac{\partial}{\partial x_j'}$$

$$(2.1.5)$$

where $C_{k\ell}$ is the inverse of $B_{k\ell}$.

$$\frac{\partial}{\partial t} \rho' + B_{kj} \frac{\partial}{\partial x_b'} \rho' u_j' = - B_{kj} A_{j\ell} C_{\ell k} \rho' - B_{kjk} E_m C_{mk} u_j'$$

$$- (\dot{B}_{jk} + B_{j\ell} A_{\ell k}) C_{k\ell} x_\ell' \frac{\partial}{\partial x_j'} \rho' - E_m \left[\dot{B}_{jk} C_{k\ell} C_{mj} + B_{kj} \left(C_{m\ell} \frac{\partial}{\partial x_k'} u_j' \right. \right.$$

$$+ A_{jn} C_{n\ell} C_{mk} + A_{jn} C_{m\ell} C_{nk} \left. \left. \right) \right] x_\ell'$$

$$(2.1.6)$$

We have isolated all the coordinate coefficients in the last two terms. Ideally, we would choose some B_{jk} and the last two terms in (3.1.6) would be zero. However, there is no B_{jk} that will zero the coefficient in the last term. Therefore, E_m must be identically zero, i.e., there can be no mean gradient of density.

The second-to-last term has a coefficient that we may set equal to zero, resulting in a set of coupled ordinary differential equations:

$$\frac{d}{dt} B_{ij} + B_{ik} A_{kj} = 0 \qquad (2.1.7)$$

Solution of these equations, subject to the initial conditions,

$$B_{ij} = \delta_{ij} \quad \text{(Cartesian mesh)} \qquad (2.1.8)$$

defines the transform for a specific mean velocity gradient tensor, A_{ij}.

As stated, the same procedure is followed to transform the momentum equations. Equation (2.1.7) also results independently from the momentum equations.

When applying the procedure to the total energy equation (1.2.4), we were unable to zero all of the coordinate coefficients. The reason can be seen by inspecting the definition of the total energy, Eq. (1.2.5), the total energy is the sum of the kinetic and internal energies and is quadratic in (2.1.1) and the velocity. This leaves some terms in (1.2.4) quadratic and some cubic when Eqs. (2.1.5) are inserted. A linear coordinate transformation cannot eliminate the coordinate coefficients from all these terms at the same time.

We solve this problem by subtracting the kinetic energy equation from (1.2.4), leaving only the thermal energy equation. We may do this and retain the complete set of equations, because the kinetic energy equation is not independent of the mass and momentum equations.

Taking the time derivative of (1.2.5), we find

$$\frac{\partial}{\partial t} \rho e = \frac{\partial}{\partial t} \frac{P}{(\gamma-1)} + \frac{\partial}{\partial t} \rho \frac{u_i u_i}{2} \qquad (2.1.9)$$

which shows that the total energy equation is the sum of the internal energy $P/(\gamma-1)$ and the kinetic energy per unit volume. We subtract the kinetic energy equation and multiply by $(\gamma-1)$ to form the equation for the pressure before we apply the transformation.

$$\frac{\partial}{\partial t} P + \gamma P u_{i,i} + u_i P_{,i} = (\gamma-1) u_{i,j} \tau_{ij} - (\gamma-1) q_{,jj} \qquad (2.1.10)$$

The total energy is analytically conserved. By solving the thermal energy equation (2.1.10), we give up guaranteed numerical conservation of total energy, but we shall show later how this is regained.

Equation (2.1.10) can now be transformed in the same manner as the mass and momentum equations. Without presenting the complicated algebra, we find that F_j must be identically zero, for the same reason as found with the density. There can be no mean gradient in the pressure. This is in contrast to the incompressible case, where the mean pressure gradient is arbitrary. This is due to the fact that the

13

pressure is a true flow variable and not the result of a kinematic constraint, as it is in incompressible flow.

This derivation is general for an arbitrary mean velocity gradient, A_{ij}. Taking the A_{ij} corresponding to the shear flow, Eq. (2.1.2), and solving for the transform tensor, B_{ij}, in (2.1.7) subject to the initial condition (2.1.8), we find

$$B_{ij}(t) = \begin{bmatrix} 1 & -St & 0 \\ 0 & 1 & 0 \\ 0 & 0 & 1 \end{bmatrix} \quad ; \quad x'_j = B_{ij}x_j \qquad (2.1.11)$$

or

$$x' = x - St\ y$$

$$y' = y \qquad\qquad (2.1.12)$$

$$z' = z$$

This is the coordinate system for the homogeneous shear flow that allows the equations for the fluctuating quantities to have periodic solutions. It is effectively "glued" on top of the mean velocity of Fig. 1.1, and shears along with it.

Before presenting the final form of the equations that are used in the simulation, we show an alternative form of the momentum equations (1.2.3) that regains the total energy conservation lost by solving the thermal energy equation. This form will also guarantee that kinetic energy is not being artificially produced.

2.2   The Conservation Properties

From previous experience (Mansour, 1978), it is known that artificial generation of conserved flow-field quantities by the numerical method can destroy the validity of a simulation. For example, in incompressible flows, in the absence of viscosity and turbulent kinetic energy production, and, with PBCs, it can be proven that the total mass, momentum, and kinetic energy remain constant. Numerical simulations do not always ensure this. Kwak (1975) and Shaanan (1975) used a modified (but exact) form of the convective terms in the momentum equations, in order to ensure kinetic energy conservation under these conditions.

14

In a compressible flow under the same conditions (periodic boundary conditions, no turbulent kinetic energy production, zero viscosity), kinetic energy conservation does not hold. There is a physical mechanism for exchange of energy between the kinetic energy and the thermal energy through a pressure-volume interaction.

Artificial production or dissipation by means of finite-difference approximations to the convective terms is still possible and must be eliminated for a valid simulation. We shall again rewrite the convective terms in the momentum equations in a different but equivalent form that not only prevents artificial kinetic energy production but regains the total energy conservation that we lost earlier.

We must ensure that the numerical method that we shall use is incapable of artificially creating kinetic energy. To show this, we shall write the kinetic energy equation and integrate it over the periodic domain.

Although we do not carry a kinetic energy equation in the simulation, its effect is implicit. The equation is formed from the mass and momentum equations. Therefore, what we do with these equations numerically is reflected in the kinetic energy behavior. Applying the chain rule to the time derivative of the kinetic energy shows

$$\frac{\partial}{\partial t} \rho \frac{u_i u_i}{2} = u_i \frac{\partial}{\partial t} \rho u_i - \frac{u_i u_i}{2} \frac{\partial}{\partial t} \rho \tag{2.2.1}$$

where we see the appearance of $\frac{\partial}{\partial t} \rho u_i$ and $\frac{\partial}{\partial t} \rho$ for which we solve equations.

Integrating the kinetic energy equation over the domain, we find (with zero viscosity)

$$\int_D \frac{\partial}{\partial t} \rho \frac{u_i u_i}{2} d\vec{x} + \int_D u_i \frac{\partial}{\partial x_j} \rho u_i u_j d\vec{x} + \int_D u_i \frac{\partial}{\partial x_i} P d\vec{x} -$$
$$- \int_D \frac{u_i u_i}{2} \frac{\partial}{\partial x_j} \rho u_j d\vec{x} = 0 \tag{2.2.2}$$

Because of the periodic domain, the integral of all quantities that appear totally inside a spatial derivative (divergence quantities) are zero. In addition, all terms that are evaluated on the boundaries, such as the constants of integration are also zero for the same reason. This is true both analytically and numerically, so those terms are not written here.

Integration by parts shows that

$$\int_D u_i \frac{\partial}{\partial x_j} \rho u_i u_j \, d\vec{x} - \int_D \frac{u_i u_i}{2} \frac{\partial}{\partial x_j} \rho u_j d\vec{x} = 0 \qquad (2.2.3)$$

so that (2.2.2) becomes

$$\int_D \frac{\partial}{\partial t} \rho \frac{u_i u_i}{2} \, d\vec{x} + \int_D u_i \frac{\partial}{\partial x_i} P \, d\vec{x} = 0 \qquad (2.2.4)$$

Therefore, the only net contribution to the time development of the kinetic energy is the pressure term in (2.2.4). The convective terms have no net effect. We need this behavior in the numerical simulation.

Integrations are carried out numerically by summations. Mansour (1978) has shown that summation by parts holds for a wide variety of numerical methods. If we rewrite the convective terms as

$$\frac{\partial}{\partial x_j} \rho u_i u_j = \frac{1}{2} \frac{\partial}{\partial x_j} \rho u_i u_j + u_i \frac{\partial}{\partial x_j} \rho u_j + \rho u_j \frac{\partial}{\partial x_j} u_i \qquad (2.2.5)$$

then summation by parts is valid and (2.2.3) is satisfied numerically. We then, numerically, have the correct behavior for the kinetic energy that was described analytically in Eq. (2.2.4).

As a side benefit, we have regained the conservation of total energy. Recall from (1.2.5) that the total energy is the sum of the internal energy, $(P/(\gamma-1))$, and the kinetic energy, $\rho(u_i u_i/2)$. Therefore, the total energy behavior is determined by how we treat the mass, momentum, and pressure equations. Writing the time derivative of the total energy and integrating over the domain, we have

$$\int_D \frac{\partial}{\partial t} \rho e \, d\vec{x} = \frac{1}{(\gamma-1)} \frac{\partial}{\partial t} P \, d\vec{x} + \int_D \frac{\partial}{\partial t} \rho \frac{u_i u_i}{2} \, d\vec{x} \qquad (2.2.6)$$

16

We have just discussed the numerical behavior of the last term. It is represented by (2.2.4). The second term is obtained by integrating the pressure equation (2.1.10), resulting in

$$\int_D \frac{1}{(\gamma-1)} \frac{\partial}{\partial t} P \, d\vec{x} + \frac{\gamma}{(\gamma-1)} \int_D P \frac{\partial u_i}{\partial x_i} \, d\vec{x} + \frac{1}{(\gamma-1)} \int_D u_i \frac{\partial}{\partial x_i} P \, d\vec{x}$$

$$= \int_D \frac{\partial u_i}{\partial x_j} \tau_{ij} \, d\vec{x} - \int_D \frac{\partial q_j}{\partial x_j} \, d\vec{x} \qquad (2.2.7)$$

Upon adding (2.1.10) with the appropriate viscous terms to (2.2.7), we find that the time derivative of the integrated total energy is

$$\int_D \frac{\partial}{\partial t} \rho e \, d\vec{x} + \int_D \left[u_i \left(\frac{\partial P}{\partial x_i} + \frac{\gamma}{(\gamma-1)} P \right) \frac{\partial u_i}{\partial x_i} + \frac{1}{(\gamma-1)} u_i \frac{\partial}{\partial x_i} P \right] d\vec{x}$$

$$= \int_D u_i \frac{\partial}{\partial x_j} \tau_{ij} + \frac{\partial u_i}{\partial x_j} \tau_{ij} \, d\vec{x} \qquad (2.2.8)$$

Since numerical summation by parts holds, we find that

$$\int_D \frac{\gamma}{(\gamma-1)} u_i \frac{\partial P}{\partial x_i} + P \frac{\partial u_i}{\partial x_i} \, d\vec{x} = 0$$

$$\int_D u_i \frac{\partial}{\partial x_j} \tau_{ij} + \frac{\partial u_i}{\partial x_j} \tau_{ij} \, d\vec{x} = 0 \qquad (2.2.9)$$

and therefore, numerically,

$$\int_D \frac{\partial}{\partial t} \rho e \, d\vec{x} = 0 \qquad (2\text{-}2\text{-}10)$$

as it is analytically, so that we have regained total energy conservation.

This modification (2.2.5) to the equations is completely independent of the coordinate transformation. We use both ideas in conjunction in the simulations.

2.3 Summary of the Equations

The previous two sections describing the coordinate transformation and the conservation properties provide the basis for the simulation. Since virtually all tensor equations that we shall discuss after this point have been transformed by the method of Section 2.1, we make the following definition. Recall from (2.1.5) that

$$\frac{\partial}{\partial x_j^r} \rightarrow B_{kj} \frac{\partial}{\partial x_1^r} \qquad (2.3.1)$$

We shall absorb the B_{kj} into the derivative definition and drop the primes. After this point, when we write $\frac{\partial}{\partial x_i}$ the transform is implicit in the derivative. For example, in the shear flow

$$\frac{\partial}{\partial x_i} \rightarrow \begin{cases} \dfrac{\partial}{\partial x_1} & ; \quad i = 1 \\[2mm] \dfrac{\partial}{\partial x_2} - St \dfrac{\partial}{\partial x_1} & ; \quad i = 2 \\[2mm] \dfrac{\partial}{\partial x_3} & ; \quad i = 3 \end{cases} \qquad (2.3.2)$$

This notation will be used unless specified otherwise. Keeping this definition in mind, we present the equations as simulated.

Mass Equation

$$\frac{\partial}{\partial t} \rho + (\rho u_i) = 0 \qquad (2.3.3)$$

Momentum Equations

$$\frac{\partial}{\partial t} (\rho u_i) + \frac{1}{2} \left[(\rho u_i u_j)_{,j} + u_i (\rho u_j)_{,j} + \rho u_j u_{i,j} \right]$$

$$\qquad (2.3.4)$$

$$+ P_{,i} = - \delta_{11} S(\rho u_2) + \mu \left[u_{i,jj} + \frac{1}{3} u_{j,ij} \right]$$

Pressure Equation

$$\frac{\partial}{\partial t} P + \gamma P u_{i,i} + u_i P_{,i} = u_{i,j} \tau_{ij} - q_{j,j} + \mu \left[S^2 + S(u_{2,1} + u_{1,2}) \right]$$

$$\qquad (2.3.5)$$

where

$$S = \frac{\partial U}{\partial y} \quad \text{(mean velocity gradient)}$$

$$\tau_{ij} = \mu \left[u_{i,j} + u_{j,i} - \frac{2}{3} \delta_{ij} u_{k,k} \right] \tag{2.3.6}$$

$$q_{j,j} = - \kappa\, T_{,jj} \tag{2.3.7}$$

It should be emphasized that numerical considerations influenced the form that these equations (2.3.3) to (2.3.7) take, but they are in analytic form, with no approximations. The numerical method used to advance the flow fields in time is discussed in the next section.

2.4 Desire for High Time and Spatial Accuracy

These simulations are time-dependent and three-dimensional. It is necessary to choose numerical methods to compute the spatial derivatives and to follow the development in time. As stated in Section 1.5, we desire as accurate a simulation as possible, if the flow fields are to be used as a data base.

Before discussing the numerical methods, we must discuss the concept of stiffness. The one-dimensional Euler or inviscid Navier-Stokes equations serve to illustrate this property. The equations are

$$\frac{\partial}{\partial t} \rho + u \frac{\partial}{\partial x} \rho + \rho \frac{\partial}{\partial x} u = 0 \tag{2.4.1}$$

$$\frac{\partial}{\partial t} u + u \frac{\partial}{\partial x} u + \frac{1}{\rho} \frac{\partial}{\partial x} P = 0 \tag{2.4.2}$$

$$\frac{\partial}{\partial t} P + \gamma P \frac{\partial}{\partial x} u + u \frac{\partial}{\partial x} P = 0 \tag{2.4.3}$$

Eqs. (2.4.1)-(2.4.3) can be rewritten in vector form

$$\frac{\partial}{\partial t} \vec{Q} + \underline{J} \frac{\partial}{\partial x} \vec{Q} = 0 \tag{2.4.4}$$

where

$$\vec{Q} = \begin{bmatrix} \rho \\ u \\ P \end{bmatrix} \quad ; \quad \underline{J} = \begin{bmatrix} u & \rho & 0 \\ 0 & u & \rho^{-1} \\ 0 & \gamma P & u \end{bmatrix} \tag{2.4.5}$$

A similarity transformation exists (Warming, 1975) that converts the Jacobian matrix, $\underline{J}$ to a diagonal form. Let:

$$\underline{P}^{-1} \underline{J} \, \underline{P} = \underline{\Lambda} \tag{2.4.6}$$

where Λ is a diagonal matrix containing the eigenvalues of $\underline{J}$ and $\underline{P}$ is the corresponding eigenvector matrix. It is found that:

$$\underline{\Lambda} = \begin{bmatrix} u & 0 & 0 \\ 0 & u+c & 0 \\ 0 & 0 & u-c \end{bmatrix} \quad ; \quad \frac{\gamma P}{\rho} = c^2 \tag{2.4.7}$$

where u is the convective speed and c the speed of sound. This diagonalization is used on the nonlinear equation (2.4.4) only to show the various speeds at which information propagates. With a nonlinear equation it is not useful for the solution process, because the eigenvector matrix P varies with time.

There are several characteristic speeds at which information propagates: the convective and acoustic speeds and their sum and difference. In homogeneous turbulent flows, the fluctuating velocity, i.e., the convective speed u, is usually much less than the acoustic speed c. It is believed that the flow develops at a rate corresponding to the convective speed. However, in explicit numerical methods the size of the allowable time step is limited by events that develop at a rate corresponding to the acoustic speed. Hence, with these methods, numerical stability requires a very small time step (and consequently many time steps) so the cost will be high.

This can be illustrated by solving the linearized form of (2.4.5) where $\underline{J}$ is made constant by linearizing about the initial conditions. We subject the solution to periodic boundary conditions and a given initial condition Q_0.

Assuming that the equations have periodic solutions, we expand the solution in spatial Fourier transforms. Since this is a linear problem,

all Fourier modes behave independently. Therefore, for simplicity we choose a single representative mode associated with wave number k.

Fourier transforming the linearized version of (2.5.5) results in

$$\frac{\partial}{\partial t}\begin{bmatrix}\hat{\rho}\\\hat{u}\\\hat{P}\end{bmatrix} + ik\begin{bmatrix}u_o & \rho_o & 0\\0 & u_o & \rho_o^{-1}\\0 & \gamma P_o & u_o\end{bmatrix}\begin{bmatrix}\hat{\rho}\\\hat{u}\\\hat{P}\end{bmatrix} \qquad (2.4.9)$$

which is a coupled set of linear ordinary differential equations with constant coefficients.

We solve the system (2-5-9) by diagonalizing it in the fashion of (2-4-6).

$$\underline{P}_o^{-1}\frac{\partial}{\partial t}\hat{\vec{Q}} + \underline{P}_o^{-1}\,\underline{J}_o\,\underline{P}_o\,\underline{P}_o^{-1}\,ik\,\hat{\vec{Q}} = \frac{\partial}{\partial t}\hat{\vec{R}} + ik\,\underline{\Lambda}_o\,\hat{\vec{R}} \qquad (2.4.10)$$

resulting in an uncoupled set of ordinary differential equations. The exponential solutions of (2-5-10) are subject to the initial conditions

$$\hat{\vec{R}}_o = P_o^{-1}\hat{\vec{Q}}_o \qquad (2.4.11)$$

and the solution is transformed back by

$$\hat{\vec{Q}} = P_o\hat{\vec{R}} \qquad (2.4.12)$$

resulting in

$$\hat{\vec{Q}} = e^{iu_okt}\begin{bmatrix}\rho_o\,(\frac{\gamma-1}{\gamma} + \frac{1}{\gamma}\cos(c_okt) - i\frac{u_o}{c_o}\sin(c_okt))\\c_o\,(\frac{u_o}{c_o}\cos c_okt - i\frac{1}{\gamma}\sin c_okt)\\P_o\,(\cos(c_okt) - i\frac{\gamma u_o}{c}\sin(c_okt))\end{bmatrix} \qquad (2.4.13)$$

It can be seen that information propagates at different speeds involving u_o and c_o. If a simulation is to be accurate, it must properly represent all of those propagation speeds. The stiffness of the systems (2.4.4) and (2.4.9) are characterized by the wide range in

magnitude amongst the eigenvalues of Λ requiring very small time steps for numerical accuracy. This can be a severe limitation in that the speed of sound c_o can be many times the convective speed u_o. To see a significant development in the flow could take a tremendous amount of processor time.

2-5. Numerical Method Characterization

We have spoken of explicit methods and their restrictive stability criteria in compressible flows. In recent years implicit methods have been developed (Warming & Beam, 1978; Briley & MacDonald, 1973) into very sophisticated algorithms that can greatly exceed the restrictions on time step required by explicit methods.

Naturally, we are interested in such methods, as they could significantly reduce the computer time required. However, some procedure for comparing the behavior of the various methods has to be chosen. We choose the von Neumann analysis, (Lomax, 1967). This method is illustrated by application to two very simple numerical methods, one explicit and one implicit.

We choose a linear test equation, the linear form of the viscous Burger's equation.

$$\frac{\partial}{\partial t} u + a \frac{\partial u}{\partial x} = \nu \frac{\partial^2}{\partial x^2} u \qquad (2.5.1)$$

We again impose periodic boundary conditions and Fourier transform the equation in space:

$$\frac{\partial}{\partial t} \hat{u} + (ika + \nu k^2) \hat{u} = 0 \qquad (2.5.2)$$

The solution is:

$$\hat{u} = u_o \, e^{-(ika+\nu k^2)t} \qquad (2.5.3)$$

At $t = nh$, the solution is:

$$\hat{u}^n = u_o \left[e^{-(ika+\nu k^2)h} \right]^n \qquad (2.5.4)$$

22

Equation (2.5.4) shows that the solution at time (n+1) is related to time (n) by the constant factor:

$$\alpha = e^{-(ika+\nu k^2)h} = e^{-\lambda} = 1 - \lambda + \frac{1}{2}\lambda^2 - \frac{1}{6}\lambda^3 + \ldots (2.5.5)$$

The factor α holds the information about how the solution develops in time and space. All numerical methods produce an approximation to this factor, and their performance can be evaluated and compared by how well they approximate this exact linear solution.

The spatial derivative information is represented by the wave number, k. All difference methods produce an approximation to k, so we may include their effect on the numerical solution by introducing the "modified wave number" k' and using it to replace the exact k in the following analysis. We show how k' is related to k as follows.

For periodic solutions, the spatial derivatives can be represented in a general way by a discrete Fourier transform. Let

$$f(x_j) = \sum_{n=-(N/2)}^{+(N/2)-1} \hat{f}(k_n) e^{ik_n x_j} \qquad (2.5.6)$$

Take the derivative of (2.5.6) and equate it to, for example, a central finite difference.

$$\frac{\partial}{\partial x} f(x_j) = \sum_{n=(-N/2)}^{(+N/2)-1} ik_n \hat{f}(k_n) e^{ik_n x_j} \qquad (2.5.7)$$

$$\frac{f(x_{j+1}) - f(x_{j-1})}{2\Delta x} = \sum_{n=(-N/2)}^{(N/2)-1} \hat{f}(k_n) \frac{e^{ik_n x_{j+1}} - e^{ik_n x_{j-1}}}{2\Delta x}$$

$$= \sum_{n=(-N/2)}^{(N/2)+1} \hat{f}(k_n) e^{ik_n x_j} \frac{e^{ik_n \Delta x} - e^{-ik_n \Delta x}}{2\Delta x}$$

$$= \sum_{n=(-N/2)}^{(N/2)+1} \frac{i \sin k_n \Delta x}{\Delta x} \hat{f}(k_n) e^{ik_n x_j} \qquad (2.5.8)$$

23

Comparison of (2.5.7) and (2.5.8) shows them to be identical if

$$k_n = \frac{\sin k_n \Delta x}{\Delta x} = k'_n \qquad (2.5.9)$$

Hence the concept of a modified wave number as used by Mansour (1978). The modified wave numbers for other difference schemes can be derived in a similar manner. Therefore, the characteristics of each type of differencing scheme can be analyzed in a general sense by using an equation like (2.5.10) to represent a derivative.

$$\frac{\partial}{\partial x} f(x_j) = \sum_{n=(-N/2)}^{(N/2)-1} ik'_n f(k_n) e^{ik_n x_j} \qquad (2.5.10)$$

We can illustrate the behavior of some finite-difference schemes by plotting the modified wave number, k', against the analytic wave number, k. This is done in Fig. 2-1, where we show the behavior for second- and fourth-order central approximations to the first derivative. We also show the pseudo-spectral derivative behavior where discrete Fourier transforms are used directly, to calculate the derivative.

A perfect numerical derivative is represented by a 45° line on Fig. 2.1. It can be seen that the behavior of the fourth-order method is better than that of the second order method, but both methods do not represent the high wave numbers or the small-scale structure well. The pseudo-spectral method is exact up to the maximum wave number representable on the mesh. Higher wave numbers in the solution are misrepresented as lower wave numbers. They masquerade as contributions to resolvable wave numbers; hence they are called aliased. With the pseudo-spectral method, care must be taken not to allow information into wave numbers greater than this maximum, or the solution accuracy will deteriorate and instability can result. The pseudospectral method is far more accurate than the finite-difference methods, but is strictly limited to periodic flows. These derivatives are the most suitable for our simulations.

Analysis for a Simple Explicit Method: Euler

The Euler explicit method represents the time advance.

$$\hat{u}^{n+1} = \hat{u}^n + h \frac{\partial}{\partial t} \hat{u}^n \qquad (2.5.11)$$

Using Eqs. (2.5.1), (2.5.2), and (2.5.11),

$$\hat{u}^{n+1} = \alpha_{EE}\hat{u}^n = \hat{u}^n - h(ik\alpha + \nu k^2) \hat{u}^n$$

$$\alpha_{EE} = 1 - (ik\alpha + \nu k^2)h = 1 - \lambda \qquad (2.5.12)$$

It can be seen that (2.5.12) approximates (2.5.5) only to first order in λ --hence its classification as a first-order method. Other measures of the method's behavior occur in dissipation error and phase error, as illustrated below.

Let

$$C = k\,\alpha h \quad ; \quad V = \frac{k'^2 h}{\nu} \qquad (2.5.13)$$

C and V are the Fourier space equivalents of, respectively, the Courant number and the viscous stability number; they depend on both the time step h and the modified wave number k'.

In Fig. 2.2, V has been set equal to zero. The two curves show the behavior of α and α_{EE} as the Courant number C increases. The analytic solution α neither decays nor grows in magnitude, but the Euler solution grows monotonically with time. It is unconditionally unstable for $V = 0$. The argument of α_{EE} can be at most $\pi/2$, but the argument of α increases indefinitely. Phase information is increasingly inaccurate as C increases.

Figure 2.3 illustrates the behavior of α and α_{EE} when $C = 0$. In this case the solution should simply decay. It can be seen that α_{EE} follows α fairly closely up to about $V = 0.3$ and then diverges, and its magnitude finally becomes greater than 1 at $V = 2.0$, after which the method is unstable.

25

Dissipation error (actually, antidissipation or growth) is evident in Fig. 2.2 in that the magnitude of α_{EE} does not remain 1.0, and in Fig. 2.3 in that the viscous dissipation is inaccurately represented for higher viscous stability numbers. For general $\lambda = (iC + V)$, these effects work in combination.

Simple Implicit Method: Crank-Nicholson

We next present a simple implicit method. Certain advantages of implicit methods are shown by the Crank-Nicholson method. It will also be shown why methods of this type are insufficient for accurate time-dependent simulations when used with time step greater than the explicit stability condition.

The Crank-Nicholson method and implicit methods in general use the value of the unknown time derivative at the new time step. This involves solution of coupled equations which must be simultaneously solved, hence the designation "implicit." Crank-Nicholson is represented by:

$$\hat{u}^{n+1} = \hat{u}^n + \frac{1}{2} h \left[\frac{\partial}{\partial t} \hat{u}^{n+1} + \frac{\partial}{\partial t} \hat{u}^n \right] \qquad (2.5.14)$$

Analysis similar to (2.5.4) and (2.5.12) produces

$$\alpha_{CN} = \frac{(1 - \frac{1}{2} \lambda)}{(1 + \frac{1}{2} \lambda)} = 1 - \lambda + \frac{1}{2} \lambda^2 - \frac{1}{4} \lambda^3 + \ldots \qquad (2.5.15)$$

which approximates (2.5.4) to second order in λ. Figure 2.4 shows the phase angle θ of α_{CN} when $V = 0$ and Fig. 2.5 the magnitude of α_{CN} when $C = 0$.

With $V = 0$, the magnitudes of α and α_{CN} are identically equal to 1.0, for all values of C. In other words, Crank-Nicholson produces neutrally stable solutions for any size time step. Fig. 2.4 plots the arguments of α and α_{CN}. It can be seen that, while Crank-Nicholson solutions are stable for Courant numbers greater than 1.0, their accuracy as represented by phase information can be very poor (likewise for other implicit methods).

26

Figure 2.5 shows that for C = 0 the solution can be alternately positive and negative at large viscous stability numbers because α_{CN} becomes negative. While this behavior is stable, it is an incorrect representation of the true behavior of the solution (2.5.4).

We can apply this type of reasoning to more complicated sets of test equations such as (2.4.9) that have several propagation speeds. One finds that, if all motions in the problem are to be simulated accurately, the Courant number based on the fastest propagation speed must be of the order of magnitude of 1.0 or less. Also, the viscous stability number must be 1.0 or less.

Since implicit methods require more work per time step, their restriction to small Courant and viscous stability numbers makes them inefficient. We therefore abandon implicit methods for our time-accurate simulations.

Some work was performed in incorporating the previously discussed conservation properties into an implicit method. Additional problems were encountered in designing an efficient implicit algorithm that incorporated highly accurate spatial derivatives. As stated above, the implicit methods are not suitable for highly accurate time-dependent simulations. They lack sufficient accuracy for a time-accurate solution. They may find use in simulations of variable density, low Mach number flow, where the acoustic speeds are unimportant in the solution, but are troublesome numerically.

2.6 Advanced Explicit Methods

There are two fully explicit methods that were finally considered. MacCormack's (1969) method was analyzed and programmed into a three-dimensional code to run on a CDC 7600. The final method of choice, however, was a combination of the classical fourth-order Runge-Kutta with spatial derivatives based on fast Fourier transforms, the pseudospectral method.

MacCormack's method is well known, having been successfully used in many compressible flow codes over the last decade. It is a modification of a Lax-Wendroff scheme that incorporates forward and backward differ-

ences alternately on the predictor and corrector steps. Its formal accuracy is second order in both space and time. The reader is referred to the original paper, in which the method is laid out and estimates made of its accuracy and stability.

For purposes of comparison, we shall apply the analysis developed in the previous section to compare these two methods.

In most numerical algorithms for partial differential equations, the method for representing the spatial derivatives can be discussed separately from the method for the time advance. To a limited extent, one is free to choose combinations. MacCormack's method, however, is a specific combination of the two and derives its unique qualities from this combination of methods.

Following the analysis in Section 2.5, the computational root of MacCormack's method is

$$\alpha = 1 - V' - \frac{1}{2} C'^2 + \frac{1}{2} V'^2 + i(C'' V' - C'') \qquad (2.6.1)$$

where

$$V' = h\nu k_c'^2 \quad ; \quad C' = hak' \quad ; \quad C'' = hak'' \qquad (2.6.2)$$

and

$$k' = \frac{\sin k \frac{\Delta x}{2}}{\Delta x/2} \quad ; \quad k'' = \frac{\sin k\Delta x}{\Delta x} \qquad (2.6.3)$$

The forward and backward differences result in the two modified wave numbers of (2.6.3). These wave numbers correspond to central difference approximations to the first derivative that are taken over mesh spacings of $\Delta x/2$ and Δx, respectively. The highly dissipative behavior of this method results from the combination of modified wave numbers (2.6.3).

Figure 2.6 shows the computational root for zero viscosity (V' = 0). Both time and spatial behavior are represented. Keeping in mind that the exact solution lies on the unit circle, it can be seen that for high wave numbers (kΔ approaching π) or large time steps, the

28

dissipation is severe without the inclusion of viscous terms. If an initial flow field containing all resolvable length scales is advanced by this method, the smallest scales (highest wave numbers) will swiftly disappear through the action of the numerical method.

It was found in an isotropic homogeneous flow that this numerical viscosity was sufficient to maintain a stable calculation at a Taylor microscale Reynolds number of several thousand. At the relatively small mesh size of $16 \times 16 \times 16 = 16^3$, this is unphysical. In addition, statistics that have to do with high wavenumbers, such as velocity derivative skewness, were incorrect in comparison with experiment.

Since an accurate method for all resolvable wave numbers is desired, this method must be abandoned for our purposes.

2.7 Method of Choice

The numerical method that we have chosen has a combination of the highest time accuracy that can conveniently be implemented on the ILLIAC IV and the highest spatial accuracy. We shall use fourth-order Runge-Kutta for the time advance and the pseudo-spectral method for the spatial derivatives. For completeness we show both.

Fourth-order Runge-Kutta is written:

$$u^* = u^n + \frac{\Delta t}{2} \frac{\partial}{\partial t} u^n$$

$$u^{**} = u^n + \frac{\Delta t}{2} \frac{\partial}{\partial t} u^*$$

$$u^{***} = u^n + \Delta t \frac{\partial}{\partial t} u^{**}$$

$$u^{n+1} = u^n + \frac{\Delta t}{6} \left[\frac{\partial}{\partial t} u^n + 2 \frac{\partial}{\partial t} u^* + 2 \frac{\partial}{\partial t} u^{**} + \frac{\partial}{\partial t} u^{***} \right]$$

(2.7.1)

and the pseudo-spectral spatial derivatives directly implement

$$\frac{\partial}{\partial x} f(x_j) = \sum_{n=(-N/2)}^{(+N/2)-1} ik_n \hat{f}(k_n) e^{ik_n x_j}$$

(2.7.2)

by means of the Fast Fourier Transform algorithm.

The computational root for pseudo-spectral fourth-order Runge Kutta is, by the kind of analysis used above.

$$\alpha = 1 - \lambda + \frac{1}{2} \lambda^2 - \frac{1}{6} \lambda^3 + \frac{1}{24} \lambda^4 \qquad (2.7.3)$$

For zero viscosity $(v = 0)$, this root is depicted in Fig. 2.7. For Courant numbers less than one, the method is very accurate, since it closely follows the analytic root. In using this method, the time step is chosen such that the Courant number associated with the maximum wave number is one. Courant numbers associated with the lower wave numbers are then less than one, and the computational root more accurately follows the analytic root for these larger scale motions.

Figure 2.8 shows behavior of the viscous terms alone $(C = 0)$. In this combination of methods, the computational root accurately approximates the analytic root up to a viscous stability number of one.

The combination of fourth-order Runge-Kutta and pseudo-spectral spatial derivatives requires a large number of operations (and consequently CPU time) per time step. Additionally, it requires four levels of storage in the computer for intermediate predicted steps, placing a burden on the memory resources of the machine for large meshes. This compares to two levels of storage for second-order methods. However, we are able to use the method at a Courant number of one, in contrast to many common second-order explicit methods that must have Courant numbers much less than one. Although the method requires more CPU time per time step, its time steps are correspondingly longer than any suitable second-order method.

We are still limited by accuracy constraints to a Courant number of one. To perform a complete simulation in a compressible flow with the large mesh system that we wish to use will absorb an incredible amount of processor time. In the next chapter we show how this method is used to solve Eqs. (2.3.3)-(2.3.7) in a code for the ILLIAC-IV computer at NASA-Ames Research Center. We shall discuss how the code is constructed and tested and show the amount of CPU time that it absorbs.

Chapter III

PROGRAM DEVELOPMENT AND TESTING ON THE ILLIAC IV

The construction and testing of the computer code are described in this chapter, as well as the characterization of a typical run.

3.1 The ILLIAC IV

The ILLIAC IV is a large, one-of-a-kind, parallel, processing computer built by Burroughs. Codes designed for the ILLIAC IV can be run only on it (although the algorithms could be converted to other vector computers). Illiac IV is composed of 64 individual computers called PEs that operate in lockstep under the control of a central managing computer called the CU. The PEs have access to the large rotating disk memory that contains the bulk of the memory on the computer. The in-core memory of each PE is quite small, so all of the flow field data resides on the disk and is brought into core a small piece at a time to be operated upon. The efficiency with which this transfer is accomplished has a great effect on how fast a code will run. This operation is directed by a set of instructions called a disk map that controls the transfer of specific data between the disk memory and core.

3.2 The Pencil Data Management System

The flow field must be divided into regions that are transferred into core one at a time. Because the fast Fourier transform is used so extensively in this code, data from a line of mesh points that extend entirely across the computational box must be in core all at once. the memory-management system chosen is the "Pencil System," as developed by Pulliam and Lomax (1979).

The ILLIAC IV is run in 32-bit word mode, which allows the pencil size to be $8 \times 16 \times$ (mesh size) words in size. This is depicted in Fig. 3.1. The spatial derivatives are handled, in order, such that all derivatives in the x-direction are performed while the pencils

in that direction are in core. The other two directions are handled consecutively, in a similar manner. A typical predictor or corrector step involves processing each of the x pencils in turn, then each of the y pencils, and then the z pencils. Each set of pencils requires one complete pass over the entire flow field. Since fourth-order Runge-Kutta requires four function evaluations per time step, the code requires twelve passes over the flow field. While this is very time-consuming, the pencil system allows great freedom in constructing means of analyzing the simulated flow fields and allows easy modification of the code for other purposes.

3.3 Coordinate Remeshing

The linear coordinate transformation as described in Chapter II is analytic and is incorporated into the equations in its entirety. This transformation allows the transformed coordinates x and y to become almost parallel after a length of time. To avoid accuracy problems in the code, it is necessary to stop the calculation after a time, shift the sheared mesh back to the other side of Cartesian, and then proceed again (Fig. 3.2). It has been found that this remeshing process is essentially exact if the calculation is stopped when the top of the computational box has moved one-half period (St = 0.5). The mesh is then shifted back one period to (St = -0.5). When the remeshing is done at this point, there is no interpolation necessary, as the points of the new and old meshes fall exactly on top of each other. There is one numerical problem associated with this. Because the orientation of the mesh in the y-direction is changed, there is aliasing in that direction associated with remeshing. Let a particular Fourier mode be represented in two dimensions on the second mesh in Fig. 3.2 as

$$u(x,y) = \hat{u}(k_1,k_2) e^{i(k_1 x + k_2 y)} \qquad (3.3.1)$$

(Recall that the mesh system shears with the mean velocity.) If the remeshing is done at St = 0.5, then the new coordinates, as measured on the third mesh in Fig. 3.2, are

$$x' = x + y \rightarrow x = x' - y'$$

$$(3.3.2)$$

$$y' = y$$

Substituting (3-3-2) into (3-3-1), we find that the same Fourier mode is represented on the "remeshed" mesh as

$$u(x',y') = \hat{u}(k_1,k_2) \, e^{ik_1 x'} \, e^{i(k_2-k_1)y'} \qquad (3.3.3)$$

If (k_2-k_1) falls outside the range of available wave numbers, that information will appear in a lower wave number in the y-direction. This problem is eliminated by filtering the high wave number parts of the solution in the y-direction both before and after the remesh process. The filtering is performed by Fourier transforming all the flow variables in y, truncating the top one-third of the wave number coefficients and retransforming back to real space. This is performed on flow fields which contain little information in the highest wave numbers and only at remeshings. It removes at most 1% of the turbulent kinetic energy. Its effect on the solution is small, and it eliminates a known source of error.

3.4 Initial Conditions

Turbulent initial conditions as used in low Reynolds number and large eddy simultions will always be somewhat artificial. There are many statistics used to describe these flows but no organized algorithm for producing these statistics in an initial flow field. The hope, that is generally borne out by numerical experiment, is that, if some statistics are enforced on the initial field, the others will develop through the action of the equations. In other words, the initial flow fields do not represent a turbulent flow field, but after being advanced for a time by the code they develop the characteristics that allow us to call them truly turbulent.

In the compressible flow, the five flow variables are completely independent and subject only to the restriction that both density and pressure be positive.

The variables may be thought of as being in nondimensional form. They are non-dimensionalized on a sound speed c_0, a density ρ_0, and the computational box length L_0. Because of this nondimensionalization the velocities are closely related in magnitude to Mach numbers. The average value of the computational density is one, as is the computational pressure. This makes the average initial computational sound speed c (different from c_0) of magnitude 1.18.

$$c^2 = \gamma \frac{P}{\rho} \, , \quad c = \sqrt{\gamma} = 1.18 \quad\quad (3.4.1)$$

We have chosen to start each calculation with a velocity divergence free field, as in an incompressible simulation. Since the initial flow fields are artificial, any dilatation introduced is unphysical. If any is to appear, it should grow through the action of the equations of motion. Wray (1980) has found in two-dimensional simulations of isotropic turbulence that these initial divergences decay very quickly, leaving behind density variations and a flow that behaves almost incompressibly. In the shear flow we felt it best to allow compressible characteristics to develop under the forcing action of the mean shear rather than introducing them as Wray did in the unforced isotropic flow.

The procedure for producing the initial velocity field is as follows. We first choose a completely arbitrary random set of velocities through the action of a random number generator. We add the gradient of a yet to be determined potential function onto this velocity field.

$$u_i^S = u_i^R + \frac{\partial}{\partial x_i} \phi \quad\quad (3.4.2)$$

where u_i^S is the solenoidal (dilatation-free) velocity field and u_i^R is the original random field. Since u_i^S is solenoidal, it disappears when we take the divergence of (3.4.2), producing a Poisson equation for ϕ.

$$\nabla^2 \phi = - \frac{\partial u_j^R}{\partial x_j} \qu\quad\quad (3.4.3)$$

Because of the periodic boundary conditions and the availability of fast Fourier transforms, we have a particularly convenient and accurate way to solve this equation. It is first Fourier transformed.

$$- k^2 \hat{\phi} \ = \ - i k_j \hat{u}_j^R \qquad (k^2 = k_j k_j)$$

$$\hat{\phi} \ = \ \frac{i k_j \hat{u}_j}{k^2} \qquad\qquad (3.4.4)$$

Inverse Fourier transforming provides the solution ϕ. The constant of integration is fixed by setting the zero wave number coefficient to zero.

The velocity field u_i^s is solenoidal, real, and free of mean velocity but has a white noise type of velocity spectrum. We take this spectrum by transforming the velocities into Fourier space and integrating the kinetic energy in spherical shells to produce a 3-D energy spectrum.

$$E(k) \ = \ < \hat{u}_i(\vec{k}) \ \hat{u}_i^*(\vec{k}) > \qquad\qquad (3.4.5)$$

Here, $< \ >$ indicates an integration over all directions, leaving the kinetic energy as a function of the wave number magnitude alone.

All of the velocities in each spherical shell are then adjusted by the same constant (a function of k) to enforce a specified energy spectrum, $E(k)$ onto the flow field.

We also enforce that the time derivative of the divergence be zero, as in an incompressible flow, so that there is no violent behavior when the simulation starts. This is done by specifying the pressure field through another Poisson equation. We take the divergence of the momentum equations

$$\frac{\partial}{\partial x_i} \frac{\partial}{\partial t} \rho u_i + \frac{\partial}{\partial x_i} \frac{\partial}{\partial x_j} \rho u_i u_j + \nabla^2 \rho \ = \ \frac{\partial}{\partial x_i} \frac{\partial}{\partial x_j} \tau_{ij} \qquad (3.4.6)$$

For the initial flow field with zero dilitation and constant density, (3.4.6) becomes

$$\nabla^2 p = - \frac{\partial u_i}{\partial x_j} \frac{\partial u_j}{\partial x_i} \qquad\qquad (3.4.7)$$

which we solve in the same manner as (3.4.3).

All flow fields used as initial conditions were set up in this manner. Initially they are incompressible, but their development is then guided by the full Navier-Stokes equations. Velocity divergences develop quickly.

3.5 Performance of the Code

There are actually three codes involved in the simulations. The severe limitation on in-core memory of each processing element (PE) has forced the dissection into codes:

1. TB-LOD.IHICS. Creates and stores the initial flow fields.
2. TB-LOD.HSTA. The time advance code, which does some preliminary data reduction.
3. TB-LOD.REDUCE-DATA. Performs the bulk of the data reduction.

The mnemonics TB is the author's identifier on the ILLIAC system. The LOD indicates an executable load module. IHICS stands for isotropic homogeneous initial conditions. HSTA means homogeneous shear time advance.

All three codes operate with the same pencil data-management system. This system can operate with three mesh sizes, 16^3, 32^3, or 64^3. For the time-advance load module, the code requires 28 words of memory for each mesh point. In 64^3, this is 7.34 million words. Including additional disk areas needed for data output and temporary storage, the management system allocates 12.17 million words out of an available 15.9 million. Although the data-reduction load module does not require the large amount of memory that the time-advance module needs, this storage capability is very convenient in processing the simulated flow fields.

The time-advance load module consumes most of the central processor time. In 32^3 form, this load module requires 8.5 seconds per time step. In 64^3 form, it requires 89 seconds per time step. Most of the work was performed with the 64^3 version.

There are eight simulations associated with this thesis. The shortest, corresponding to the highest shear rate, took 7.5 hours. The longest, the isotropic simulation, took 18.0 hours. This does not include all the data reduction, which was also performed on the Illiac.

3.6 Testing the Code

As was stated in Chapter II, one must be particularly careful to run checks on the code to ensure that it is properly constructed. To this end, checks were performed in three categories. The code was written to be quite readable and was thoroughly sight checked. The second category involved simulation of two-dimensional Taylor-Green problems, which are known to be exact solutions to the incompressible flow equations. The third category involved simulation at low Mach number of isotropic turbulence and comparison of some statistics with experiment.

3.6.1 Two-Dimensional Taylor-Green Problems

There is an exact analytic solution to the two-dimensional, incompressible, Navier-Stokes equations. It is known as the two-dimensional Taylor-Green solution. The solution is as follows:

$$u = - A^{1/2} \cos k_1 x \sin k_2 y \; e^{-(k_1^2 + k_2^2) \nu t}$$

$$v = A^{1/2} \sin k_1 x \cos k_2 y \; e^{-(k_1^2 + k_2^2) \nu t} \qquad (3.6.1)$$

$$P = - \frac{A}{4} (\cos 2k_1 x + \cos 2k_2 y) \; e^{-2(k_1^2 + k_2^2) \nu t}$$

The flow fields consist of 2-D vortices, arranged rectangularly, that simply decay in strength with time.

This is not an exact solution for the full compressible equations. It was thought that, for low Mach numbers, the compressible flow field should behave almost incompressibly and the solution (3.6.1) should be closely approximated by the compressible code. By numerical experiment this is true.

37

The initial conditions were Eqn. (3.6.1) at $t = 0$, $k_1 = k_2 = 1$, and $A = .05$ (about Mach = 0.04). The code was first run with a Cartesian mesh ($St = 0$). After 40 time steps the maximum deviation from the analytic solution was 1.42×10^{-5} or .028% of the maximum velocity. With the mesh sheared to $St = 1.0$, which preserves the periodic boundary conditions on the solution, the corresponding numbers are 1.47×10^{-3} and 2.94%.

The numerical solution is in quite close agreement with (3.6.1), even though it is not an exact solution of (1.2.2)-(1.2.7). These experiments were run in 16^3 and for all orientations of the initial conditions in x, y, z for the $St = 0$ mesh. For $St = 1.0$, they were performed in the x,y plane (downstream, cross-stream).

3.6.2 Low Mach Number Isotropic Turbulence

As in the previous section, it is felt that at low Mach numbers the flow fields should be virtually incompressible and therefore should produce turbulence statistics quite similar to incompressible codes and to experiment. Again this is true by numerical experiment.

A 64^3 run was performed with the shear rate set equal to zero. The initial conditions were constructed by the code TB-LOD.IHICS in the manner of Section 3.4. The initial spectrum was a box between wave numbers 8 and 16. The initial average Mach number was $M_o = .078$ and the initial Taylor microscale Reynolds number was $Re_{\lambda_{11}} = q\lambda_{11}/\nu = 40$. Figures 3.3 to 3.10 show the evolution of the flow during the simulation. Figures 3.3 and 3.4 are three-dimensional energy spectra. In each figure the lower curves are 3-D spectra of the normal stresses of the Reynolds strss tensor. It can be seen that the flow evolves from the very artificial initial spectrum to a realistic-looking low Reynolds number spectrum as the simulation proceeds. There is no linear region to represent an inertial range, but the slope does pass through the value of $-5/3$ as the wave number increases. At low k the slope passes through a value of 4, an analytic shape for low wave numbers. After wave number 32, a steeper slope in the spectrum is observed. This is a result of the way the spectra are taken. The scalar wave number k is the magnitude of the vector $\vec{k}$. The energy in each spherical

38

shell is simply summed over the number of points (samples) in that shell. After wave number 32, the shell begins to grow outside the cubic domain of $\vec{k}$ and therefore the number of contributing points decreases above $k = 32$. The decrease in energy simply reflects the decrease in sample size. No attempt is made to extrapolate beyond $k = 32$. Figure 3.5 is representative of lateral and longitudinal two-point correlations in the z-direction; z was arbitrarily chosen for display, as all directions are equivalent. The figure was produced at the same time as Fig. 3.4, $t = 7.8$. It shows the expected primarily positive behavior of the longitudinal correlation $R_{33}(0,0,r_3)$.

$$R_{ij}(r_1,r_2,r_3) = \frac{< u_i(\vec{x})\ u_j(\vec{x}+\vec{r}) >}{< u_i(\vec{x})\ u_j(\vec{x}) >} \qquad (3.6.2)$$

and the close agreement between the two lateral correlations, $R_{22}(0,0,r_3)$ and $R_{11}(0,0,r_3)$. Figure 3.6 shows the three longitudinal, one-dimensional spectra, $E_{11}(k_1)$, $E_{22}(k_2)$, $E_{33}(k_3)$. $E_{11}(k_1)$ is defined as

$$E_{11}(k) = \iint \hat{u}_1(\vec{k})\ \hat{u}_1^*(\vec{k})\ dk_2 dk_3 \qquad (3.6.3)$$

$E_{22}(k_2)$ and $E_{33}(k_3)$ are defined similarly. The similarity of the three curves shows that the flow remains quite isotropic at all wave numbers, as it should. The one-dimensional spectra are Fourier transforms of the two-point correlations. Because there is little information in the high wave number region, microscales as calculated from the correlations should be quite accurate. Figures 3.7 and 3.8 show the time evolution of the microscales and the integral scales, respectively. The Taylor microscales are defined in the usual way by fitting the osculating parabola to the two-point correlation at small separation. The integral scales are defined as twice the separation where the two-point correlation first reaches a value of 0.1. The reason for this will be explained in the next section. After $t = 5.0$, both micro- and integral scales grow almost linearly, but very slowly.

Figure 3.9 shows the time evolution of the kinetic energy and its three normal components. A power-law fit to this curve shows a best fit with a slope of about −1.25, in good agreement with theory (Hinze

39

(1975)) and experiment (CBC (1971)) for low Reynolds number isotropic turbulence.

Figure 3.10 shows the time development of the velocity derivative skewness defined as:

$$Sk_i = \left\langle \frac{\partial u_i}{\partial x_i}^3 \right\rangle \Bigg/ \left\langle \frac{\partial u_i}{\partial x_i}^2 \right\rangle^{3/2} \quad \text{(no summation)} \quad (3.6.4)$$

The skewness is associated with the energy cascade process and is measurable in the wind tunnel for the downstream direction. Its value is quoted in several experiments (Tavoularis et al. (1978)) as about -0.40.

It can be seen that all three curves in Fig. 3.10 come to asymptotic values of about -0.35 to -0.41.

Although the time-advance code is designed for compressible flow, these results give confidence that it is capable of simulating low Mach number (incompressible) turbulence. It must be able to simulate this flow before it can be used in a higher Mach number problem.

3.7 Description of a Typical Sheared Run

A typical sheared run is described, along with the limitations and troubles generally encountered. This is presented to show the limits of validity of these simulations and the criteria used to judge this validity.

As described in Section 3.4, the initial conditions used to start the simulation are quite artificial. The initial conditions are simply described as a constant density field, a dilatation-free, random, isotropic, initial velocity field with a square wave (top hat), 3-D energy spectrum, and a pressure field set according to the velocity field to maintain $\partial/\partial t(\partial u_i/\partial x_i) = 0$ at time zero. As described in the previous section, the flow field requires a certain time to develop turbulent flow field characteristics. In the isotropic flow this was judged as the time when the velocity derivative skewness reached an asymptotic value.

In the shear flow, this time was judged by several different standards. Fortunately, they all point to a common time when the flow field might truly be judged turbulent. These criteria are:

40

1. The shear stress coefficient reaches an asymptotic value.

$$\langle u'v' \rangle / \sqrt{\langle u'^2 \rangle \langle v'^2 \rangle} = \text{const} \qquad (3.7.1)$$

2. The kinetic energy is seen to increase.
3. The 3-D energy spectrum reaches an asymptotic "shape" as it changes from the initial square wave spectrum.

The last criterion is a matter of judgment, but estimates made by criterion 3 agree quite well those with criteria 1 and 2.

After this initial period, during which the flow field evolves from the artificial initial conditions, there is a period during the simulation when the judging criteria indicate that a true turbulent flow field is being simulated. These criteria will be discussed below in the description of the simulation HS64B. This period, during which the statistics are extracted from the flow field, is thoroughly discussed as the subject of Chapter IV.

The simulation gradually moves out of this valid stage into a phase in which the scales of motion grow too large for the computational box. In the homogeneous shear flow, the length scales associated with the turbulent motion are known to grow with time. This indicates that structures or eddies in the flow grow to a size where they are influenced by the imposed periodic boundary conditions. Beyond this point, the flow field is no longer representative of an infinite, homogeneous shear flow, so the simulation is stopped. This time is judged by the appearance of the two-point correlations, which are a statistical measure of the spatial relationships in the computational box. These correlations were defined in Eq. (3.6.2).

As will be discussed in Chapter IV, the time is nondimensionalized by multiplying it by the shear rate. In terms of this nondimensional time, St, all of the simulations were judged to be valid between times $St = 4.0$ and $St = 6.0$.

The simulation chosen to illustrate the history of a sheared run is labeled HS64B. As discussed in Section 3.4, the flow-field variables are nondimensionalized on a density ρ_o, a sound speed C_o, and the

computational box length L_0. Other nondimensional quantities may be formed directly from the nondimensional flow variables, in which case the original nondimensionalizing values of ρ_0, C_0, and L_0 drop out. In these terms the initial characteristics may be summed up:

1. Shear rate $S = 1.5$.

2. Initial fluctuating velocity $q = 0.1$.

3. Square wave 3-D spectrum $8 < k < 16$.

4. Box Reynolds number $Re_b = C_0 L_0 / \nu = 500$.

Some nondimensional measures:

1. Taylor microscales Reynolds number $Re_\lambda = 25.5$.

2. Average fluctuation Mach number $M = .078$.

The initial spectra appear exactly the same as Fig. 3.3, so they are not repeated here. Figure 3.11 shows the development of the coefficients associated with the off-diagonal elements of the Reynolds stress tensor. The $< u'v' >$ coefficient was defined in Eq. (3.7.1). In this shear flow the other two coefficients associated with $< u'w' >$ and $< v'w' >$ should remain zero. It can be seen that this is so to a few percent through $St = 6.0$. The shear stress coefficient associated with $< u'v' >$ starts from its isotropic value of zero at $St = 0.0$ and reaches an asymptotic value of $-.64$ by $St = 4.0$ and remains virtually flat through $St = 6.0$.

The development of the kinetic energy as a function of St is depicted in Fig. 3.12. It can be seen that it reaches a minimum at about $St = 4.5$ and increases afterward. The $< \rho u'^2 >$ component of kinetic energy reaches a minimum much earlier at about $St = 2.0$, but energy is quickly drained from this term into $< \rho v'^2 >$ and $< \rho w'^2 >$ through the action of the pressure-strain terms in the dynamic equations for these quantities.

The mechanism of kinetic energy production is obviously in operation almost from the start of the calculation, but the shear stress coefficient which represents this mechanism reaches its asymptotic value about the same time that the kinetic energy begins to increase.

Figures 3.13 and 3.14 show the 3-D energy spectra at times St = 4.0 and St = 6.0, respectively. It can be seen that they have evolved considerably from the initial spectrum and that they closely resemble each other. Kinetic energy originally present in the initial spectrum and the kinetic energy added to the flow through the action of the production term have been redistributed among the wave numbers in the 3-D spectra through the action of the nonlinear convective terms. This process fills in both the low wave numbers, $k < 8$, and the high wave numbers $k > 16$. The viscosity chosen for the simulation plays a great role in determining the shape of this spectrum (alternatively, the box Reynolds number). The nonlinear convective terms will continue to propagate kinetic energy to higher and higher wave numbers (smaller and smaller scales), unless there is sufficient viscous dissipation to change this kinetic energy into heat. If there is insufficient viscosity or, equivalently, the box Reynolds number is too high, the higher wave numbers collect too much kinetic energy, as it is not being dissipated quickly enough. The phenomenon of aliasing occurs, where information destined for higher, non-existent wave numbers returns to masquerade in, and pollute, the low wave numbers. This occurs when there is any information in the wave numbers greater than 2/3 of the maximum wave number. Figure 3.15 shows the one-dimensional, longitudinal kinetic energy spectra at time St = 6.0. It can be seen that information contained in each direction in the 2/3 k_{max} wave number (in our case $k = 21$) is two orders of magnitude less than the energy peak at low wave number.

The simulation begins to degrade when the structures in the flow grow large enough to be affected by the periodic boundary conditions. This is shown in Figs. 3.16 through 3.18. Figure 3.16 shows the two-point correlation at St = 4.0. Figure 3.16 shows the correlation at time St = 6.0 and Fig. 3.18 at St = 7.0. At St = 4.0, the curves still show almost zero correlation at Delta R = 3.2, which is half of the computaitonal box width. For a valid use of periodic boundary conditions, motions in regions separated by half the box width must be uncorrelated. By St = 7.0, the $R_{33}(0,0,r_3)$ correlation has reached 18% at the half width, indicating interference of the boundary

conditions. By limiting the maximum tolerable half-width correlation to 10%, we restrict the region of validity to $St < 6.0$.

In summary, each calculation passes through three stages:

1. Develoment away from the initial conditions.
2. Turbulent simulation.
3. Interference of the boundary conditions.

The validity of the second stage is affected by the value of the box Reynolds number. There must be sufficient viscosity to hold the energy in the high wave numbers much below that in the peak wave number. For the simulations in this thesis, we use one order of magnitude.

We have confidence that the computer codes are operating properly and now proceed to use them as a numerical wind tunnel.

In the next chapter we discuss the seven complete compressible, homogeneous, shear flow simulations and present the measurements that have been made from the simulated flow fields.

Chapter IV

CALCULATIONS AND RESULTS

The calculations and results are discussed in this chapter. The independent dimensional parameters of the flow are listed, as are the nondimensional groups formed from them. A description of the simulations that were performed is presented. We then discuss the behavior of the Reynolds stresses and the Reynolds stress equations, with particular attention paid to modeling of the various terms.

4.1 Dimensional Parameters and Nondimensional Groups

There are eight independent dimensional parameters that can be used to characterize compressible, homogeneous shear flow. They are:

1. ρ Density
2. μ Molecular viscosity
3. $q^2 = \langle u_i u_i \rangle$ Turbulent intensity
4. c Speed of sound
5. $S = dU/dy$ Mean velocity gradient (shear rate)
6. L Integral length scale ($L=L_{11}$ used throughout)
7. λ Taylor microscale
8. κ Coefficient of heat conductivity

Some of these quantities are related through the dynamics of the flow and are, therefore not truly independent.

The density is the average density in the domain, a constant. The molecular viscosity is fixed for a given simulation. The turbulent intensity is the trace of the Reynolds stress tensor divided by the density. The speed of sound is defined by $\left.\frac{\partial P}{\partial \rho}\right|_s = c^2$. For a perfect gas, $c^2 = \frac{\gamma P}{\rho}$, where the ratio of specific heats γ is 1.4. The shear rate can be chosen arbitrarily.

We define the integral length scale, L, as twice the separation at which the two-point correlation first reaches a value of one-tenth. This definition differs from the standard integral definition. The two-point correlations can have large negative loops, and therefore definite integrals of these functions can be poorly behaved. Figure 4.1 shows three correlations for a typical flow field. Harris et al. (1970)

45

encountered these problems and defined L by integrating up to the first zero crossing. His definition and ours are both portrayed. Our definition gives a length scale which is always larger than both Corrsin's and the standard one. It has been adopted for ease of calculation. The Taylor microscale is defined in the usual way by fitting the osculating parabola to the two-point correlation at small separation. The coefficient of heat conductivity is set by fixing the Prandtl number, using $\gamma = 1.4$ with the perfect gas law constant.

Dimensional analysis shows that five nondimensional groups may be formed. Three of these are shown in Table 4.1, where we also include values of these quantities found in our simulations and in experiments. We choose values of the shear number that are similar to those in high-speed mixing layers and homogeneous flow experiments. We choose a range of fluctuating Mach numbers which spans the range from incompressible flow to values observed in high-speed flows. Mesh resolution limits the Taylor microscale. We use the highest value allowed. The ratio of length scales is known to be a function of the Reynolds number. It is, therefore, not independent. In our simulations it has a value of about 4. As just stated, we have fixed the Prandtl number. In all our simulations we use $Pr = 0.74$, a value suitable for air. This leaves just three truly independent nondimensional groups that we vary during the simulations.

Other nondimensional groups can be formed from combinations of the groups in Table 4.1. For instance, SL/q times q/c is the "shear Mach number," SL/c. We mention this number because it is more akin to the conventional external flow Mach number. It represents the change in Mach number across a typical large eddy. Note we take $L=L_{11}$.

In some results we show the time-dependence. The nondimensional time is St.

4.2 Description of the Simulations Performed

Eight complete simulations were performed. Including the inevitable waste, approximately 250 hours of central processor time were consumed on the ILLIAC-IV. Seven of these simulations were homogeneous shear flows. The eighth was the low Mach number isotropic flow that was

46

described in Chapter III. We present data from the seven shear flow simulations in this chapter. As discussed in Chapter III, we start the code with artificial initial conditions, and the flow field must develop into a truly turbulent field through the action of the equations of motion. Consequently, in each simulation, there is a time before which we cannot accept the data. Correspondingly, there is a time after which the scales of motion are too large for the computational box and periodic boundary conditions are no longer appropriate. We find the flow fields to be satisfactory between nondimensional times, St, of four and six in all runs, which we hereafter designate as the "good times."

Turbulent statistics are evaluated only when St is an integer. This was done as a matter of convenience and because a short sample time would give flow fields that were not sufficiently independent. This leaves us with 21 flow fields to analyze.

Figures 4.2 and 4.3 show the 21 flow fields in the parameter space of shear number, S, fluctuating Mach number, M, and Taylor microscale Reynolds number, Re_λ.

In Table 4.2 we tabulate the variation of the three nondimensional parameters and show our labeling for each of the simulations. there is no simulation labaled HS64E (there was, but it had far too high a viscosity and was discontinued). In many cases we show plots for each of the seven simulations (seven plots), and we shall designate the plots by labels a through h. To make the plot numbers correspond to the flow labels, we always skip the label e.

Initial data reduction was performed on the ILLIAC-IV. Calculations of spectra and integrations over the 64 × 64 × 64 mesh require the entire flow field and are practical only on this machine. However, once these quantities are calculated, they are transferred to a more conventional serial computer for further processing.

The appendix presents the raw data from the ILLIAC and may be useful for further investigations. All correlation data that we present are further reduced from the appendix.

47

4.3 Averaging for Statistics; Connection between Favre and Conventional Averages

There are many types of averaging that have been used in turbulent flows. We have presented the averaged equations and our approach to solving the unaveraged equations, but the averaging process is still unspecified.

The ideal averaging process is an ensemble average, in which many realizations of the same flow are averaged. A homogeneous flow is statistically the same at each point. A volume-average over the entire mesh approximates an ensemble average. We carry out this volume average by a summation over the entire mesh and indicate the average of a by $\langle a \rangle$.

In Chapter I we spoke of the equivalence of Favre (mass weighted) and conventional Reynolds averaging in the homogeneous shear flow. This can be illustrated rather simply as follows.

Using the definitions in Chapter I, we write the total velocity as the sum of mean and fluctuating parts without specifying the type of average. Recall that the Favre average $\tilde{u}_i$ is defined by $\tilde{u}_i = \overline{\rho u_i}/\overline{\rho}$ and that the Favre and conventional fluctuating quantities, u_i'' and u_i', are the differences between the unaveraged velocity and the respective mean.

$$u_i = \tilde{u}_i + u_i'' = \overline{u}_i + u_i'$$

$$\tilde{u}_i = \overline{u}_i + (u_i' - u_i'') \tag{4.3.1}$$

Using the definitions of the averages,

$$\overline{\rho \tilde{u}_i} = \overline{\rho}\tilde{u}_i, \quad \overline{\rho \overline{u}_i} = \overline{\rho}\ \overline{u}_i, \quad \overline{u_i'} = 0, \quad \overline{\rho u_i''} = 0,$$

$$\overline{\rho \tilde{u}_i} = \overline{\rho}\ \overline{u}_i + \overline{\rho u_i'} = \overline{\rho}\ \overline{u}_i + \overline{\rho' u_i'} \tag{4.3.2}$$

or

$$\tilde{u}_i = \overline{u}_i + \frac{\overline{\rho' u_i'}}{\overline{\rho}} \tag{4.3.3}$$

The last term in (4.3.3) is the integral of the fluctuating momentum. Momentum is analytically conserved in a periodic domain, so that this term is a constant in time. The two velocity fields are then related by an additive constant. For convenience we choose the constant to be zero, which makes the Favre and conventional averages identical.

4.4 Nonlinear Least-Squares Data-Fitting

In many places in this work we use a least-squares fit to data as a tool to study its behavior. We have 21 flow fields from which we take measurements. As discussed above, these flow fields span a range of shear, Mach, and Reynolds numbers. this allows us to least-squares fit the 21 realizations of a particular quantity with a function that will show us the statistical variation of the quantity with these numbers.

The fitting function that we use varies somewhat, depending on the quantity that we fit. In some cases we know what the behavior should be for the limits where one or more of the numbers becomes zero. The fitting functions reflect this known behavior.

As an example we discuss the function

$$ f = d \left(\frac{SL}{q} \right)^a (1+bM^2)(Re_\lambda)^c \qquad (4.4.1) $$

which has been used for a number of results. We would use this function for a quantity that would disappear when the shear rate became zero or infinity, depending on the sign of a -- hence the appearance of $\left(\frac{SL}{q} \right)^a$. The Mach number term represents the first two terms in an expansion. This is a relatively standard analysis that may be found, for example, in Van Dyke (1975). It would be used for a quantity that would exist in an incompressible flow, but could be altered in compressible flow.

The Reynolds number dependence is represented by the last term. In some cases we have arguments as to the behavior in the limits of zero and infinite Reynolds number. In this function, we have used a power law that disappears at zero or infinite Reynolds number, depending on the sign of c.

The coefficient , d, is simply a scaling parameter.

49

As each function is used, we shall give a short explanation of why it has its form. The errors that are quoted are the r.m.s. deviations between the actual values and those predicted from the fitting function. These are then normalized on the actual values. They are percentage r.m.s. errors.

4.5 Measures of Reynolds Stress Behavior

We first discuss structural measures of the Reynolds stress tensor, $R_{ij} = \langle \rho u_i u_j \rangle$, in general and then seek changes that occur in the compressible flow.

4.5.1 Shear-Stress Correlations

The shear-stress correlation coefficient is defined

$$C = \langle uv \rangle / [\langle u^2 \rangle \langle v^2 \rangle]^{1/2} \qquad (4.5.1)$$

It is a measure of the strength of the turbulent shear stress and is experimentally known to be about $C = 0.5$ in shear flows. Figures 4.4a through 4.4h show the time development of this correlation coefficient. It will be noticed that the magnitude of the coefficient becmes quite large and then decreases throughout, the "good time" indicating that the flows are still evolving throughout this period. There is too much scatter in the experimental data to say whether this trend is also observed in the laboratory. It is yet unclear in both numerical and laboratory experiments whether there is an asymptotic structural state to which these flows evolve. Evidence indicates that this may be so, but we are unable to carry the simulations far enough in time to determine this. Further evidence will be given in support of the hypothesis that an asymptotic state exists.

The value of the coefficient during the good time is larger than experiment. The average value over the 21 flow fields is $C = 0.67$, the standard deviation is 0.03. The corresponding value for the HGC (1977) flow is $C = 0.47$. The larger value that we calculate agrees with the simulations of Shirani (1981) and of Rogallo (1979).

Suspecting that this difference may be a low Reynolds number effect, we least-squares fit the shear-stress coefficients with the fitting function.

$$f = d\left(\frac{SL}{q}\right)^a (1 + b(M)^2)(Re_\lambda)^c \qquad (4.5.2)$$

We used this form because we expect that c will be zero if the shear number becomes zero, i.e., there will be no shear stress if there is no mean velocity gradient. We do not expect c to disappear at zero Mach number, and we look for Reynolds number dependence as a power of Reynolds number.

The values of the calculated constants in (4.5.2) indicate which of the nondimensional parameters is most important in the variation of the shear stress coefficient. We find that the three constants a, b, c are essentially zero, indicating no dependence on the Reynolds number or the other parameters. We now suspect that these larger than experimental values are due to the fact that the flow is still evolving.

4.5.2 Principal Axis Measures

The orientation of the coordinate system used in these simulations, although arbitrary, is the conventional choice. There is a coordinate system in which the stress tensor becomes diagonal. This is the principal axis coordinate system. The angle α between the two systems is defined as

$$\alpha = \frac{1}{2} \tan^{-1}\left[\frac{-2 \langle \rho uv \rangle}{\langle \rho u^2 \rangle - \langle \rho v^2 \rangle} \right] \qquad (4.5.3)$$

This measure of the stress tensor structure has been used by Corrsin. We least-squares fit α by the fitting function, Eq. (4.5.2), in order to discover which parameter is most important in determining this rotation.

We have again used (4.5.2) as a fitting function, but for a slightly different reason. At zero shear number a flow that has come to equilibrium will be isotropic. In this case (4.5.3) is indeterminate, because any orientation of the coordinate system is equivalent.

51

However, at infinite shear number the coordinate systems coincide. We expect a negative exponent on the shear number. We do not expect α to disappear with the Mach number, and we again look for Reynolds number effects with an exponent on Re_λ.

In Fig. 4.5, we plot the angle α against the estimate from the fitting function. The constants that were determined are shown in the upper left corner of the plot. If Eq. (4.5.2) were a perfect fit, the data would lie on a single 45° line radiating from the origin. We see from the constants that the greatest dependence is on the shear number, as indicated by $A = -0.40$. For comparison we also plot the experimental point of HGC (1977) on Fig. 4.15 and note that it falls at one end of our correlation region, in good agreement with our results.

In our simulations the principal axes of the stress tensor lie between 11 and 22° from the x-axis. The principal axis of the mean strain-rate tensor lies at 45°. Since eddy viscosity models force these two sets of axes to coincide, an eddy-viscosity model would not be appropriate in this flow. This conclusion also applies to one and two equation models, as defined by Reynolds (1976). These models calculate an eddy viscosity from the kinetic energy and a length scale. They cannot represent all the components of the Reynolds stress tensor at the same time and should not be used in flows in which more than one component of the stress tensor is important.

4.5.3 Principal Stress Ratio

We may also examine the ratio of the principal stresses. These stresses are related to the stresses in the unrotated corodinates by

$$-\sigma_{a,b} = \frac{<\rho u^2> + <\rho v^2>}{2} \pm \left[\left(\frac{<\rho u^2> - <\rho v^2>}{2} \right)^2 + <\rho uv>^2 \right]^{1/2}$$

(4.5.4)

The transverse stress $<\rho w^2>$ is also a principal stress and is not changed by the rotation.

We calculate the ratio of the principal stresses in the $X - Y$, or shear plane, and least-squares fit these values with the function

$$f = 1.0 + d\left(\frac{SL}{q}\right)^a (1 + bM^2)(Re_\lambda)^c \qquad (4.5.5)$$

We use (4.5.5) because we know the principal stress ratio is one in an equilibrium flow with a zero shear number. We expect a positive exponent on (SL/q). The arguments for the Mach and Reynolds numbers remain as before.

In Fig. 4.6, we plot this ratio vs. an estimate from the fitting function (4.5.5) and show the values of the calculated constants in the upper left corner. We again note a large dependence on the shear number indicated by $a = 0.74$. For comparison we also plot the HGC (1977) value.

For a shear flow, Eqs. (4.5.2) and (4.5.5) could be used to check the effectiveness of a model in reproducing these measures of turbulent structure.

4.5.4 Invariants of the Reynolds Stress Anisotropy Tensor

As described by Lumley (1970, 1977, 1978, 1980), the invariants of the Reynolds stress anisotropy tensor can be used to characterize the Reynolds stresses. We first define the anisotropy tensor as

$$R_{ij} = \langle \rho u_i u_j \rangle$$
$$b_{ij} = \frac{R_{ij}}{R_{kk}} - \frac{1}{3}\delta_{ij} \qquad (4.5.6)$$

This tensor is symmetric, traceless, has bounded maximum and minimum values, and vanishes when the stress tensor is isotropic.

In Figs. 4.7a through 4.7h, we show the time development of the four nonzero components of this tensor in the shear flow. In all cases the diagonal components seem to approach an asymptotic state faster than the shear stress component. We cannot show that the shear flow comes to structural equilibrium (constant values of b_{ij}), because we are unable to carry the simulations further in time. However, the results strongly suggest that this is the case. In a later section we shall use this idea to derive a class of models for the pressure strain terms in the Reynolds stress equations.

The values of b_{ij}, like those of R_{ij}, depend upon the coordinate system. We seek a measure of the stress tensor that is "invariant" with the coordinates. We do this by contraction of various powers of b_{ij} and define

$$I = b_{ii} \; ; \quad II = b_{ij} b_{ij} \; ; \quad III = b_{ik} b_{kj} b_{ji} \; ; \quad \text{etc.} \quad (4.5.7)$$

From the Cayley-Hamilton theorem, as discussed by Lumley (1970), we find that I, II, and III are the only independent invariants of b_{ij}. In addition, b_{ij} is traceless, so $I = 0$. We are left with two independent scalars to characterize the stress tensor.

Figure 4.8 is an adaptation of Fig. 1 in Lumley and Newman (1977). In it we plot the values of II vs. III for the 21 simulated flow fields. We also plot the value for the HGC flow and show the limits within which all turbulence must lie.

In seeking a key to the variation of I and II, we least-squares fit both of the invariants with the function (4.5.2) for the same reasons that we used in Section 4.5.1. The results of this fit are shown in Table 4.3. We again find the shear number to be the most important nondimensional parameter in determining this measure of stress-tensor structure.

We have consistently found that the shear number is the most important nondimensional parameter in determining the structure of the stress tensor. These fits can be used as correlations in methods of predicting shear flows. In many flows the shear number is fixed, and it may be possible to base a model on this "structural similarity."

4.6   Direct Measures of Compressible Behavior

As discussed in Chapter I, some of the original approaches to studying compressible turbulence involved decomposing the flow fields into parts and studying their interactions. Moyal (1951) decomposed the velocity spectra into "eddy turbulence" and "random noise" parts. For very low turbulence levels, he analytically calculated the interaction of these parts to second order.

Numerical simulations allow us to perform these decompositions directly on the simulated flow fields and calculate their interactions without a limit on the strength of the turbulence. We carry Moyal's ideas further by using his spectral decomposition to define two real-space velocity fields. We shall label the incompressible part (solenoidal) u_i^S and the compressible part (dilatation) u_i^D.

In Fourier space, a solenoidal (dilatation-free) velocity vector is perpendicular to the wave number vector. We can decompose the Fourier transform of the velocity vector into the sum of a vector parallel with the wave number vector, u_i^D and one perpendicular to it u_i^S. Upon inverse-Fourier transforming, we have the velocity fields u_i^S and u_i^D. Operationally, we perform this decomposition as follows. We define

$$u_i = u_i^S + u_i^D = u_i^S + \frac{\partial}{\partial x_i} \phi \qquad (4.6.1)$$

where u_i^D is identified with the gradient of an undetermined scalar potential. Taking the divergence of (4.6.1), we find a Poisson equation for ϕ.

$$\nabla^2 \phi = u_{i,i} \qquad (4.6.2)$$

The solenoidal velocity field is calculated as the difference, $u_i^S = u_i - u_i^D$.

We can then decompose the Reynolds stress tensor into compressible (divergence) and incompressible (solenoidal) parts. Substituting the first equality in (4.6.1) into the definition of the Reynolds stress and dividing the density into mean and fluctuating parts, we have

$$\langle \rho u_i u_j \rangle = \underbrace{\langle \bar{\rho} u_i^S u_j^S \rangle}_{R_{ij}^S} + \underbrace{\langle \bar{\rho}(u_i^S u_j^D + u_i^D u_j^S + u_i^D u_j^D) \rangle + \langle \rho' u_i u_j \rangle}_{R_{ij}^D} \qquad (4.6.3)$$

where R_{ij}^S is the incompressible part and R_{ij}^D is the compressible part of the stress.

In Figs. 4.9a through 4.10h, we show the time development of the decomposed stress tensor for the 21 simulated flow fields. Only the

$i = 2$, $j = 2$ component of the stress tensor h as a significant compressible component. We believe that R_{22}^D is related to acoustic noise, which is known to propagate preferentially in the Y or gradient direction away from a mixing layer.

We see similar behavior in the calculation of 3-D spectra of the decomposed components of the stress tensor. We divide R_{ij} by the density. In Fourier space the stress tensor becomes

$$< \hat{u}_i \hat{u}_j > \; = \; < \hat{u}_i^S \hat{u}_j^S > + < (\hat{u}_i^S \hat{u}_j^D + \hat{u}_i^D \hat{u}_j^S + \hat{u}_i^D \hat{u}_j^D) > \qquad (4.6.5)$$

$$\text{Incompr.} \qquad\qquad \text{Compressible}$$

We have written this tensor as the sum of compressible and incompressible parts.

The spectra of the terms in (4.6.5) are then calculated by the method described in Chapter III. The incompressible spectra contain information only from the solenoidal velocity field. The compressible spectra contain the remainder. We designate these spectra as E_{ij}^S and E_{ij}^D, respectively.

In Figs. 4.11a through 4.12h, we show the 3-D spectra of the diagonal components of E_{ij}^S and E_{ij}^D at nondimensional time $St = 6$. The solid lines represent the spectra of the trace of E_{ij}. The spectrum of the trace of E_{ij} is the standard 3D energy spectra, designated $E(k)$. It represents the distribution of the kinetic energy per unit mass over the range of turbulent length scales in the flow. Most of the information, as we have already seen, resides in the solenoidal component of the velocity field. This can also be seen by comparing the values on the ordinates of the two sets of spectra, E_{ij}^S and E_{ij}^D.

The compressible energy spectra are dominated by the $i = 2$, $j = 2$ components, especially at high wave number. Searching for a reason for this behavior, we formed the dynamic equations for $u_i^D u_j^D$. The production term appears to be responsible for the dominance of this component. So we write only this term

$$\frac{\partial}{\partial t} \left[\hat{u}_i^D, \hat{u}_i^D \right] + \ldots \; = \; \ldots + -Sk_1 \, k_i \left[\hat{u}_i^D, (\hat{u}_2^D + \hat{u}_2^S) \right] \qquad (4.6.6)$$

$$\text{(no summation)}$$

56

Note that this equation allows for production only when $i = 2$. This may be the mathematical reason for the dominance of the $i = 2$, $j = 2$ term and it is probably associated with noise production.

For completeness, we present the 3-D spectra of the shear stress as decomposed by (4.6.5). Again, most of the information is carried by the solenoidal part of the velocity field. These results are presented in Figs. 4.12a through 4.13h.

We have used a velocity decomposition based on Moyal's ideas. By dividing the velocity field into compressible and incompressible parts, we are able to decompose the Reynolds stress tensor. Our general conclusion is that the stress tensor in compressible flow is very similar to its counterpart in incompressible flow. The only exception is the $i = 2$, $j = 2$ component which is associated with noise production. These results are in keeping with Morkovin's hypothesis that compressibility has little effect on the structure of the stress tensor.

However, turbulence models still do not perform very well in high Mach number flows. We suspect that the problem may be found in the modeling of the terms that contribute to the stress tensor. Perhaps these models cannot properly represent some compressible effect that occurs at higher Mach number, and, therefore, they do not produce the incompressible-like stress tensor that we have just examined.

In the next section we discuss the dynamic equations for the Reynolds stresses in hopes of finding this problem.

4.7 Reynolds Stress Equations

The Reynolds stress equations are the time-dependent governing equations for the Reynolds stresses. As stated earlier, modeled versions of these equations are solved in conjunction with the Navier-Stokes equations in the approach called stress-equation modeling. This more complicated type of modeling is introduced in hopes of capturing more of the dynamics of the Reynolds stresses and has found a great deal of favor in the literature. Although not yet an engineering tool, it shows promise in replacing lower-order models.

The stress equations are formed by taking moments of the Navier-Stokes equations. Due to the nonlinearity of the parent equations, the stress equations also contain correlations between fluctuating quantities. Unfortunately, these new correlations are of higher order in the velocity than the Reynolds stresses. If we are to use the Reynolds stress equations, we must model some of the terms that they contain. These modeled terms are generally not measurable by experiment—hence it is attractive to measure them in a simulation.

The Reynolds stress equations for a homogeneous flow are written in Eq. (4.7.1). These equations incorporate the linear coordinate transformation described in Chapter II. The spatial derivatives that appear in (4.7.1) include the mesh metric St and are defined in 2.3.2.

$$\frac{\partial}{\partial t} < \rho u_i u_j > \quad = \quad - < \rho u_i u_k > U_{j,k} - < \rho u_j u_k > U_{i,k} \qquad \text{Production}$$

$$+ \; < P(u_{i,j} + u_{j,i}) > \qquad\qquad \text{Pressure Strain}$$

$$\text{(4.7.1)}$$

$$- \; \mu < u_{i,j} u_{j,i} > \qquad\qquad \text{Homogeneous Dissipation}$$

$$- \; \frac{1}{3} \mu < u_{k,k}(u_{i,j} + u_{j,i}) > \qquad \text{Dilatation Dissipation}$$

$$\frac{\partial}{\partial t} R_{ij} = P_{ij} + \phi_{ij} - (D^H_{ij} + D^D_{ij}) \qquad\qquad \text{(4.7.2)}$$

Labels for each term are included.

As can be seen, the terms divide into three types: production, pressure strain, and dissipation. The convective terms do not appear in homogeneous flows, so we can concentrate on the homogeneous terms.

Inspection of (4.7.1) shows that the production term, P_{ij}, is the product of the Reynolds stress and the mean velocity gradient. These terms are responsible for amplifying the stresses and generally drive the flow away from isotropy. Since the stresses appear explicitly, along with the mean velocity gradient, these terms require no modeling.

The pressure strain term, ϕ_{ij}, involves correlations between the fluctuating pressure and the fluctuating strain rate tensor. Most attention in stress equation modeling is focused on these terms. They are responsible for redistributing the information among the components of the stress tensor. In the homogeneous shear flow, the pressure strain terms drain energy out of the $i = 1$, $j = 1$ component (where the only production occurs) and distributes it to the $i = 2$, $j = 2$ and $i = 3$, $j = 3$ terms, which have no direct sources of production. They also have a large effect on the $i = 1$, $j = 2$ or shear stress term. It is thought that at high Reynolds number this term is responsible for most of this redistribution. In compressible flows, this tensor is not traceless and therefore can have a net effect on the turbulent kinetic energy. The pressure strain terms must be modeled in a simulation.

The homogeneous dissipation tensor, D_{ij}^H, is familiar to incompressible turbulence modelers. At high Reynolds numbers it is thought to be nearly isotropic. However, it can have a redistributive character much like the pressure strain terms, if it is not. It is responsible for destroying the Reynolds stresses, and its trace dissipates turbulent kinetic energy. Like the pressure strain terms, it must be modeled.

The last term in (4.7.1) is the dilatation dissipation, D_{ij}^D. This term occurs only in compressible flows. It is composed of the fluctuating dilatation and the fluctuating strain rate, and also requires modeling. We shall show that this term is small in comparison to the homogeneous dissipation term and that it may be neglected.

We shall discuss the behavior of the terms in the stress equations as calculated from the simulations, and then discuss some models used to approximate these terms.

4.7.1 Time Behavior of the Reynolds Stresses

We now discuss the time history of the Reynolds stress equations, as simulated in the compressible homogeneous shear flow.

The contributing terms in the Reynolds stress equations (4.7.1) are plotted vs. the nondimensional time, St, in Figs. 4.14a through 4.17h. All terms have been normalized by the shear rate times the trace of the stress tensor.

In this geometry, the production terms operate only in the $i = 1$, $j = 1$ and $i = 1$, $j = 2$ equations, i.e., there is production only in the the equations for $\langle \rho u^2 \rangle$ and $\langle \rho uv \rangle$. This is seen by examining the figures. These terms increase the magnitude of $\langle \rho u^2 \rangle$ and $\langle \rho uv \rangle$. During the good time of each simulation, each of these terms has become relatively constant.

The pressure strain terms show the expected behavior in the shear flow. The term in the $\langle \rho u^2 \rangle$ equation acts to drain energy from $\langle \rho u^2 \rangle$. The pressure strain terms are the only terms that contribute positively to ρv^2 and ρw^2. In the shear stress equation, the pressure strain term acts to destroy the stress.

The homogeneous dissipation terms act to destroy the stresses in all four equations. Note that the dilatation dissipation is virtually zero in all cases. In comparison to the homogeneous dissipation, it is very small and, therefore, we neglect it in the rest of the analysis.

In Figs. 4.18a through 4.18h, we show the time development of terms in the turbulent kinetic energy equation. This equation results from taking the sum of the diagonal Reynolds stress equations. We show these data to point out the dissipative behavior of the pressure dilatation term. In an incompressible flow, the pressure strain tensor is traceless because the velocity field is dilatation-free. However, in compressible flow, the pressure dilatation term may have a net effect. Our simulations show this term to be dissipative of turbulent kinetic energy. This effect is not represented in turbulence models derived from the incompressible equations, but we feel that it should be.

4.7.2 Dissipation Anisotropy

In high Reynolds number flows, the homogeneous dissipation tensor D_{ij}^H (hereafter referred to as just the dissipation tensor, D_{ij}) is thought to be isotropic. We investigate this by forming the dissipation anisotropy tensor in the same way that we formed the stress anisotropy tensor.

$$d_{ij} = \frac{D_{ij}}{D_{kk}} - \frac{1}{3} \delta_{ij} \qquad (4.7.3)$$

60

If the dissipation is isotropic, then d_{ij} would be zero.

In Fig. 4.19, we plot d_{ij} vs. the stress anisotropy b_{ij}. We find that they are nearly proportional. This is a very surprising result, which we first attributed to the low Reynolds number of our simulations. It does not seem to be spurious in that it is also seen in the simulations of Shirani (1981) and of Rogallo (1979). We have a Taylor microscale Reynolds number range of about 18-120, so we thought that we could search for Reynolds number dependence by studying the invariants of d_{ij}. These invariants should disappear as the Reynolds number increases.

We form the invariants in the same was as for the stress tensor and least-square fit these scalars by the fitting function.

$$f = d \left(\frac{SL}{q} \right)^a (1 + bM^2)(Re_\lambda)^C \qquad (4.7.4)$$

We chose this function to look for power-law dependence on both shear and Reynolds numbers and because we do not expect the invariants to disappear with Mach number.

We expected to find a positive exponent, a, on the shear number, and a negative exponent, c, on the Reynolds number. We were surprised to find a positive exponent on the Reynolds number. The results are shown in Table 4.4. This indicates that there is no tendency for the dissipation to become isotropic at high Reynolds number. This is a very important result that we believe may be characteristic of shear flows. This fact does not seem to be generally recognized and is very important in turbulence modeling. It plays an important role in some of the models that we subsequently evaluate.

4.8 Character of the Pressure

Before discussing the pressure strain terms, we must look at the character of the pressure field itself.

In compressible flows the pressure field obeys a hyperbolic equation. It has a wavelike character and information travels at a finite speed. Incompressibility results from assuming that this speed of

propagation is very large in comparison to convective velocities. This is reflected mathematically by the elliptic nature of the pressure in incompressible flows, in which the pressure field adjusts instantaneously everywhere to changes in the velocity field.

This can be shown by taking the divergence of the incompressible momentum equations to form a Poisson equation for the pressure.

$$\frac{1}{\rho} \nabla^2 P = - u_{i,j} u_{j,i} - u_{i,j} U_{j,i} \qquad (4.8.1)$$

The Poisson equation is elliptic. In incompressible flows, it is solved in conjunction with the momentum equations to enforce the condition of zero dilatation or mass conservation. Equation (4.8.1) shows the pressure to be completely determined by the velocity field. It is not really an independent variable. In compressible flows the pressure is determined from the thermal energy equation. It is truly a flow variable and represents an additional degree of freedom.

We may show the connection between the two ways of calculating the pressure by taking the divergence of the momentum equation (2.3.4).

$$\nabla^2 P + \frac{\partial}{\partial t} (\rho u_i)_{,i} = - (\rho u_i u_j)_{,ij} - (\rho u_i)_{,j} U_{j,i} \qquad (4.8.2)$$

Using the conservation of mass equation (2.3.3), (4.8.2) becomes

$$\nabla^2 P - \frac{\partial^2}{\partial t^2} \rho = g_1 + g_2 \qquad (4.8.3)$$

where g_1 and g_2 represent the right-hand side terms of (4.8.2). Using the definition of the speed of sound, we may write (4.8.3) as

$$\nabla^2 P - \frac{\partial^2}{\partial t^2} \frac{P}{c^2} = g_1 + g_2 \qquad (4.8.4)$$

which is a nonlinear, inhomogeneous wave equation. This illustrates the wavelike or hyperbolic nature of the pressure, in contrast to the elliptic behavior in incompressible flows.

As the sound speed, c, becomes very large, the time derivative term in (4.8.4) becomes small, and in the limit we are left with the Poisson equation (4.8.1).

It is emphasized that all pressure fields in these simulations are calculated from the full compressible Navier-Stokes equations.

Turbulence modelers have exploited the fact that the pressure field is the solution of a Poisson equation. In the next several sections we apply this reasoning to the compressible flow in order to relate the pressure strain terms to commonly used models that were derived from the incompressible equations.

4.9 Poisson Decomposition of the Pressure Field

Existing pressure strain models have been derived from the incompressible flow equations. Historically, modelers have decomposed the pressure strain tensor into two parts, in order to construct models individually for each part. The Poisson equation (4.8.1) is used to divide the pressure field into two parts, which are then combined with the fluctuating strain rate to form two pressure strain tensors.

In order to relate existing models to our simulated flow fields, we follow the same process in the compressible shear flow. Remembering that the mathematical nature of the flow field has changed, we decompose the actual pressure strain field in the manner that we shall describe. This can be done only in a numerical simulation. This is the first time that these terms have been directly calculated.

We take our direction from (4.8.3). If we define

$$g_3 = \frac{\partial^2}{\partial t^2} \rho \qquad (4.9.1)$$

we then rewrite (4.8.3) as:

$$\nabla^2 P = g_1 + g_2 + g_3$$
$$= \underbrace{-(\rho u_i u_j)_{,ij}}_{\text{Rotta}} \underbrace{- (\rho u_i)_{,j} U_{j,i}}_{\text{Fast}} + \underbrace{\frac{\partial^2}{\partial t^2} \rho}_{\text{Compressible}} \qquad (4.9.2)$$

This is a Poisson equation for the pressure, with g_3 written as a source term representing the compressible contribution to the pressure field. Equation (4.9.2) does not reflect the hyperbolic behavior of the

63

pressure, but we use it here to make a connection with models commonly proposed for incompressible flow.

We note that (4.9.2) is linear in the pressure. Therefore, the pressure field can be regarded as the sum of three fields derived from each of the three source terms on the right-hand side of (4.9.2). We write:

$$\nabla^2 P_i = g_i \tag{4.9.3}$$

Combining each pressure with the fluctuating strain rate, we have

$$_k\phi_{ij} = \langle P_k(u_{i,j} + u_{j,i}) \rangle \tag{4.9.4}$$

where we have again used the symbol $\langle \rangle$ to denote volume average. We now have three distinct pressure strain tensors that sum to the total tensor. We identify each piece in keeping with its pressure term in (4.9.2).

$_1\phi_{ij}$ is the "Rotta" term involving a pressure resulting from the turbulence interacting with itself, originally identified by Rotta in 1951. $_2\phi_{ij}$ is the mean-fluctuating term involving a pressure resulting from interactions between the turbulence and the mean velocity. We hereafter call this term the "Fast" term (Lumley, 1978). $_3\phi_{ij}$ we call the compressible component, as it accounts for the wavelike behavior and does not exist in the incompressible flow. Other decompositions are possible. The inclusion of the fluctuating density alters the definition of the Rotta and Fast terms slightly; however, their essential character is preserved in making this analogy.

4.10 Magnitude of the Pressure-Strain Terms

It is customary to propose models for each part of the pressure-strain tensor separately, and then use them in combination to replace the total pressure strain tensor. The performance of the model is then judged indirectly by its effect on measurable quantities, such as the stresses or the mean velocity.

64

We find ourselves in the fortunate position of being able to directly calculate these pressure-strain terms and compare models to them immediately. We decompose these terms in the manner suggested by Eqs. (4.9.2) through (4.9.4).

Having expected the compressible part to be small in comparison to the Rotta and Fast parts, we are surprised to find it of the same order of magnitude as the others. As a measure of the magnitude of this part of the tensor, we form the second invariant and divide it by the sum of the second invariants of the Rotta and Fast parts. We performed a least-squares fit to this quantity, to look for the important parameters in its development. In Fig. 4.20, we show this ratio of invariants plotted against the least-squares fitting function. The fitting function and the determined constants are also shown. There is a positive dependence on both the shear number and on the fluctuating Mach number. Recall from Section 4.1 that the product of these two parameters is the shear Mach number. It seems as though the magnitude of the compressible part of the pressure-strain term probably scales on this "external flow-like" Mach number. In these simulations, the magnitude of this term seems to vary almost linearly with the shear Mach number, as indicated by the exponents a and b. This term will become important in mixing layers and boundary layers in which the Mach number difference across a large eddy becomes greater than one.

It will be useful to describe the procedure used to verify this result. The procedure used involves the direct calculation of the first three terms in (4.9.2). The fourth, the compressible source term, is calculated by difference. Equation (4.9.2) is analytically satisfied by the flow field. It is numerically satisfied if the same method of spatial derivatives is used for it as for the original simulation. We have used pseudo-spectral derivatives in all cases as described earlier, for numerical consistency.

The "compressible" part of the pressure will be very small in a low-Mach-number isotropic flow. We know that, at low Mach numbers, this flow is virtually incompressible. In the simulation labeled IH64A, we calculated the ratio of the pressure fluctuations for a flow field at the end of the computation, when the fluctuating Mach number was less

65

than 0.03. The second portion of the pressure does not exist in this flow, as there is no mean velocity gradient. We found the ratio of the squares of the fluctuating pressures to be

$$P_3^{'2}/P_1^{'2} = 0.0056 \qquad (4.10.1)$$

This is quite small, consistent with our hypothesis.

The third source term was calculated from the divergence of the momentum equations. As a check, we evaluated g_3 in an independent way. From (4.8.2) and (4.8.3), it can be seen that this source term is the second time derivative of the density. The code is run two time steps to produce three consecutive flow fields, and $\partial^2/\partial t^2 \rho$ was then approximated by a three-point central difference formula. We then found this ratio of pressure fluctuation to be

$$P_3^{'2}/P_1^{'2} = 0.0050 \qquad (4.10.2)$$

iin good agreement with (4.10.1). The magnitude of (4.10.2) is slightly less than (4.10.2), as might be expected, because of the high wave number dissipation inherent in the three-point formula.

This confirms that our hypothesis and method of calculating the pressure is correct. At very low Mach number, the compressible part of the pressure disappears and, with it, its contribution to the pressure-strain terms.

In order to find out what physical mechanism was responsible for the size of P_3, we applied the chain rule to the source term g_3 and calculated four pressure fields that comprise P_3.

$$g_3 = \frac{\partial}{\partial t}(\rho u_i)_{,i} = u_i \frac{\partial}{\partial t}\rho_{,i} + \rho_{,i}\frac{\partial}{\partial t}u_i + u_{i,i}\frac{\partial}{\partial t}\rho - \rho\frac{\partial}{\partial t}u_{i,i}$$
$$(4.10.3)$$

This was done in the simulation HS64D at $St = 6.0$. We again formed the fluctuating pressures and found that the last term in (4.10.3) was responsible for more than 95% of the P_3 pressure field. The other three terms are insignificant. This indicates that the third or compressible part of the pressure field is a result of the velocity dilatation in the flow field and not a result of variations in density.

66

4.11 Modeling of the Decomposed Pressure-Strain Terms

In this section we discuss and evaluate models for the three components of the decomposed pressure-strain tensor.

4.11.1 Rotta Pressure-Strain Term

The Rotta pressure-strain term, $_1\phi_{ij}$, was first identified by Rotta (1951). The pressure field associated with this tensor results from interactions of the turbulent velocity field with itself. It may therefore exist in a flow which has no mean velocity. In a flow with no turbulence production, this term is thought to be responsible for the experimentally observed return to isotropy of the Reynolds stresses.

In order to model this part of the pressure strain tensor, Rotta related the $_1\phi_{ij}$ to the stress anisotropy, b_{ij}, by reasoning that the effect of the model should stop when isotropy is reached. He proposed the simplest model that is linear in b_{ij}.

$$_1\phi_{ij} = -c_1 \, \varepsilon b_{ij} \qquad (4.11.1)$$

where ε is the isotropic part of the dissipation defined as

$$\varepsilon = \frac{1}{2} D_{ii} \qquad (4.11.2)$$

Although Rotta proposed this model solely as a replacement for ϕ_{ij}, we shall show that there are other terms that should be combined with the Rotta term and modeled this way. We can also make an estimate of the value of c_1.

Consider the time-dependent equations for b_{ij}, the Reynolds stress anisotropy tensor, in a homogeneous flow with no turbulence production (no mean velocity gradient). We do this to isolate the effects of the Rotta term only. In this relaxing flow, there is no fast pressure-strain term, $_2\phi_{ij}$, but the pressure-strain tensor remains the sum of the Rotta part and the compressible part. Wray (1980), however, has shown that the velocity dilatation quickly becomes insignificant in a relaxing, compressible, homogeneous flow and therefore the pressure-strain tensor, in this flow, is almost entirely due to the Rotta term.

In addition, the trace of ϕ_{ij} is small, so its dissipation may be neglected for this case.

Manipulation of the Reynolds stress equations produces the Reynolds stress anisotropy equation.

$$\frac{\partial}{\partial t} b_{ij} = \frac{1}{R_{kk}}\left[_1\phi_{ij} - 2\varepsilon d_{ij}\right] + \frac{1}{R_{kk}}\varepsilon b_{ij} \qquad (4.11.3)$$

where we have used d_{ij} for the dissipation anisotropy, defined by (4.7.2) and assumed that ϕ_{ij} is traceless.

In (4.11.3) the term in square brackets can alter the relative magnitudes of the elements of b_{ij}, i.e., it has redistributive behavior and is responsible for the return to isotropy. The last term cannot do this. This indicates that the entire bracketed term should be replaced by a model rather than just the pressure-strain term.

If we use the Rotta model, (4.11.1), to replace $[_1\phi_{ij} - 2\varepsilon d_{ij}]$, we find

$$\frac{\partial}{\partial t} b_{ij} = (2-c_1) b_{ij} \qquad (4.11.4)$$

For b_{ij} to relax to isotropy, c_1 must be greater than two.

Thus it makes sense to use the Rotta term in place of the term in square brackets. The constant will be evaluated for both applications.

We are able to directly calculate the constant c_1 from our simulated flow fields. All three pressure-strain tensors exist in the homogeneous shear flow, so we calculate the Rotta pressure-strain term by (4.9.2) through (4.9.4).

In Table 4.5 we show the value of the constant c_1 for each of the four nonzero Reynolds stress equations. Note that, for both applications, c_1 is not a constant. It varies among the Reynolds stress equations and has a spread of values for each equation alone. We fit the constants, c_1, calculated from each flow fields with the following two equations:

$$f = 2 + 1 +\left(\frac{SL}{q}\right)^a (1 + bM^2)(Re_\lambda)^c \qquad (4.11.5a)$$

68

$$f = d \left(\frac{SL}{q}\right)^a (1 + bM^2)(Re_\lambda)^c \qquad (4.11.5b)$$

in hopes of determining which nondimensional parameter varies with the constant. The 2 appears in the first fitting function because c_1 should approach 2 (no return to isotropy) at zero Reynolds number, at least for the case where the dissipation anisotropy is included. This argument is discussed in Lumley and Newman (1977) and motivated the first form. We were unable to find a suitably converged set of constants for this equation, which led us to the second form in (4.11.5), which we found to be a better fit to the data. These results are presented in Table 4.5.

From the values of the fitted constants in Table 4.5 it can be seen that the shear number is important in determining the variation of c_1. It seems as though the mean velocity gradient has an indirect effect on the structure of this term.

The values of Table 4.5 are shown graphically in Figs. 4.21 and 4.22. Figures 4.21 and 4.22 are actually four plots in one. We determined the constants in Eq. (4.11.5b) by least squares. We then used these constants in (4.11.5b) to make an estimate of c_1 in each flow field. We divided the predicted value by the actual value and plot this ratio on the ordinate. If the least squares were perfect, this value would be one. For clarity, we shift the origin for each plot by successively adding two to the results from each of the four stress equations. The results for the $i = 1$, $j = 1$ equation appear at the top of the plot beside the number 7. On the abscissa we plot the corresponding values of c_1. We may then visually compare the range in values of c_1 and the accuracy of the fitting function for the four stress equations.

If the model were a perfect representation of the terms it replaces, the figures would have only four points, each immediately above the others, at a common value of c_1. However, the horizontal spread of values shows the variation of c_1 in each equation, and the vertical spread shows the adequacy of the least-squares fit.

The values of c_1 for the case where the dissipation anisotropy is included are, within the variance, greater than two, consistent with the

69

requirement for return to isotropy. For the simple Rotta model, this is not true. (Note that, when c_1 is evaluated from experiment, the dissipation anisotropy is usually included with the Rotta term by default, because the dissipation is assumed to be isotropic. Thus the resulting models are fairly accurate, even though some of the assumptions are not correct.)

In the relaxing, homogeneous simulations of Rogallo, c_1 is calculated to be constant at a value of about 2.37. The values of c_1 calculated by Schumann and Patterson (1975) are of the same order of magnitude as we calculate for the simple model. They do not include the dissipation anisotropy in their analysis. The incompressible, homogeneous shear simulations of Shirani (1981) also show a variation of c_1 when the Rotta term is calculated directly. It seems as though the Rotta model breaks down in the shear flow.

Bearing this in mind, we have looked at some arguments about the variation of c_1. Various workers have recognized that c_1 is not a constant and have proposed arguments as to how it should vary. Lumley and Newman (1977) argue that c_1 should be a function of the Reynolds number and the two nonzero invariants of the stress anisotropy tensor. They propose the equation

$$c_1 = 2 + e^{-a/Re_L^{1/2}} \frac{72}{Re_L^{1/2}} + b \, \ell n(1 + c(dIII - II)) \left(\frac{1}{9} + 3III + II \right) \tag{4.11.6}$$

They chose the form of this function by determining how c_1 should behave in the limits of zero and infinite Re and anisotropy invariants. The equation is simply an interpolation between these limits. We performed a least-squares fit to the four constants in (4.11.6) and present these data along with error estimates in Table 4.6. We were unable to find a converged set of constants for the $i = 3$, $j = 3$ equation, but found reasonable values for the other three. The values that Lumley proposes are also included. The quantitative agreement with his constants is not good, but they are all of the same order of magnitude.

Chung and Adrian (1979) use a similar argument to propose the fitting equations:

70

$$c_1 = 2 + \frac{\pi(II,III)}{\mu(Re_L)}$$

$$\pi = aII\ e^{(-bII)}\ (1 - dIII^{1/3} + e^{III}) \qquad (4.11.7)$$

$$\mu = 1 + f\ Re_L^{-1/2}$$

We were unable to find a converged set of constants for this equation.

A simpler suggestion by Lumley and Newman (1977) does not depend on the stress invariants.

$$c_1 = 2 + A\ Re_L^{-1/2} \qquad (4.11.8)$$

Table 4.7 shows the values of A that we calculate from the shear flow. Note the variation and especially the change of sign.

We have to conclude that the Rotta model (4.11.1) is inadequate to represent the Rotta and dissipation anisotropy terms, when analyzed by this method. The constant c_1 is a function of i and j and perhaps should be a tensor. As previously stated, the Rotta model is linear in b_{ij}. Perhaps higher-order terms in b_{ij} should be investigated that would represent this variation with a scalar constant. We suspect that the Poisson decomposition is at fault and that perhaps the Rotta model is not as bad as this analysis shows. We shall return to this model when we attempt to model the entire pressure-strain tensor.

4.11.2 Fast Pressure-Strain Term

The Fast portion of the pressure-strain tensor was recognized by Rotta (1951), but its name is due to Lumley (1978). It arises from interactions between the turbulence field and the mean velocity gradient. Many workers have proposed models for this term which have grown in sophistication over the years. Modern models are generally constructed from combinations of b_{ij}, but there is some controversy as to whether these models should be linear or of higher order in b_{ij} (Lumley, 1978).

The reasoning that leads to the use of b_{ij} in these models was given by Lumley (1974). Assuming incompressible homogeneous flow, we may write the Fourier transform of the fast part of the pressure as

$$\hat{P}_2 = \frac{-ik_j u_i}{k^2} U_{j,i} \qquad (4.11.9)$$

The pressure-strain term is written as an integral in Fourier space.

$$\langle P_2(u_{i,j}+u_{j,i}) \rangle = \frac{1}{2} \int_{D_k} \left\{ ik_j(\hat{P}_2^* \hat{u}_i + \hat{P}\hat{u}_i^*) + ik_i(\hat{P}_2^* \hat{u}_j + \hat{P}\hat{u}_j^*) \right\} dk \qquad (4.11.10)$$

Inserting (4.11.9) into (4.11.10) and remembering that $U_{j,i}$ is a constant, we find

$$\langle P_2(u_{i,j}+u_{j,i}) \rangle = \frac{1}{2} U_{\ell,k} \int_{D_k} \left\{ \frac{k_i k_\ell}{k^2} (\hat{u}_j^* \hat{u}_k + \hat{u}_j \hat{u}_k^*) + \frac{k_j k_\ell}{k^2} (\hat{u}_i^* \hat{u}_k + \hat{u}_i \hat{u}_k^*) \right\} dk$$

$$= U_{\ell,k} G_{ijk\ell} \qquad (4.11.11)$$

Equation (4.11.11) is an exact representation of the fast term for an incompressible homogeneous flow. It shows that the fast term is composed of a fourth-rank tensor multiplied by the mean-velocity gradient.

Models for this term approximate the fourth-rank tensor because we cannot directly evaluate the integral. Note that the integrand is composed of Fourier-space representations of the Reynolds stress. This justifies constructing models for the tensor from combinations of the b_{ij}.

The most sophisticated model in use is linear in b_{ij}. It has been derived in several forms by various workers, but all are essentially the same. We shall discuss the form found in Reynolds (1976). The tensor $G_{ijk\ell}$ is approximated by linear combinations of b_{ij}, each term multiplied by its own undetermined constant. Constraints implied by (4.11.11) eliminate all but one of these constants, which must then be determined empirically. When combined with the mean-velocity gradient, $U_{\ell,k}$, the model is

$$2\phi_{ij} = \frac{2}{5}(1+A_1)S_{ij}\rho q^2 - \frac{3}{5}A_1 \left[R_{ik}S_{kj} + R_{jk}S_{ki} + \frac{2}{3}\delta_{ij} \right] \qquad (4.11.12)$$

$$- \frac{4}{5}\left(\frac{5}{3} + \frac{7}{12}A_1\right)\left[R_{ik}\Omega_{kj} + R_{jk}\Omega_{ki} \right]$$

72

$$S_{ij} = \frac{1}{2}(U_{i,j} + U_{j,i})$$

$$\Omega_{ij} = \frac{1}{2}(U_{i,j} - U_{j,i})$$

This is exactly the form used by Hanjalic and Launder (1974).

For the homogeneous shear flow, the four nonzero terms are:

$$2^{\phi}11 = -\left(\frac{4}{15}A_1 + \frac{4}{3}\right)\mathcal{P}$$

$$2^{\phi}22 = \left(\frac{2}{3}A_1 + \frac{4}{3}\right)\mathcal{P}$$

$$2^{\phi}33 = \left(-\frac{2}{5}A_1\right)\mathcal{P} \hspace{3cm} (4.11.13)$$

$$2^{\phi}12 = \frac{1}{5}(1+A_1)\,S\rho q^2 - \left(\frac{8}{15}A_1 + \frac{2}{3}\right)S <\rho u_1^2> - \left(\frac{1}{15}A_1 - \frac{2}{3}\right)S <\rho u_2^2>$$

As with the Rotta term, we can directly calculate the value of the constant A_1 from our simulations. Table 4.8 shows the value of A_1 for the four nonzero Reynolds stress equations. It can be seen that the average value of A_1 varies among the four equations, but that the variance of A_1 is quite small relative to the average for three of the four. The values calculated for the R_{33} term have some scatter due to the small value of b_{33}, and are less reliable. We present them for completeness.

To look for variations of the constant with the nondimensional parameters, we have least-squares fit the constants A_1 from each of the four equations with the function

$$A_1 = d\left(\frac{SL}{q}\right)^a (1 + bM^2)(Re_{\lambda})^c \hspace{2cm} (4.11.14)$$

We have chosen this form rather arbitrarily to look for power-law variations of A_1 with shear and Reynolds numbers and because we do not expect A_1 to disappear with Mach number. There have been arguments proposed that this "constant" should vary with the stress anisotropy also (Lumley, 1978). There is no clear indication of how it should behave in the limits of zero and infinity for the shear and Reynolds number and for the invariants, and therefore no function has been

73

proposed. We justify (4.11.14) solely by the accuracy of the fit shown by the small rms error in Table 4.8. Figure 4.23 presents the constant A_1 in the same manner used to present the Rotta model constant.

The constants are quite constant for each equation, leading us to suspect that much of the important physics is captured by this model. However, the average value still varies from equation to equation. Improvements still need to be made, perhaps along the lines suggested by Lumley (1978), where he discussed Schumann's (1977) concept of realizability.

A simplified version of this model has found favor among some workers. It is known as the Gibson-Launder model, and is

$$2\phi_{ij} = -A_2(P_{ij} - \frac{2}{3}\delta_{ij}\mathcal{P})$$

where

$$P_{ij} = -\langle \rho u_i u_k \rangle U_{j,k} - \langle \rho u_j u_k \rangle U_{i,k} \qquad (4.11.15)$$

and

$$\mathcal{P} = \frac{1}{2}P_{ii}$$

where $\mathcal{P}$ is the rate of turbulence energy production per unit volume. For the homogeneous shear flow,

$$\begin{aligned} 2\phi_{11} &= -\frac{4}{3}A_2\,\mathcal{P} \\ 2\phi_{22} &= {}_1\phi_{33} = \frac{2}{3}A_2\,\mathcal{P} \qquad (4.11.16) \\ 2\phi_{12} &= A_2\langle \rho u_2^2 \rangle S \end{aligned}$$

The values of A_2 are presented in Table 4.9 and graphically in Fig. 4.24. This model does not perform as well as the more general fourth-rank tensor model from which it is derived. One problem is the equality of the model for $_2\phi_{22}$ and $_2\phi_{33}$. There is no reason why these terms should be equal, and there is evidence that they are not (Champagne et al. (1970) and Harris et al. (1977), but the model is incapable of representing this. It seems as though some essential

74

physics has been left out by the simplification, and we would therefore prefer the more general model (4.11.12) over the Gibson-Launder model (4.11.15).

In hopes of improving the fourth-rank tensor model, we have added terms involving d_{ij}, the dissipation anisotropy. This addition is motivated by our experience with the Rotta term and also by the appearance of the integrand in (4.11.11). The wave numbers multiplying the velocities represent spatial derivatives and appear similar to the Fourier space representation of the dissipation tensor.

We added terms linear in the dissipation anisotropy d_{ij} into the model (4.11.12). We applyed the kinematic constraints discussed in Reynolds (1976) and also in Lumley (1978). Writing the model for the shear flow, we have:

$$2\phi_{11} = \left(\frac{4}{15} A_1 + \frac{4}{3}\right)\mathcal{P} + (c_2 + 2c_3)\frac{D_{12}}{\varepsilon} s\rho q^2$$

$$2\phi_{22} = -\left(\frac{2}{3} A_1 + \frac{4}{3}\right)\mathcal{P} - (3c_2 + 8c_3)\frac{D_{12}}{\varepsilon} s\rho q^2$$

$$2\phi_{33} = \frac{2}{5} A_1 \mathcal{P} + c_2 \frac{D_{12}}{\varepsilon} s\rho q^2$$

$$2\phi_{12} = \frac{1}{5}(1 + A_1) s\rho q2 - \left[\frac{8}{15} A_1 + \frac{2}{3}\right] s < \rho u_1^2 >$$

$$- \left[\frac{1}{15} A_1 - \frac{2}{3}\right] s < \rho u_2^2 > + \left[\frac{2}{3} c_2 + 2c_3\right] s\rho q^2 \quad (4.11.17)$$

$$- \left(2c_2 + 4c_3\right)\frac{D_{11}}{\varepsilon} s\rho q^2 + c_3 \frac{D_{22}}{\varepsilon} s\rho q^2$$

where D_{ij} is the dissipation tensor (D_{ij}^H of Eq. (4.7.2)). Note the appearance of three undetermined constants, A_1, c_2, c_3. To determine these constants we did a least-squares fit to $2\phi_{ij}$, using (4.11.17). The results of this fit appear in Table 4.10.

The constant A_1 which multiplies the same terms as in the original model (4.11.12) varies much less from equation to equation than it does in the case where d_{ij} is not included. This is an improvement. However, c_2 and c_3 do not appear to be constants at all (c_2 and c_3 were determined simultaneously in the R_{11} and R_{22} equations and are therefore equal). We therefore do not expect this model to be an improvement over (4.11.12).

75

There are serious objections to the form that the fourth-rank tensor model takes (Leslie (1980) and Lumley (1978)), but in the absence of any demonstrably better model we would use (4.11.12) with carefully chosen individual constants for each Reynolds stress equation.

4.11.3 Compressible Pressure-Strain Terms

The pressure strain terms associated with the compressible part of the pressure can be thought of as a deviation of the compressible terms from the equivalent incompressible terms.

In seeking a clue as to how they behave, we plotted the ratios of the individual terms in $_3\phi_{ij}$ to the corresponding terms in the Rotta and fast parts of the pressure-strain tensor. We noted that $_3\phi_{ij}$ is similar to the fast tensor $_2\phi_{ij}$. The ratio of these two terms seems to be a function of the shear Mach number SL/c, as shown in Figs. 4.25a through 4.25d, where we have plotted the ratio $_3\phi_{ij}/_2\phi_{ij}$ for the four nonzero components vs. SL/c. This trend may be seen in all except the $i = 2$, $j = 2$ term, where we see too much scatter to draw conclusions. We are led to suspect that the models for the fast term may be applicable to the compressible term.

We applied the most successful model (the general fourth-rank tensor model) for the fast pressure-strain terms to the compressible term. The results are shown in Table 4.11 and Fig. 4.26. By comparison with Table 4.4 and Fig. 4.23, it can be seen that the compressible terms behave in much the same way as the fast terms.

Since these two tensors are quite similar, we thought that their sum should be modeled. Applying the fourth-rank tensor model to $_2\phi_{ij}$ + $_3\phi_{ij}$, we find the results shown in Table 4.12 and Fig. 4.27. The average value of A_1 does not vary as much among the equations as when applied to the compressible terms alone.

We evaluated several other models for these terms, including the Rotta model and the fourth-rank tensor model with the dissipation anisotropy terms, but found none that performed as well as the original fourth-rank tensor model.

4.11.4 Conclusions for Modeling of the Decomposed Pressure Strain Tensor

Using the simulated flow fields, we decomposed the pressure field by means of a Poisson equation. This is a standard decomposition used in incompressible flow modeling and is used to give insight into constructing models for the pressure-strain terms. We carried out this decomposition in the compressible flow to relate existing pressure-strain models to the "exact" terms.

We found three components instead of the two found in incompressible flows. The third component we labeled the compressible pressure-strain terms and regarded it as a deviation from incompressible flow.

We evaluated models against the exact terms, but found variations in the values of the constants. On the basis of these calculations, we would recommend the use of the Rotta model to replace both the Rotta term and the dissipation anisotropy. We recommend the use of the fourth-rank tensor model to replace the sum of the fast and the compressible pressure-strain terms.

However, we have reservations about the validity of this Poisson decomposition in a compressible flow. As discussed in Section 4.8, the pressure is a hyperbolic quantity, not elliptic as in the incompressible flow. A Poisson equation introduces an elliptic character into the pressure and is perhaps incorrect in a compressible flow. This leads us to two approaches described in the next two sections, where we first look into decomposition of the pressure by means of a wave operator. We then evaluate several models for the entire pressure-strain tensor without decomposition.

4.12 Wave-Operator Decomposition

Because the Poisson decomposition is mathematically incorrect in a compressible flow, we have investigated the use of a wave operator. We rewrite Eq. (4.8.3)

$$\nabla^2 p - \frac{\partial^2}{\partial t^2} \frac{p}{c^2} = g_1 + g_2 \qquad (4.12.1)$$

where g_1 and g_2 are the Rotta and fast source terms defined in Section 4.8. Ideally, we would like to calculate two pressure fields corresponding to the source terms g_1 and g_2. We would then combine them with the fluctuating strain-rate tensor in the manner of (4.11.10), to form a Fourier space representation of two pressure-strain tensors. Equation (4.12.1) is a nonlinear wave equation which we cannot directly solve. However, we can retain the hyperbolic character of (4.12.1) by approximating the sound speed c as a constant, leaving a linear wave equation.

Setting $c = c_o$, a constant, and Fourier transforming (4.12.1), we find:

$$\frac{\partial^2}{\partial t^2} \hat{P} + (k^2 c_o^2) \hat{P} = \hat{g}_1 + \hat{g}_2 \qquad (4.12.2)$$

For each source term g_i, the general solution of (4.10.2) is

$$\hat{P}_i(k,t) = P_1 e^{ikc_o t} + P_2 e^{-ikc_o t} + \frac{1}{kc_o} \int^t \sin(t-t') \hat{g}_i(t') \, dt' \qquad (4.12.3)$$

We are unable to explicitly evaluate the integral in (4.12.3). It represents history effects that would appear in the pressure-strain terms. This is to be expected in that the pressure is truly a flow variable that develops according to its own dynamic equation. It is not a result of a kinematic constraint, as it is in incompresible flows and therefore is not completely determined by the instantaneous velocity field.

It seems that models developed from this decomposition must have history effects built into them. This appears prohibitively expensive for useful models in that the entire history of the simulation must be preserved to construct the pressure-strain model. It is possible that models could be constructed on this basis, but we abandoned it for lack of time.

We were therefore led to look elsewhere. In the next section we discuss attempts to model the entire pressure-strain tensor without any decomposition.

4.13 Modeling of the Entire Pressure-Strain Tensor

We have discussed our reservations about the use of the Poisson decomposition for the pressure-strain tensor in a compressible flow. We then described a decomposition based on a wave operator that appears impractical to use.

We are led to models for the entire tensor without a decomposition. The models we evaluated follow two different lines of thought. Combinations of existing models were evaluated and their constants were simultaneously determined. We also constructed and evaluated models based on a structural similarity assumption. First we discuss combinations of existing models. We then discuss models based on a structural similarity concept.

4.13.1 Combinations of Existing Models

In a previous section we evaluated models against the exact parts of the decomposed pressure-strain tensor. Because of our reservations about the decomposition, we reevaluated the constants in two sets of models by sumultaneously determining them. Following our tentative recommendations at the end of Section 4.11, we model the sum of the total pressure-strain tensor and the dissipation anisotropy by the sum of the Rotta model and a fast model.

$$(\phi_{ij} - 2\varepsilon d_{ij}) \rightarrow \begin{matrix} \text{Fast model} \\ \text{with constant} \end{matrix} + \begin{matrix} \text{Rotta model} \\ \text{with constant} \end{matrix} \quad (4.13.1)$$

The two constants are then determined by a least-squares fit using the models as a fitting function. We did this hoping that any artificiality associated with the decomposition could be eliminated.

Both the Gibson-Launder model and the fourth-rank tensor model were evaluated. The results are shown in Table 4.13 where we have written the values of the two constants and the normalized RMS error associated with the fit.

The $i = 3$, $j = 3$ term has a large amount of uncertainty associated with it because of the small and erratic value of the stress anisotropy in this term. We notice, however, that the three remaining terms

79

are better approximated by the fourth-rank tensor model. (There is less variation of the constants from equation to equation.) Comparison with Tables 4.4 and 4.5, where we have written the individually determined constants, shows less variation in their values We take this to confirm our suspicion that a Poisson decomposition should not be used in the compressible flow.

The combination of fourth-rank tensor and Rotta models is still the best one we have evaluated. Our recommendation of Section 4.11 still holds.

4.13.2 Structural Similarity Models

When analyzing their time history, we noticed that the elements of the stress anisotropy tensor seemed to approach asymptotic values. This was particularly true for the diagonal terms, but less so for the shear stress. It was thought that we could exploit this fact to create a pressure strain model.

As discussed earlier, it is by no means certain that the shear flow comes to structural equilibrium $(\frac{\partial}{\partial t} b_{ij} = 0)$. However, the time rate of change of b_{ij} becomes small during the "good time" of the simulations, and we use this to justify the zeroing of $(\partial/\partial t)b_{ij}$. This is an assumption similar to that used in Rodi's (1976) algebraic stress model.

We derive the time-dependent equations for b_{ij} from the Reynolds stress equations (4.7.1) and (4.7.2). Applying the chain rule to the time derivative of the definition of b_{ij}.

$$\frac{\partial}{\partial t} b_{ij} = \frac{\partial}{\partial t} \frac{R_{ij}}{R_{kk}} - \frac{1}{3} \delta_{ij} = \frac{1}{R_{kk}} \frac{\partial}{\partial t} R_{ij} - \frac{1}{(R_{kk})^2} \frac{\partial}{\partial t} R_{kk} \qquad (4.13.2)$$

We can show that

$$\frac{\partial}{\partial t} b_{ij} = \frac{1}{\rho q^2} \left[P_{ij} + \phi_{ij} - D_{ij} - 2 \frac{R_{ij}}{\rho q^2} (\mathcal{P} + \Phi - \varepsilon) \right] \qquad (4.13.3)$$

where P_{ij} is the production tensor, ϕ_{ij} as the pressure-strain tensor, and D_{ij} as the dissipation tensor. The turbulent kinetic energy production is $\mathcal{P}$, the turbulent dissipation is ε, and the

trace of the pressure strain tensor is Φ. The trace of the Reynolds stress tensor R_{kk} is ρq^2.

Setting $(\partial/\partial t)b_{ij}$ equal to zero and solving for ϕ_{ij}, we have

$$\phi_{ij} = \left[\mathscr{P}(b_{ij} - p_{ij}) - \epsilon(b_{ij} - d_{ij}) \right] + 2\Phi \left[b_{ij} + \frac{1}{3}\delta_{ij} \right] \qquad (4.13.4)$$

where we have used p_{ij} for the production anisotropy, defined as

$$p_{ij} = \frac{P_{ij}}{2\mathscr{P}} - \frac{1}{3}\delta_{ij} \qquad (4.13.5)$$

Equation (4.13.4) gives us a form from which to construct models. To test the assumption that $(\partial/\partial t)b_{ij} = 0$, we calculated the ratio of the right side of (4.13.4) to the left side and calculated the average value and variance of this ratio. If (4.13.4) were identically satisfied, this ratio would be one and the variance would be zero. Table 4.14 shows these results. We see that this assumption is reasonable for the $i = 1$, $j = 1$ and $i = 3$, $j = 3$ components, but questionable for the other two.

We constructed several models by simplifying. Ignoring the trace of the pressure-strain tensor and using the observed fact that the dissipation anisotropy is proportional to the stress anisotropy, we have

$$\phi_{ij} = 2\mathscr{P}(b_{ij} - p_{ij}) - 2\epsilon b_{ij}(1-c_1) \qquad (4.13.6)$$

where c_1 represents this proportionality. The average value of c_1 is shown in Table 4.15, along with its variance. We also show the results graphically in Fig. 4.29, in the same way we presented the values in Section 4.9.

There is reasonable agreement for the diagonal terms, but the off-diagonal or shear-stress term is not well represented. Since c_1 represents the proportionality between b_{ij} and d_{ij}, we know that its value should be about one. We suspect that the failure on the off-diagonal term is due to the changing value of b_{12}. As was seen earlier, this off-diagonal compnent of the stress anisotropy tensor changes more rapidly throughout the "good time" than the diagonal components.

The failure in this term may be due to the lack of structural similarity in the shear stress.

Searching for improvements to this model, we put an adjustable constant in front of the first term in (4.13.6) and rewrite the equation as

$$\phi_{ij} = c_1 \mathscr{P}(b_{ij} - P_{ij}) - c_2 \epsilon b_{ij} \qquad (4.13.7)$$

where the second term is written to appear like the Rotta model. Note that (4.13.7) looks very much like the Gibson-Launder plus Rotta models, but with the inclusion of b_{ij} in the first term. Table 4.16 shows the values of c_1 and c_2 determined from a least-squares fit using (4.13.7) as the fitting function. We again see a large variation in the values for $i = 3$, $j = 3$. The agreement among the other three equations is not good, with a four-to-one variation on c_2 and two-to-one on c_1.

Perhaps models based on structural similarity would be appropriate for this flow, if we could carry the simulation further in time. However, we are limited to simulation times before the flow reaches this hypothetical similarity, and therefore we should not dismiss this idea. It deserves a reinvestigation in a more fully developed homogeneous shear flow.

Table 4.1

NON-DIMENSIONAL GROUPS

	Computational Range	Experimental Range
$\dfrac{SL}{q}$ Shear Number	$8.5 < \dfrac{SL}{q} < 26.6$	$7.8 < \dfrac{SL}{q} < 14.8$
$M = \dfrac{q}{c}$ Fluctuating Mach Number	$0.06 < M < 0.31$	< 0.3
$Re_{\lambda} = \dfrac{\rho q \lambda}{\mu}$ Taylor Microscale Reynolds Number	$18.4 < Re_{\lambda} < 120.6$	$133 < Re_{\lambda} < 398$

Table 4.2

TABLE OF SIMULATIONS

	Designation	Type	Parameter Range		
			SL/q	M = q/c	Re_{λ}
	IH64A	Isotropic	0.0	0.078–0.034	15.0–40.0
A.	HS64A	Shear	22.0–25.8	0.064–0.065	18.4–23.3
B.	HS64B	Shear	9.7–12.5	0.144–0.146	30.1–39.0
C.	HS64C	Shear	8.5–11.1	0.312–0.316	40.7–53.3
D.	HS64D	Shear	13.1–14.9	0.207–0.222	43.6–56.7
F.	HS64F	Shear	24.0–26.6	0.238–0.262	54.9–77.7
G.	HS64G	Shear	9.9–13.3	0.268–0.273	29.3–37.9
H.	HS64H	Shear	10.7–11.4	0.250–0.282	93.8–120.6

Table 4.3

INVARIANTS OF THE REYNOLDS STRESS ANISOTROPY TENSOR b_{ij}

Fitting function: $f = d \left(\dfrac{SL}{q} \right)^a (1+bM^2)(Re_\lambda)^c$

II:

$a = 0.54$

$b = 0.61$ rms error $= 0.048$

$c = 0.19$

$d = 0.01$

III:

$a = 1.27$

$b = 2.37$ rms error $= 0.010$

$c = 0.55$

$d = 0.001$

Table 4.4

INVARIANTS OF THE DISSIPATION ANISOTROPY TENSOR d_{ij}

Fitting function: $f = d \left(\dfrac{SL}{q} \right)^a (1+bM^2)(Re_\lambda)^c$

II:

$a = 0.688$

$b = -2.079$ err $= .072$

$c = 0.334$

$d = 0.008$

III:

$a = 1.787$

$b = -6.142$ err $= 0.024$

$c = 1.473$

$d < 0.001$

Table 4.5

ROTTA MODEL EVALUATION

Fitting function: $f = d \left(\dfrac{SL}{q}\right)^a (1+bM^2)(Re_\lambda)^d$

Rotta Term Alone (ϕ_{ij}):

Equation	c_1	a	b	c	d	rms Error
i = 1, j = 1	1.114 ± 0.723	−1.519	−3.763	0.912	1.949	0.049
i = 2, j = 2	1.730 ± 0.899	−0.776	3.614	0.674	0.762	0.074
i = 3, j = 3	0.680 ± 0.583	−1.965	−7.352	1.226	1.481	0.119
i = 1, j = 2	1.559 ± 1.090	−0.592	−2.311	1.219	0.067	0.079

Rotta Term with Dissipation Anisotropy $(\phi_{ij}-2\varepsilon d_{ij})$:

i = 1, j = 1	2.886 ± 0.722	−0.458	−2.840	0.443	2.059	0.057
i = 2, j = 2	3.727 ± 0.824	−0.352	0.105	0.325	2.652	0.049
i = 3, j = 3	1.719 ± 0.921	−0.126	−4.981	1.059	0.053	0.154
i = 1, j = 2	3.035 ± 1.122	−0.294	−2.252	0.725	0.445	0.057

Table 4.6

CONSTANTS IN LUMLEY'S FITTING FUNCTION

FOR THE ROTTA CONSTANT

(See Eq. (4.9.6))

Equation	a	b	c	d	rms Error
i = 1, j = 1	7.795	244.196	21.233	−5.81	0.067
i = 2, j = 2	4.275	152.380	21.765	−1.842	0.043
i = 1, j = 2	9.191	525.294	2.106	31.064	0.054

Lumley predicts   a = 7.77,   b = 80.1,   c = 62.4,   d = 2.3.

Table 4.7

LUMLEY AND NEWMAN'S FITTING FUNCTION

FOR THE ROTTA CONSTANT

$$f = 2.0 + a\ \text{Re}^{1/2}$$

(See Eq. (4.9.8))

Equation	a	rms Error
i = 1, j = 1	1.682	0.334
i = 2, j = 2	3.681	0.376
i = 3, j = 3	−1.550	0.411
i = 1, j = 2	1.624	0.439

Table 4.8

GENERAL FOURTH-RANK TENSOR MODEL

Fitting function: $f = d \left(\dfrac{SL}{q}\right)^a (1+bM^2)(\text{Re}_\lambda)^c$

(See Eq. (4.9.8))

Equation	A_1	a	b	c	d	rms Error
i = 1, j = 1	−4.090 ± 0.173	0.088	−0.225	0.061	−2.595	0.010
i = 2, j = 2	−2.134 ± 0.052	0.073	0.799	−0.001	−1.930	0.014
i = 3, j = 3	−0.482 ± 0.147	−0.701	−3.593	−0.333	−13.190	0.088
i = 1, j = 2	−1.153 ± 0.098	0.190	−0.675	0.030	−0.642	0.025

Table 4.9

GIBSON/LAUNDER MODEL FOR FAST TERM

Fitting function: $f = d \left(\dfrac{SL}{q}\right)^a (1+bM^2)(Re_\lambda)^c$

Equation	A_2	a	b	c	d	rms Error
i = 1, j = 1	0.324 ± 0.061	−0.423	0.707	−0.274	2.673	0.047
i = 2, j = 2	−0.134 ± 0.052	0.471	48.117	−0.156	−0.020	0.179
i = 3, j = 3	0.289 ± 0.088	−0.701	−3.592	−0.333	7.914	0.088
i = 1, j = 2	0.198 ± 0.029	0.000	−0.705	−0.236	0.501	0.059

Table 4.10

GENERAL FOURTH-RANK TENSOR WITH
DISSIPATION ANISOTROPY TERMS FOR FAST TERM

Equation	A_1	C_2	C_3	rms Error
i = 1, j = 1	−1.818	1.624	0.612	0.033
i = 2, j = 2	−2.221	1.624	0.612	0.016
i = 3, j = 3	−1.926	0.403	0.0	0.217
i = 1, j = 2	−1.731	0.132	−0.055	0.011

Table 4.11

COMPRESSIBLE PRESSURE-STRAIN TERMS

General Fourth-Rank Tensor Model

(Compressible terms alone)

Fitting function: $f = d\left(\dfrac{SL}{q}\right)^a M^b (Re_\lambda)^c$

Equation	A_1	a	b	c	d	rms Error
i = 1, j = 1	−3.962 ± 0.199	−0.015	−0.111	0.095	−2.397	0.032
i = 2, j = 2	−1.989 ± 0.076	−0.101	−0.083	0.034	−1.995	0.020
i = 3, j = 3	−0.678 ± 0.138	−0.430	0.071	−0.232	−5.663	0.093
i = 1, j = 2	−1.228 ± 0.094	0.208	0.060	−0.033	−0.882	0.033

Table 4.12

COMPRESSIBLE PRESSURE-STRAIN TERMS

General Fourth-Rank Tensor Model on Compressible and

Fast Pressure-Strain Terms

Fitting function: $f = d\left(\dfrac{SL}{q}\right)^a (1+bM^2)(Re_\lambda)^c$

Equation	A_1	a	b	c	d	rms Error
i = 1, j = 1	−3.052 ± 0.323	0.121	−1.889	0.167	−1.302	0.056
i = 2, j = 2	−2.123 ± 0.068	−0.054	−0.065	0.009	−2.369	0.025
i = 3, j = 3	−1.160 ± 0.261	−0.556	−1.232	−0.262	−14.409	0.070
i = 1, j = 2	−1.388 ± 0.069	0.073	0.592	−0.065	−1.418	0.034

Table 4.13

SIMULTANEOUSLY DETERMINED CONSTANTS FOR THE TOTAL

PRESSURE-STRAIN TENSOR PLUS DISSIPATION ANISOTROPY

Modeling of $(\Phi_{ij} - 2\varepsilon d_{ij})$

Gibson/Launder + Rotta Models

Equation	Fast Const	Rotta const	rms Error
i = 1, j = 1	0.334	3.234	0.120
i = 2, j = 2	0.022	3.106	0.099
i = 3, j = 3	1.122	-4.571	0.163
i = 1, j = 2	0.426	0.899	0.057

Fourth-Rank Tensor + Rotta Models

Equation	Fast const	Rotta const	rms Error
i = 1, j = 1	-3.332	3.234	0.325
i = 2, j = 2	-1.978	3.106	0.042
i = 3, j = 3	-1.869	-4.571	0.163
i = 1, j = 2	-1.500	2.074	0.020

89

Table 4.14

TEST OF STRUCTURAL SIMILARITY

$$C_1 = \phi_{ij} / \left[\mathscr{P}(b_{ij} - p_{ij}) - \varepsilon(b_{ij} - d_{ij}) + \Phi(b_{ij} + \frac{1}{3}\delta_{ij}) \right]$$

Fitting function: $f = d \left(\frac{SL}{q}\right)^a (1+bM^2)(Re_\lambda)^c$

Equation	C_1	a	b	c	d	rms Error
i = 1, j = 1	0.868 ± 0.067	-0.120	0.475	0.045	0.979	0.045
i = 2, j = 2	0.616 ± 0.208	-0.078	10.25	-0.062	0.618	0.257
i = 3, j = 3	0.944 ± 0.09	-0.207	-0.862	0.089	1.214	0.054
i = 1, j = 2	1.381 ± 0.268	0.379	0.403	0.212	0.218	0.099

Table 4.15

STRUCTURAL SIMILARITY MODEL

$$\phi_{ij} = 2(b_{ij} - p_{ij}) - 2\varepsilon b_{ij}(1-C_1), \quad \text{see Eq. (4.12.5)}$$

Fitting function: $f = d \left(\frac{SL}{q}\right)^a (1+bM^2)(Re_\lambda)^c$

Equation	C_1	a	b	c	d	rms Error
i = 1, j = 1	1.005 ± 0.170	-0.012	-2.811	-0.038	1.411	0.125
i = 2, j = 2	1.340 ± 0.202	-0.069	-2.564	0.218	0.813	0.118
i = 3, j = 3	0.920 ± 0.452	0.873	3.833	0.006	0.071	0.318
i = 1, j = 2	0.023 ± 0.529	10.570	-224.900	-4.53	0.0	0.649

Table 4.16

STRUCTURAL SIMILARITY MODEL

$$\phi_{ij} = C_1 \mathscr{P}(b_{ij} - p_{ij}) - C_2 \varepsilon b_{ij}), \quad \text{see Eq. (4.12.6)}$$

Equation	C_1	C_2	rms Error
i = 1, j = 1	0.977	0.128	0.057
i = 2, j = 2	0.480	0.217	0.210
i = 3, j = 3	1.201	-0.946	0.056
i = 1, j = 2	1.454	0.245	0.204

Chapter V

CONCLUSIONS AND RECOMMENDATIONS

While much turbulence research has been done in incompressible flows, most turbulent flows of technological interest are compressible. Knowledge about turbulence modeling gained from incompressible studies has been widely used in compressible simulations, sometimes with excellent results and other times with failure. Because measurements in high-speed flows are so difficult, little is known about the structure of the Reynolds stresses and their dynamic equations in these cases, and consequently there is little guidance on how to construct turbulence models.

To study these stresses, we used the power of a large, modern vector computer to simulate directly the full, compressible Navier-Stokes equations, with no turbulence model. By using the computer in this way, as a "numerical wind tunnel," we were able to measure turbulence quantities that are of particular interest to modelers. Some of these quantities, for example the pressure-strain terms in the Reynolds stress equations, cannot be directly measured by experimental means. This type of simulation allows these terms to be directly measured and studied for the first time.

To this end, we chose a simple, homogeneous shear flow that is an approximation to a small part of a more complicated shear flow. We have extended and developed incompressible techniques for the simulation of compressible homogeneous flows with a general mean-velocity gradient. A code that runs on the ILLIAC IV computer was constructed to implement these techniques. After thorough testing, eight complete 64 × 64 × 64 mesh size simulations were performed, and the resulting simulated flow fields were used as a data base in which to study turbulence quantities.

Several measures of the structure of the Reynolds stresses were used to compare the simulated stress tensor to measurements from experiment. Agreement was good, with little indication that the stresses in compressible shear flows are significantly different from the incompressible case.

A spectral decomposition originally due to Moyal (1951) was implemented and extended numerically to divide the velocity field into "incompressible" and "compressible" parts. We found that the stresses arise primarily from the incompressible part of the velocity field, in agreement with Morkovin's (1962) hypothesis that compressibility has but a small effect on these stresses.

Although the question of whether or not a homogeneous shear flow comes to a state of structural equilibrium is yet unresolved, we find an indication that these shear flows are tending toward similarity, as defined by constant values of the stress anisotropy tensor. We are unable to carry the simulations far enough in time to see this state, but the time histories of the anisotropies seem to indicate this. This has an important bearing on the construction of some of the turbulence models that we have evaluated.

It is known that the performance of incompressible turbulence models deteriorates at high Mach number. To search further for this effect, we studied the Reynolds stress equations and evaluated models for the various terms.

In a compressible flow, the trace of the pressure strain tensor is not zero. Without direct measurement, it cannot be told from the turbulent kinetic energy equation whether this term is productive or dissipative. We find it to be dissipative. This is an effect that is not represented in current kinetic energy equation models, but perhaps it should be.

To gain insight into pressure strain-term modeling in incompressible flows, these terms are symbolically decomposed into two parts, the Rotta and the Fast terms. This decomposition is not actually performed but is simply used to justify the construction of models for each part. We performed this decomposition numerically for the first time and were able to evaluate the individual terms directly.

In compressible flow we found that this decomposition produces three parts. Because the third part represents the deviation of the pressure-strain tensor from the incompressible case, we call this third part the compressible term. It was found to be of the same order of magnitude as the Rotta and Fast terms, and therefore it must be modeled.

Models were separately evaluated for each part of the pressure strain tensor. We found that the Rotta model performs much better when used to replace the sum of the Rotta pressure-strain term and the dissipation anisotropy, and would recommend that it be used this way.

Several models were evaluated for the Fast and compressible terms, with varying degrees of success. Although its performance must be significantly improved, the general linear fourth-rank tensor model performs the best. There are significant mathematical objections to its use, but until more sophisticated models are developed we would recommend its use, with carefully chosen constants for the sum of the Fast and Compressible terms.

We found that the constants that must be determined for use in these models are more uniform if they are determined simultaneously from the total pressure strain tensor. We suspect that individual determination of the constants from the decomposed pressure-strain field is not advisable and recommend their simultaneous determination.

A class of models based on structural similarity was proposed for the entire pressure-strain tensor. These models show promise but need to be studied in a more fully developed turbulent flow.

The dissipation tensor was found to be very anisotropic. We searched for a dependence of this anisotropy on the Reynolds number and found a positive relation between the two, indicating that the dissipation is not necessarily isotropic at higher Reynolds number in a persistently sheared flow, as was thought. This important result may alter thinking about the structure and the modeling of the dissipation terms, which are normally considered to be isotropic at high Reynolds numbers.

The results of this work have fallen primarily into two categories: results that bear on all turbulent shear flows and results that pertain only to compressible shear flows. We have identified some differences that occur in compressible flows and evaluated models for both new and old terms. However, much that we have studied applies to all shear flows.

We have concentrated primarily on the Reynolds stresses, but there is much additional work that needs to be done.

For further research in this area, we recommend that:

1. The turbulent terms in the thermal energy equation be studied and models compared with the exact flow fields.

2. The capability be developed to follow the flow for a greater non-dimensional time (a larger computer?).

3. An exactly parallel incompressible code be developed to better assess the changes in the compressible flow.

4. The method be extended for simulation of higher Reynolds number flows (possibly via large eddy simulations?).

5. The method be extended for non-periodic boundary conditions (a compressible mixing layer would be very interesting for noise studies.)

This work simply scratches the surface of the vast new area of direct simulation of turbulent flows. Use of the computer as a numerical wind tunnel complements the use of laboratory wind tunnels and allows us to study turbulence in a way that has never before been possible. It will undoubtedly give us great insight when the next generation of super-computers becomes available, as it already does right now. It is the author's opinion that this technique will become a major tool in the turbulence modeler's inventory in the next few years.

References

1. Batchelor, G. K., The Theory of Homogeneous Turbulence, Cambridge University Press (1953).

2. Bennett, J. C., Jr., "Measurements of Grid-Generated, Nearly Isotropic Turbulence at Small Reynolds Numbers," doctoral dissertation, Dept. of Mechanics and Materials Science, The Johns Hopkins University, June, 1976.

3. Bradshaw, "Compressible Turbulent Shear Layaers," Annual Review of Fluid Mechanics, 1977, pp. 33-54.

4. Briley, W. R., and H. MacDonald, "An Implicit Numerical Method for the Multidimensional, Compressible Navier-Stokes Equations," Report M911363-6, United Aircraft Research Laboratories, East Hartford, Conn., November, 1973.

5. Brown, G. L., and A. Roshko, "On Density Effects and Large Structure in Turbulent Mixing Layers," JFM Vol. 64. Part 4. pp. 775-816. (1974).

6. Champagne, F. H., V. G. Harris, and S. Corrsin, "Experiments on Nearly Homogeneous Turbulent Shear Flow," JFM, Vol. 41, Part 1, pp. 81-139 (1970).

7. Chu, Boa-Teh, and L. S. G. Kovasznay, "Nonlinear Interactions in a Viscous Heat-Conducting Compressible Gas," JFM, Vol. 3, Part 5, pp. 494-514, Feb. 1958.

8. Chung, M. K., and R. J. Adrian, "Evaluation of Variable Coefficients in Second-Order Turbulence Models," 2nd Symposium on Turbulent Shear Flows, Imperial College, London, July 2-4, 1979, pp. 10.43-10.48.

9. Clark, R. A., J. H. Ferziger, and W. C. Reynolds, "Evaluation of Subgrid-Scale Turbulence Models Using a Fully Simulated Turbulent Flow," Report TF-9, Dept. of Mechanical Engineering, Stanford University, March, 1977.

10. Comte-Bellot, G., and S. Corrsin, "Simple Eulerian Time Correlation of Full- and Narrow-Band Velocity Signals in Grid-Generated 'Isotropic' Turbulence," JFM, Vol. 48, Part 2, pp. 273-337 (1971).

11. Deardorff, J. W., "A Numerical Study of Three-Dimensional Turbulent Channel Flow at Large Reynolds Numbers," JFM, Vol. 41, Part 2, pp. 453-480 (1970).

12. Favre, A., "Equations des Gaz Turbulents Compressibles," J. de Mecan., Vol. 4, No. 3, pp. 361-390, Sept. 1965.

13. Hanjalic, K., and B. E. Launder, "A Reynolds Stress Model of Turbulence and Its Application to Axisymmetric Boundary Layers," JFM, Vol. 52, p. 609 (1972).

14. Harris, V. G., J. A. H. Graham, and S. Corrsin, "Further Experiments in Nearly Homogeneous Turbulent Shear Flow," JFM, Vol. 81, Part 4, pp. 657-687 (1977).

15. Hinze, O., Turbulence, McGraw-Hill, 1975.

16. Hirt, C. W., "Compute Studies of Time-Dependent Turbulent Flow," Physics of Fluids, Supplement II, pp. 219-227 (1969).

17. Kovasznay, L. S. G., "Turbulence in Supersonic Flow," J. of the Aeronautical Sciences, Vol. 20, No. 10, pp. 657-675, October, 1953.

18. Kwak, D., W. C. Reynolds, and J. H. Ferziger, "Three-Dimensional, Time-Dependent Computation of Turbulent Flow," Report TF-5, Dept. of Mechanical Engrg., Stanford University, May, 1975.

19. Laufer, J., "Thoughts on Compressible Turbulent Boundary Layers," Memorandum RM-5946-PR, RAND Corp., March, 1969.

20. Launder, B. E., G. J. Reece, and W. Rodi, "Progress in the Development of a Reynolds-Stress Turbulence Closure," JFM, Vol. 68, Part 3, pp. 537-566 (1975).

21. Leslie, D. C., "Analysis of a Strongly Sheared, Nearly Homogeneous Turbulent Shear Flow," JFM, Vol. 98, Part 2, pp. 435-448 (1980).

22. Lomax, H., "An Operational Unification of Finite-Difference Methods for the Numerical Integration of Ordinary Differential Equations," NASA TR-R-262 (1967).

23. Lumley, J. L., Stochastic Tools in Turbulence, Academic Press, 1970.

24. Lumley, J. L., and B. Khajeh-Nouri, "Computational Modeling of Turbulent Transport," Advances in Geophysics, Vol. 18A, Academic Press, 1974.

25. Lumley, J. L., and G. R. Newman, "The Return to Isotropy of Homogeneous Turbulence," JFM, Vol. 82, Part 1, pp. 161-178 (1977).

26. Lumley, J. L., "Computational Modeling of Turbulent Flows," Advances in Applied Mechanics, Vol. 18 (1978).

27. Lumley, J. L., "Second-Order Modeling of Turbulent Flows," Prediction Methods for Turbulent Flows (W. Kollmann, ed.), Von Karmann Institute, Hemisphere Publishing Co. (1980).

28. MacCormack, R. W., "The Effect of Viscosity in Hypervelocity Impact Cratering," AIAA Paper No. 69-354, AIAA Hypervelocity Impact Conference, Cincinnati, Ohio, April 30-May 2, 1969.

29. Mansour, N. N., J. H. Ferziger, and W. C. Reynolds, "Large Eddy Simulation of a Turbulent Mixing Layer," Report TF-11, Dept. of Mechanical Engineering, Stanford University, April, 1978.

30. Moin, P., W. C. Reynolds, and J. H. Ferziger, "Large Eddy Simulation of Incompressible Turbulent Channel Flow," Report TF-12, Dept. of Mechanical Engineering, Stanford University, May, 1978.

31. Morkovin, M. V., "Effects of Compressibility on Turbulence," Mecanique de la Turbulence, Edition of C.N.R.S., Paris, 1962.

32. Morkovin, M. V., et al., "Report of Conference Evaluation Committee," Free Turbulent Shear Flows Conference Proceedings, Hampton, Virginia, July 20-21, 1972, NASA SP-321, pp. 673-698.

33. Moyal, J. E., "The Spectra of Turbulence in a Compressible Fluid; Eddy Turbulence and Random Noise," Proc. Camb. Phil. Soc., Vol. 48, p. 329 (1952).

34. Oh, Y. H., "Analysis of Two-Dimensional Free Turbulent Mixing," AIAA 7th Fluid & Plasma Dynamics Conference, Palo Alto, CA., June 17-19, 1974, AIAA Paper 74-594.

35. Orszag, S. A., "Numerical Simulation of Incompressible Flows Within Simple Boundaries: I. Galerkin (Spectral) Representations," Studies in Applied Math., Vol. L, No. 4, December, 1971.

36. Pulliam, T. H., and H. Lomax, "Simulation of Three-Dimensional Compressible Viscous Flow on the ILLIAC IV Computer," Paper #79-0206, 17th Aerospace Sciences Meeting, New Orleans, LA., January 15-17, 1979.

37. Reynolds, A. J., and H. J. Tucker, "The Distortion of Turbulence by General Uniform Irrotational Strain," JFM, Vol. 68, Part 4, pp. 673-693 (1975).

38. Reynolds, O., "An Experimental Investigation of the Circumstances Which Determine Whether the Motion of Water Shall Be Direct or Sinuous and of the Law of Resistance in Parallel Channels," Trans. of the Roy. Phil. Soc. of London, 174, pp. 935-982 (1883).

39. Reynolds, W. C., "Computation of Turbulent Flows," Annual Review of Fluid Mechanics, Vol. 8, pp. 183-208 (1976).

40. Rodi, W., "A New Algebraic Relation for Calculating the Reynolds Stress," ZAMM, Vol. 56, pp. 219-221 (1976).

41. Rogallo, R. S., "An ILLIAC Program for the Numerical Simulation of Homogeneous, Incompressible Turbulence," NASA TM-73203, November, 1977.

42. Rogallo, R. S., (1979), personal communication).

43. Rose, W. G., "Results of an Attempt to Generate a Homogeneous, Turbulent Shear Flow," JFM, Vol. 25, Part 1, pp. 97-120 (1966).

44. Rotta, J., "Statistiche Theorie Nichthomogener Turbulenz, Zeitschrift für Physik Bd. 129 S547-572 (1951).

45. Rubesin, M. W., and W. C. Rose, "The Turbulent Mean-Flow, Reynolds-Stress, and Heat-Flux Equations in Mass-Averaged Dependent Variables," NASA TM-X-62,248, March, 1973.

46. Schumann, U., "Realizability of Reynolds Stress Turbulence Models, Phys. Fluids, Vol. 20, pp. 721-725 (1977).

47. Schumann, U., and G. S. Patterson, "Numerical Study of the Return of Axisymmetric Turbulence to Isotropy," JFM, Vol. 88, Part 4, pp. 711-735 (1978).

48. Shanaan, S., J. H. Ferziger, and W. C. Reynolds, "Numerical Simulation of Turbulence in the Presence of Shear," Report TF-6, Dept. of Mechanical Engineering, Stanford University, August, 1975.

49. Shirani-C, E., J. H. Ferziger, and W. C. Reynolds, "Mixing of a Passive Scalar in Homogeneous Turbulent Shear Flows," Dept. of Mechanical Engineering, Stanford University (to be published).

50. Tavoularis, S., J. C. Bennett, and S. Corrsin, "Velocity-Derivative Skewness in Small Reynolds Number, Nearly Isotropic Turbulence," JFM, Vol. 88, Part 1, pp. 63-69 (1978).

51. Van Dyke, M., "Perturbation Methods in Fluid Mechanics," Parabolic Press, Stanford, CA (1975).

52. Warming, R. V., R. M. Beam, and B. J. Hyatt, "Diagonalization and Simultaneous Symmetrization of the Gas Dynamic Matrices," Math. Comp., Vol. 29, pp. 1037-1045 (1975).

53. Warming, R. F., and R. M. Beam, "On the Construction and Application of Implicit Factored Schemes for Conservation Laws," SIAM-AMS Proceedings, Vol. 11, 1978.

54. Wray, A. A. (1980), personal communication.

MEAN FLOW

Y (X_2)

$$S = \frac{DU}{DY}$$

SHEAR RATE

Z
(X_3)

X (X_1)
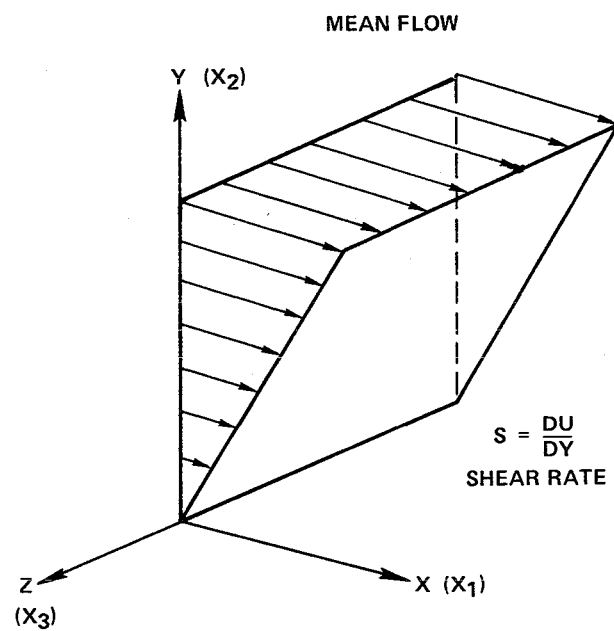
Fig. 1.1. Schematic of the Mean Velocity Profile.
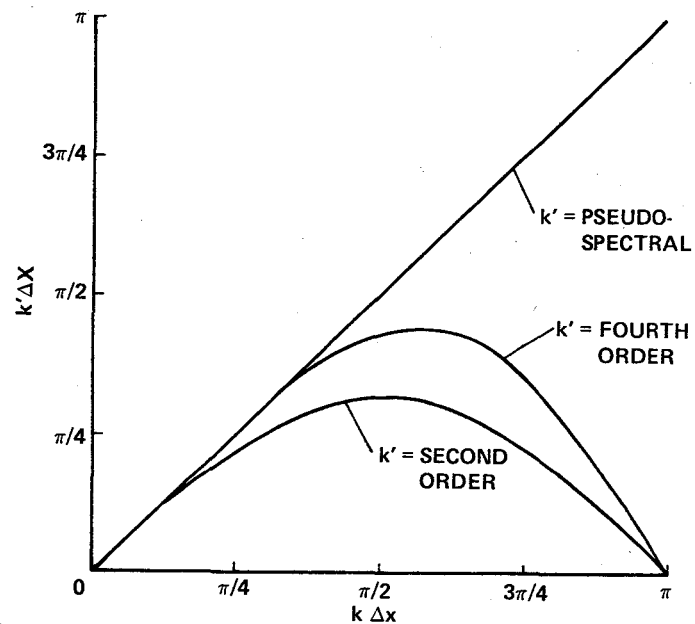
Fig. 2.1. Modified wave numbers for two finite-difference approximations and the pseudo-spectral approximation to spatial derivatives vs. the analytic wave number.
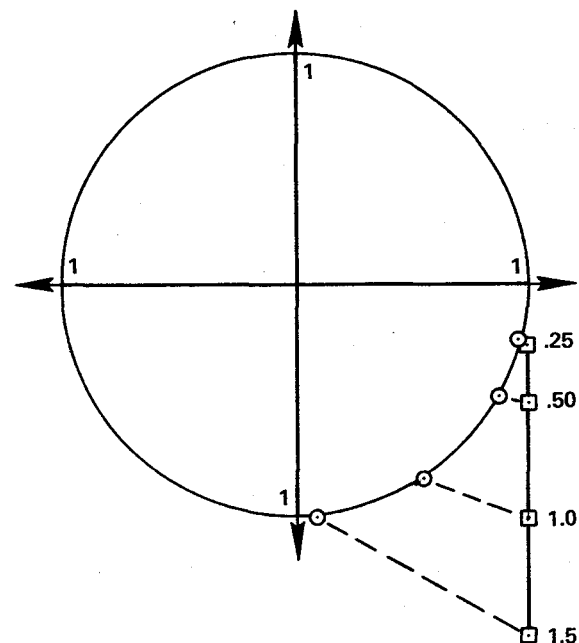
Fig. 2.2. Computational root of the Euler explicit method for linear Burgers equation in the complex plane. Viscous stability number V = 0 (convective terms only), ▢ and the analytic root, ⊙ ; for several Courant numbers.
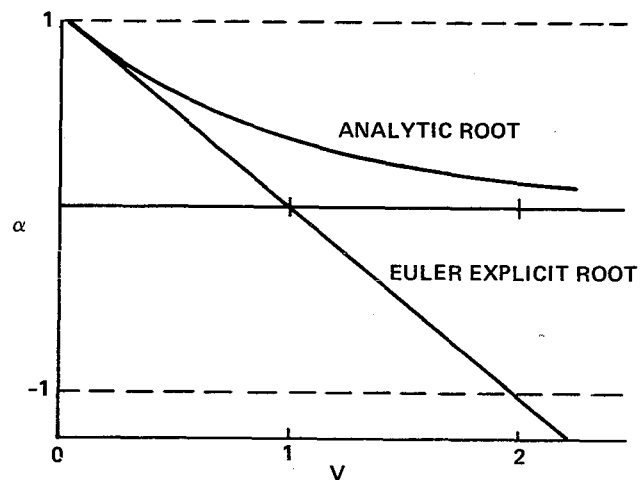
Fig. 2.3. Computational root of the Euler explicit
method for linear Burgers equation, Courant
number C = 0 (viscous terms only), and
the analytic root vs. the viscous stability
number $V = hk^2/\nu$.
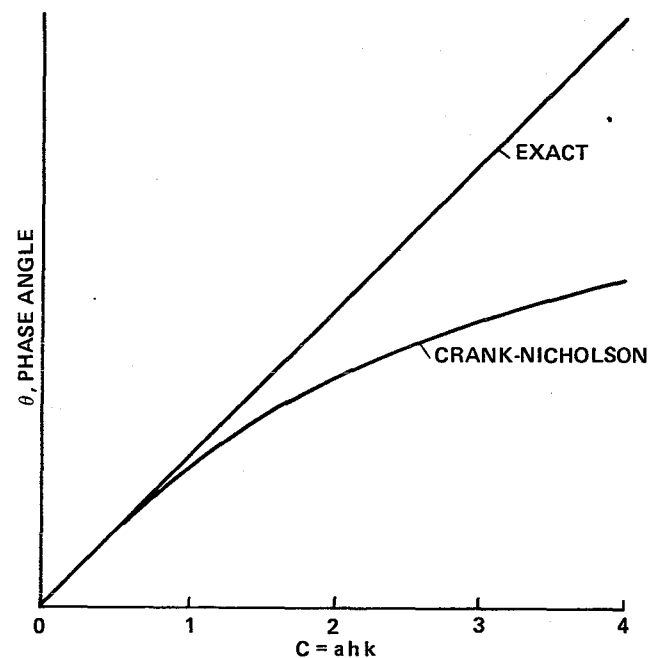
Fig. 2.4. Argument (phase angle) of the computational
root of the Crank-Nicholson method vs. the
argument of the analytic root. Linear Bur-
gers equation; viscous stability number
$V = 0$ (convective terms only).
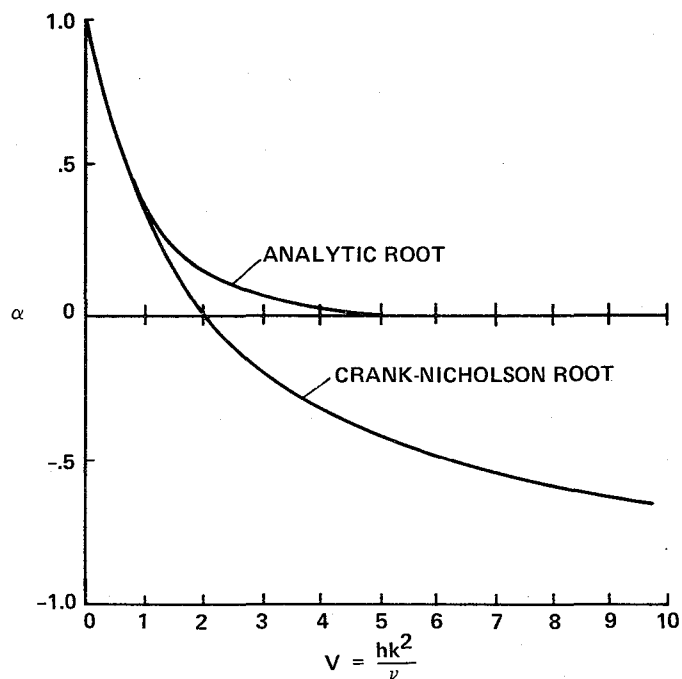
Fig. 2.5. Roots for analytic solution and Crank-Nicholson method vs. viscous stability number. Linear Burgers equation, Courant number $C = 0$ (viscous terms only).
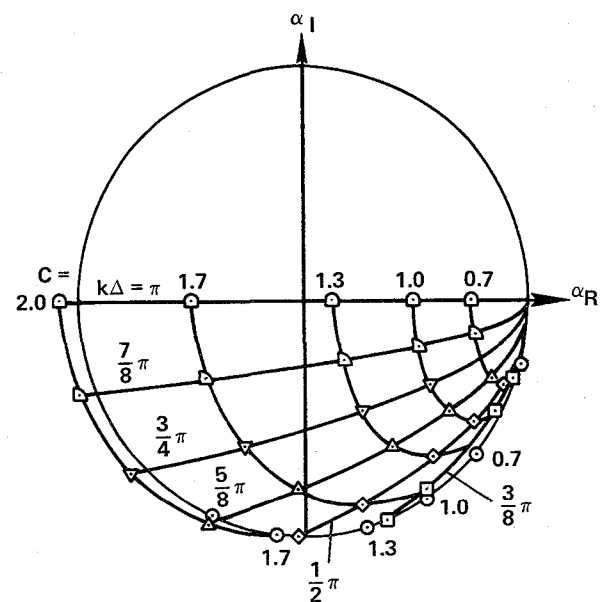
Fig. 2.6. Computational root of MacCormack's method in the complex plane. Viscous stability number $V = 0$ (convective terms only). For several wave numbers. Note the highly dissipative ($|\alpha| \ll 1.0$) behavior for the higher wave numbers. The wave numbers are labeled $k\Delta =$, the Courant numbers are labeled $C =$. The analytic root $\odot$ lies on the unit circle and is labeled with its Courant number.
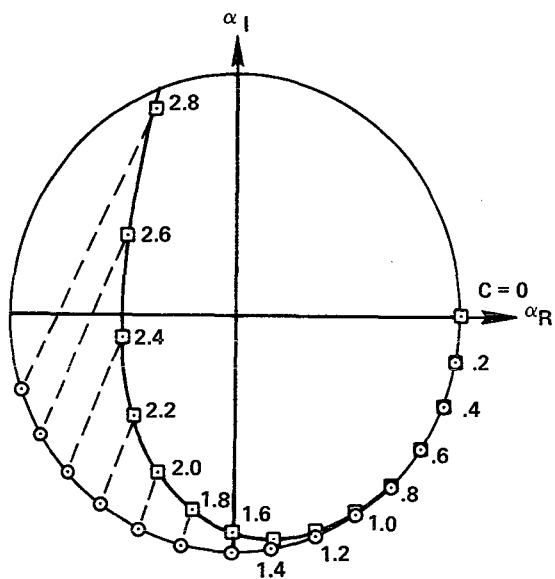
Fig. 2.7. Roots for analytic solution and 4th-order Runge-Kutta method in the complex plane. Linear Burgers equation. Viscous stability number V = 0 (convective terms only), for several Courant numbers. Analytic root $\bigcirc$, Runge-Kutta root $\boxdot$.
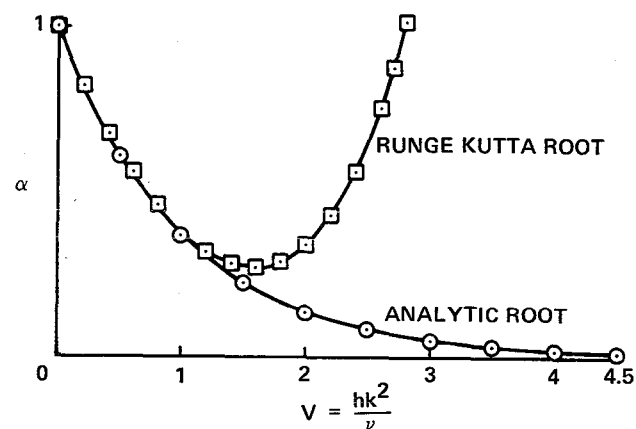
Fig. 2.8. Roots for analytic solution and 4th-order Runge-Kutta method. Linear Burgers equation. Courant number C = 0 (viscous terms only) vs. viscous stability number V. Analytic root $\odot$, Runge-Kutta root $\boxdot$.
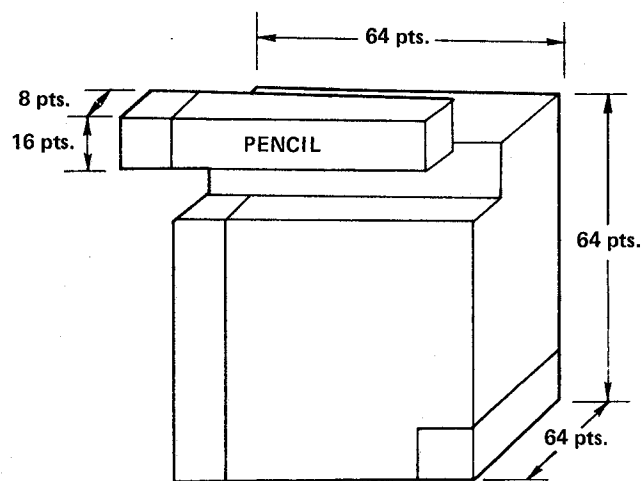
Fig. 3.1. The pencil system data base method for handling
movement of data between the ILLIAC IV disk and
core memory. Data are brought into core as a
"pencil" which is an $8 \times 16 \times 64$ point section
of the $64 \times 64 \times 64$ size mesh. Each mesh point
is part of three pencils corresponding to the
x, y, and z directions.
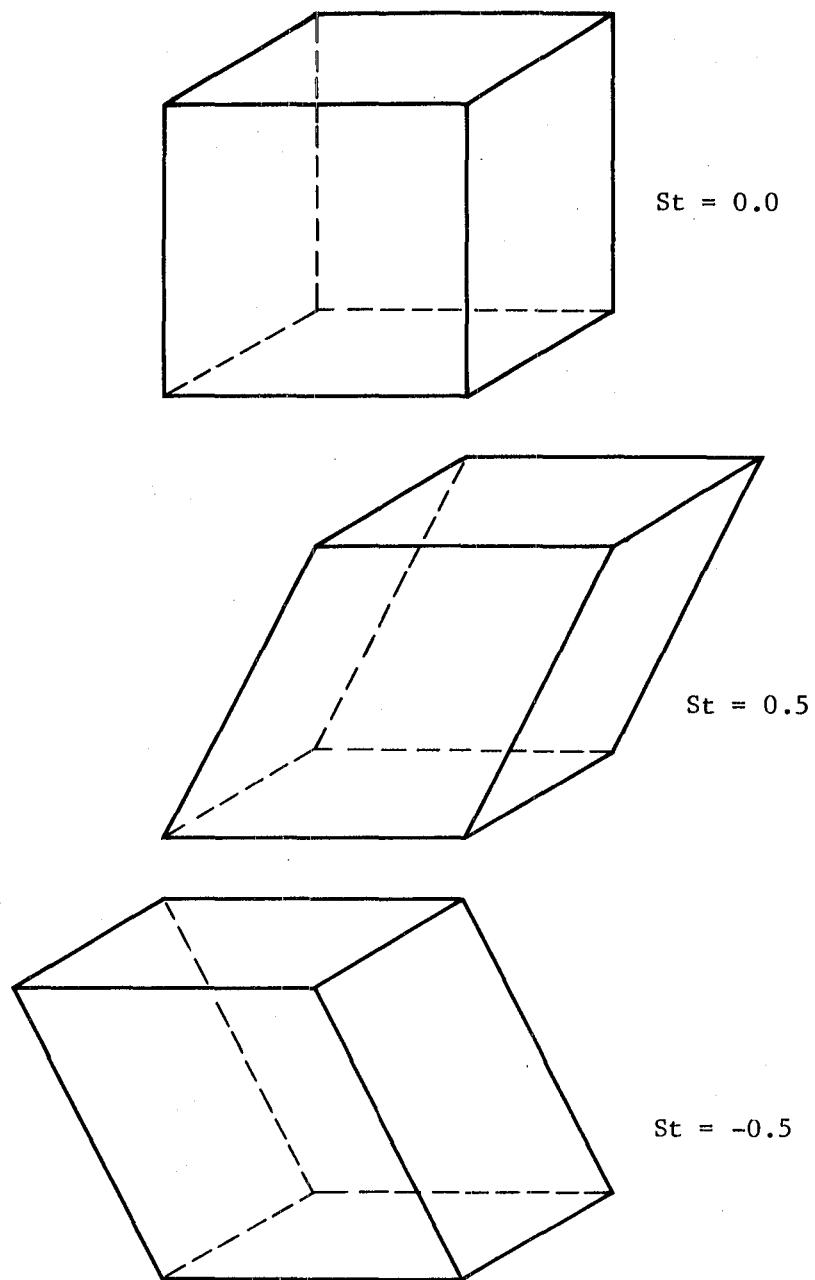
St = 0.0

St = 0.5

St = -0.5

Fig. 3.2. The "remeshing" process for the computational
mesh. Top figure: St = 0.0 (mesh metric) Car-
tesian. Middle figure: St = 0.5. Computation
is stopped here and the flow field is interp-
olated onto the mesh in the bottom figure at
St = -0.5. Computation is then resumed.
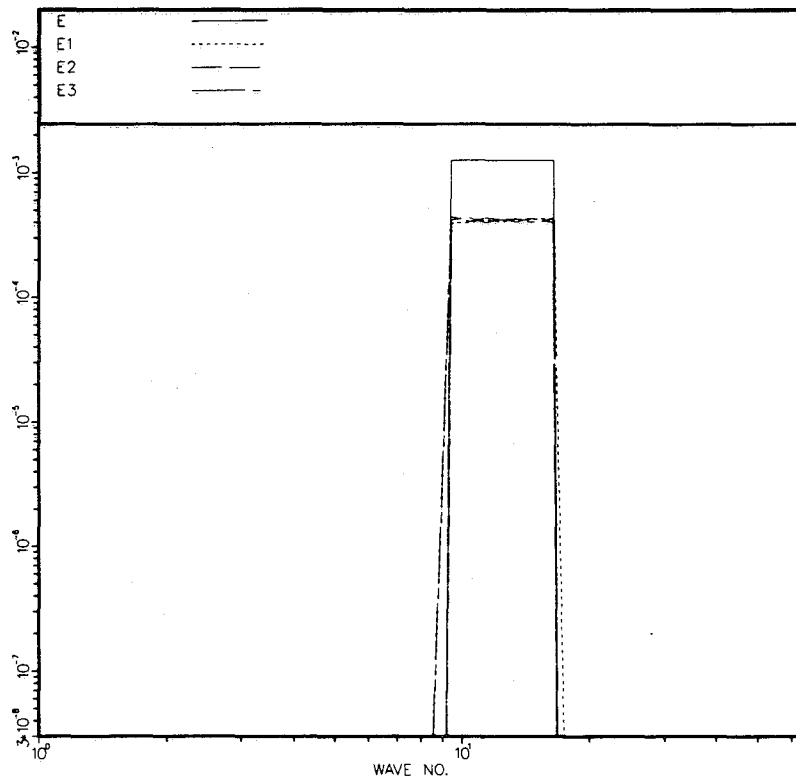
Fig. 3.3. 3-D spectra of the initial velocity field
for simulation IH64A. All initial spectra
are similar except for the intensity of
the turbulence.
E   indicates twice the turbulent kinetic
     energy $\rho u_i u_i$.
E1   indicates ρu^2.
E2   indicates ρv^2.
E3   indicates ρw^2.
Wave No. indicates the magnitude of the
wave number k.
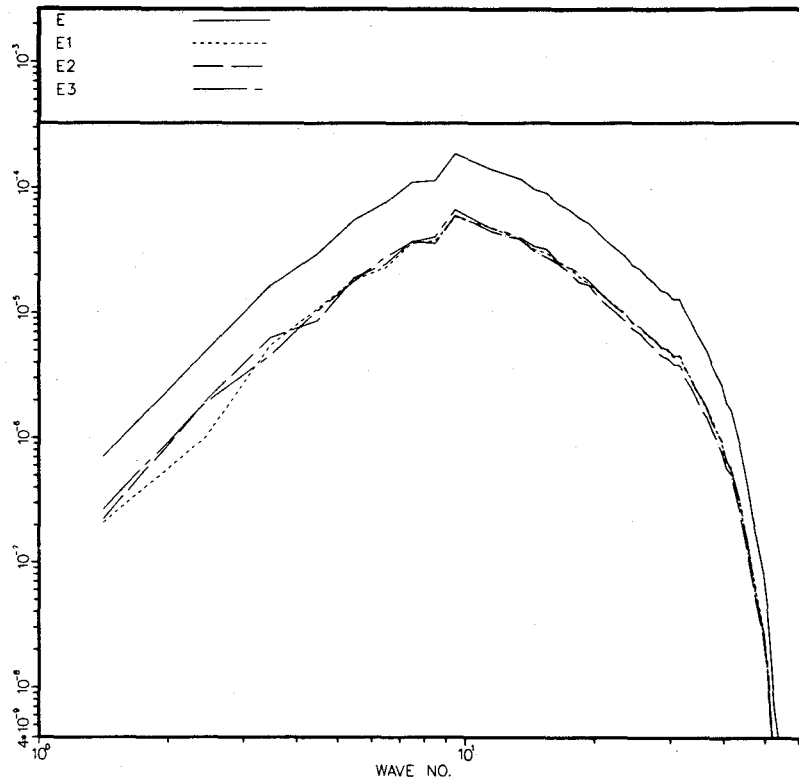
Fig. 3.4. 3-D spectra of the velocity field for the
isotropic homogeneous simulation IH64 at
time = 7.849. Same nomenclature as for
Fig. 3.3.

107

TWO POINT CORRELATIONS   1-D ENERGY SPECTRA

108
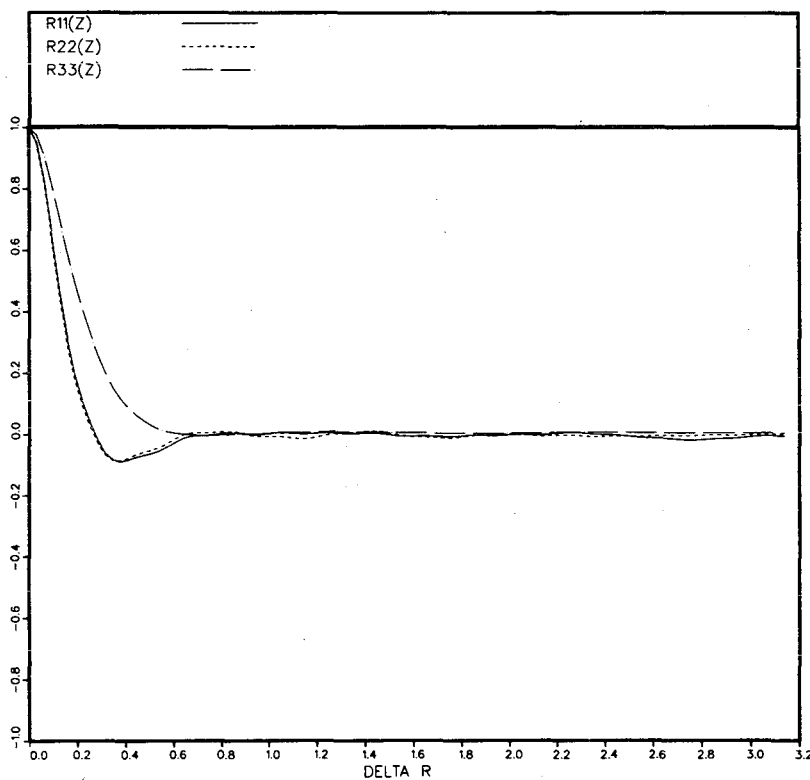
Fig. 3.5. Two-point correlations in the z-direction
           for simulation IH64A at time = 7.849.
           R11 (z) indicates the u velocity corr.
           R22 (z) indicates the v velocity corr.
           R33 (z) indicates the w velocity corr.
           Delta R indicates the separation (Delta R
           = 3.14 is half the computational box size.)
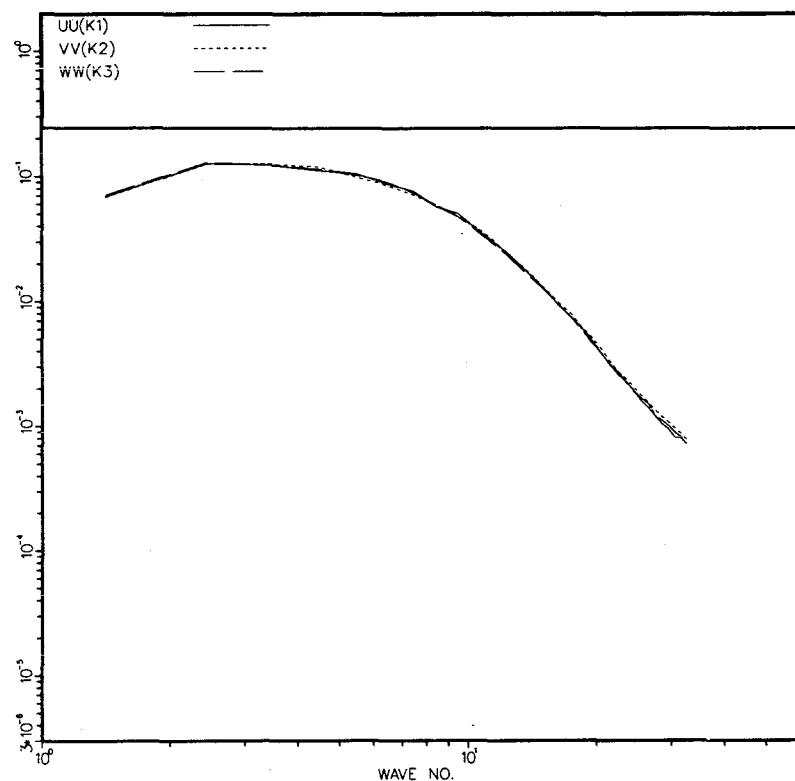
Fig. 3.6. 1-D spectra of the velocity field for simu-
           lation IH64A at time = 7.849. Wave No.
           indicates the wavenumber k_i in the re-
           spective direction.

MICRO SCALES INTEGRAL SCALES
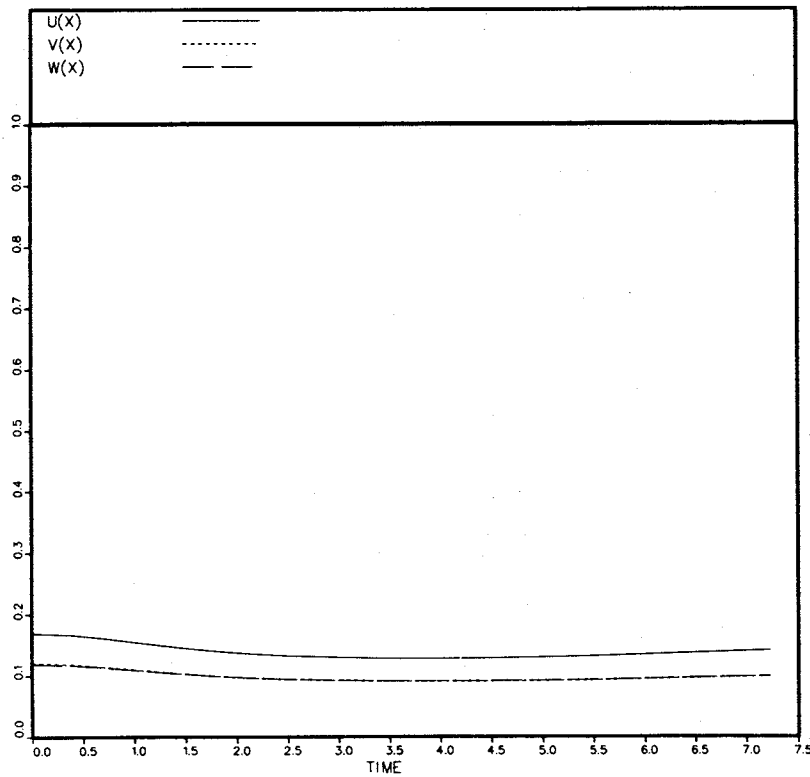
Fig. 3.7. z-direction Taylor microscales vs. time
for simulation IH64A.
U(Z) indicates the scale assoc. with u.
V(Z) indicates the scale assoc. with v.
W(Z) indicates the scale assoc. with w.
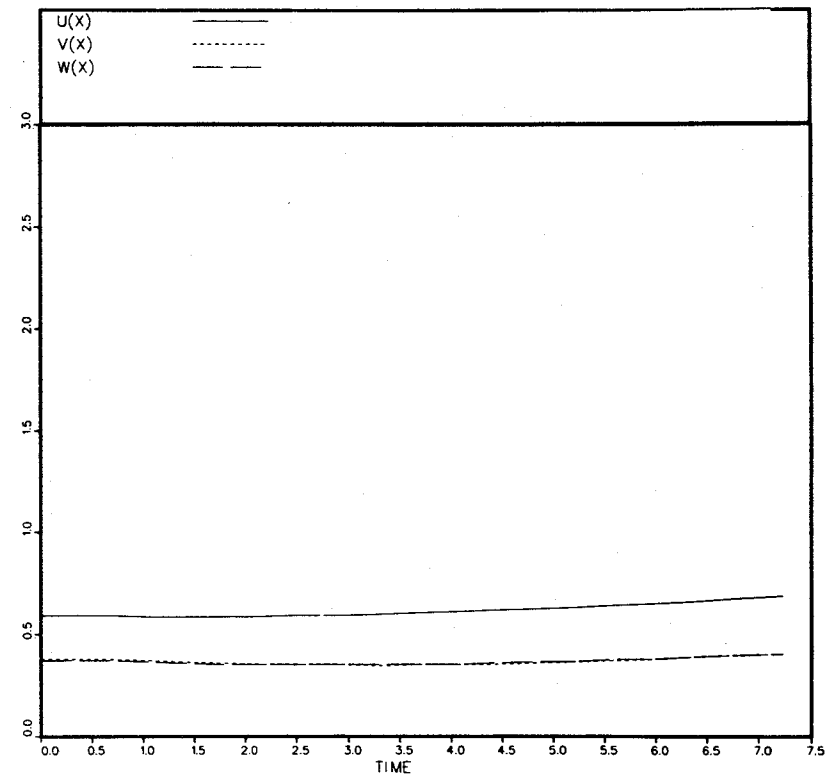
Fig. 3.8. z-direction integral length scales vs.
time for simulation IH64A. Same nomen-
clature as for Fig. 3.7.

ENERGY HISTORY   SKEWNESS HISTORY

110
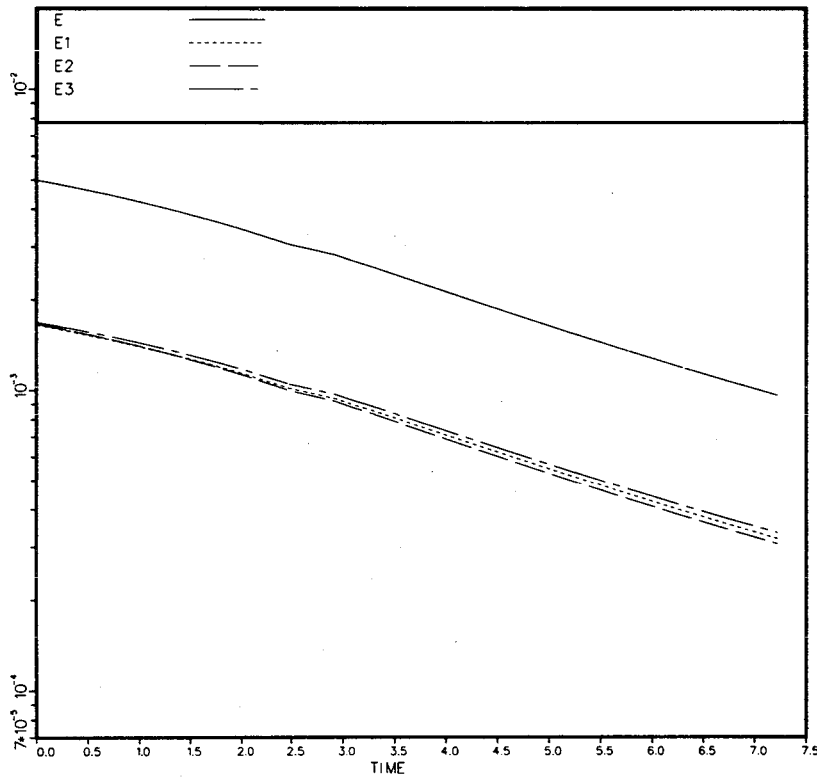
Fig. 3.9. Twice the turbulent kinetic energy and
           turbulent intensities vs. time for simu-
           lation IH64A.
           Same nomenclature as for Fig. 3.3.
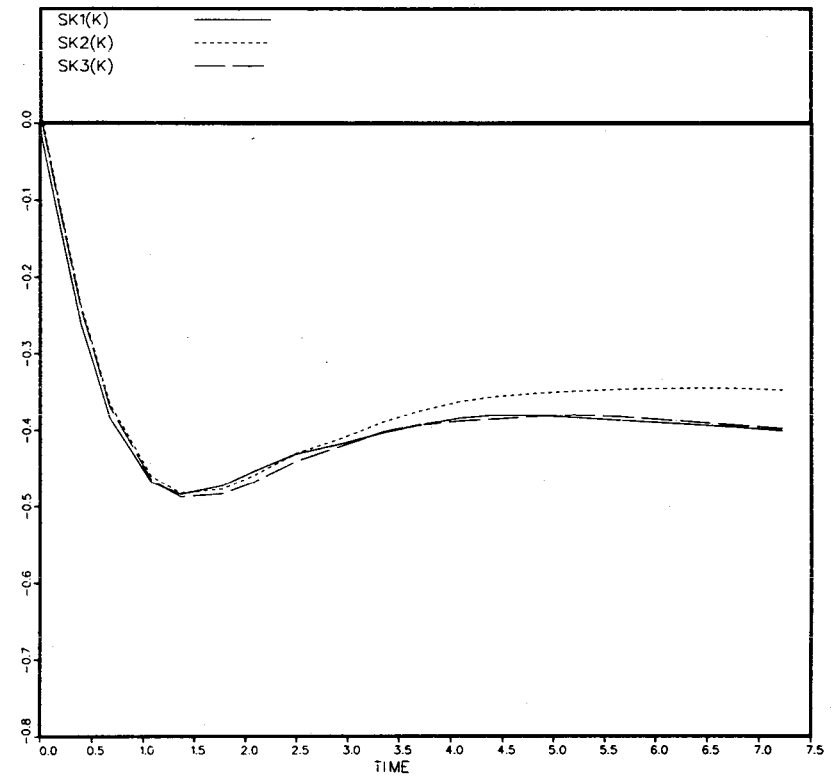
Fig. 3.10. Velocity derivative skewnesses vs. time
           for simulation IH64A.
           SK1(K) is the skewness assoc. with $u_{1,1}$.
           SK2(K) is the skewness assoc. with $u_{2,2}$.
           SK3(K) is the skewness assoc. with $u_{3,3}$.

STRESS COEFFICIENTS
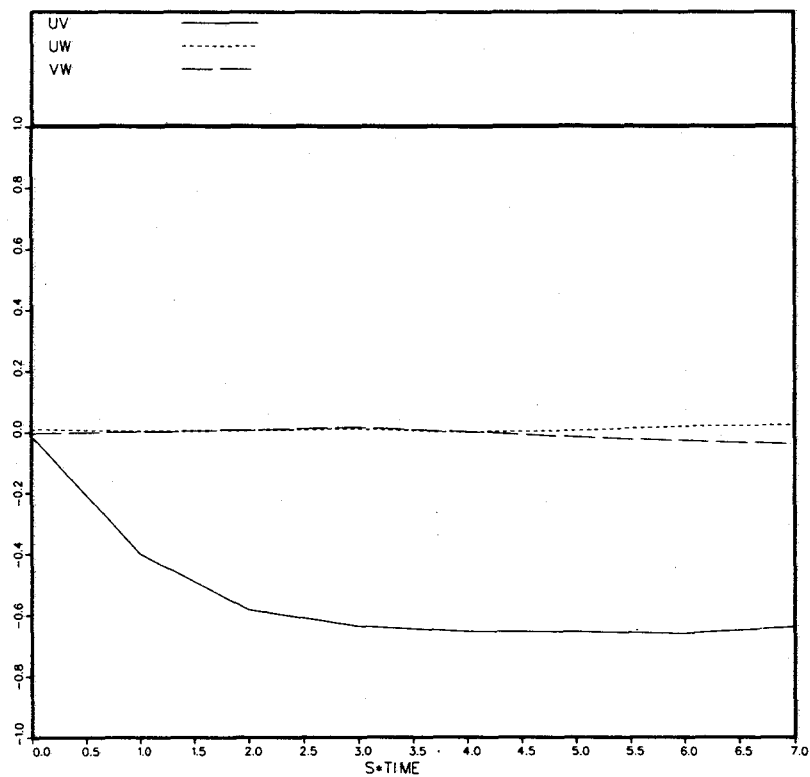
ENERGY HISTORY

Fig. 3.11. Shear stress correlation coefficients vs. St for simulation HS64B. The uv correlation is defined in Eq. (3.7.1).
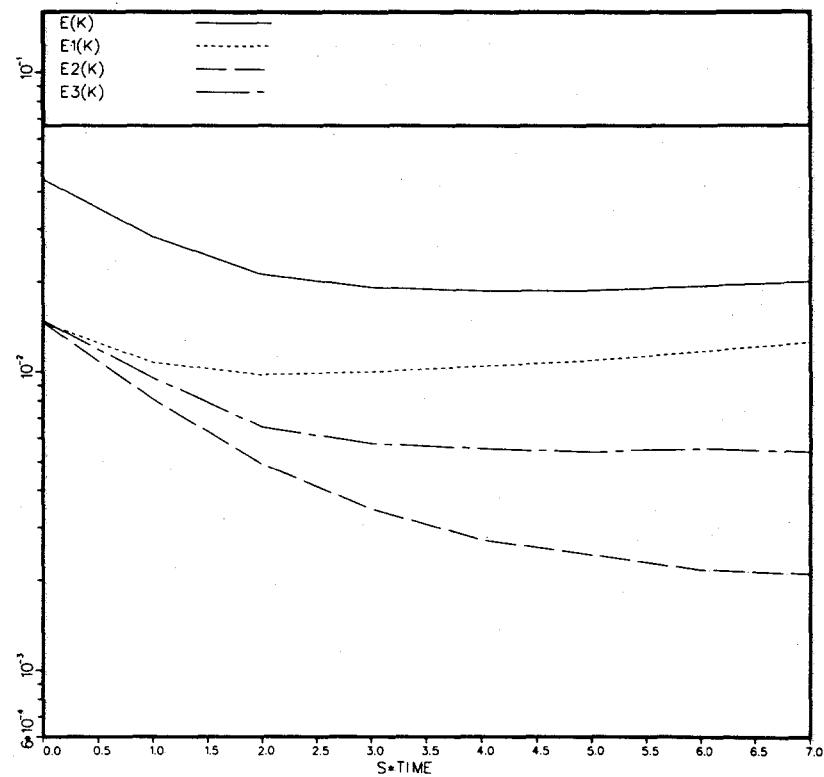
Fig. 3.12. Twice the turbulent kinetic energy and the turbulent intensities vs. time for the simulation HS64B. Same nomenclature as for Fig. 3.3.

111

3-D ENERGY SPECTRA

E(K)	————
E1(K)	·········
E2(K)	— — —
E3(K)	——— -

WAVE NO.

3-D ENERGY SPECTRA

E(K)	————
E1(K)	·········
E2(K)	— — —
E3(K)	——— -

WAVE NO.
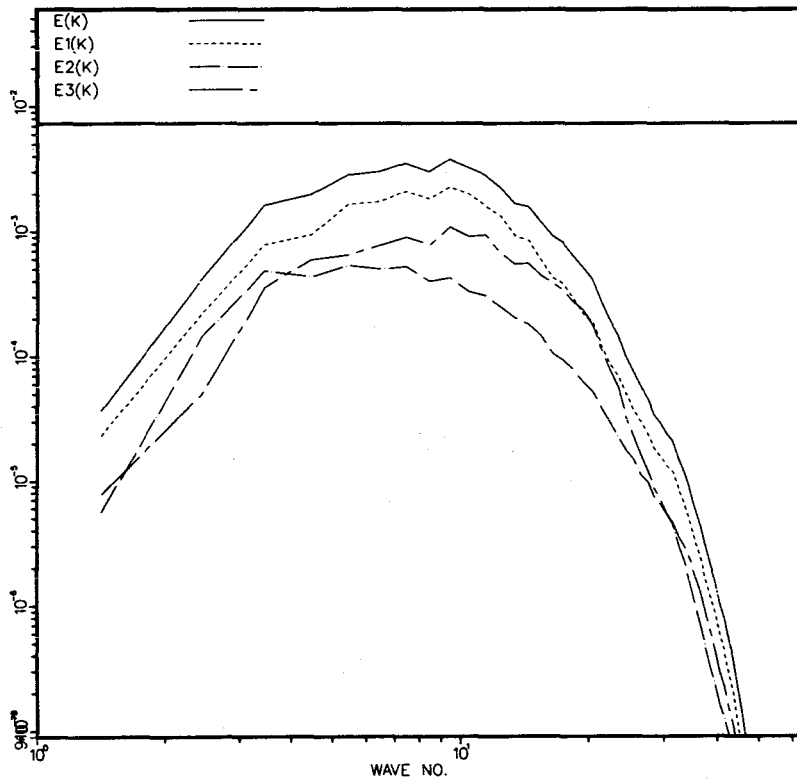
Fig. 3.13.   3-D spectra of the velocity field for
HS64B at St = 4.0.   Same nomenclature
as for Fig. 3.3.
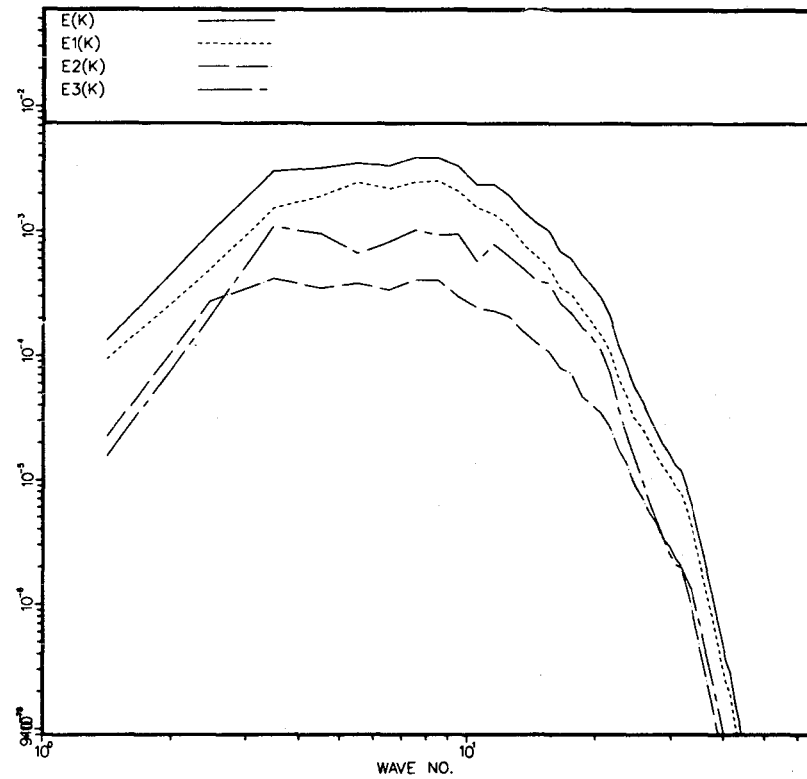
Fig. 3.14.   3-D spectra of the velocity field for HS64B
at St = 6.0.   Same nomenclature as for
Fig. 3.3.

1-D ENERGY SPECTRA

TWO POINT CORRELATIONS
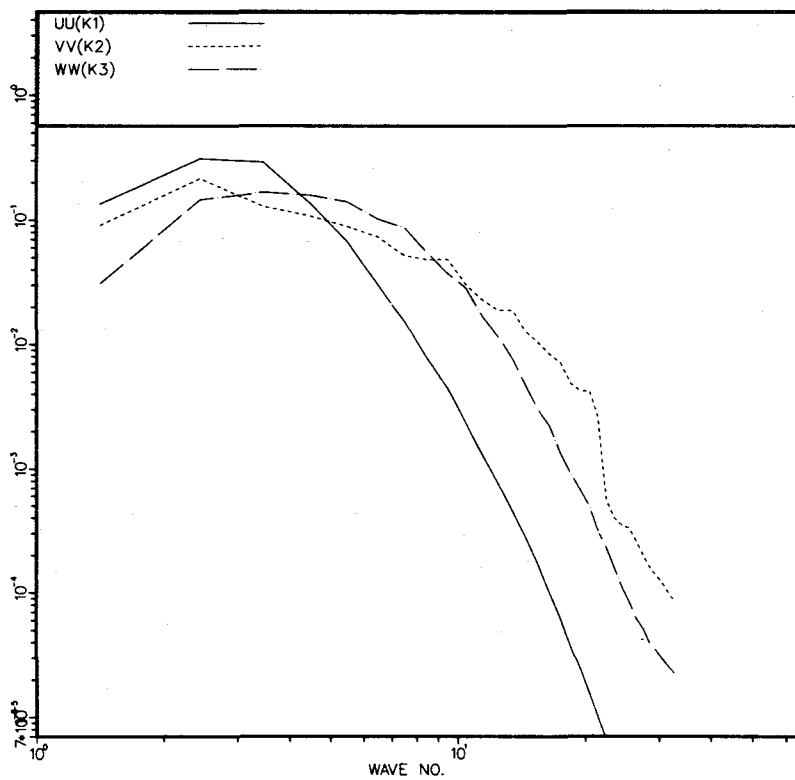
Fig. 3.15. 1-D spectra of the velocity field for
            HS64B at St = 6.0. WAVE NO. indicates
            the wave number k_i in the respective
            directions.
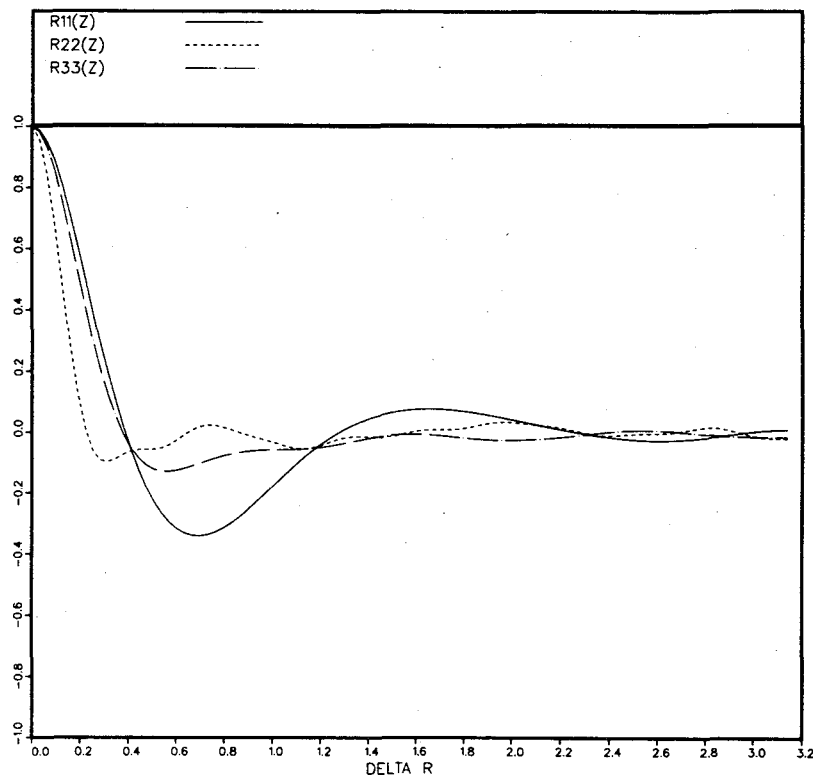
Fig. 3.16. Two-point correlations in the z-direction
            for HS64B at St = 4.0. Nomenclature same
            as for Fig. 3.5.

TWO POINT CORRELATIONS

TWO POINT CORRELATIONS
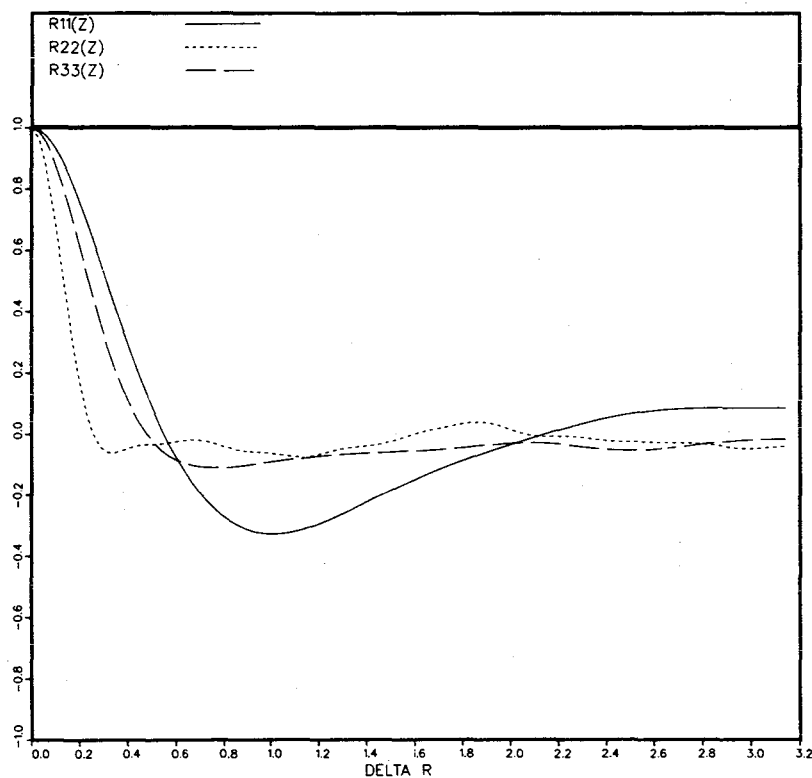
Fig. 3.17. Two-point correlations in the z-direction for HS64B at St = 6.0. Nomenclature same as for Fig. 3.5.
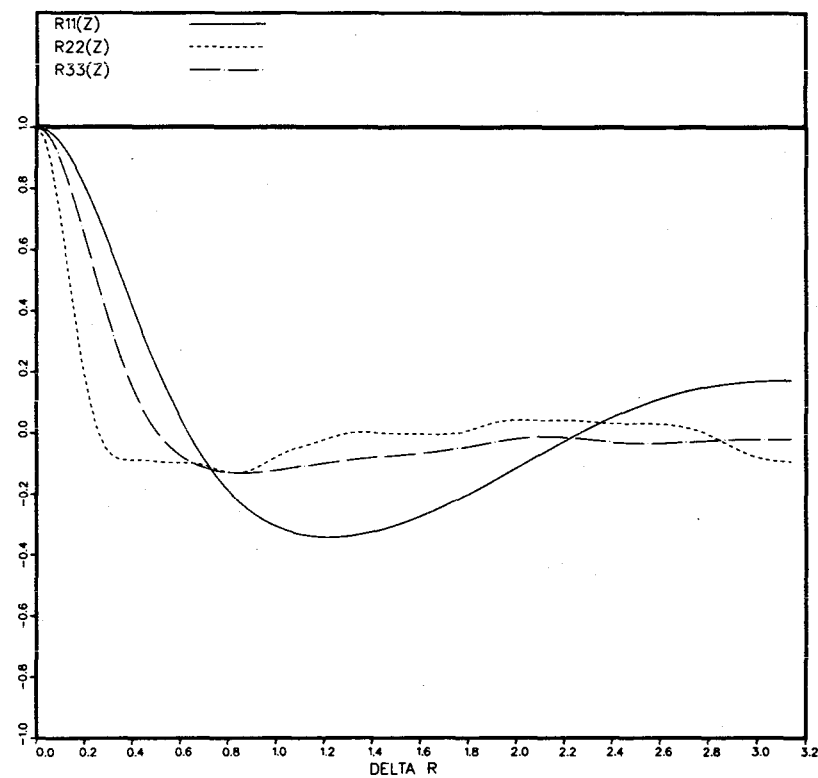
Fig. 3.18. Two-point correlations in the z-direction for HS64B at St = 7.0. Nomenclature same as for Fig. 3.5.

TWO POINT CORRELATIONS

PARAMETER SPACE SL(11)/Q   VS. AVRG. MACH NUM.
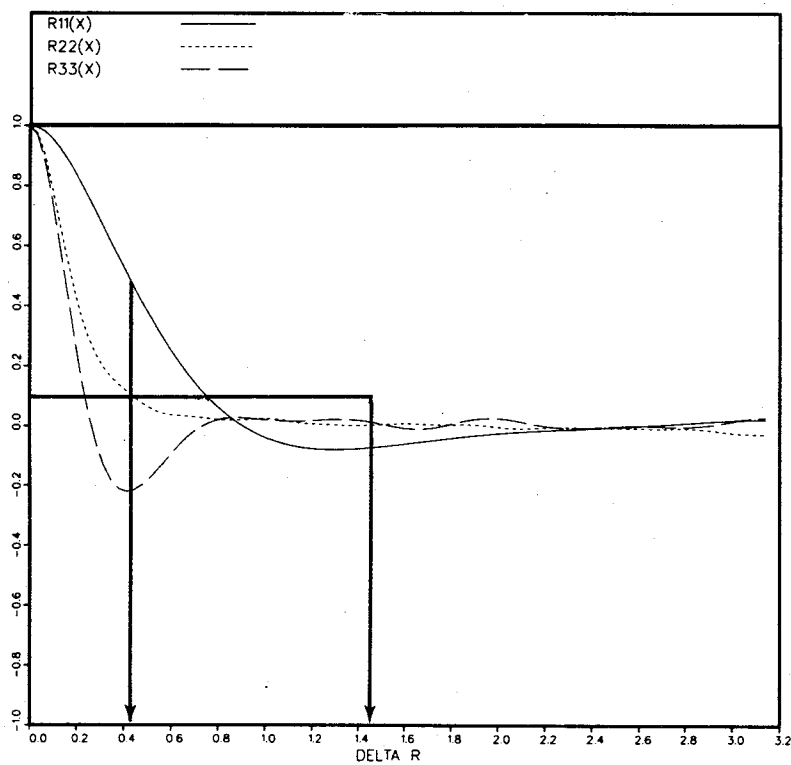
Fig. 4.1. Definitions of integral length scales
illustrated for a typical two-point cor-
relation. The arrow at 0.42 indicates
Corrsin's definition. The arrow at 1.42
indicates our definition.
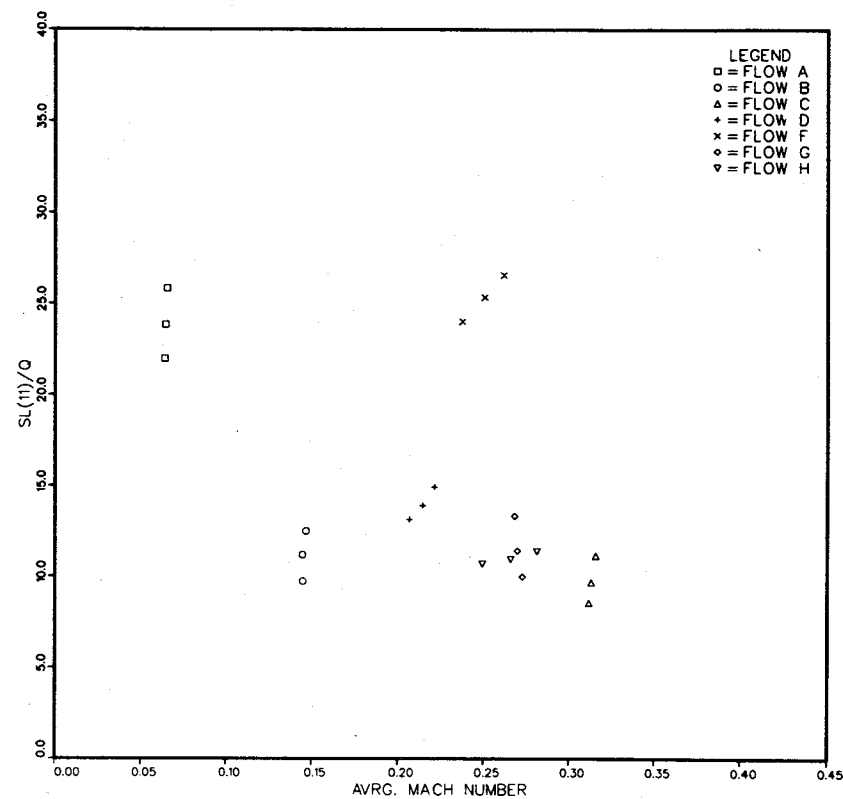
Fig. 4.2. Parameter space of shear number   SL(11)/Q
vs. fluctuating Mach number for the seven
shear-flow simulations.

116
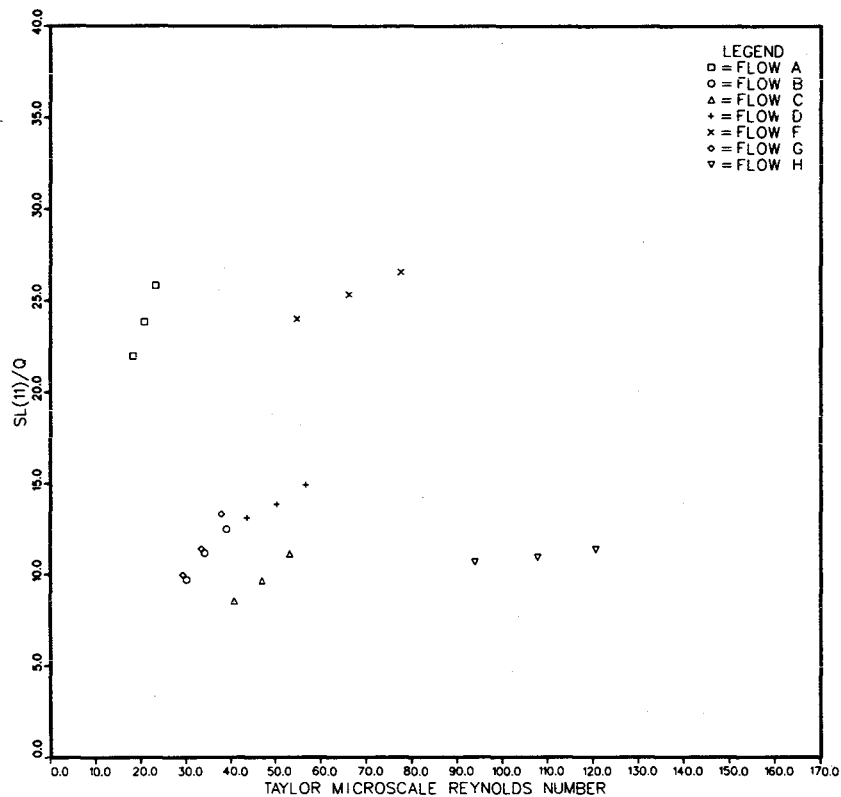
Fig. 4.3. Parameter space of shear number SL(11)/Q
vs. Taylor microscale Reynolds number for
the seven shear-flow simulations.
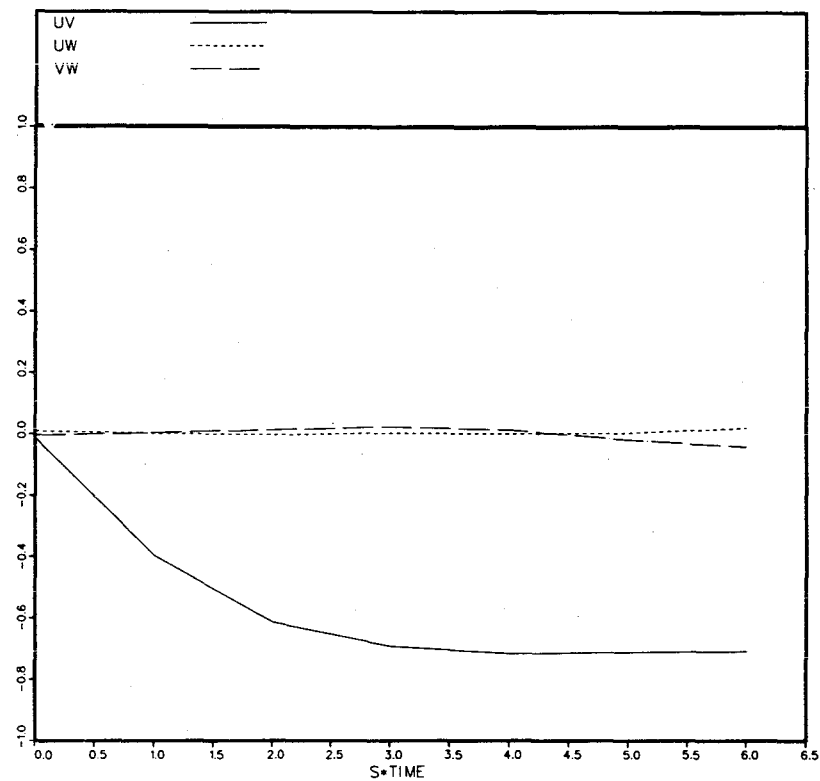
Fig. 4.4a. Shear stress correlation coefficients
vs. St. Letters in the figure number
correspond to the individual shear-flow
simulations.
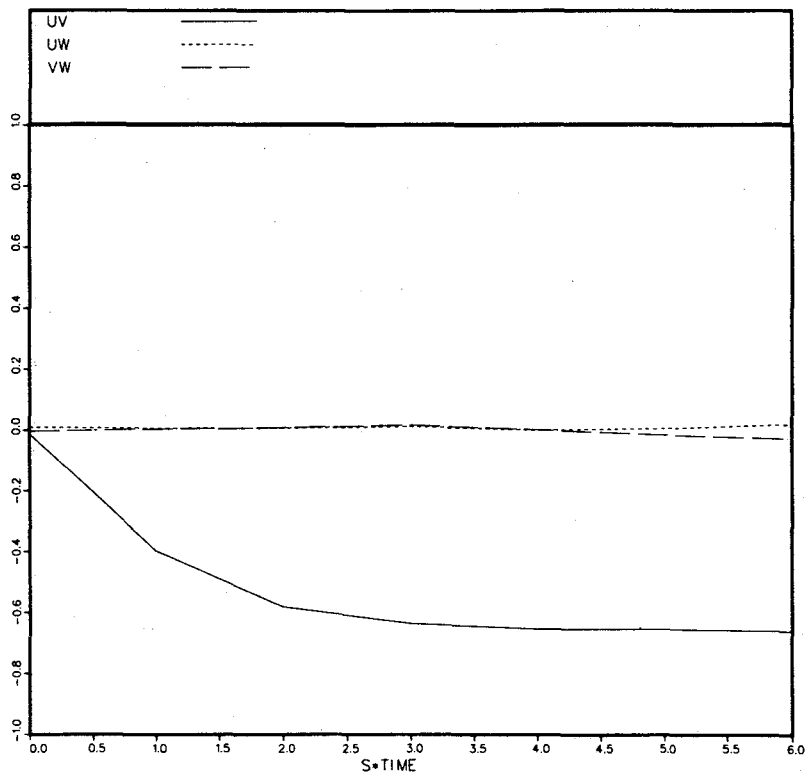
Fig. 4.4.b.   Shear stress correlation coefficients
vs. St. Letters in the figure number
correspond to the individual shear-
flow simulations.

Fig. 4.4e.   Shear stress correlation coefficients
vs. St. Letters in the figure number
correspond to the individual shear-flow
simulations.

STRESS COEFFICIENTS

STRESS COEFFICIENTS
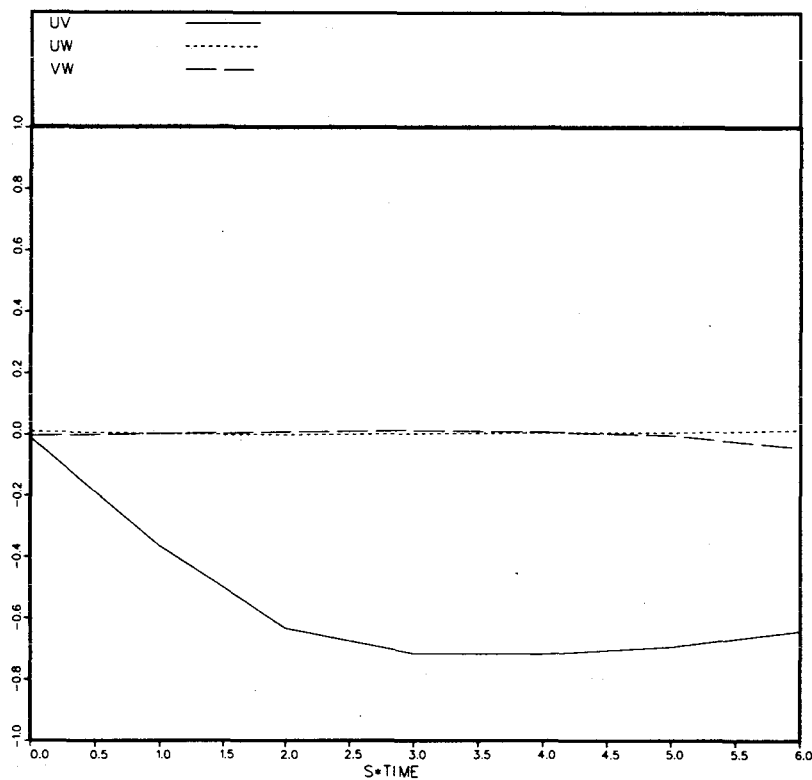
Fig. 4.4d. Shear stress correlation coefficients vs. St. Letters in the figure number correspond to the individual shear-flow simulations.
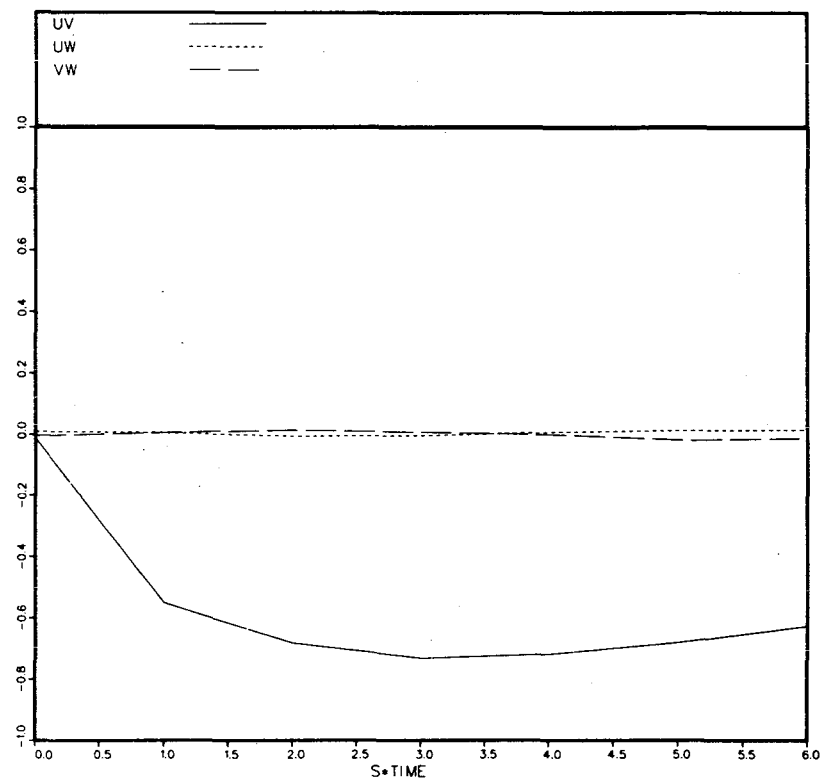
Fig. 4.4f. Shear stress correlation coefficients vs. St. Letters in the figure number correspond to the individual shear-flow simulations.

STRESS COEFFICIENTS

STRESS COEFFICIENTS
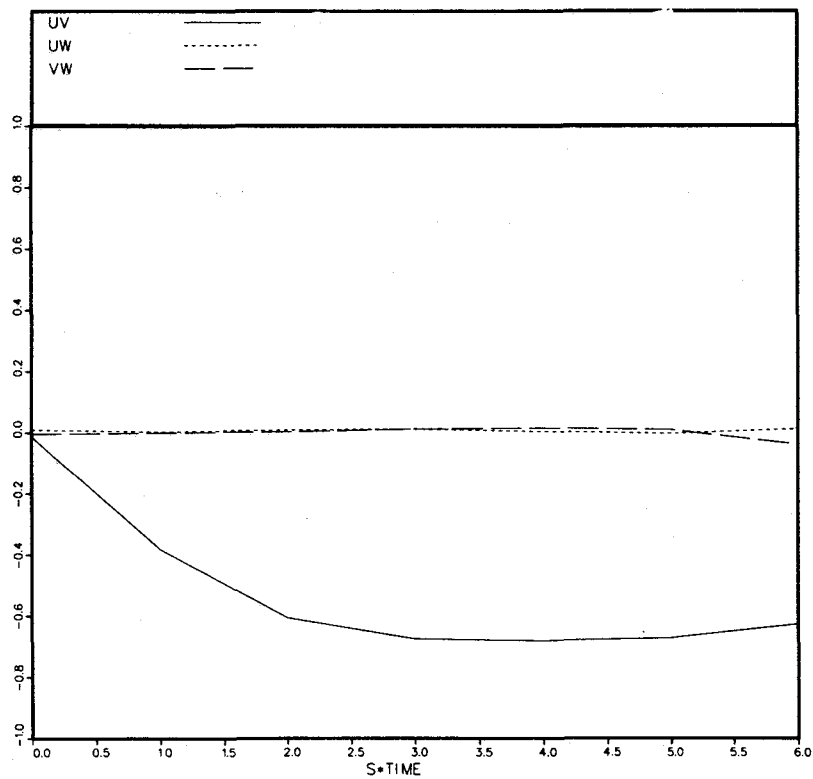
Fig. 4.4g. Shear stress correlation coefficients vs. St. Letters in the figure number correspond to the individual shear-flow simulations.
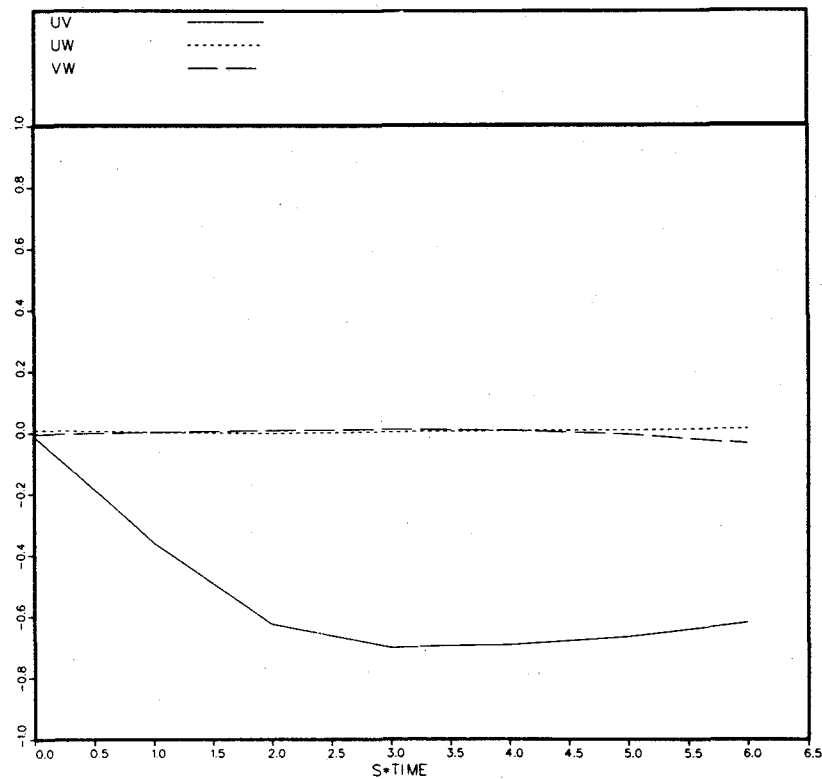
Fig. 4.4h. Shear stress correlation coefficients vs. St. Letters in the figure number correspond to the individual shear flow simulations.

STRESS TENSOR PRINCIPAL AXIS ROTATION

LEAST SQUARES FITTED FUNCTION
F = D * ((SL/Q)**A) * (1+B*M**2) * (RE**C)
A= -0.4026
B= -0.2559
C= -0.1040
D= 1.2968

LEGEND
□ = FLOW A
○ = FLOW B
△ = FLOW C
+ = FLOW D
× = FLOW F
◇ = FLOW G
▽ = FLOW H

ROTATION IN RADIANS

FITTED FUNCTION

PRINCIPAL STRESS RATIO (X-Y PLANE)

LEAST SQUARES FITTED FUNCTION
F = 1 + (D * ((SL/Q)**A) * (1+B*M**2) * (RE**C))
A= 0.7424
B= -2.1763
C= 0.1179
D= 1.1635

LEGEND
□ = FLOW A
○ = FLOW B
△ = FLOW C
+ = FLOW D
× = FLOW F
◇ = FLOW G
▽ = FLOW H

PRINCIPAL STRESS RATIO
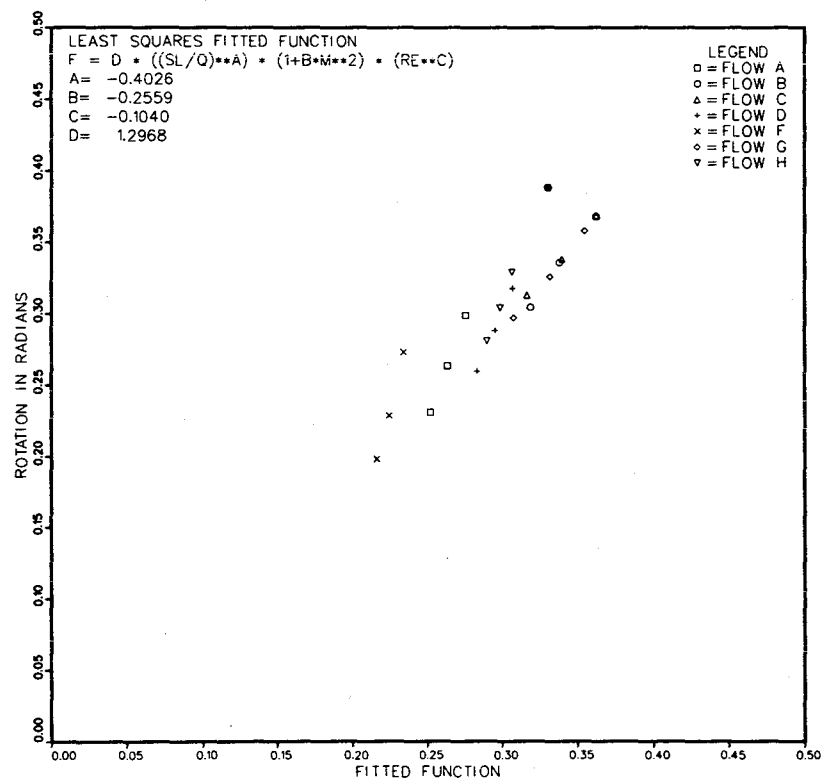
FITTED FUNCTION

Fig. 4.5. Angle, α, between Cartesian and princi-
pal axis coordinates of the Reynolds stress
tensor vs. estimated values of α from the
least-squares fitted function. The HGC
flow is indicated by the solid dot.

Fig. 4.6. Ratio of the principal stresses of the Rey-
nolds stress tensor in the x-y plane vs.
estimated values from the least-squares
fitted function. The HGC flow is indicated
by the solid dot.

REYNOLDS STRESS ANISOTROPY

REYNOLDS STRESS ANISOTROPY
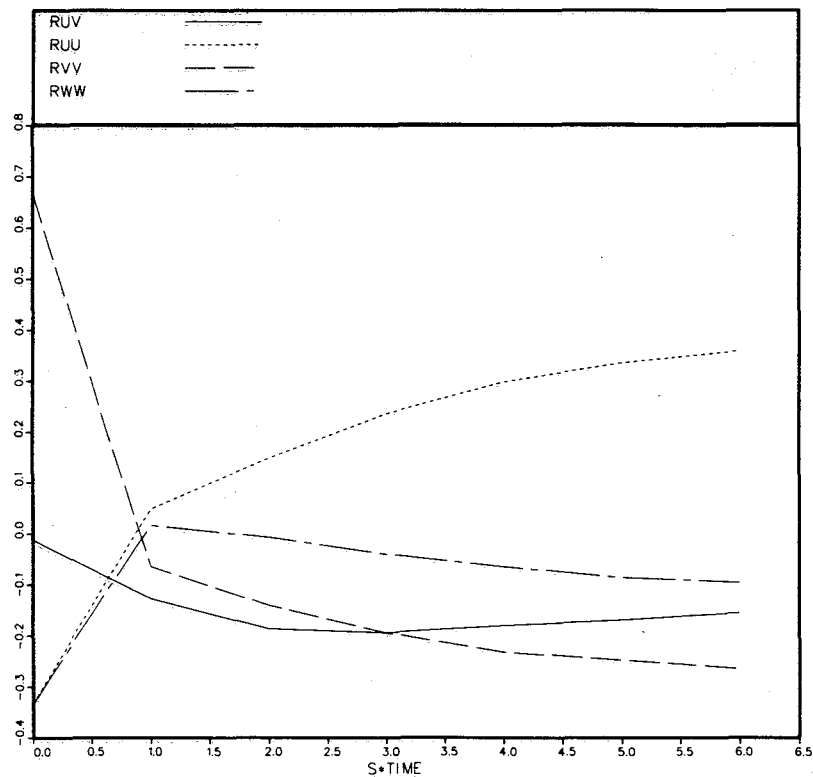
Fig. 4.7a. Reynolds stress anisotropy, b_{ij}, vs.
St for the seven shear simulations
b_{12} = RUV, b_{11} = RUU, b_{22} = RVV, b_{33} =
RWW. Letters in the figure numbers cor-
respond to the individual shear-flow
simulations.
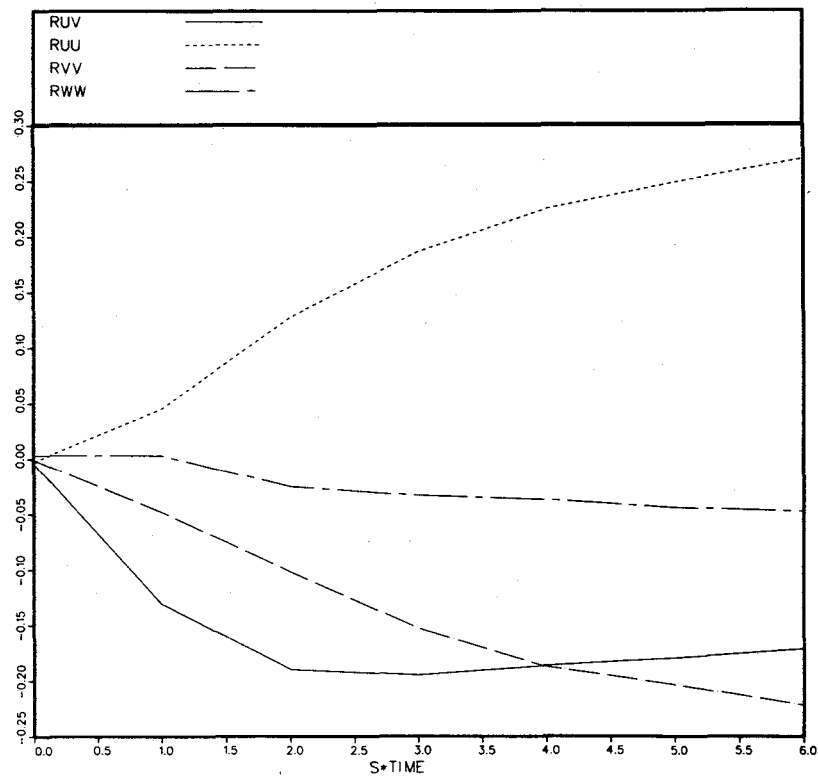
Fig. 4.7b. Reynolds stress anisotropy, b_{ij}, vs.
St for the seven shear simulations
b_{12} = RUV, b_{11} = RUU, b_{22} = RVV, b_{33} =
RWW. Letters in the figure numbers cor-
respond to the individual shear-flow
simulations.
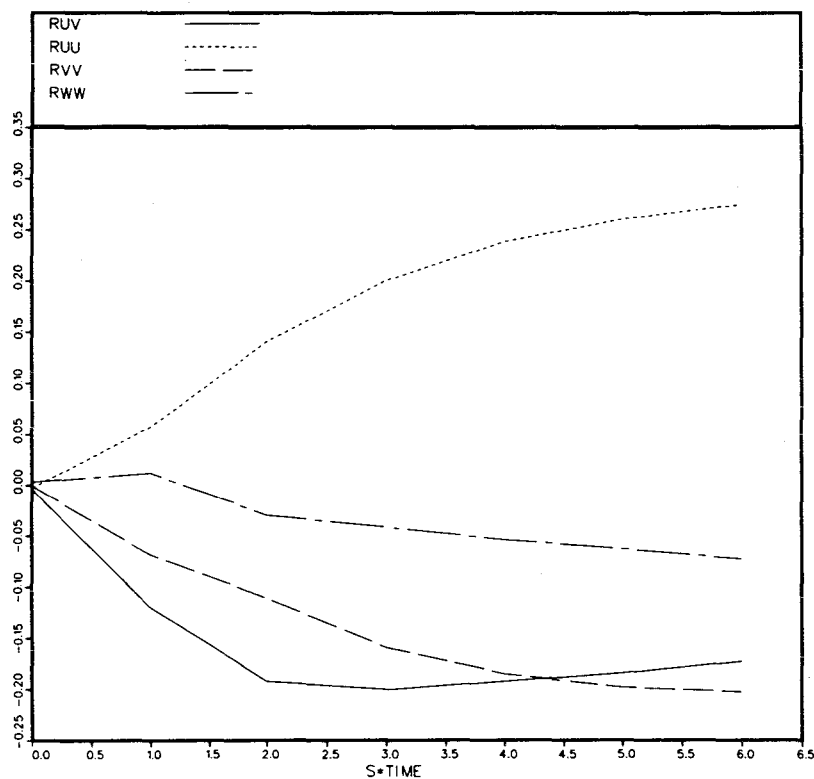
Fig. 4.7c. Reynolds stress anisotropy, b_{ij}, vs.
St for the seven shear simulations,
b_{12} = RUV, b_{11} = RUU, b_{22} = RVV, b_{33} =
RWW. Letters in the figure numbers cor-
respond to the individual shear-flow
simulations.
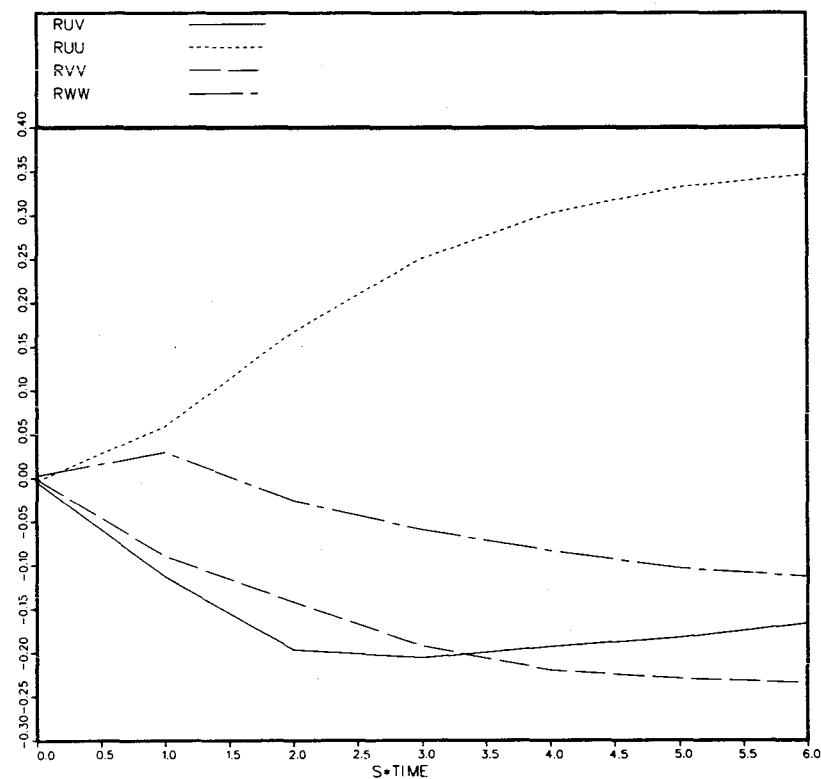
Fig. 4.7d. Reynolds stress anisotropy, b_{ij}, vs.
St for the seven shear simulations
b_{12} = RUV, b_{11} = RUU, b_{22} = RVV, b_{33} =
RWW. Letters in the figure numbers cor-
respond to the individual shear-flow
simulations.

REYNOLDS STRESS ANISOTROPY
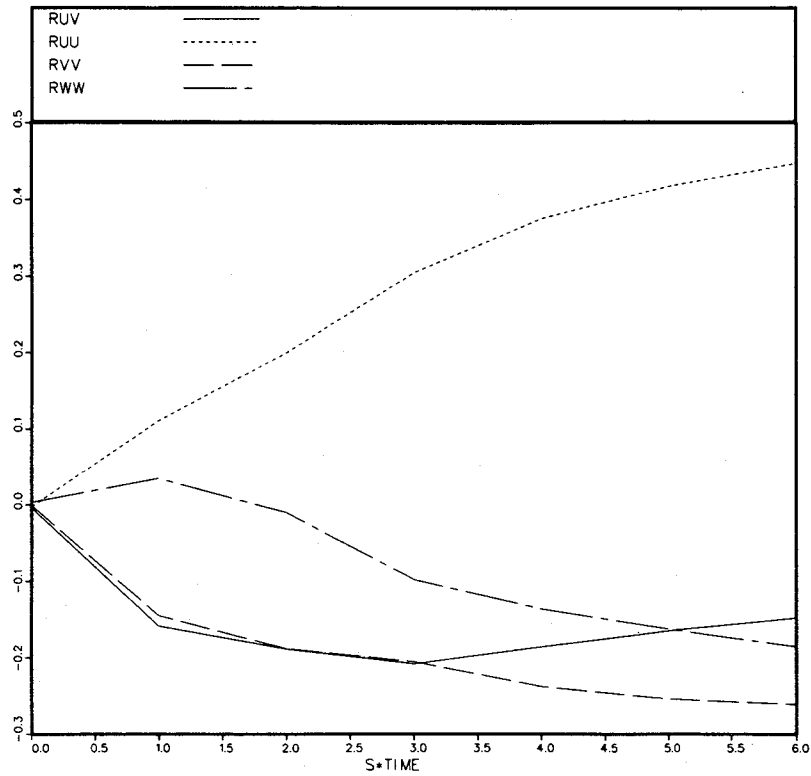
REYNOLDS STRESS ANISOTROPY
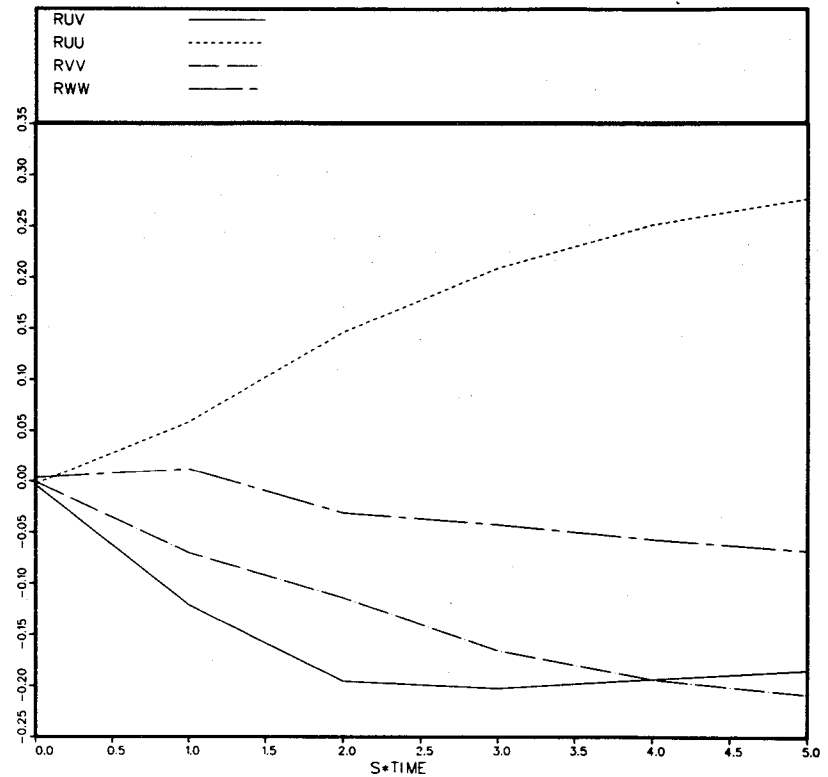
Fig. 4.7f. Reynolds stress anisotropy, b_{ij}, vs.
St for the seven shear simulations
b_{12} = RUV, b_{11} = RUU, b_{22} = RVV, b_{33} =
RWW. Letters in the figure numbers cor-
respond to the individual shear-flow
simulations.

Fig. 4.7g. Reynolds stress anisotropy, b_{ij}, vs.
St for the seven shear simulations
b_{12} = RUV, b_{11} = RUU, b_{22} = RVV, b_{33} =
RWW. Letters in the figure numbers cor-
respond to the individual shear-flow
simulations.

REYNOLDS STRESS ANISOTROPY

LUMLEYS INVARIANT MAP
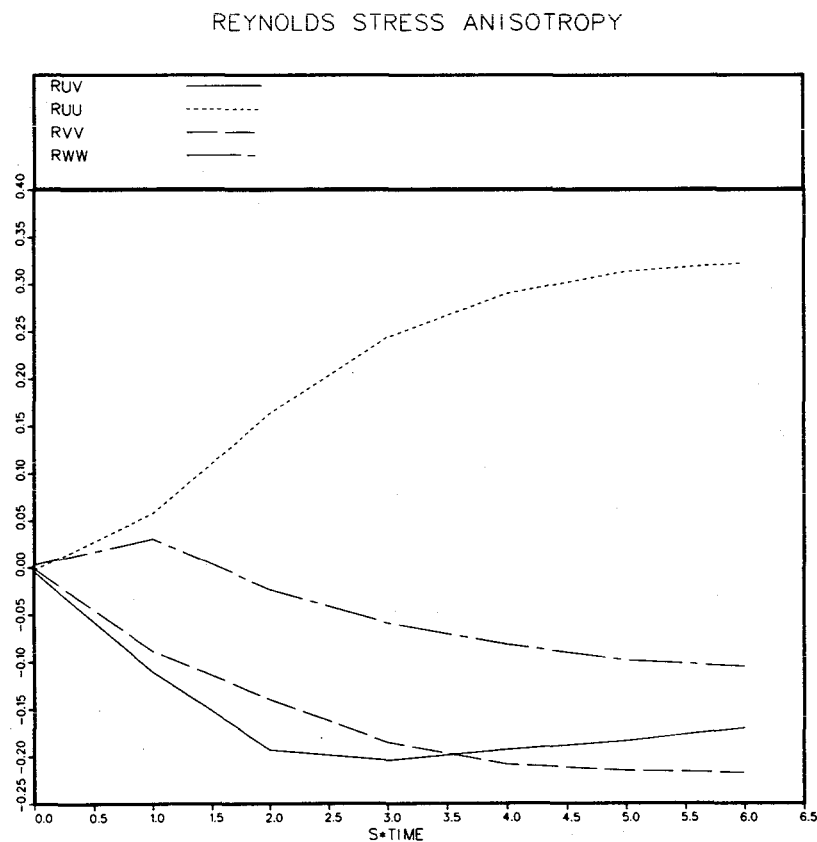
Fig. 4.7h. Reynolds stress anisotropy, b_{ij}, vs.
St for the seven shear simulations.
b_{12} = RUV, b_{11} = RUU, b_{22} = RVV, b_{33}
= RWW. Letters in the figure numbers
correspond to the individual shear-flow
simulations.
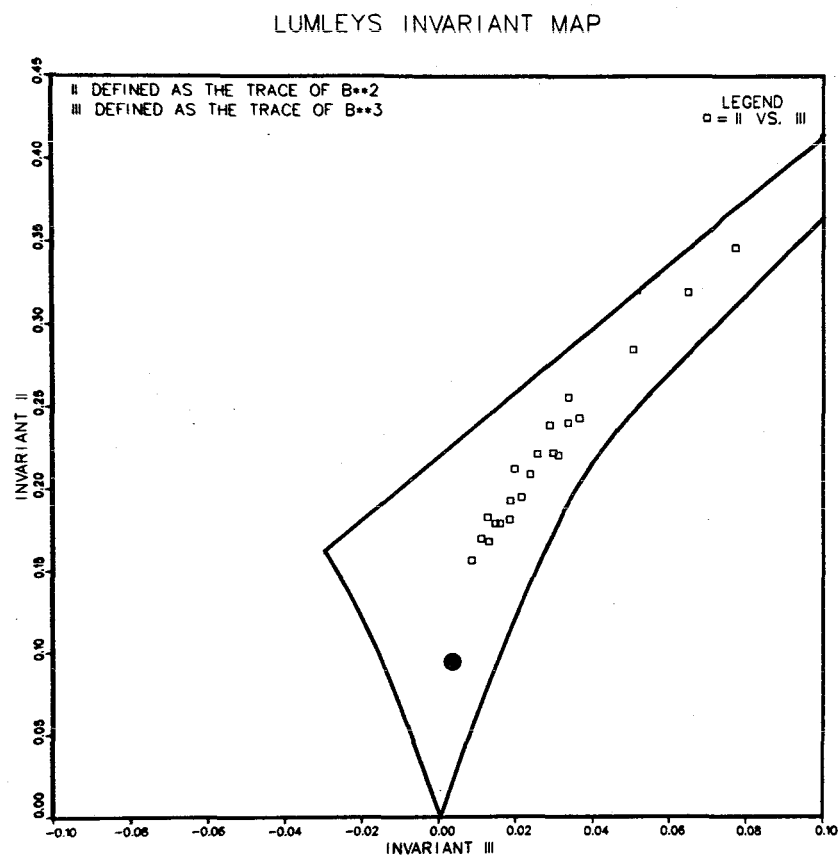
Fig. 4.8. Invariants of the Reynolds stress anisotropy.
II vs. III (defined in Eq. (4.5.6). All
turbulence must be in the triangular region.
The left and right lines indicate axisymmetric
turbulence. The top line indicates two-
dimensional turbulence. The HGC flow is
indicated by the black dot.

DECOMPOSED RUU AND RWW
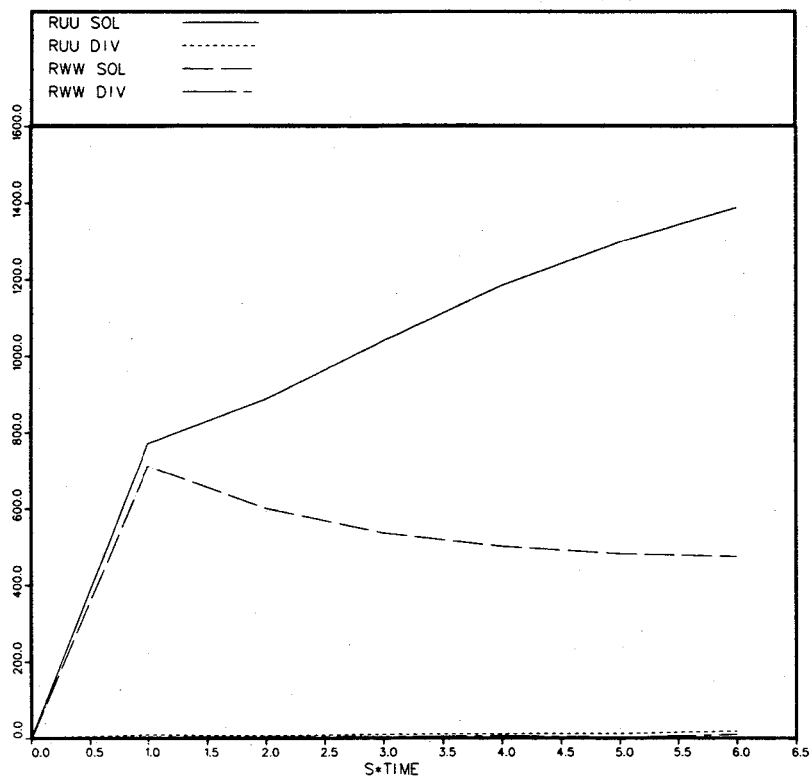
DECOMPOSED RUU AND RWW
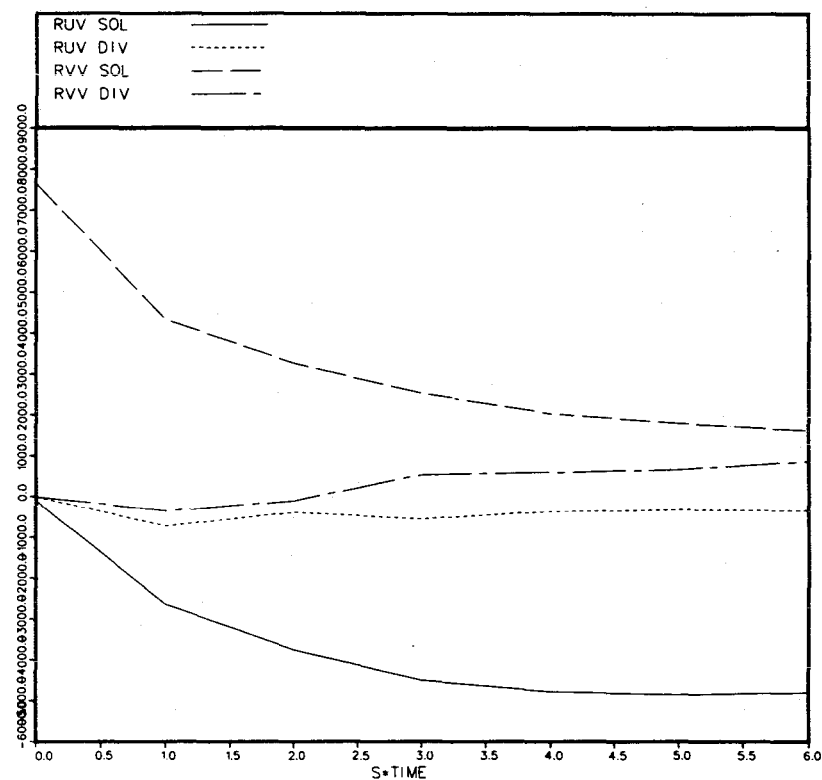

Fig. 4.9a. Moyal decomposed Reynolds stresses R_{11} and R_{33} as defined by Eq. (4.6.3) vs. St.

Fig. 4.9b. Moyal decomposed Reynolds stresses R_{11} and R_{33} as defined by Eq. (4.6.3) vs. St.

$$\text{RUU SOL} = R_{11}^S, \quad \text{RUU DIV} = R_{11}^D, \quad \text{RWW SOL} = R_{33}^S, \quad \text{RWW DIV} = R_{33}^D$$

Letters in the figure numbers correspond to the individual shear flow simulations.
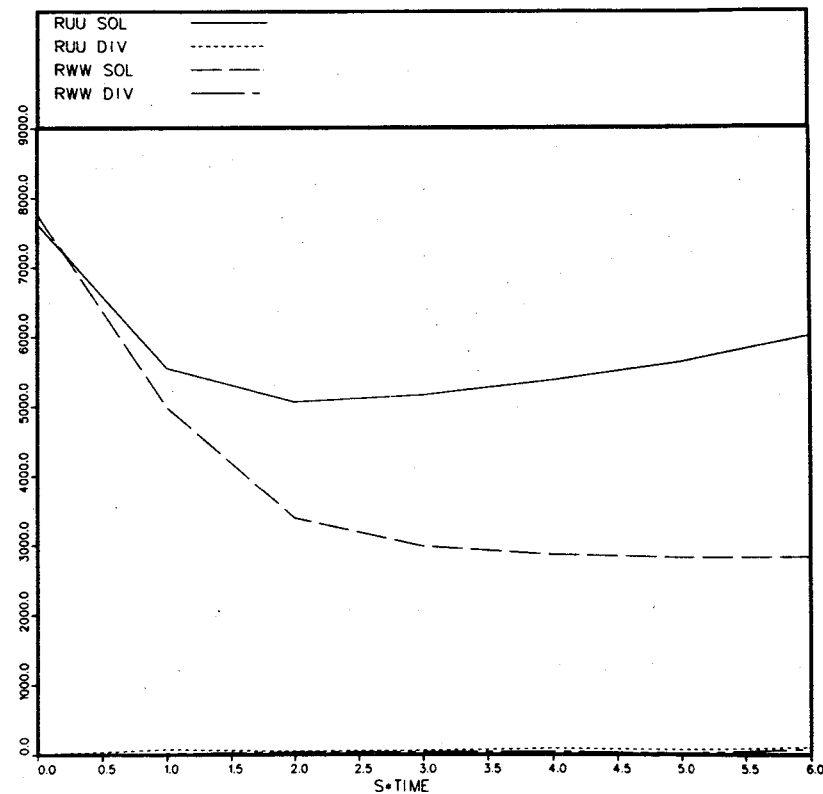
DECOMPOSED RUU AND RWW
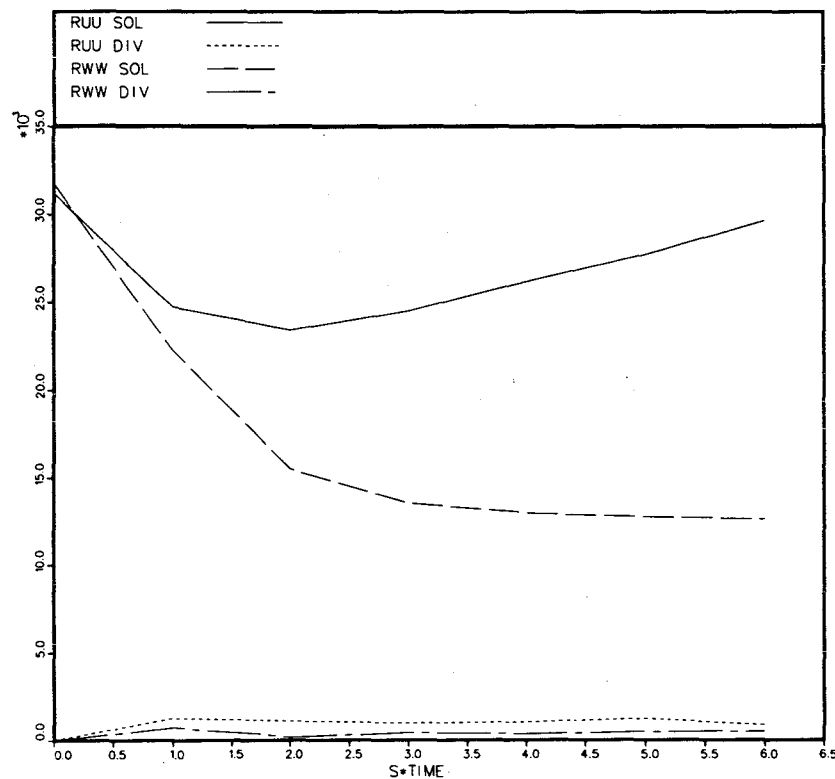
DECOMPOSED RUU AND RWW
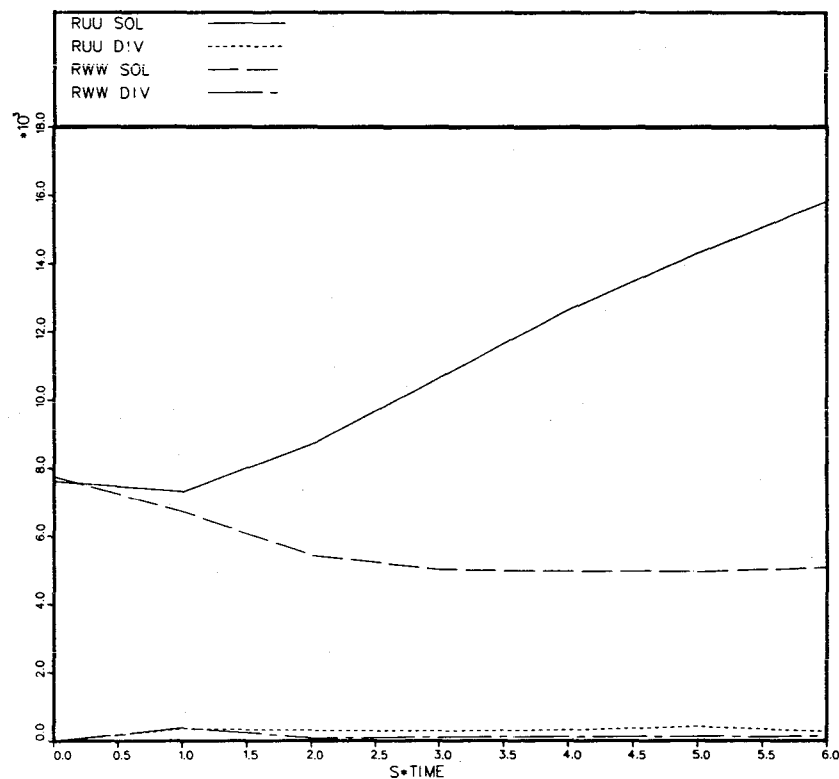
Fig. 4.9c. Moyal decomposed Reynolds stresses R_{11} and R_{33} as defined by Eq. (4.6.3) vs. St.

Fig. 4.9d. Moyal decomposed Reynolds stresses R_{11} and R_{33} as defined by Eq. (4.6.3) vs. St.

RUU SOL $= R_{11}^S$, RUU DIV $= F_{11}^D$, RWW SOL $= R_{33}^S$, RWW DIV $= R_{33}^D$

Letters in the figure numbers correspond to the individual shear flow simulations.
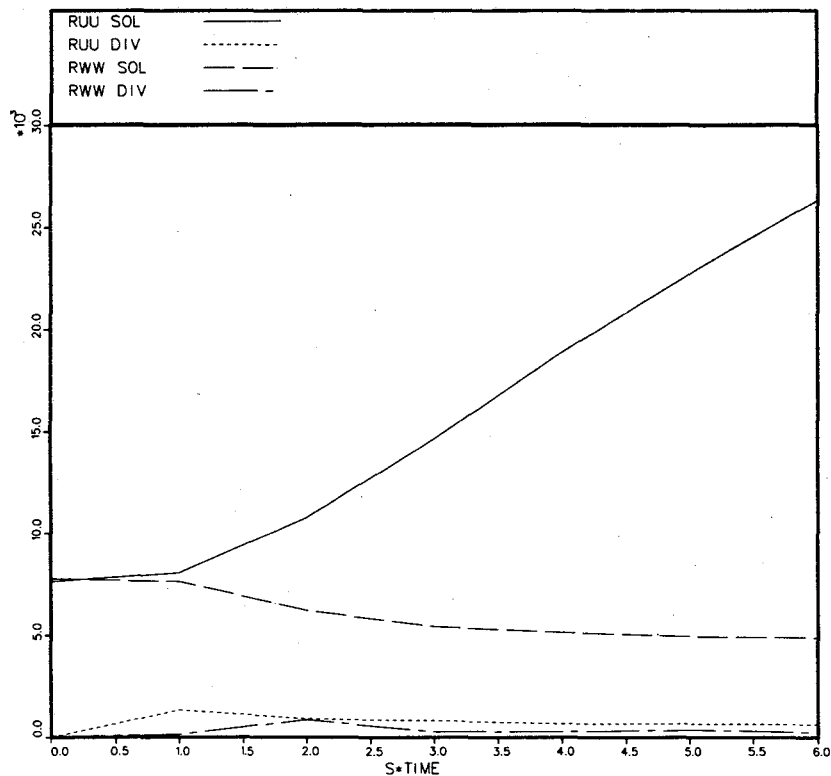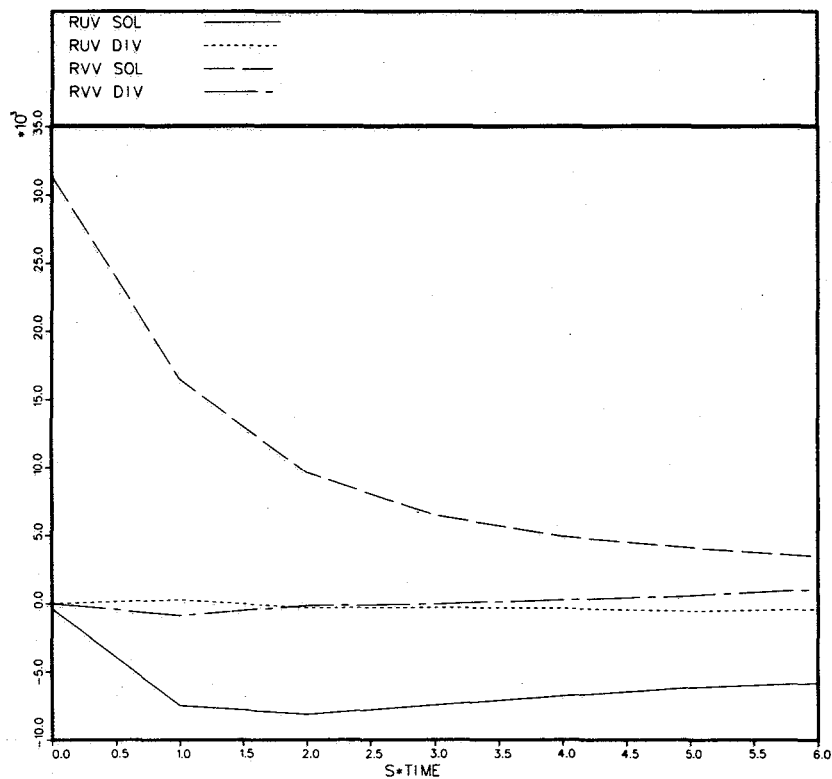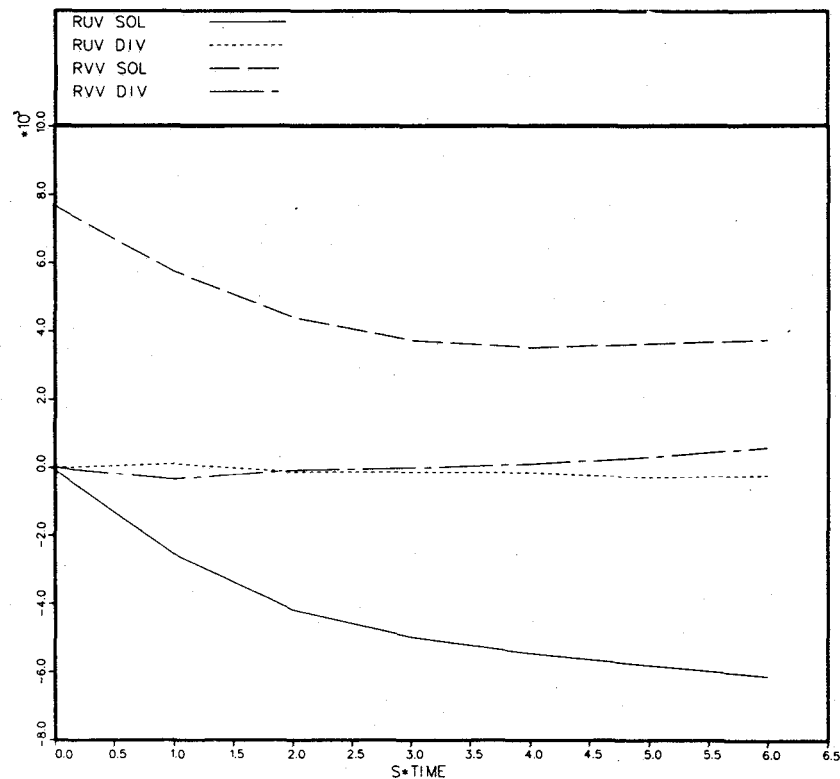
DECOMPOSED RUU AND RWW   DECOMPOSED RUU AND RWW
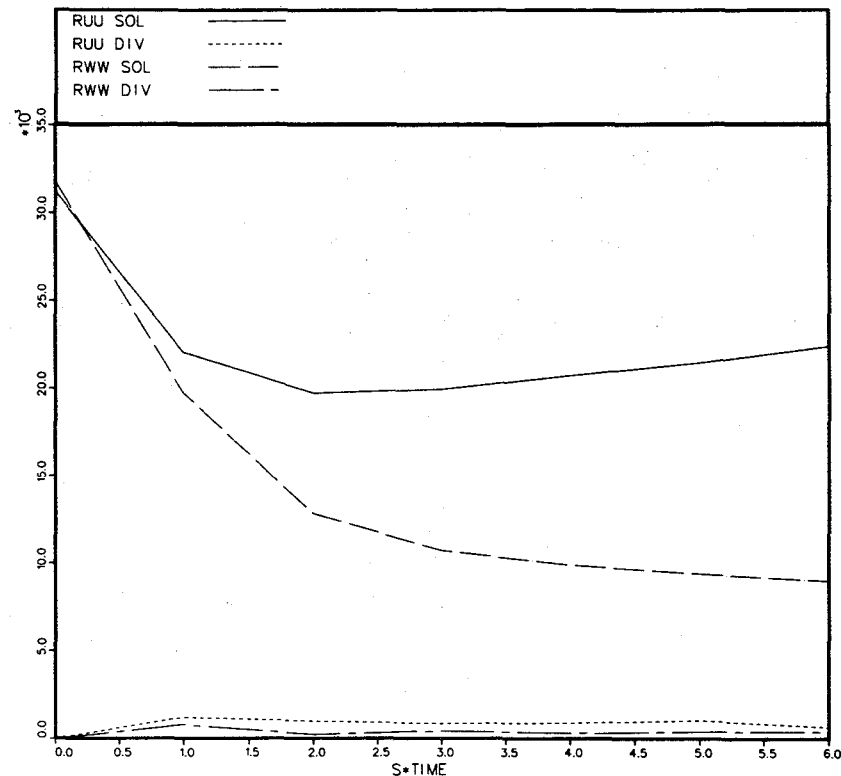
Fig. 4.9f. Moyal decomposed Reynolds stresses R_{11} Fig. 4.9g. Moyal decomposed Reynolds stresses R_{11}
          and R_{33} as defined by Eq. (4.6.3)   and R_{33} as defined by Eq. (4.6.3)
          vs. St.   vs. St.

$$RUU\ SOL = R_{11}^{S}, \quad RUU\ DIV = R_{11}^{D}, \quad RWW\ SOL = R_{33}^{S}, \quad RWW\ DIV = R_{33}^{D}$$

          Letters in the figure numbers correspond to the individual shear flow
   simulations.

DECOMPOSED RUU AND RWW
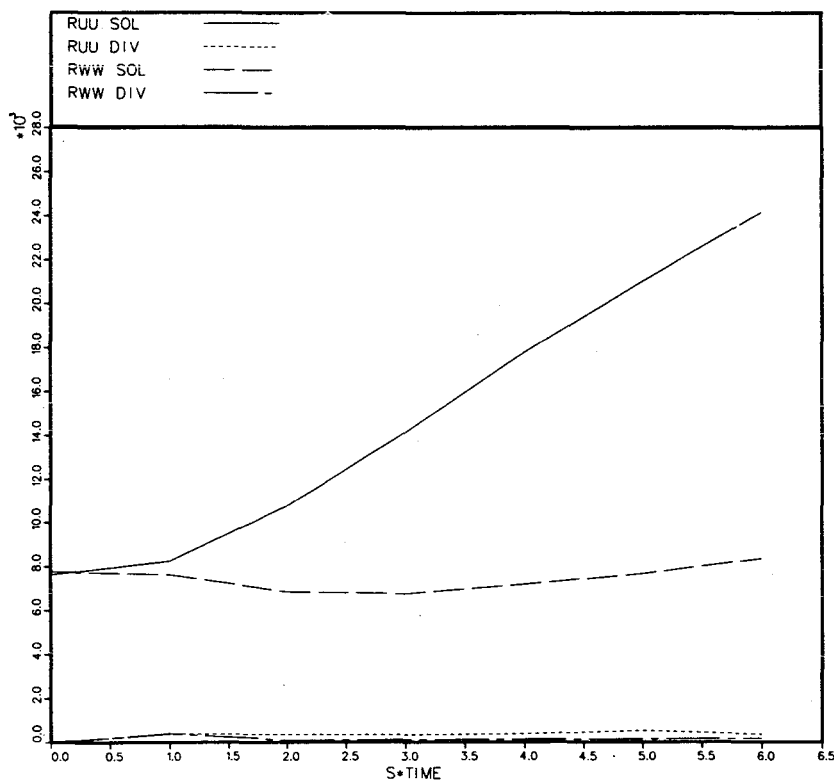
DECOMPOSED RUV AND RVV

Fig. 4.9h. Moyal decomposed Reynolds stresses R_{11} and R_{33} as defined by Eq. (4.6.3) vs. St.
RUU SOL = R^S_{11}, RUU DIV = R^D_{11}, RWW SOL = R^S_{33}, RWW DIV = R^D_{33}. Letters in the figure numbers correspond to the individual shear-flow simulations.

Fig. 4.10a. Moyal decomposed Reynolds stresses $R^{S,D}_{12}$ and $R^{S,D}_{22}$ as defined by Eq. (4.6.3) vs. St.
RUV SOL = R^S_{23}, RUV DIV = R^D_{12}, RVV SOL = R^S_{22}, RVV DIV = R^D_{22}. Letters in the figure numbers correspond to the individual shear-flow simulations.

DECOMPOSED RUV AND RVV
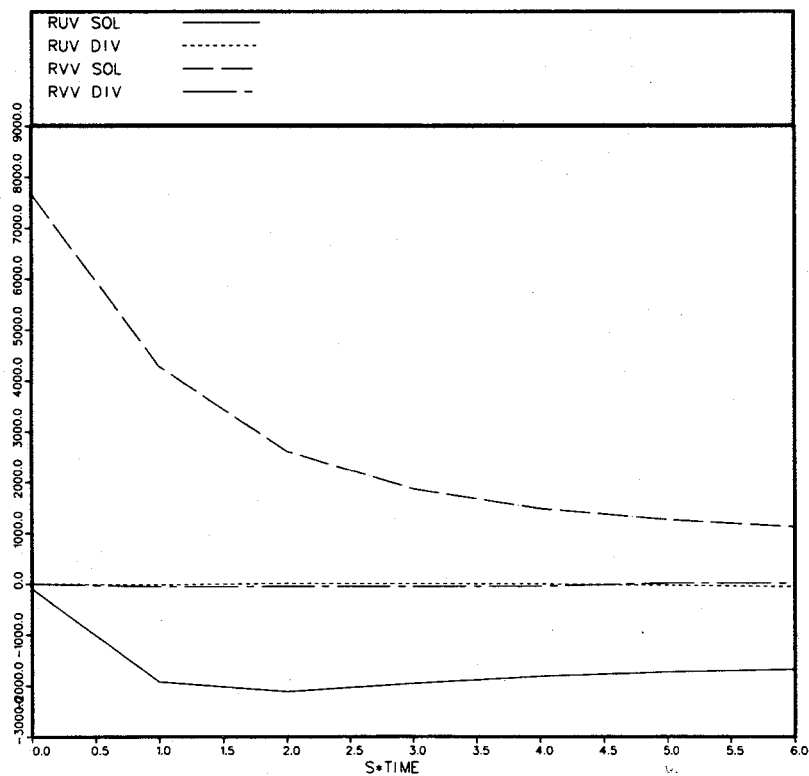
DECOMPOSED RUV AND RVV
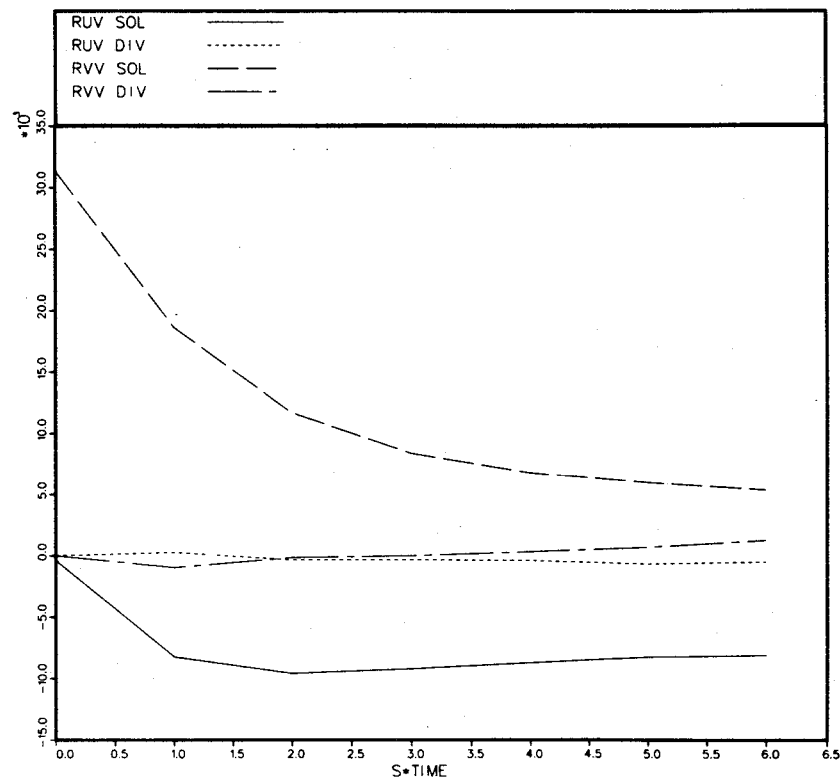
Fig. 4.10b. Moyal decomposed Reynolds stresses $R_{12}^{S,D}$ and $R_{22}^{S,D}$ as defined by Eq. (4.6.3) vs. St.

Fig. 4.10c. Moyal decomposed Reynolds stresses $R_{12}^{S,D}$ and $R_{22}^{S,D}$ as defined by Eq. (4.6.3) vs. St.

RUV SOL = R_{12}^{S}, RUV DIV = R_{12}^{D}, RVV SOL = R_{22}^{S}, RVV DIV = R_{22}^{D}

Letters in the figure numbers correspond to the individual shear-flow simulations.

DECOMPOSED RUV AND RVV
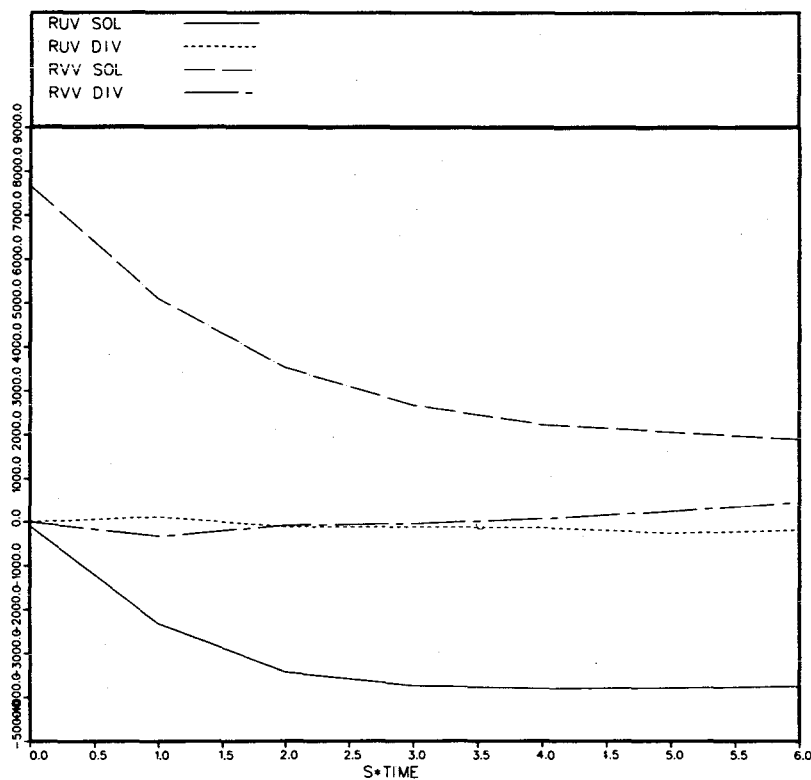
DECOMPOSED RUV AND RVV

Fig. 4.10d. Moyal decomposed Reynolds stresses $R_{12}^{S,D}$ and $R_{22}^{S,D}$ as defined by Eq. (4.6.3) vs. St.

Fig. 4.10f. Moyal decomposed Reynolds stresses $R_{12}^{S,D}$ and $R_{22}^{S,D}$ as defined by Eq. (4.6.3) vs. St.

RUV SOL = R_{12}^{S},   RUV DIV = R_{12}^{D},   RVV SOL = R_{22}^{S},   RVV DIV = R_{22}^{D}

Letters in the figure numbers correspond to the individual shear-flow simulations.

DECOMPOSED RUV AND RVV

DECOMPOSED RUV AND RVV

Fig. 4.10g. Moyal decomposed Reynolds stresses $R_{12}^{S,D}$ and $R_{22}^{S,D}$ as defined by Eq. (4.6.3) vs. St.

Fig. 4.10h. Moyal decomposed Reynolds stresses $R_{12}^{S,D}$ and $R_{22}^{S,D}$ as defined by Eq. (4.6.3) vs. St.

RUV SOL = R_{12}^{S}, RUV DIV = R_{12}^{D}, RVV SOL = R_{22}^{S}, RVV DIV = R_{33}^{D}.

Letters in the figure numbers correspond to the individual shear-flow simulations.

131
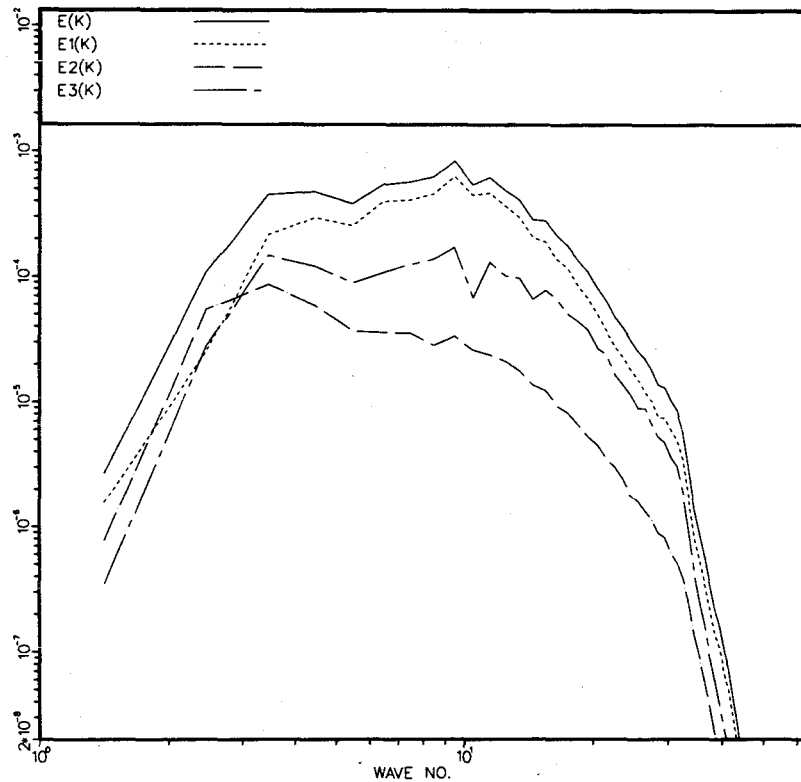
Fig. 4.11a. 3-D spectra of the solenoidal part of
the Reynolds stress field as defined
by Eq. (4.6.5).

Fig. 4.11b. 3-D spectra of the solenoidal part of
the Reynolds stress field as defined
by Eq. (4.6.5).

Nomenclature same as for Fig. 3.3. Letters in figure numbers correspond to the individual
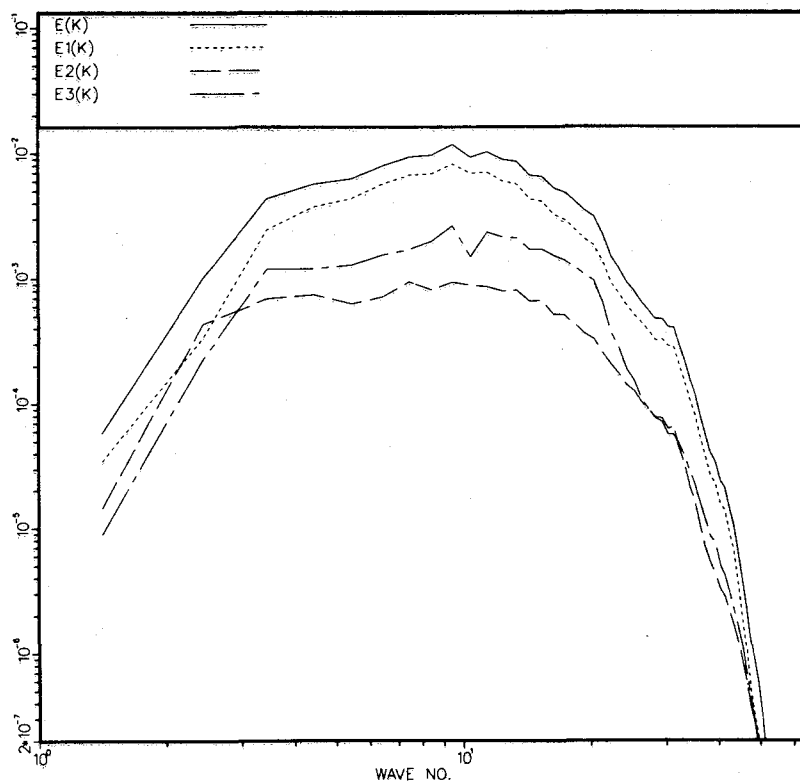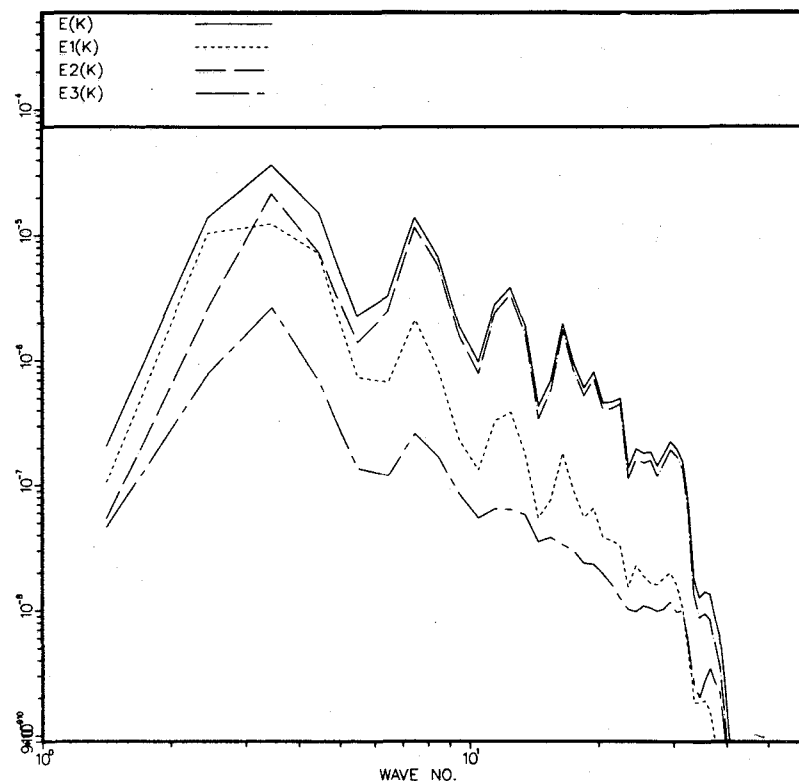shear-flow simulations.

SOLENOIDAL ENERGY SPECTRA

SOLENOIDAL ENERGY SPECTRA
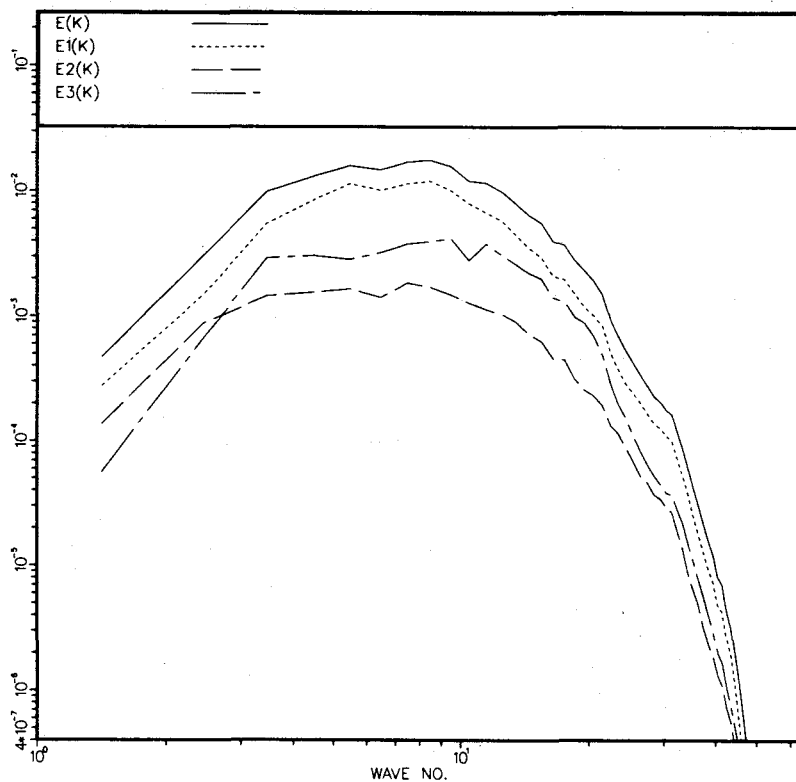
Fig. 4.11c. 3-D spectra of the solenoidal part of the Reynolds stress field as defined by Eq. (4.6.5).
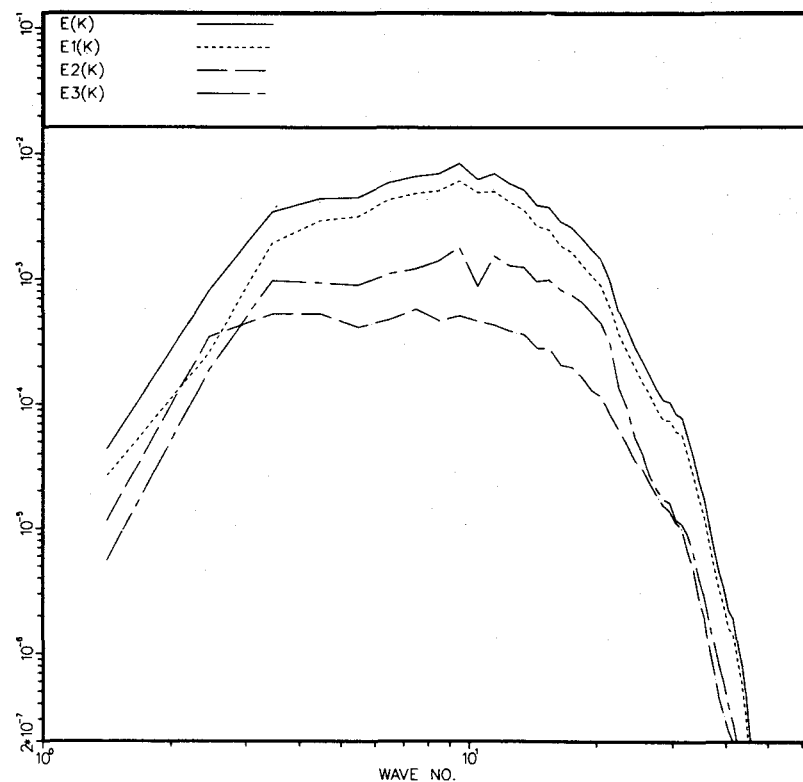
Fig. 4.11d. 3-D spectra of the solenoidal part of the Reynolds stress field as defined by Eq. (4.6.5).

Nomenclature same as for Fig. 3.3. Letters in figure numbers correspond to the individual shear-flow simulations.
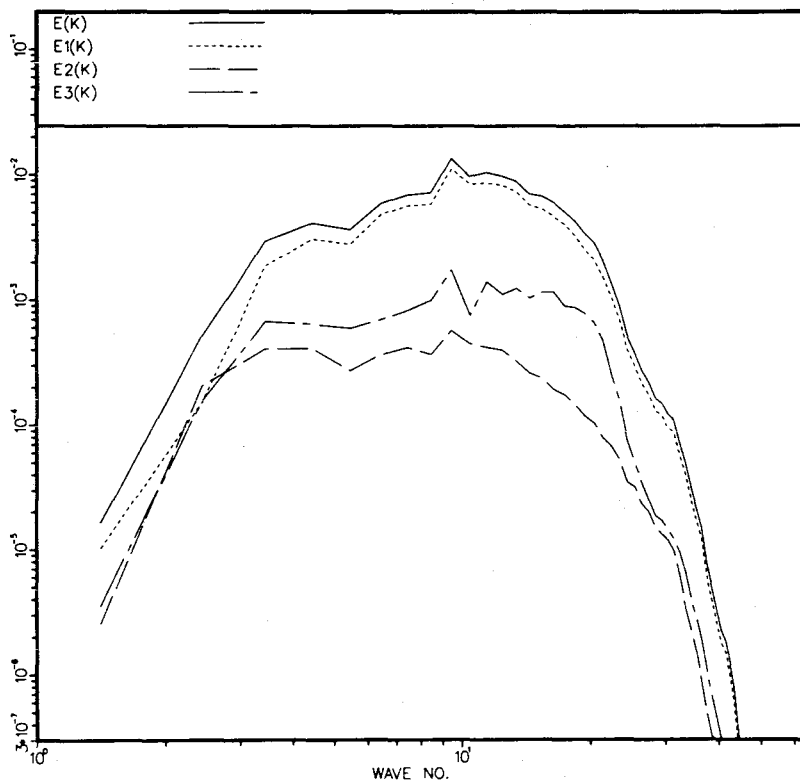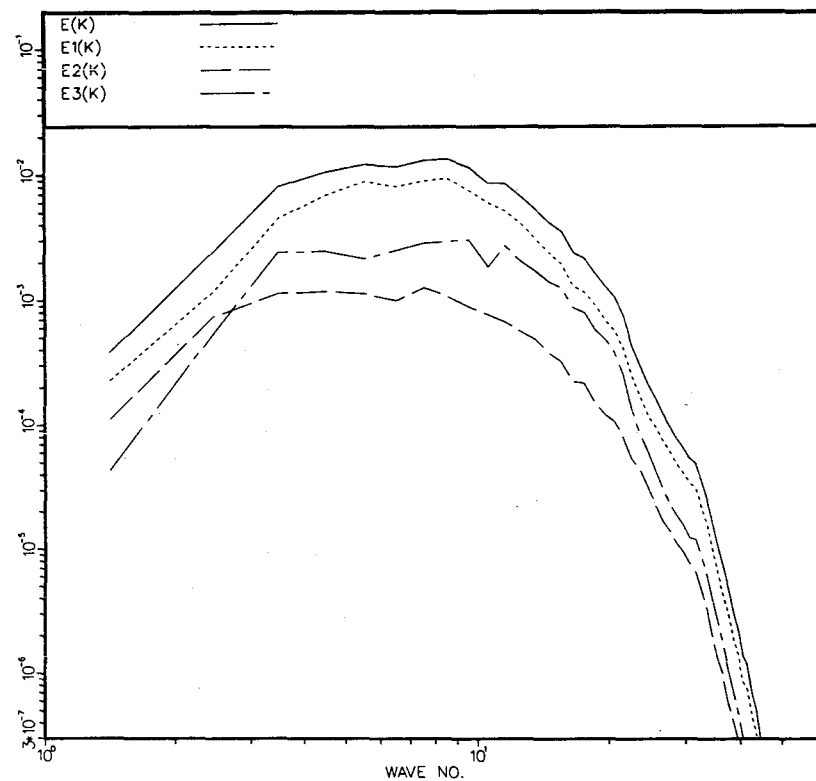
Fig. 4.11f. 3-D spectra of the solenoidal part of the Reynolds stress field as defined by Eq. (4.6.5).

Fig. 4.11g. 3-D spectra of the solenoidal part of the Reynolds stress field as defined by Eq. (4.6.5).

Nomenclature same as for Fig. 3.3. Letters in figure numbers correspond to the individual shear-flow simulations.
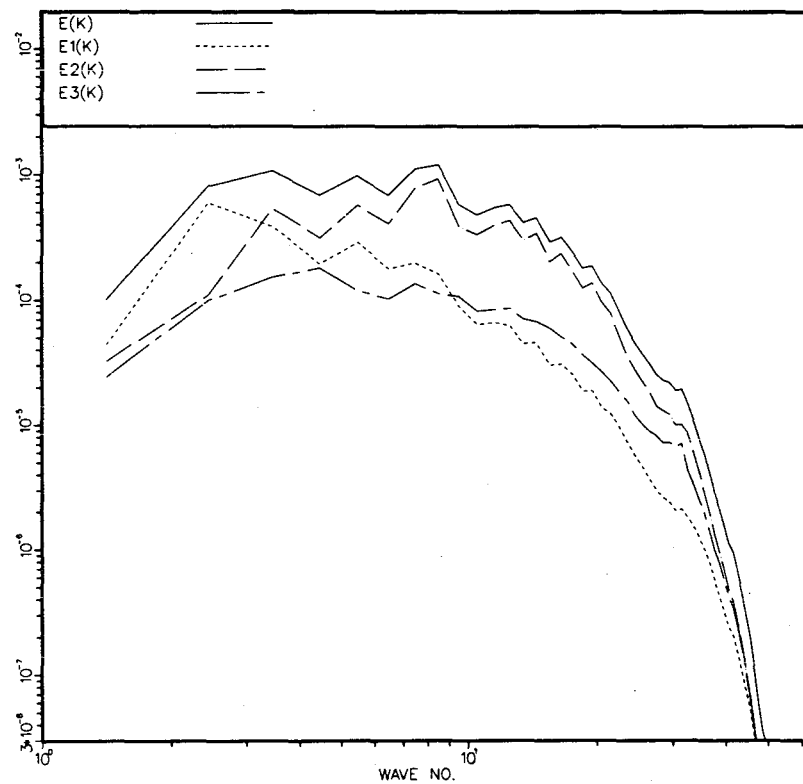
134

Fig. 4.11h. 3-D spectra of the solenoidal part of
the Reynolds stress field as defined
by Eq. (4.6.5). Nomenclature same as
for Fig. 3.3. Letters in figure numbers
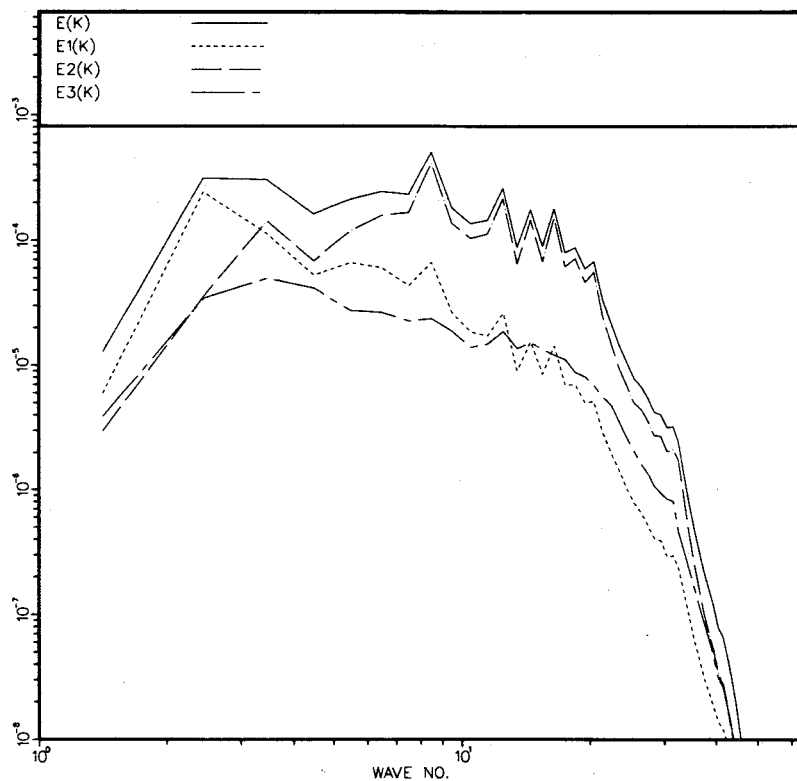correspond to the individual shear-flow
simulations.

Fig. 4.12a. 3-D spectra of the dilatation part of the
Reynolds stress field as defined by Eq.
(4.6.5). Nomenclature same as for Fig.
3.3. Letters in figure numbers correspond
to the individual shear-flow simulations.
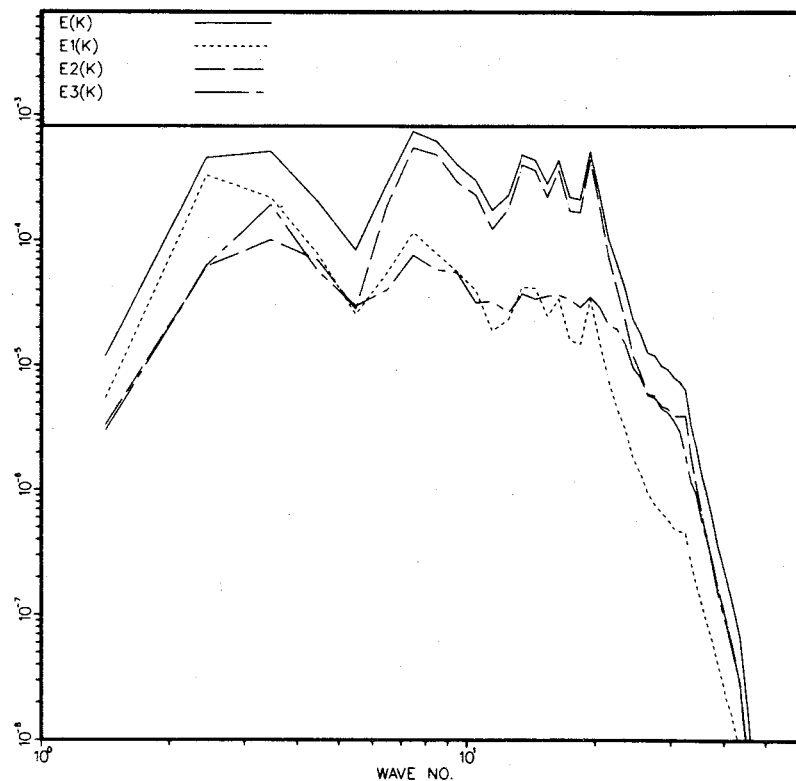
DIVERGENCE ENERGY SPECTRA

DIVERGENCE ENERGY SPECTRA

E(K)	————
E1(K)	··········
E2(K)	— —
E3(K)	—— ·

WAVE NO.
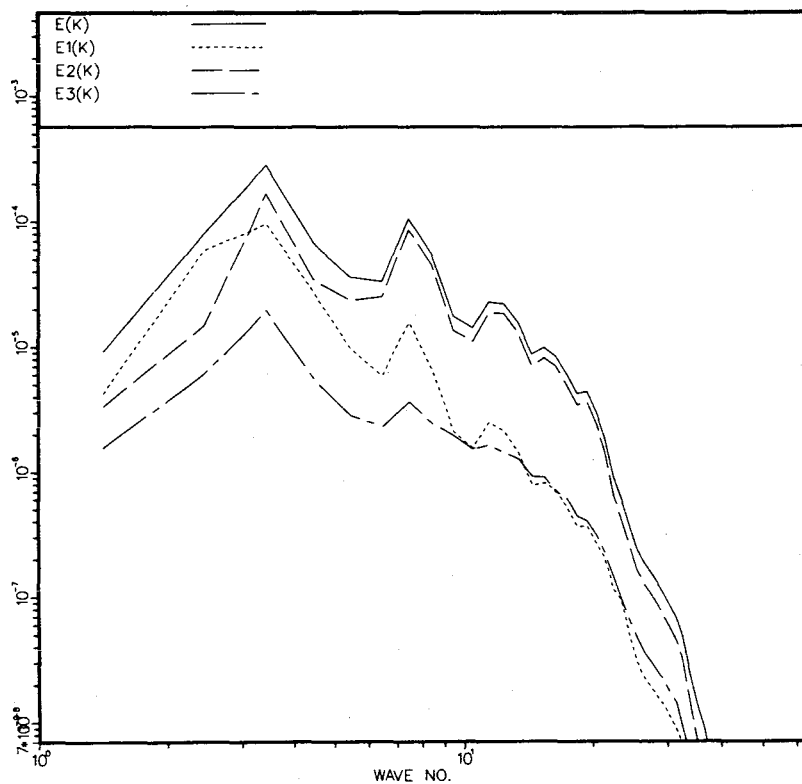
Fig.4.12b. 3-D spectra of the dilatation part of
the Reynolds stress field as defined
by Eq. (4.6.5).

Fig. 4.12c. 3-D spectra of the dilatation part of the
Reynolds stress field as defined by Eq.
(4.6.5)

Nomenclature same as for Fig. 3.3. Letters in figure numbers correspond to the individual
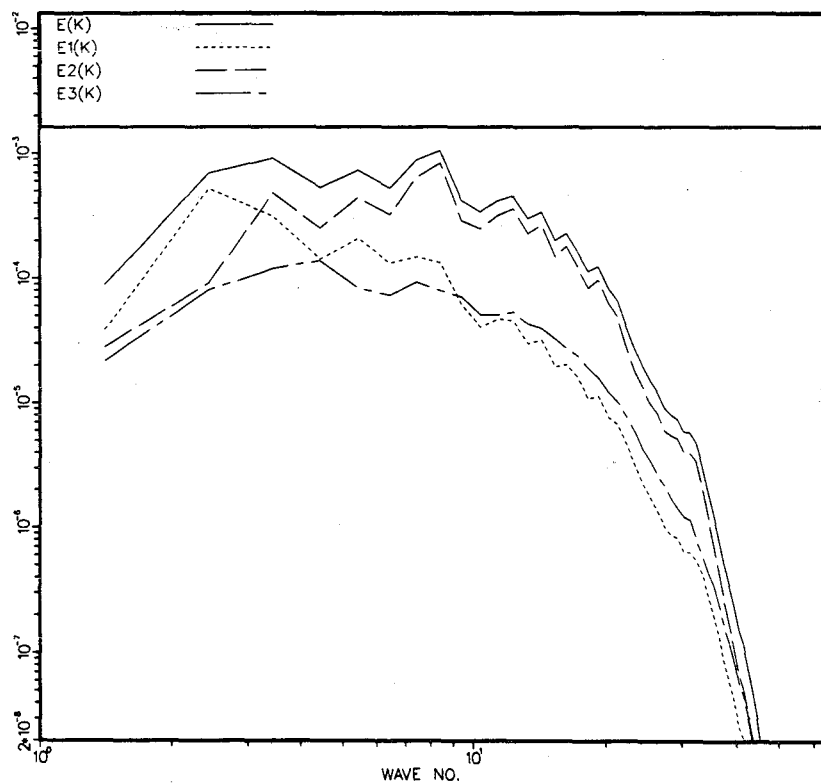shear-flow simulations.

136

DIVERGENCE ENERGY SPECTRA
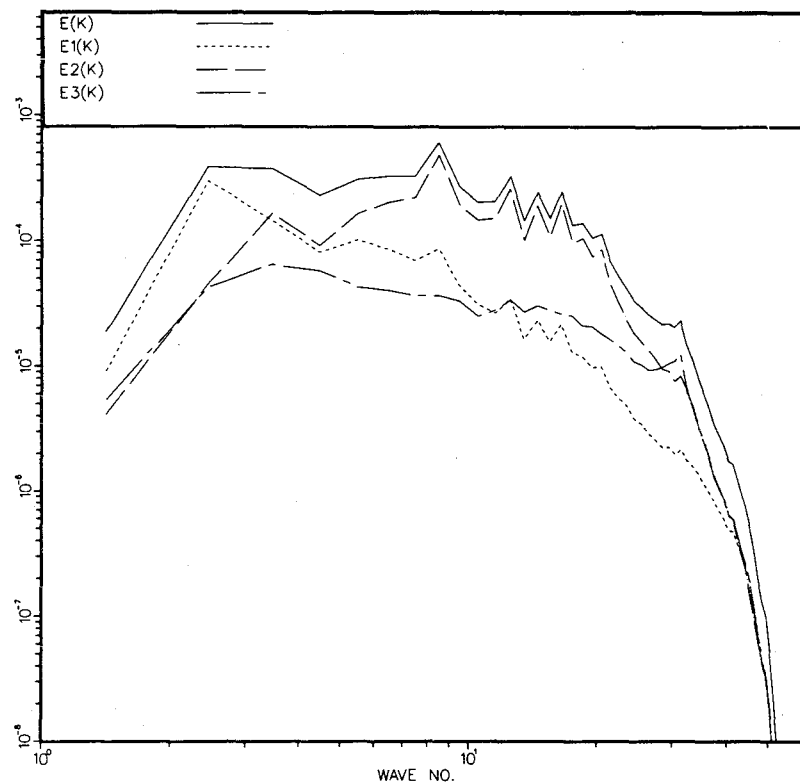
DIVERGENCE ENERGY SPECTRA

Fig. 4.12d. 3-D spectra of the dilatation part of the Reynolds stress field as defined by Eq. (4.6.5).

Fig. 4.12f. 3-D spectra of the dilatation part of the Reynolds stress field as defined by Eq. (4.6.5).

Nomenclature same as for Fig. 3.3. Letters in figure numbers correspond to the individual shear-flow simulations.

DIVERGENCE ENERGY SPECTRA

DIVERGENCE ENERGY SPECTRA

E(K) ————
E1(K) ············
E2(K) —— ——
E3(K) —— ·· —

E(K) ————
E1(K) ············
E2(K) —— ——
E3(K) —— · —

WAVE NO.

WAVE NO.

138

Fig. 4.12g. 3-D spectra of the dilatation part of
the Reynolds stress field as defined
by Eq. (4.6.5).

Fig. 4.12h. 3-D spectra of the dilatation part of
the Reynolds stress field as defined
by Eq. (4.6.5).

Nomenclature same as for Fig. 3.3. Letters in figure numbers correspond to the individual
shear-flow simulations.

DECOMPOSED STRESS SPECTRA
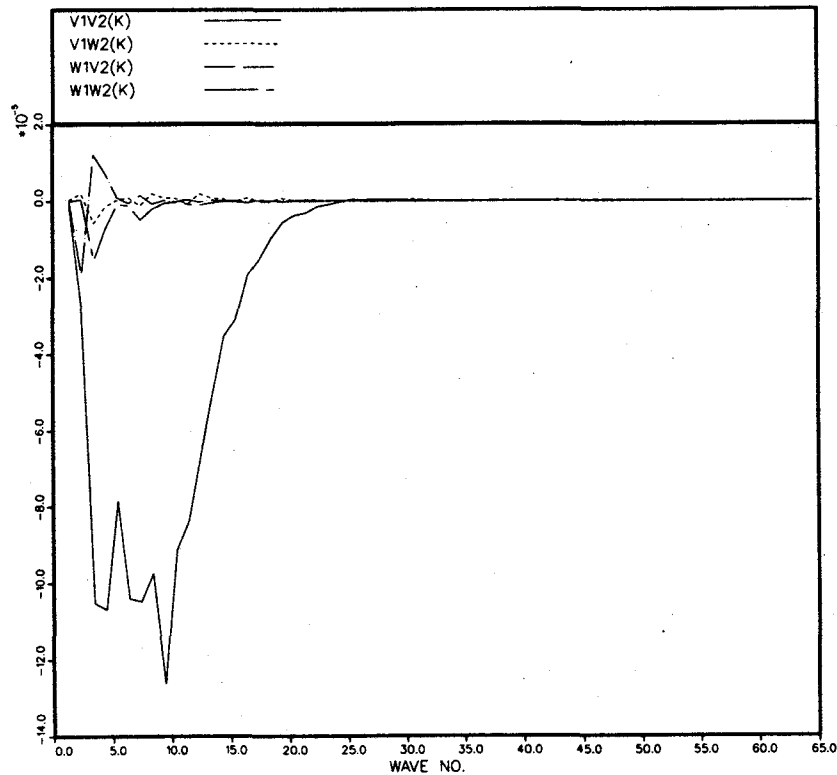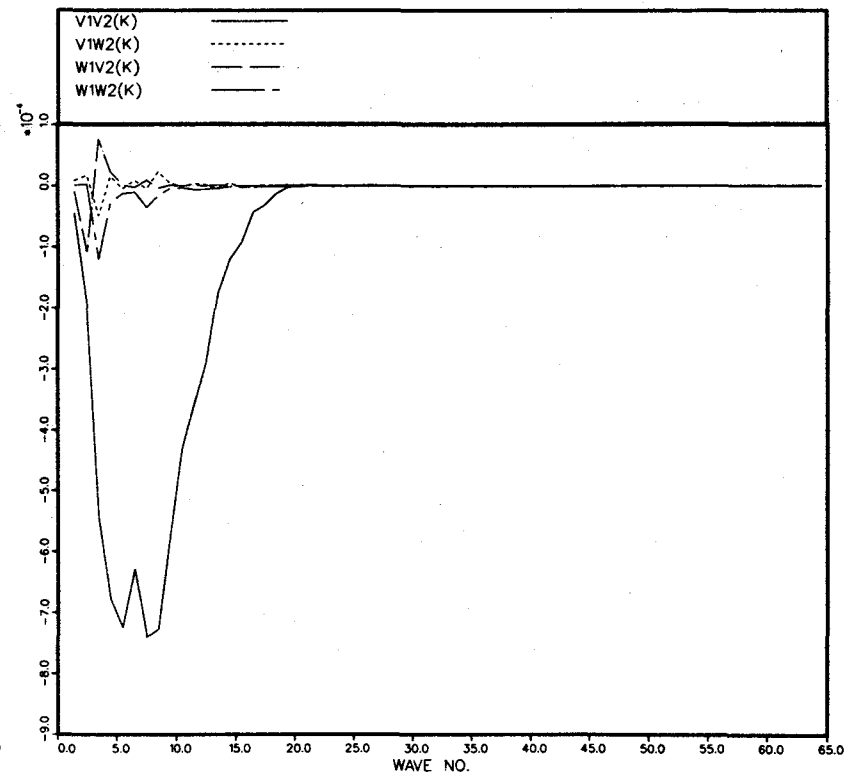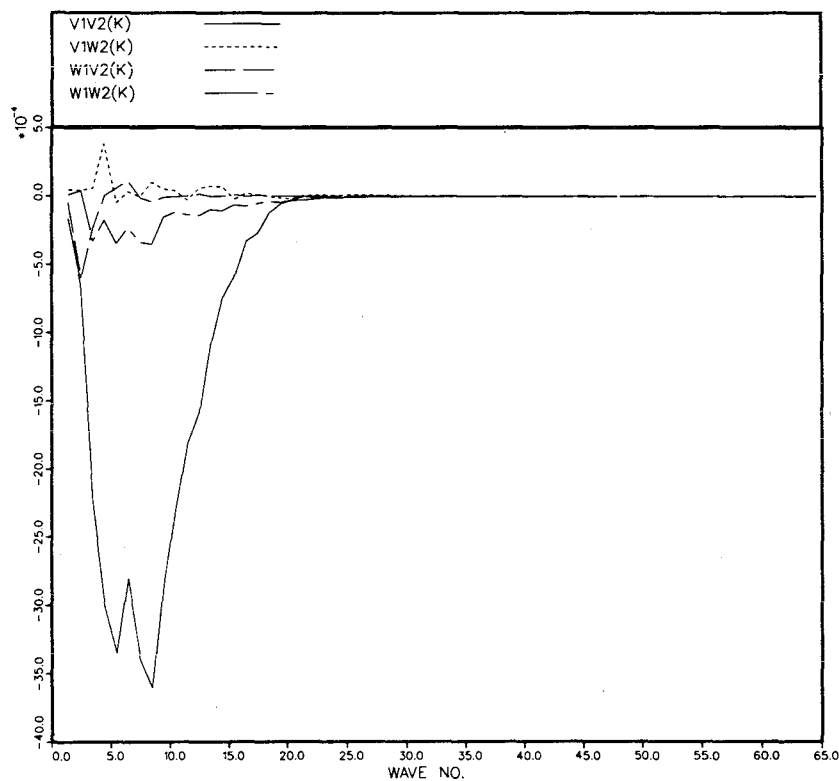
DECOMPOSED STRESS SPECTRA

Fig. 4.13a. 3-D spectra of the Moyal decomposed shear stress as defined by Eq. (4.6.5).

Fig. 4.13b. 3-D spectra of the Moyal decomposed shear stress as defined by Eq. (4.6.5).

V1V2(K) indicates R_{12}^{S}, V1W2(K), W1V2(K), W1W2(K) are the contributions to R_{12}^{D}.

WAVE NO. indicates the magnitude of the wavenumber vector. Letters in the figure numbers correspond to the individual shear flow simulations.

DECOMPOSED STRESS SPECTRA

DECOMPOSED STRESS SPECTRA

Fig. 4.13c. 3-D spectra of the Moyal decomposed
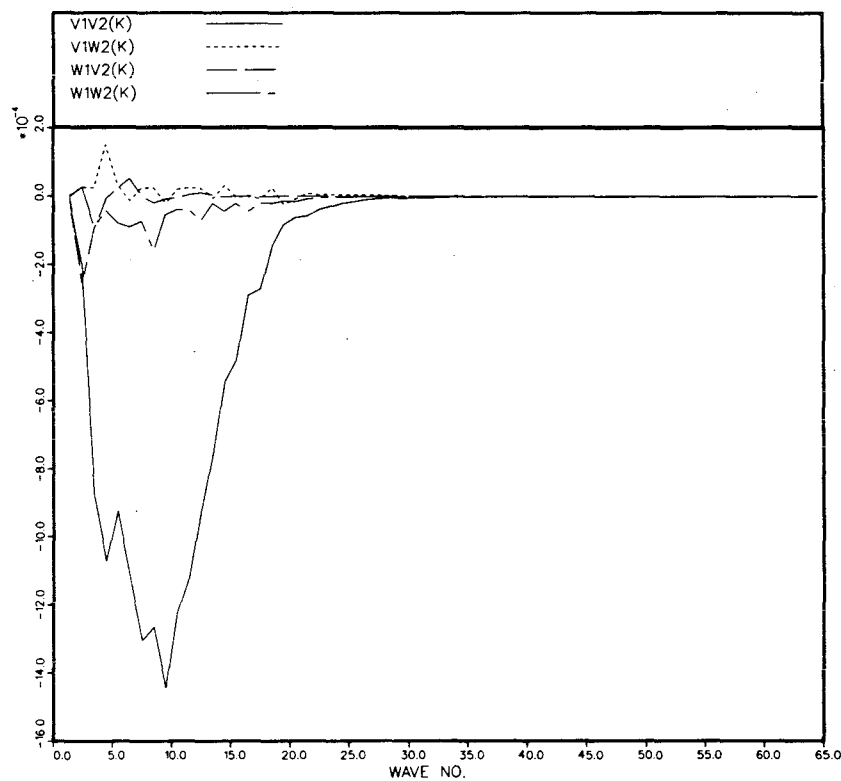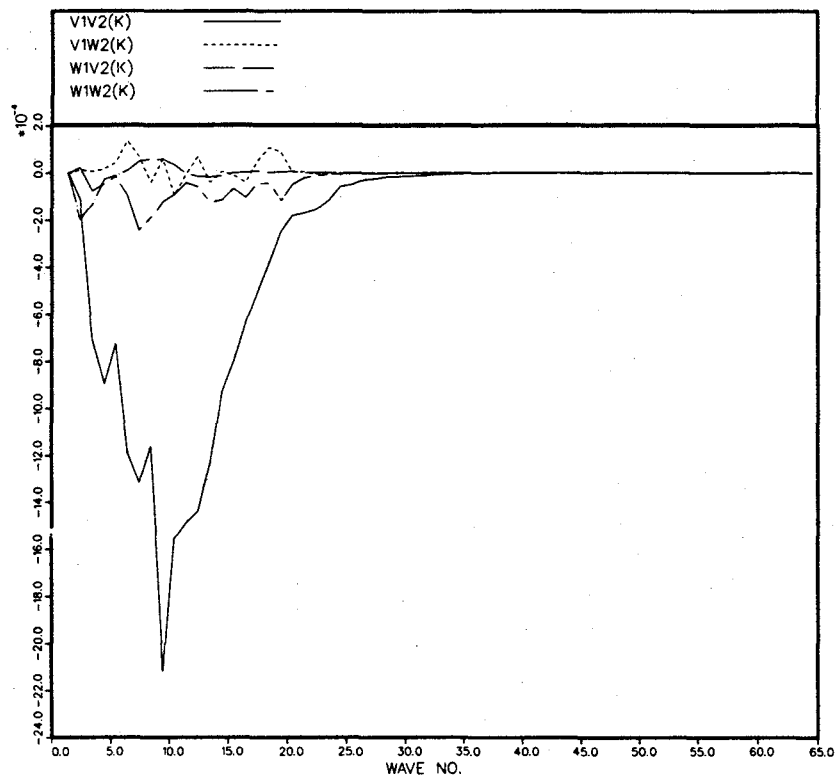shear stress as defined by Eq. (4.6.5).

Fig. 4.13d. 3-D spectra of the Moyal decomposed
shear stress as defined by Eq. (4.6.5).

V1V2(K) indicates R_{12}^{S}, V1W2(K), W1V2(K), W1W2(K) are the contributions to R_{12}^{D}.

WAVE NO. indicates the magnitude of the wavenumber vector. Letters in the figure
numbers correspond to the individual shear flow simulations.

DECOMPOSED STRESS SPECTRA

Fig. 4.13f. 3-D spectra of the Moyal decomposed
shear stress as defined by Eq. (4.6.5).

Fig. 4.13g. 3-D spectra of the Moyal decomposed
shear stress as defined by Eq. (4.6.5)

V1V2(K) indicates R^S_{12}, V1W2(K), W1V2(K), W1W2(K) are the contributions to R^D_{12}.

WAVE NO. indicates the magnitude of the wavenumber vector. Letters in the figure
numbers correspond to the individual shear-flow simulations.

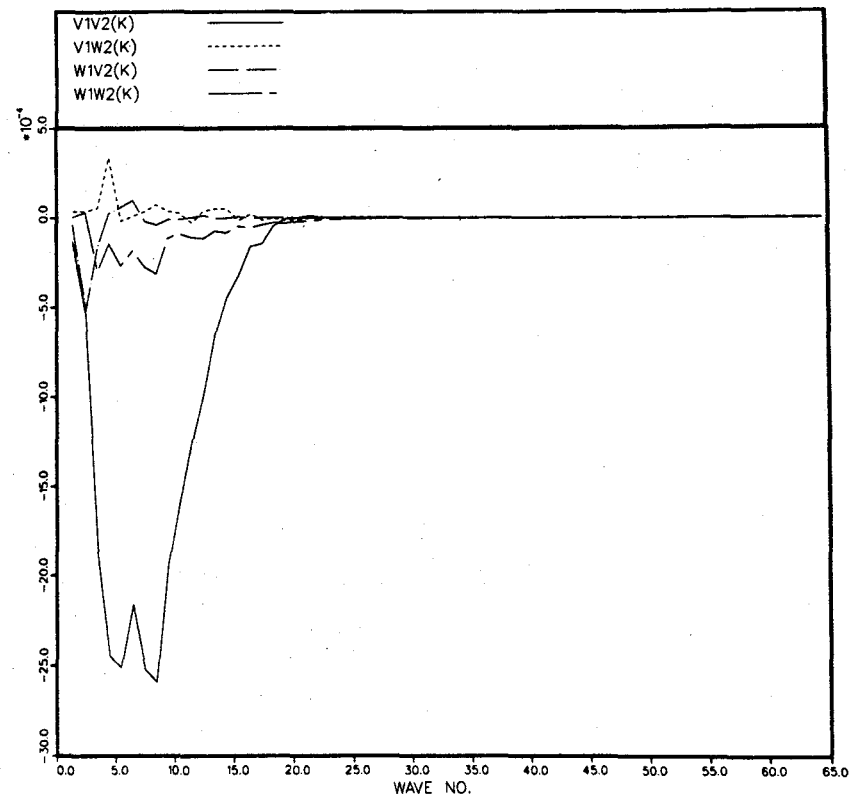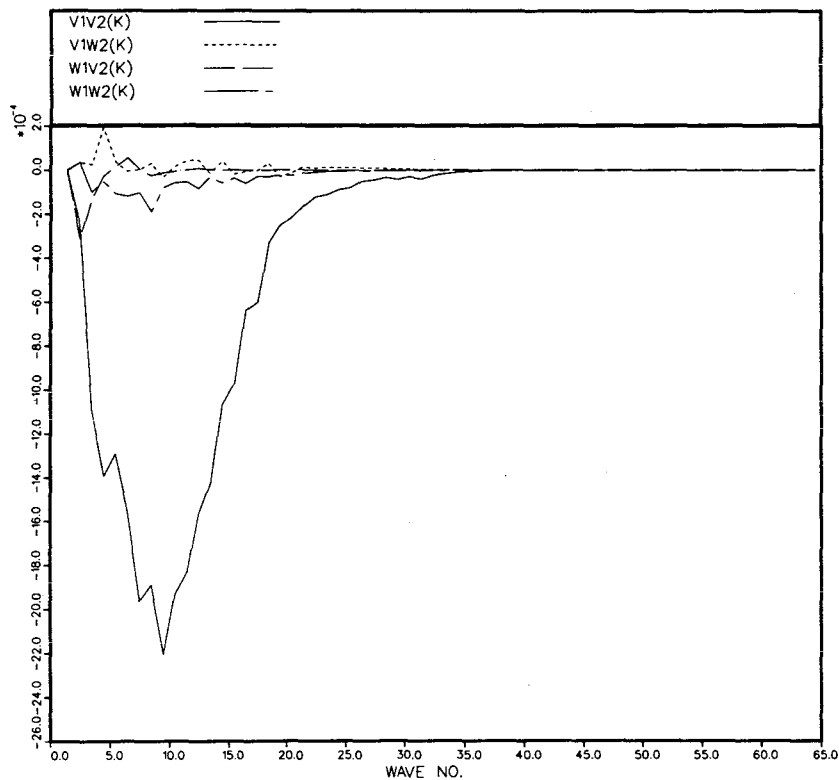## DECOMPOSED STRESS SPECTRA

RUU STRESS EQUATION

Fig. 4.13h. 3-D spectra of the Moyal decomposed shear stress as defined by Eq. (4.6.5). V1V2(K) indicates R^S_{12}, V1W2(K), W1V2(K), W1W2(K) are the contributions to R^D_{12} WAVE NO. indicates the magnitude of the wavenumber vector. Letters in the figure numbers correspond to the individual shear-flow simulations.

Fig. 4.14a. Contributing terms in the R_{11} Reynolds stress equation defined as in Eq. (4.7.1) vs. St. Letters in the figure numbers correspond to the individual shear-flow simulations.

RUU STRESS EQUATION

PRODUCTION ————
P-STRAIN ----------
HOMO DISP —— ——
DIV DISP ———— -

S•TIME

RUU STRESS EQUATION

PRODUCTION ————
P-STRAIN ----------
HOMO DISP —— ——
DIV DISP ———— -

S•TIME

Fig. 4.14b. Contributing terms in the R_{11} Reynolds stress equation defined as in Eq. (4.7.1) vs. St.
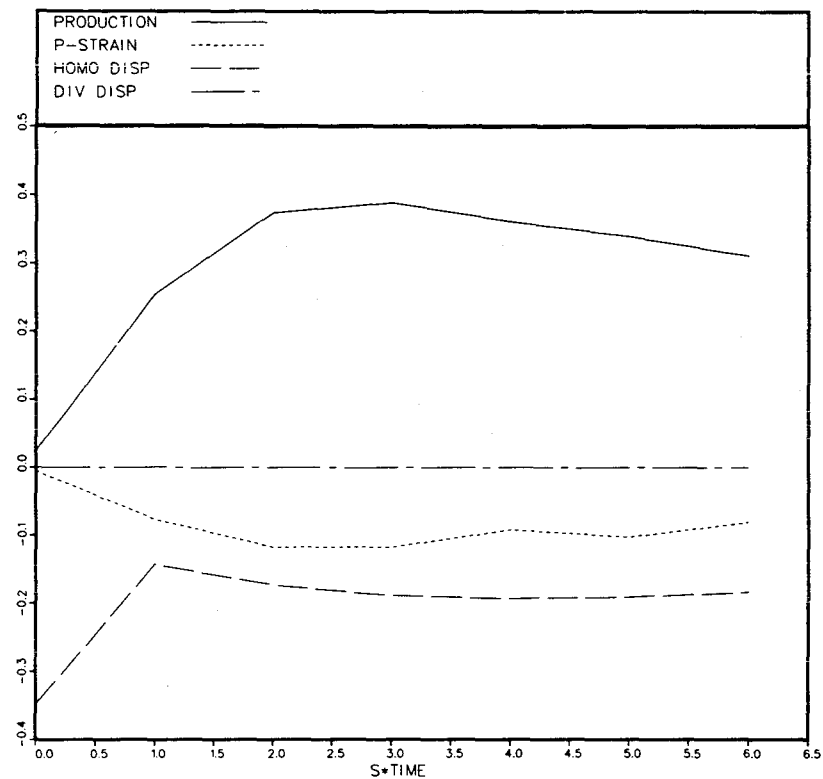
Fig. 4.14c. Contributing terms in the R_{11} Reynolds stress equation defined as in Eq. (4.7.1) vs. St.

Letters in the figure numbers correspond to the individual shear-flow simulations.

143

RUU STRESS EQUATION

RUU STRESS EQUATION

Fig. 4.14d. Contributing terms in the R_{11} Reynolds stress equations defined as in Eq. (4.7.1) vs. St.
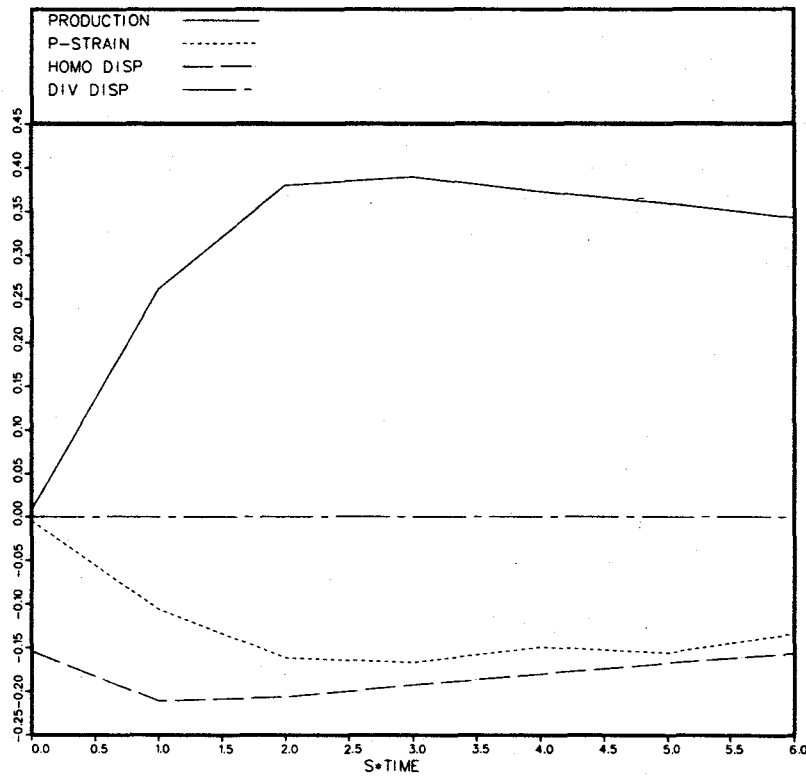
Fig. 4.14f. Contributing terms in the R_{11} Reynolds stress equations defined as in Eq. (4.7.1) vs. St.

Letters in the figure numbers correspond to the individual shear-flow simulations.
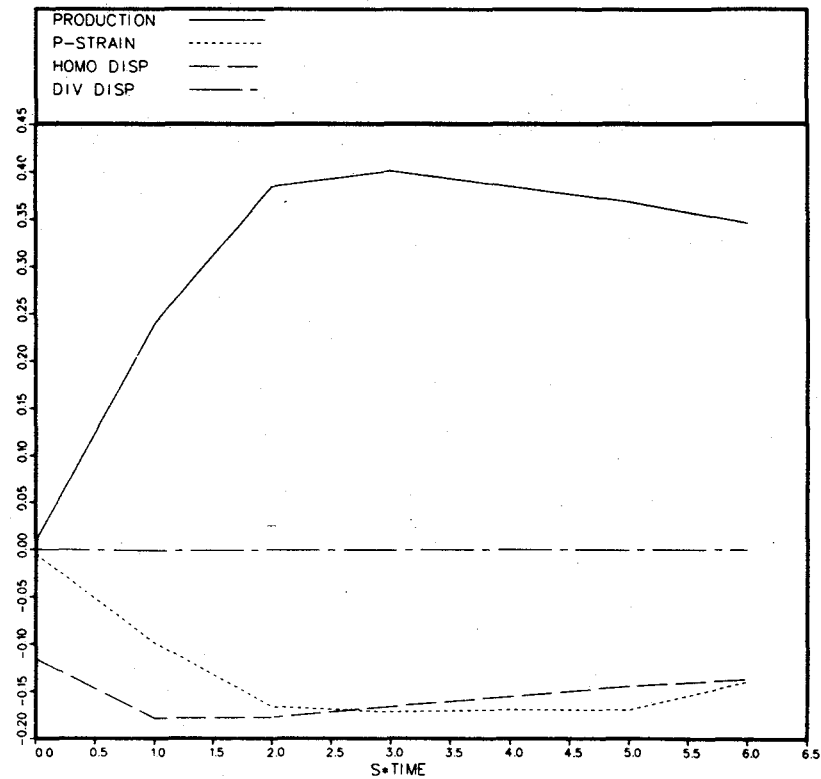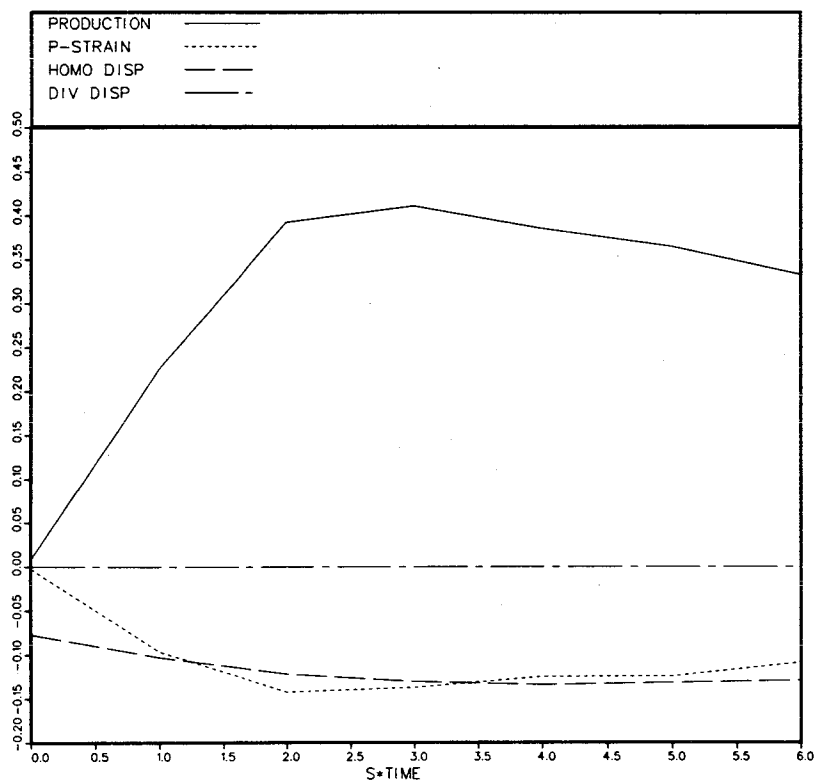
RUU STRESS EQUATION   RUU STRESS EQUATION

PRODUCTION ————   PRODUCTION ————
P-STRAIN   ··········   P-STRAIN   ··········
HOMO DISP —— ——   HOMO DISP —— ——
DIV DISP   ———— -   DIV DISP   ———— -

S*TIME   S*TIME

Fig. 4.14g. Contributing terms in the R_{11} Reynolds Fig. 4.14h. Contributing terms in the R_{11} Reynolds
stress equations defined as in Eq. (4.7.1)   stress equations defined as in Eq. (4.7.1)
vs. St.   vs. St.

Letters in the figure numbers correspond to the individual shear-flow simulations.

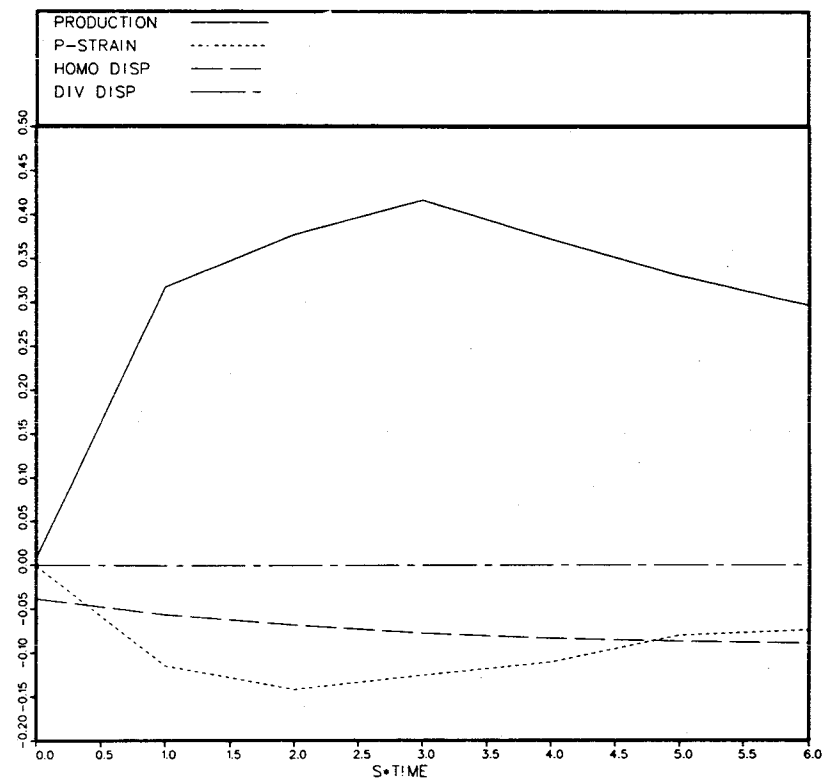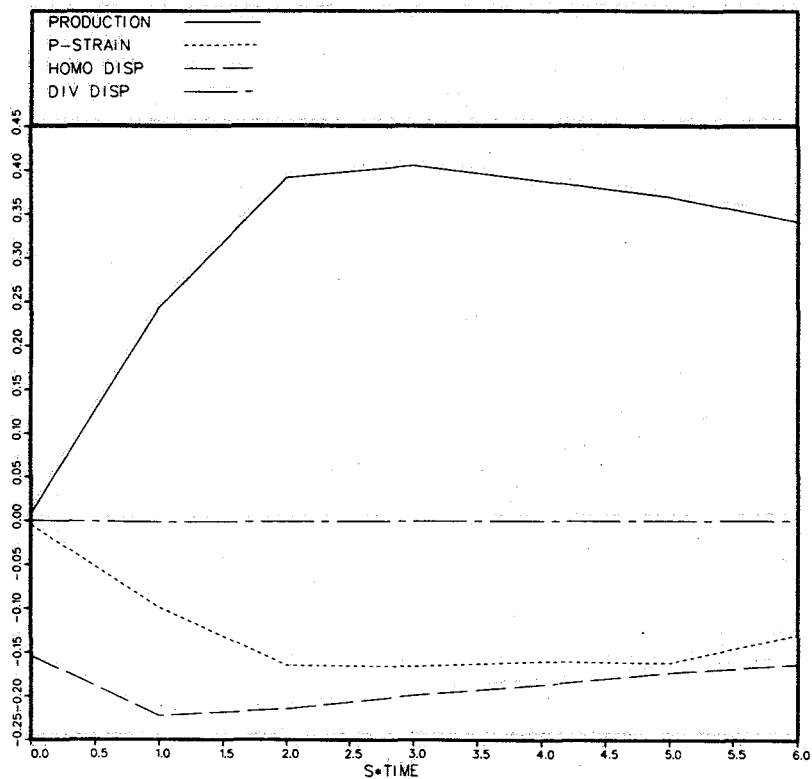RVV STRESS EQUATION   RVV STRESS EQUATION

Fig. 4.15a. Contributing terms in the R_{22} Reynolds   Fig. 4.15b. Contributing terms in the R_{22} Reynolds
        stress equations defined as in Eq. (4.7.1)   stress equations defined as in Eq. (4.7.1)
        vs. St.   vs. St.

        Letters in the figure numbers correspond to the individual shear-flow simulations.

RVV STRESS EQUATION

RVV STRESS EQUATION

Fig. 4.15c. Contributing terms in the R_{22} Reynolds
stress equations defined as in Eq. (4.7.1)
vs. St.

Fig. 4.15d. Contributing terms in the R_{22} Reynolds
stress equations defined as in Eq. (4.7.1)
vs. St.

Letters in the figure numbers correspond to the individual shear-flow simulations.
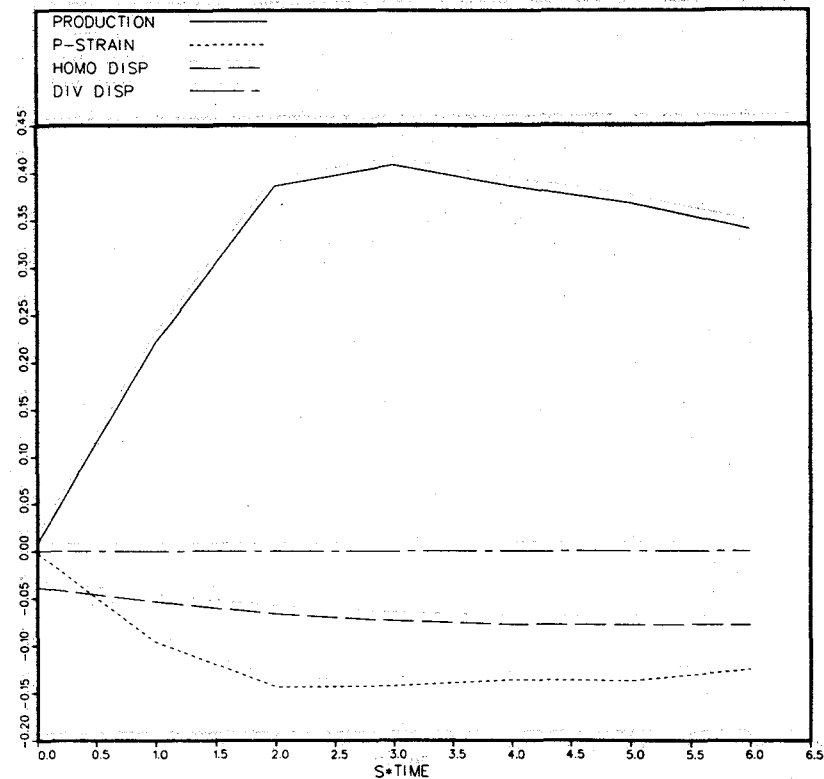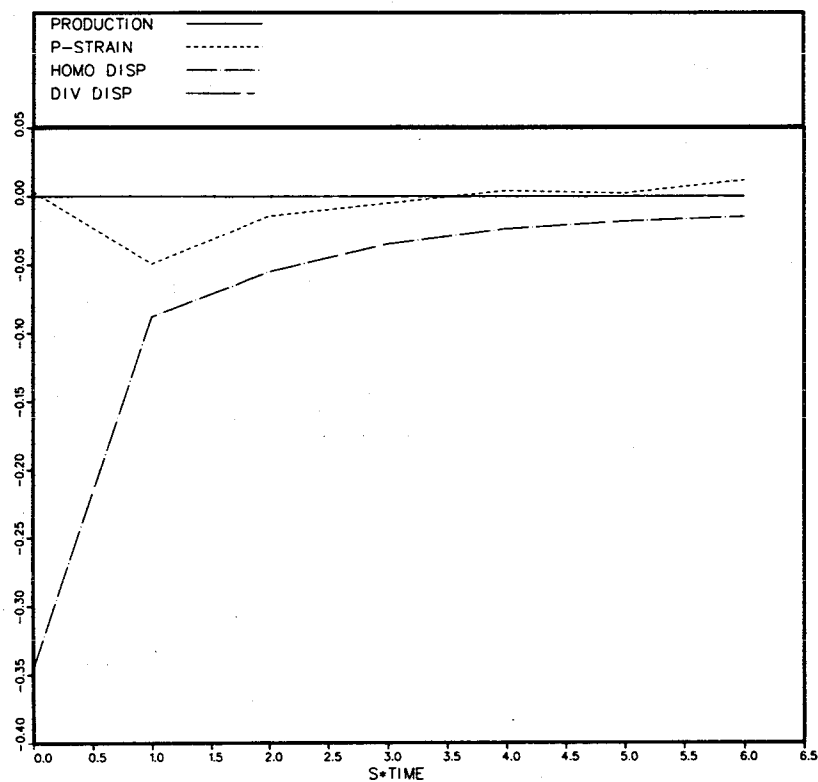
RVV STRESS EQUATION

RVV STRESS EQUATION

Fig. 4.15f. Contributing terms in the R_{22} Reynolds stress equations defined as in Eq. (4.7.1) vs. St.

Fig. 4.15g. Contributing terms in the R_{22} Reynolds stress equations defined as in Eq. (4.7.1) vs. St.

Letters in the figure numbers correspond to the individual shear-flow simulations.

RVV STRESS EQUATION

RWW STRESS EQUATION

PRODUCTION ———
P-STRAIN ....
HOMO DISP — —
DIV DISP ——— -

S*TIME

PRODUCTION ———
P-STRAIN ....
HOMO DISP — —
DIV DISP ——— -

S*TIME

149

Fig. 4.15h. Contributing terms in the R_{22} Reynolds
stress equations defined as in Eq. (4.7.1)
vs. St.

Fig. 4.16a. Contributing terms in the R_{33} Reynolds
stress equations defined as in Eq. (4.7.1)
vs. St.

Letters in the figure numbers correspond to the individual shear-flow simulations.
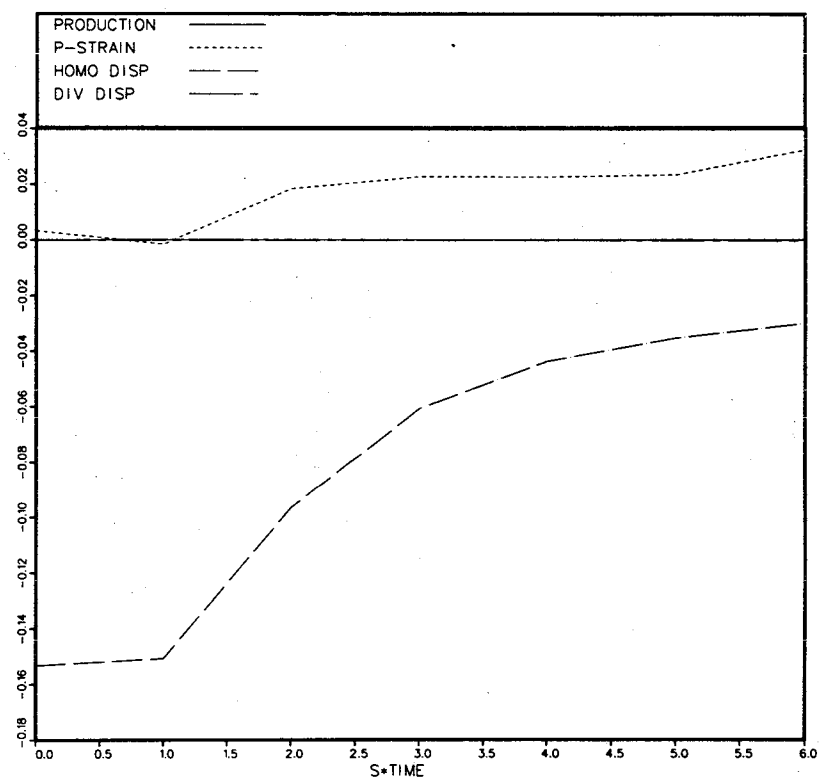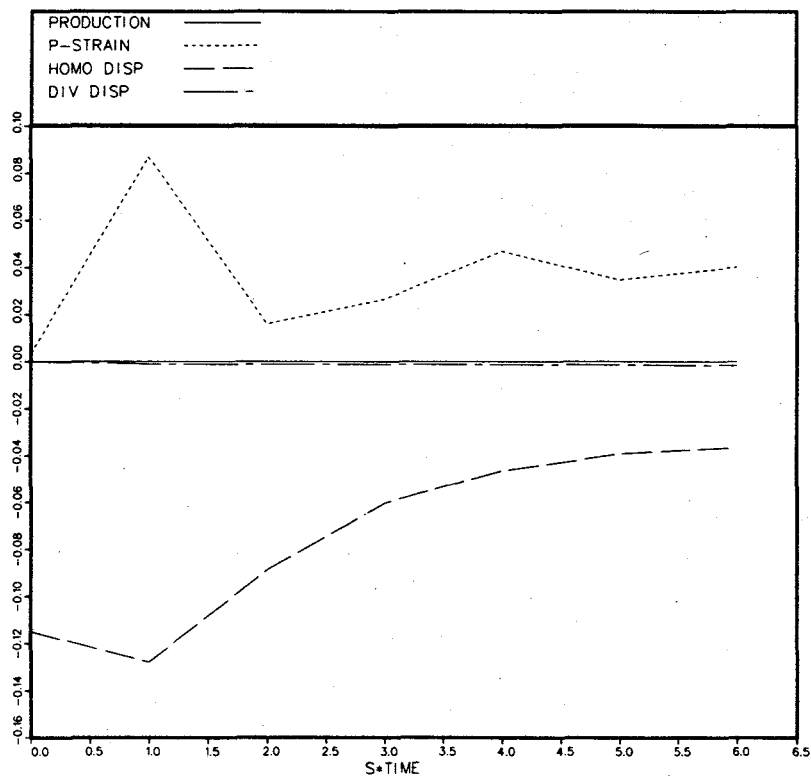
RWW STRESS EQUATION

RWW STRESS EQUATION

Fig. 4.16b. Contributing terms in the R_{33} Reynolds   Fig. 4.16c. Contributing terms in the R_{33} Reynolds stress equations defined as in Eq. (4.7.1) vs. St.

stress equations defined as in Eq. (4.7.1) vs. St.

Letters in the figure numbers correspond to the individual shear-flow simulations.

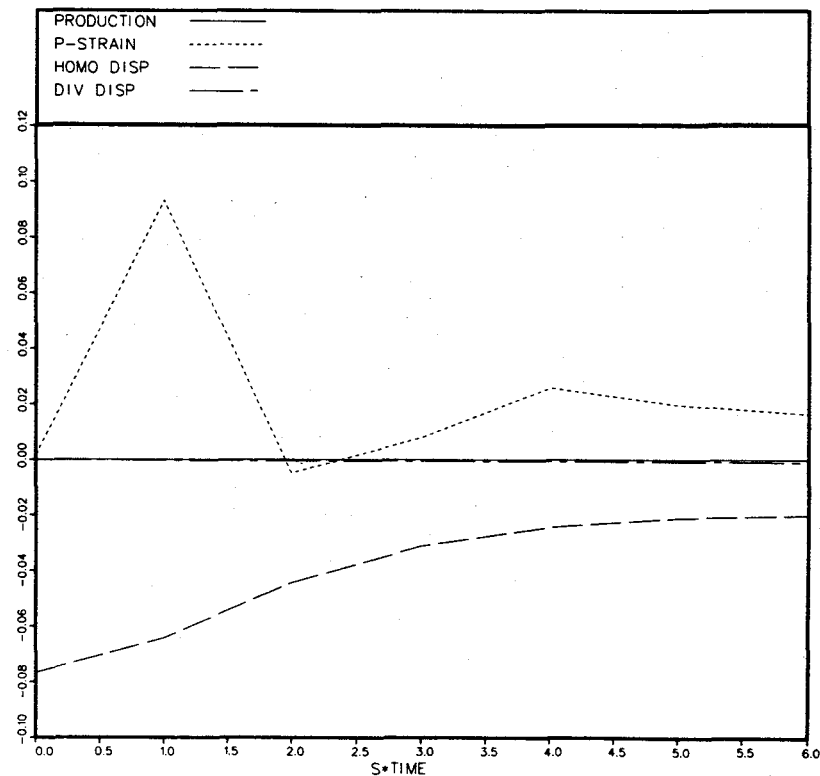RWW STRESS EQUATION

RWW STRESS EQUATION
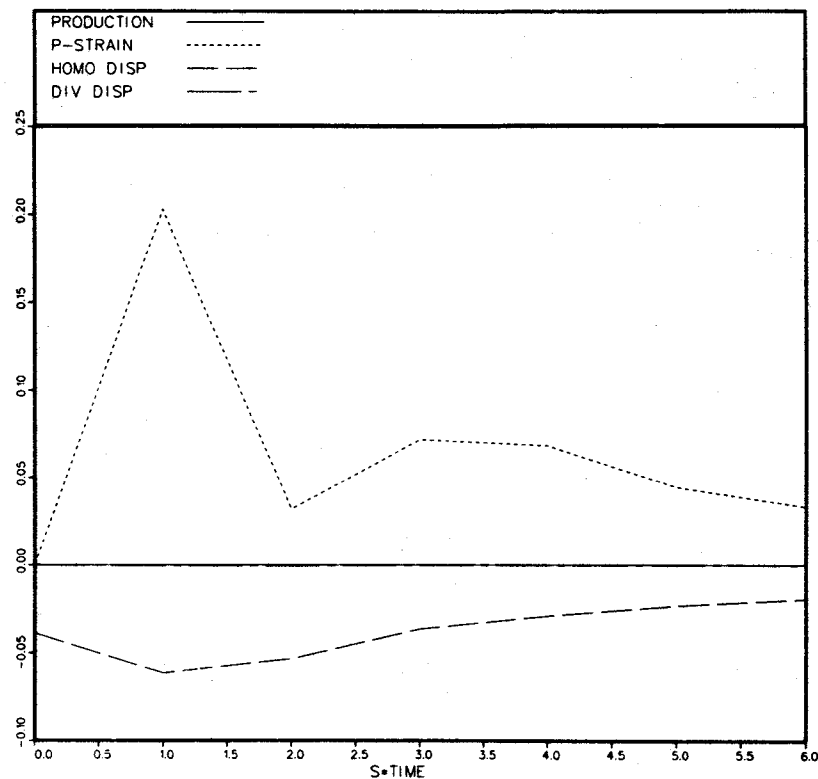
Fig. 4.16d. Contributing terms in the R_{33} Reynolds stress equations defined as in Eq. (4.7.1) vs. St.

Fig. 4.16f. Contributing terms in the R_{33} Reynolds stress equations defined as in Eq. (4.7.1) vs. St.

Letters in the figure numbers correspond to the individual shear-flow simulations.

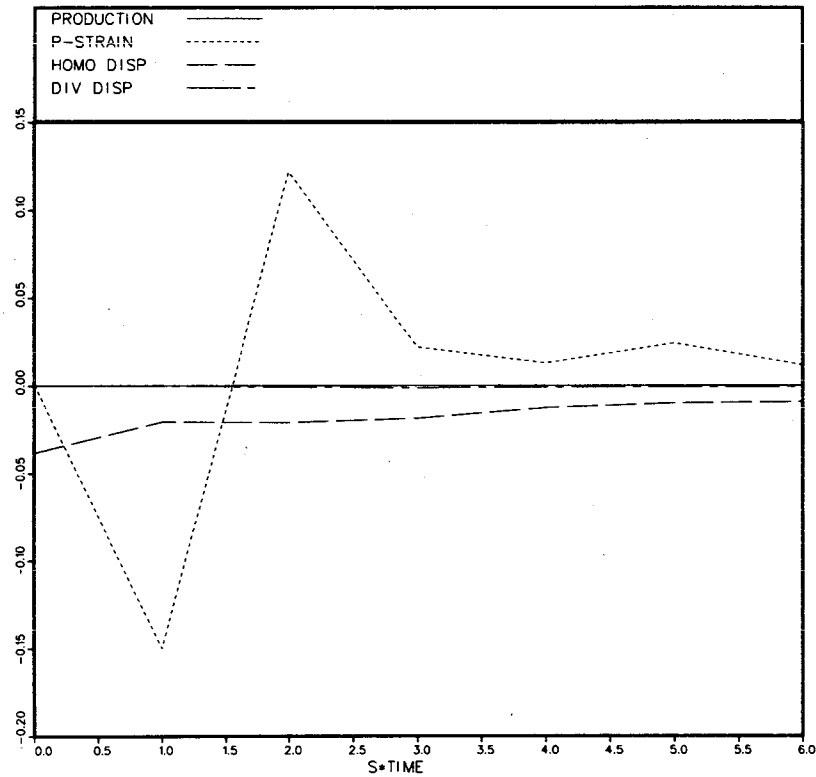RWW STRESS EQUATION

RWW STRESS EQUATION
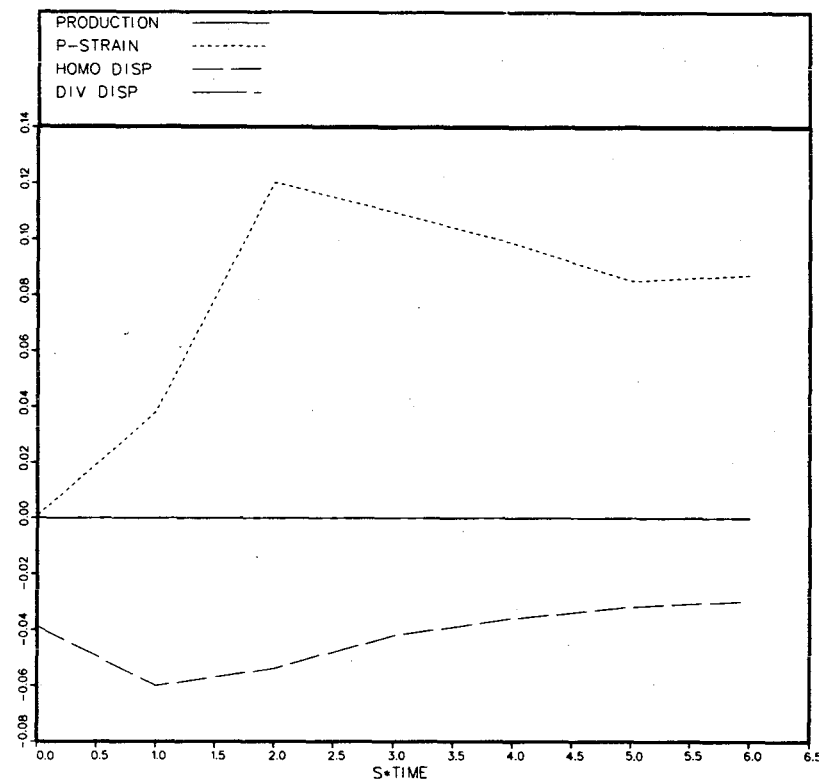
Fig. 4.16g. Contributing terms in the R_{33} Reynolds stress equations defined as in Eq. (4.7.1) vs. St.

Fig. 4.16h. Contributing terms in the R_{33} Reynolds stress equations defined as in Eq. (4.7.1) vs. St.

Letters in the figure numbers correspond to the individual shear-flow simulations.
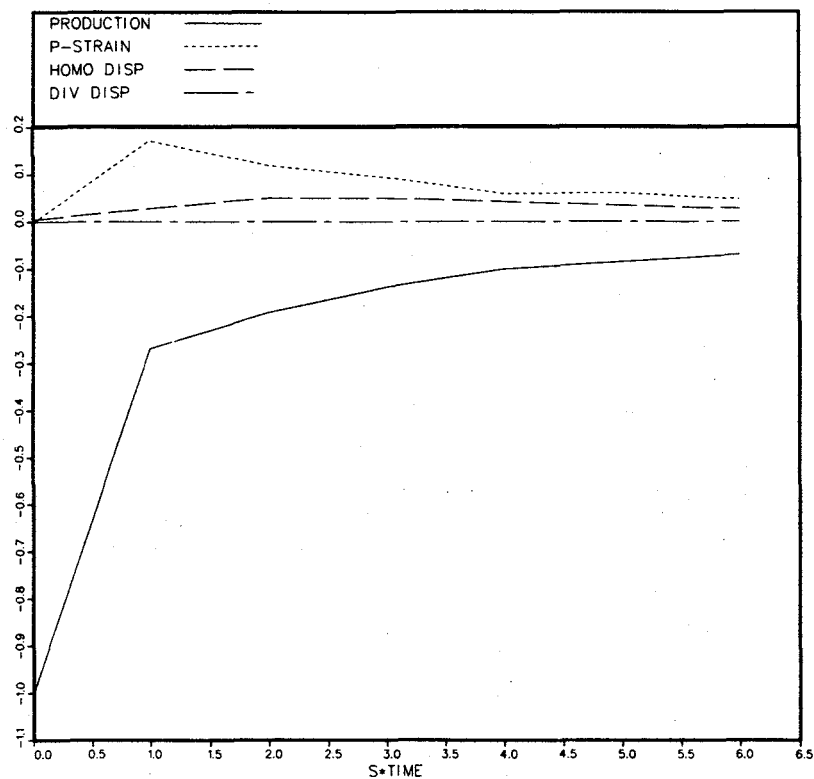
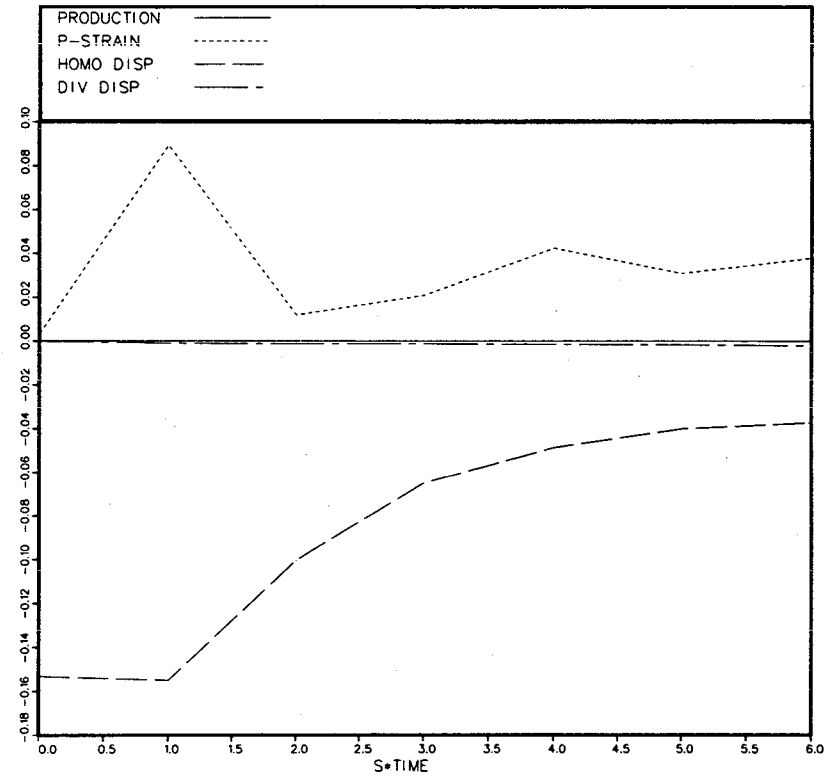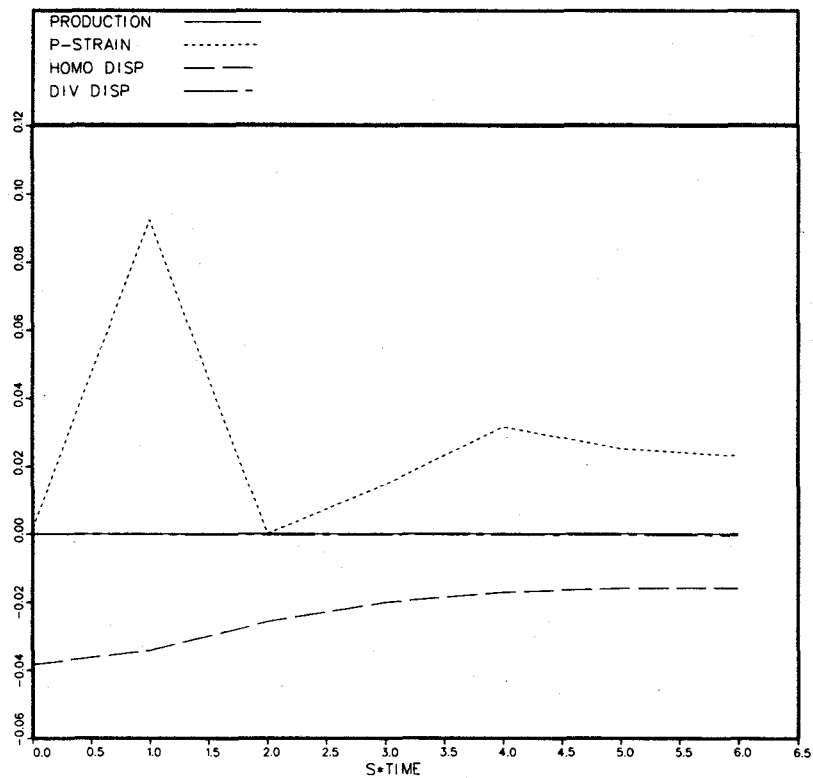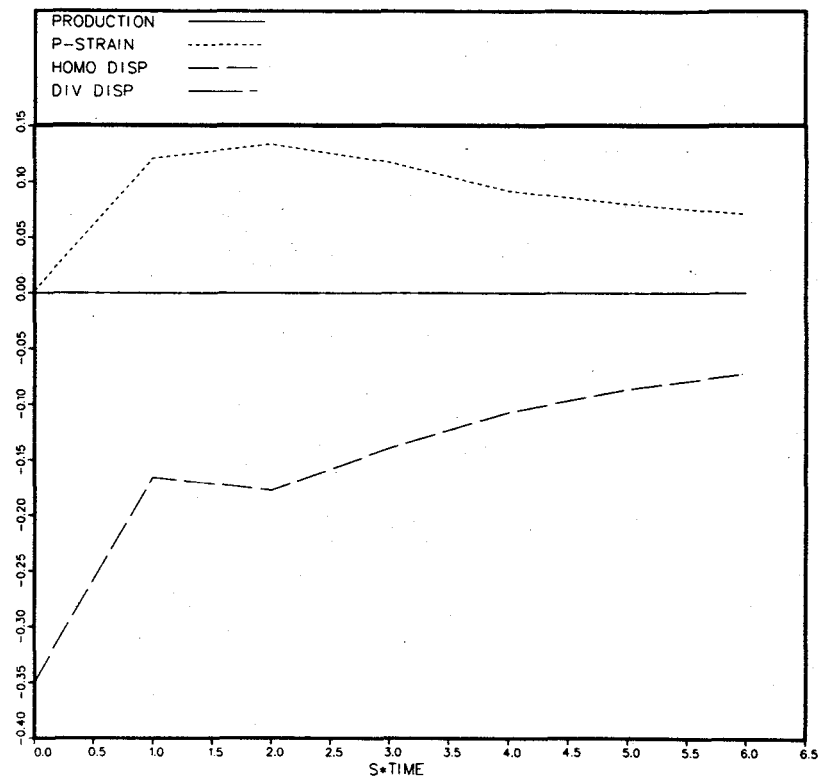RUV STRESS EQUATION   RUV STRESS EQUATION
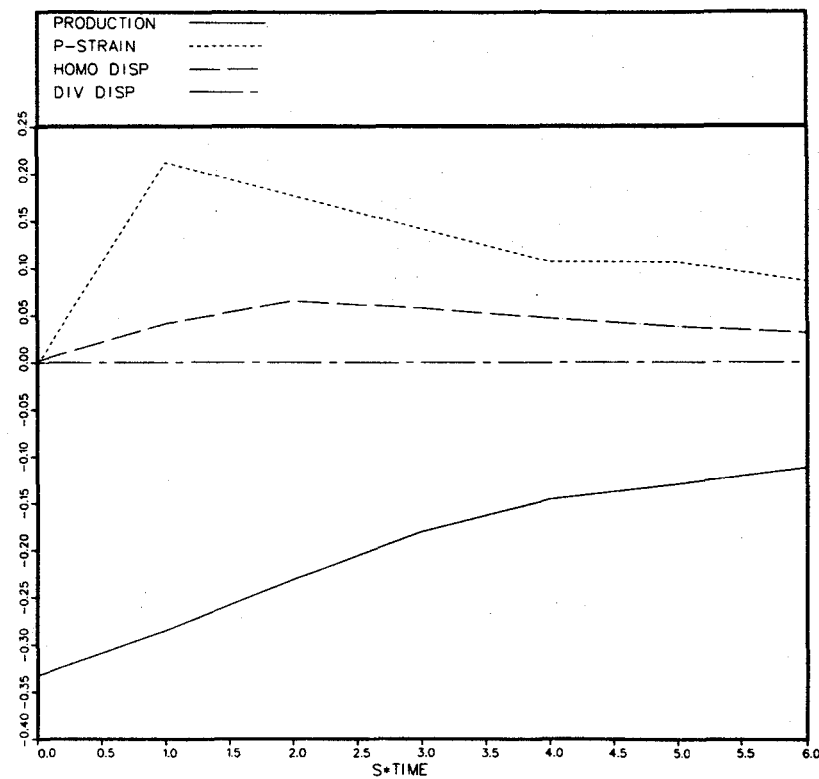
Fig. 4.17a. Contributing terms in the R_{12} Reynolds   Fig. 4.17b. Contributing terms in the R_{12} Reynolds
             stress equations defined as in Eq. (4.7.1)   stress equations defined as in Eq. (4.7.1)
             vs. St.   vs. St.

             Letters in the figure numbers correspond to the individual shear-flow simulations.
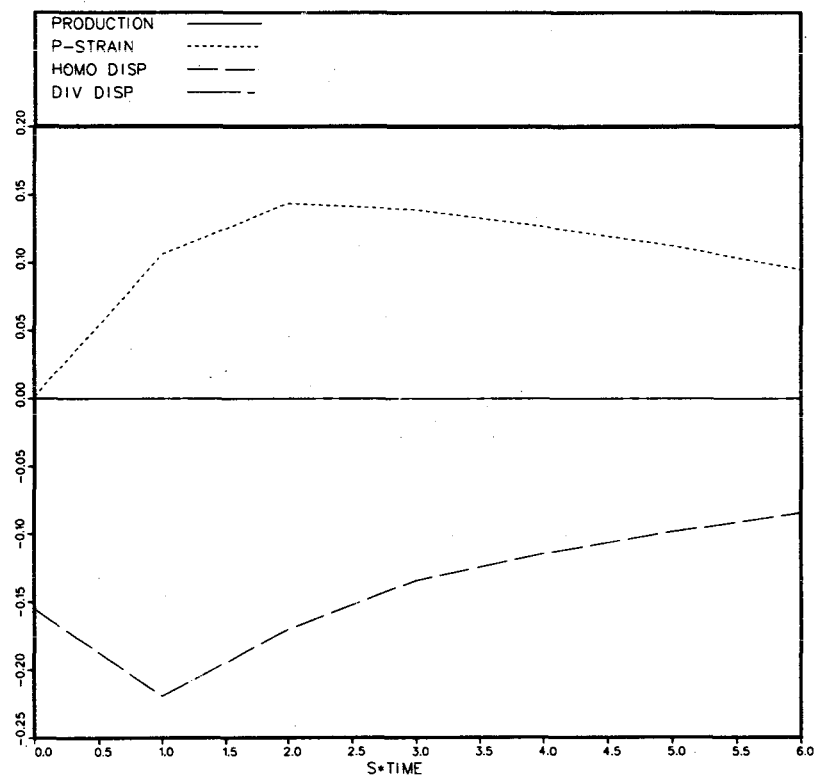
RUV STRESS EQUATION
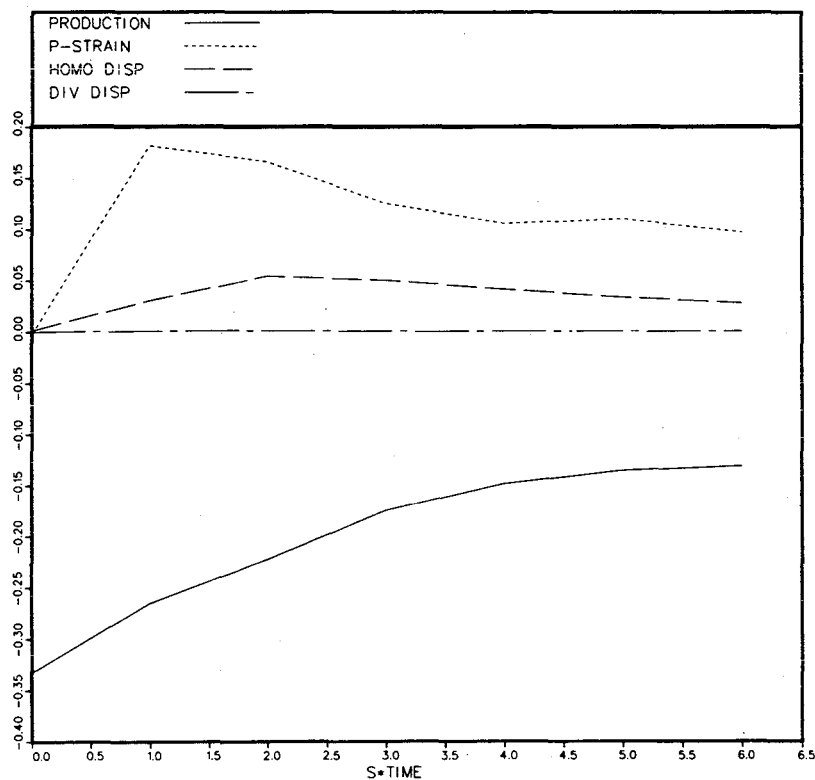
RUV STRESS EQUATION
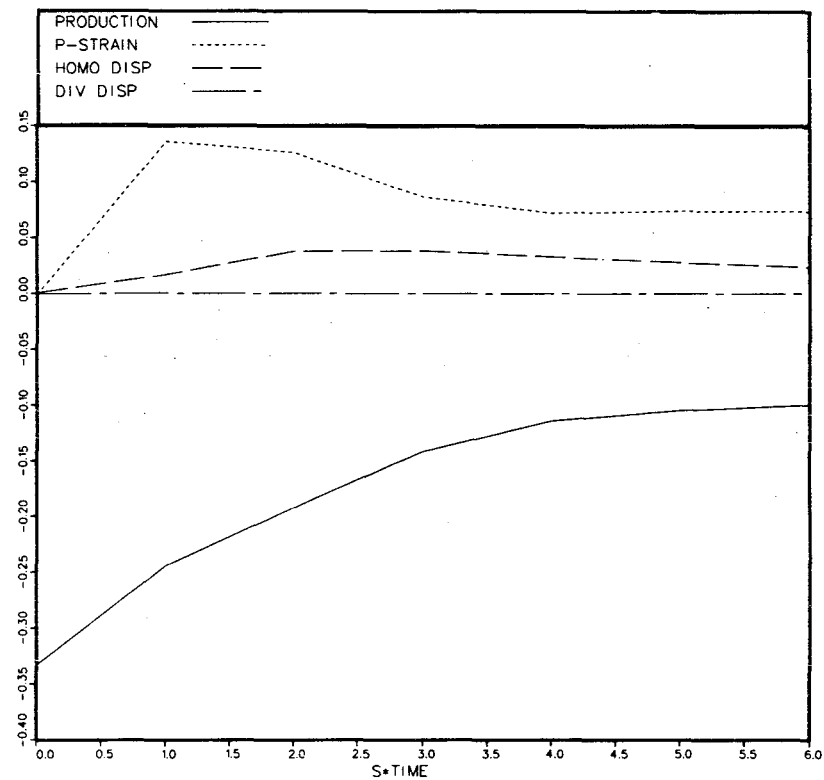
Fig. 4.17c. Contributing terms in the R_{12} Reynolds stress equations defined as in Eq. (4.7.1) vs. St.

Fig. 4.17d. Contributing terms in the R_{12} Reynolds stress equations defined as in Eq. (4.7.1) vs. St.

Letters in the figure numbers correspond to the individual shear-flow simulations.

RUV STRESS EQUATION

PRODUCTION ————
P-STRAIN ··········
HOMO DISP —— ——
DIV DISP ———— -

RUV STRESS EQUATION

PRODUCTION ————
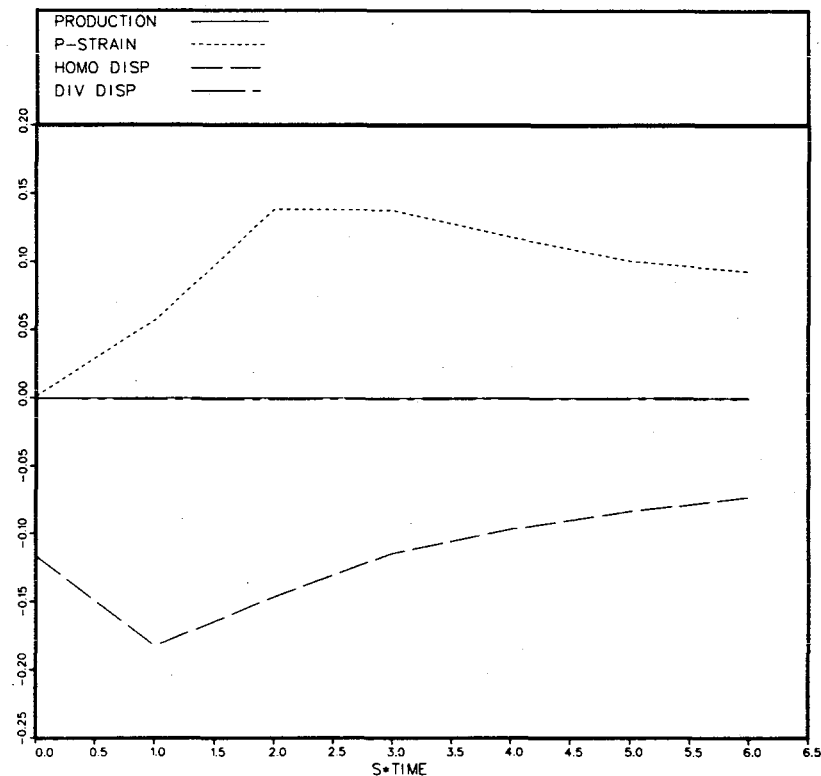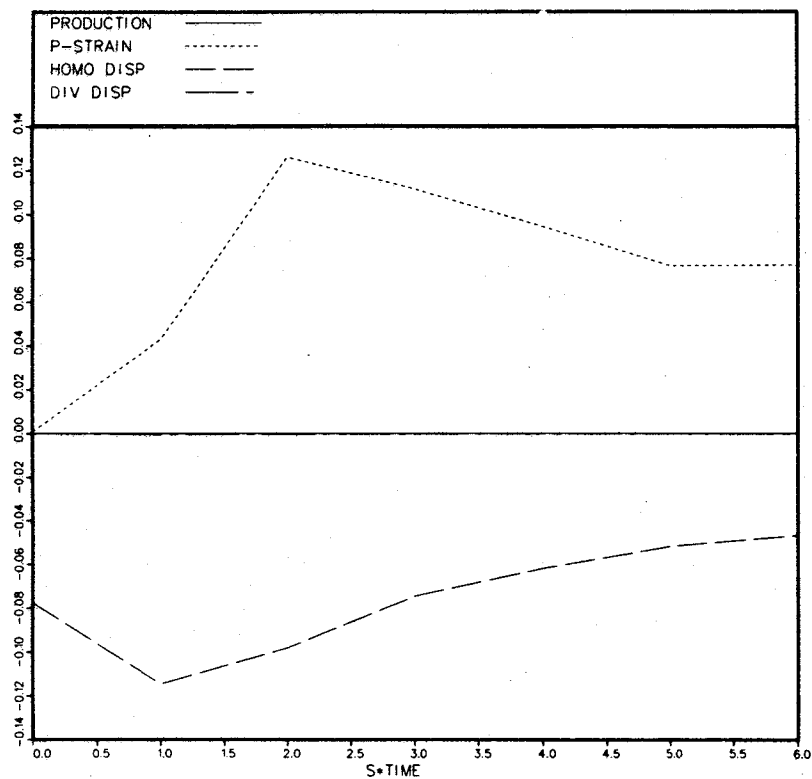P-STRAIN ··········
HOMO DISP —— ——
DIV DISP ———— -
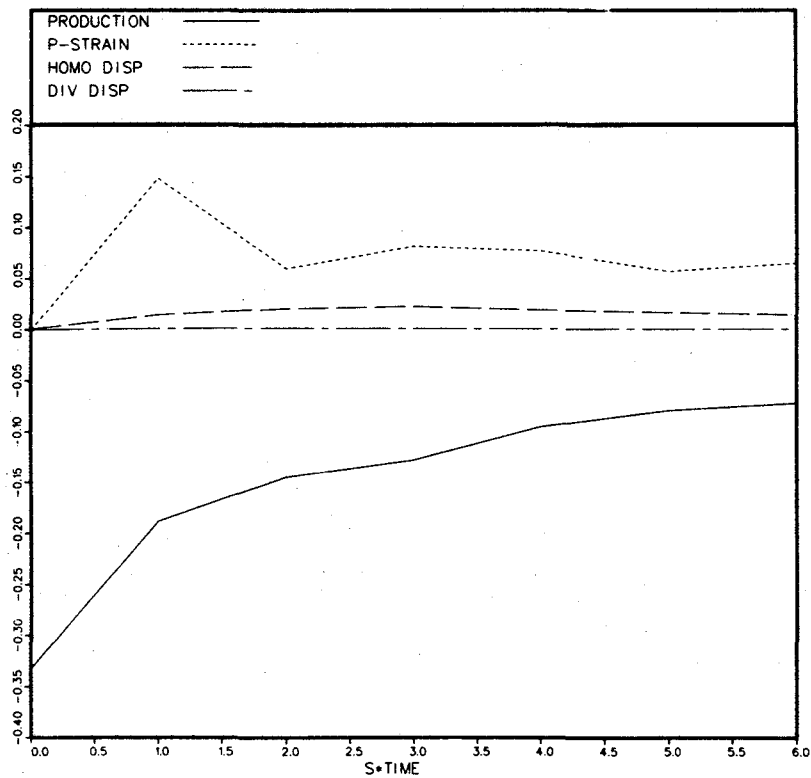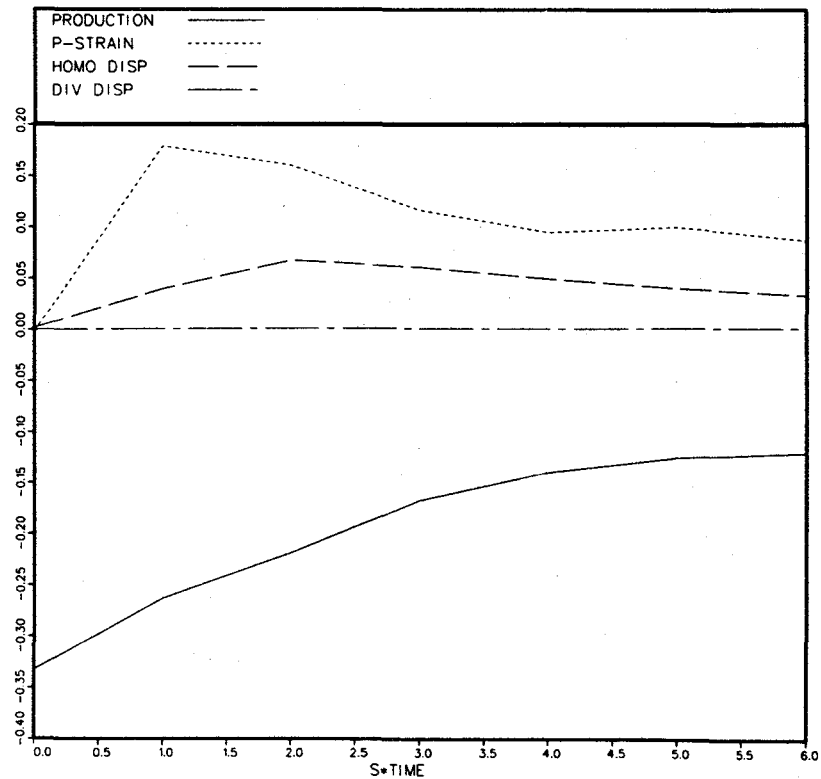
Fig. 4.17f. Contributing terms in the R_{12} Reynolds stress equations defined as in Eq. (4.7.1) vs. St.

Fig. 4.17g. Contributing terms in the R_{12} Reynolds stress equations defined as in Eq. (4.7.1) vs. St.

Letters in the figure numbers correspond to the individual shear-flow simulations.

155

RUV STRESS EQUATION
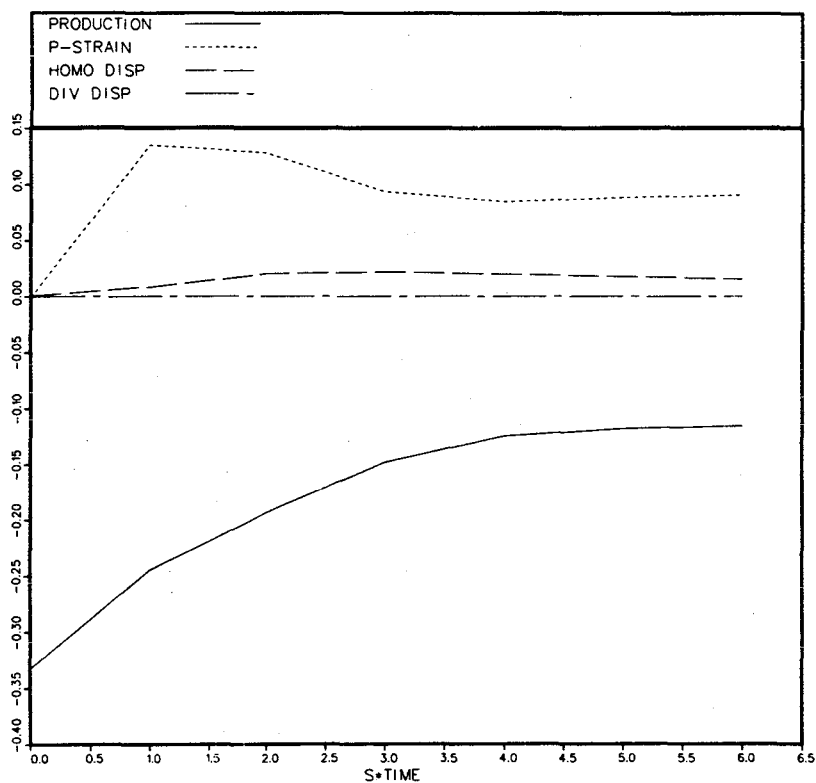
KE EQUATION
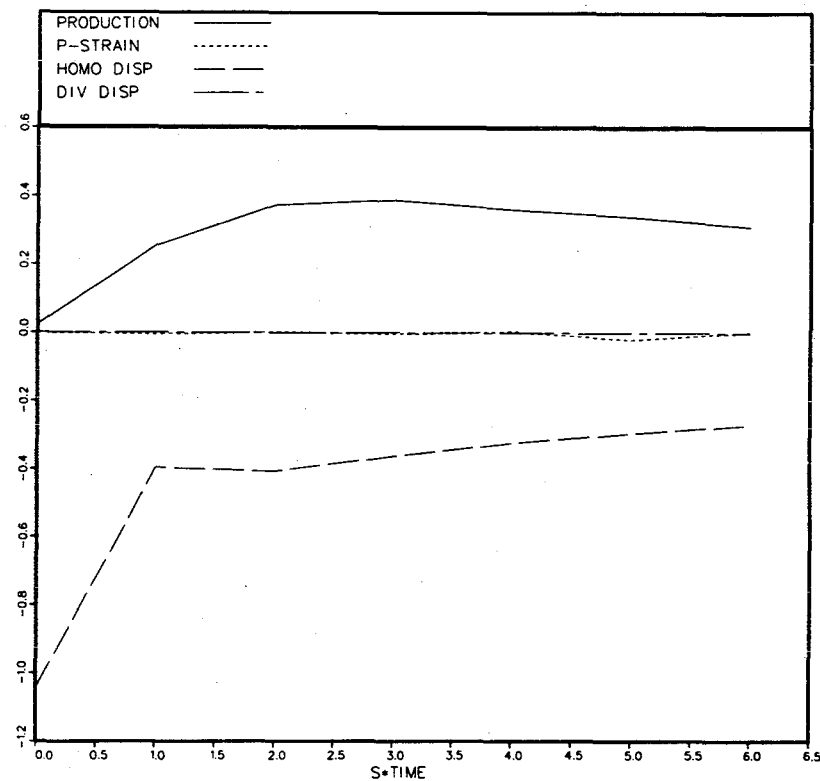
Fig. 4.17h. Contributing terms in the R_{12} Reynolds   Fig. 4.18a. Contributing terms in the turbulent kinetic
stress equations defined as in Eq. (4.7.1)   energy equation vs. St.
vs. St.

Letters in the figure numbers correspond to the individual shear-flow simulations.

KE EQUATION

KE EQUATION

| PRODUCTION | ——— |
P—STRAIN	··········
HOMO DISP	—— —
DIV DISP	——— -

PRODUCTION	———
P—STRAIN	··········
HOMO DISP	—— —
DIV DISP	——— -

S*TIME

S*TIME
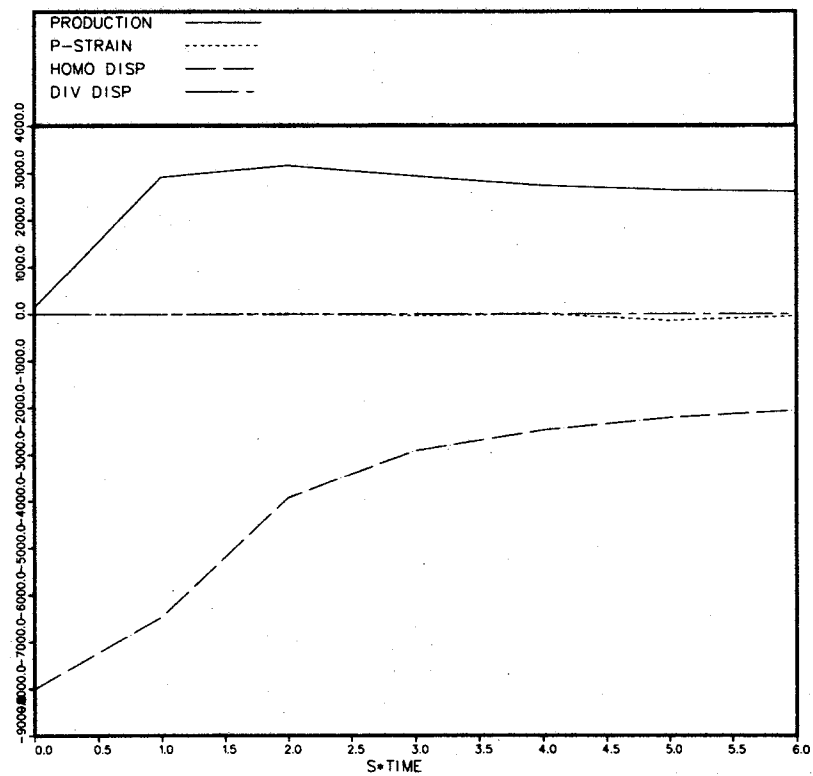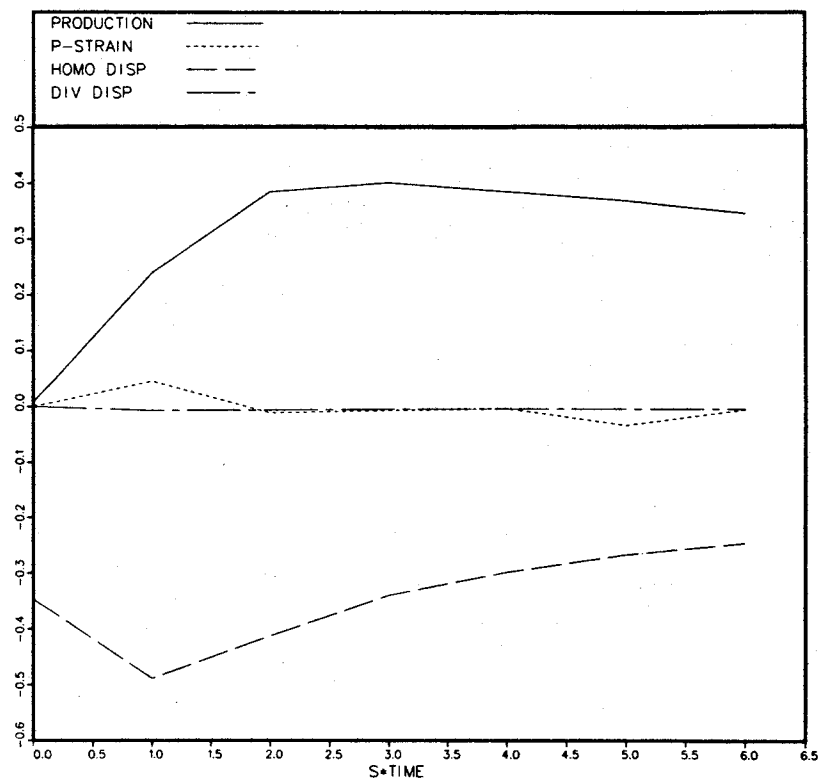
Fig. 4.18b. Contributing terms in the turbulent
kinetic energy equation vs. St.

Fig. 4.18c. Contributing terms in the turbulent
kinetic energy equation vs. St.

Letters in the figure numbers correspond to the individual shear-flow simulations.
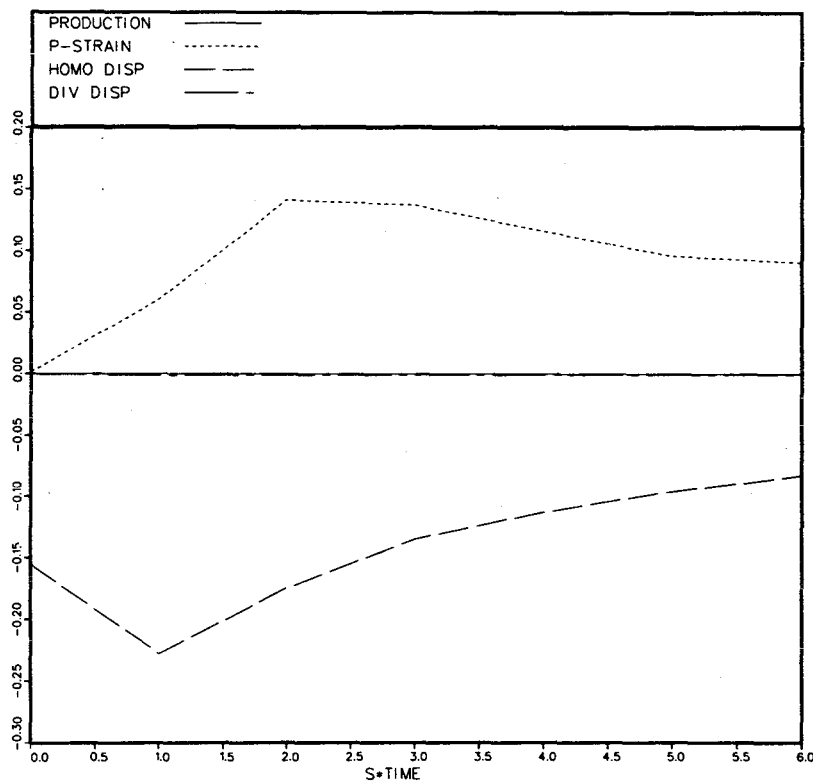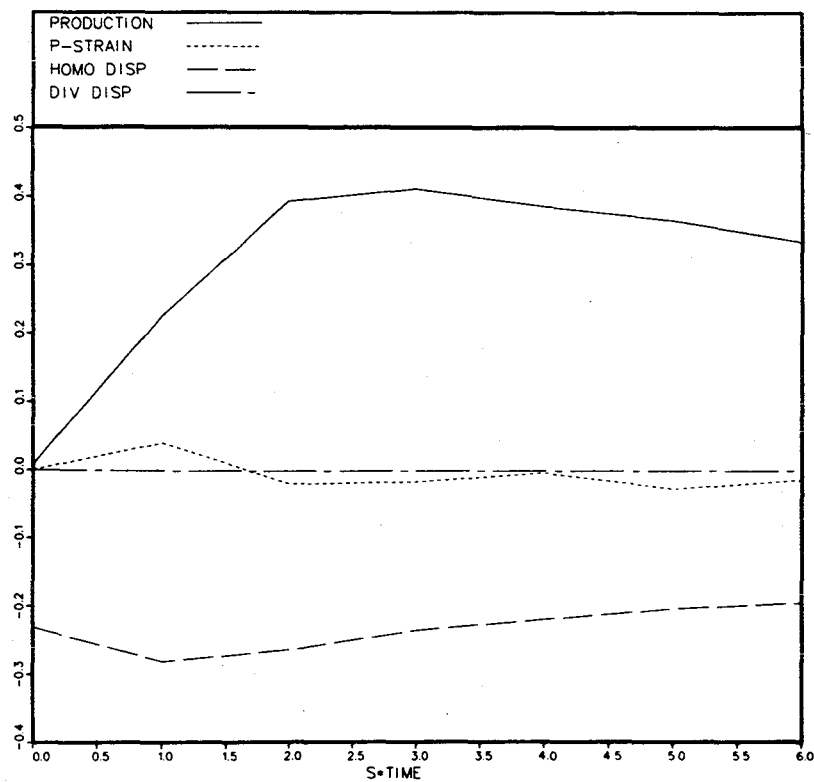
KE EQUATION
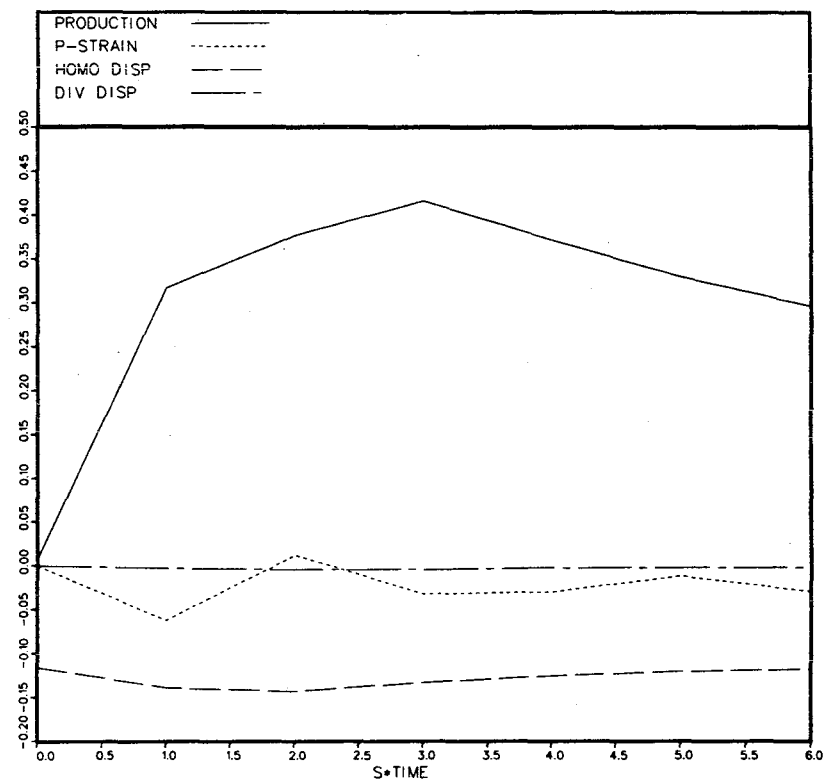
KE EQUATION

Fig. 4.18d. Contributing terms in the turbulent
kinetic energy equation vs. St.

Fig. 4.18f. Contributing terms in the turbulent
kinetic energy equation vs. St.

Letters in the figure numbers correspond to the individual shear-flow simulations.

KE EQUATION

KE EQUATION

PRODUCTION
P-STRAIN
HOMO DISP
DIV DISP

PRODUCTION
P-STRAIN
HOMO DISP
DIV DISP

S•TIME

S•TIME
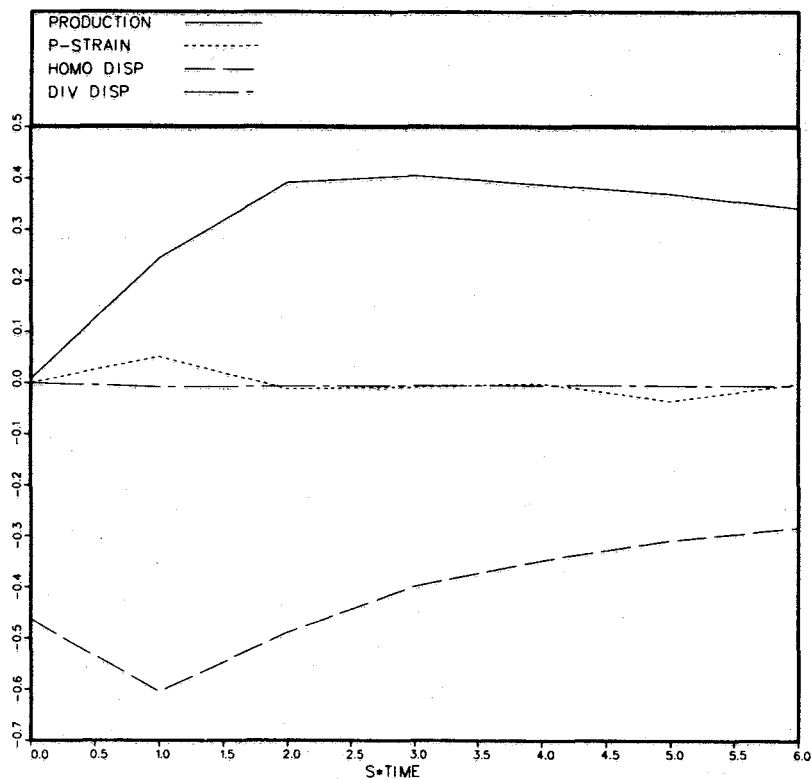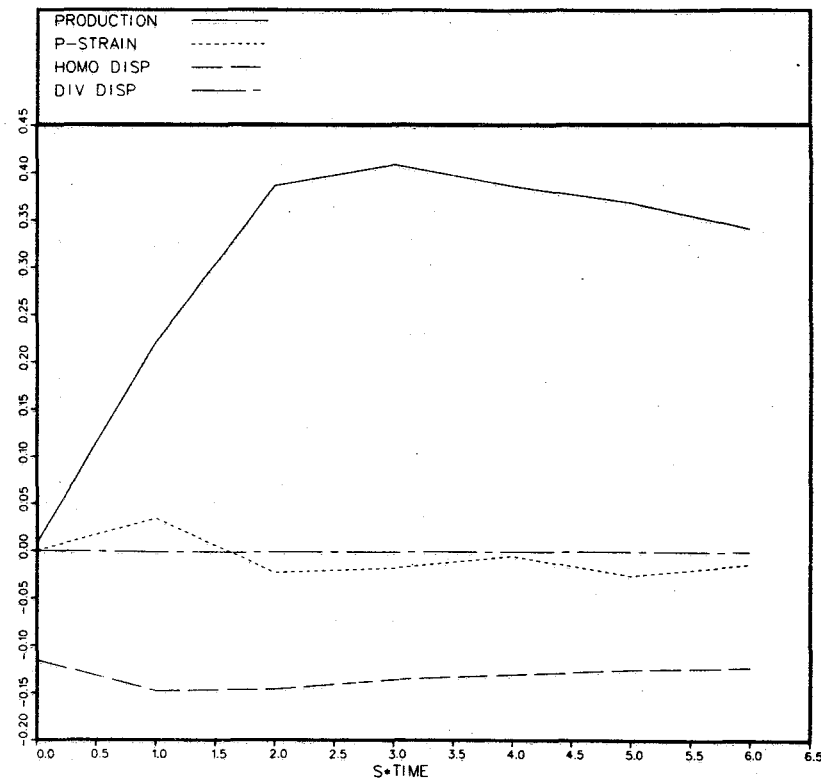
Fig. 4.18g. Contributing terms in the turbulent
kinetic energy equation vs. St.

Fig. 4.18h. Contributing terms in the turbulent
kinetic energy equation vs. St.

Letters in the figure numbers correspond to the individual shear-flow simulations.

DISSIPATION VS. REYNOLDS STRESS ANISOTROPIES

RATIO OF INVARIANTS (DECOMPOSED PRESSURE STRAIN)
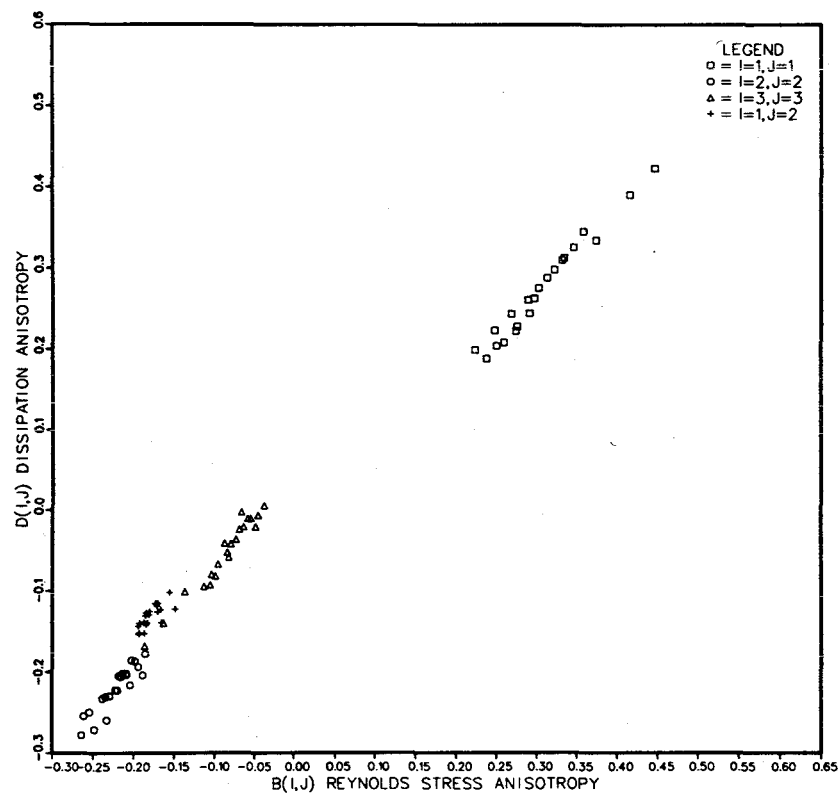
Fig. 4.19. Dissipation anisotropies vs. Reynolds stress anisotropies, all four nonzero components.
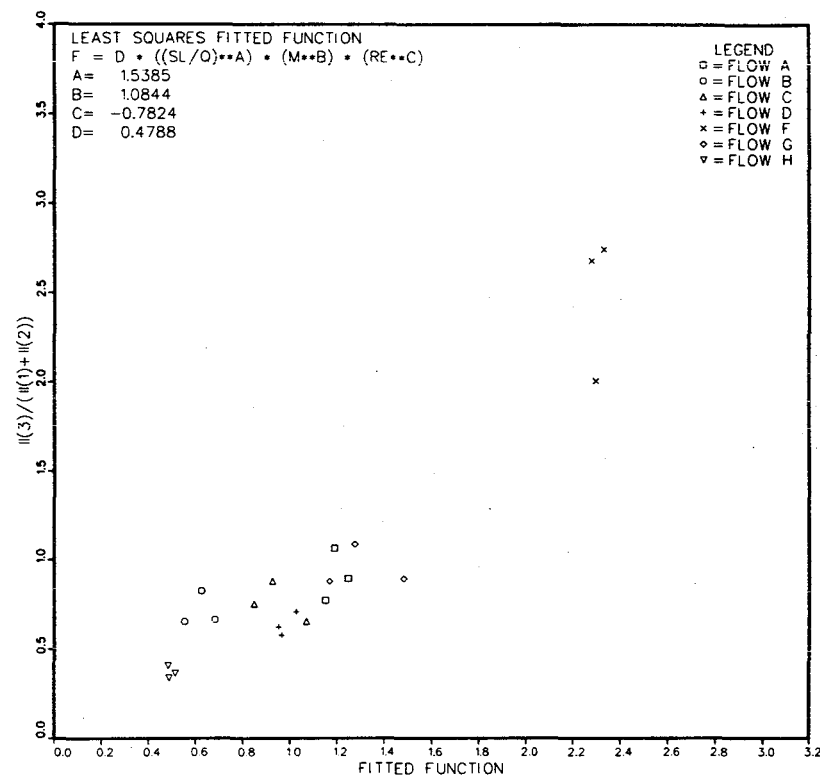
Fig. 4.20. Second invariant of the compressible pressure-strain tensor divided by the sum of the second invariants of the Rotta and Fast pressure-strain tensors vs. the estimate of the least-squares fitted function.

ROTTA MODEL (CONSTANT(C(1)) ROTTA TERM ALONE
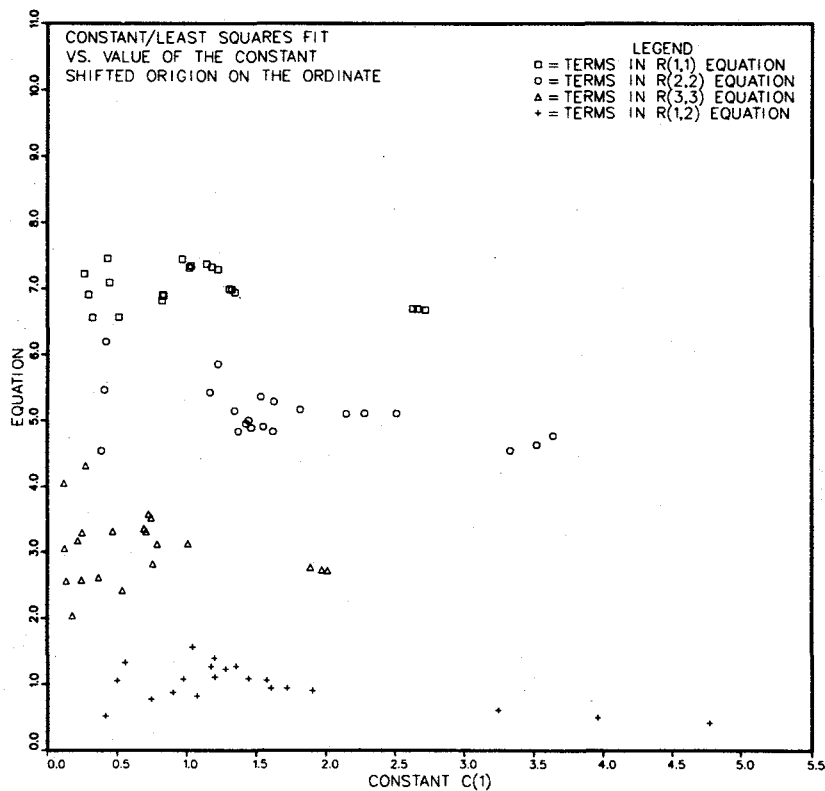
ROTTA MODEL (CONSTANT(C(1)) 2*EPS*DIJ INCLUDED

CONSTANT/LEAST SQUARES FIT
VS. VALUE OF THE CONSTANT
SHIFTED ORIGION ON THE ORDINATE

LEGEND
□ = TERMS IN R(1,1) EQUATION
o = TERMS IN R(2,2) EQUATION
Δ = TERMS IN R(3,3) EQUATION
+ = TERMS IN R(1,2) EQUATION

EQUATION

CONSTANT C(1)

CONSTANT/LEAST SQUARES FIT
VS. VALUE OF THE CONSTANT
SHIFTED ORIGION ON THE ORDINATE

LEGEND
□ = TERMS IN R(1,1) EQUATION
o = TERMS IN R(2,2) EQUATION
Δ = TERMS IN R(3,3) EQUATION
+ = TERMS IN R(1,2) EQUATION

EQUATION

CONSTANT C(1)

Fig. 4.21. Constant C_1 in the Rotta pressure-strain model as used to replace just the Rotta pressure-strain term.

Fig. 4.22. Constant C_1 in the Rotta pressure-strain model as used to replace just the Rotta pressure-strain term.

An estimate of C_1 from the least-squares fitted function is divided by C_1 and plotted on the ordinate (the origin of the results for each of the four nonzero equations is shifted by two for clarity). The value of C_1 is plotted on the abscissa.

FOURTH RANK TENSOR MODEL (CONSTANT(A(1)))

CONSTANT/LEAST SQUARES FIT
VS. VALUE OF THE CONSTANT
SHIFTED ORIGION ON THE ORDINATE

LEGEND
□ = TERMS IN R(1,1) EQUATION
○ = TERMS IN R(2,2) EQUATION
△ = TERMS IN R(3,3) EQUATION
+ = TERMS IN R(1,2) EQUATION

EQUATION

CONSTANT A(1)

GIBSON−LAUNDER MODEL (CONSTANT A(2))

CONSTANT/LEAST SQUARES FIT
VS. VALUE OF THE CONSTANT
SHIFTED ORIGION ON THE ORDINATE

LEGEND
□ = TERMS IN R(1,1) EQUATION
○ = TERMS IN R(2,2) EQUATION
△ = TERMS IN R(3,3) EQUATION
+ = TERMS IN R(1,2) EQUATION

EQUATION
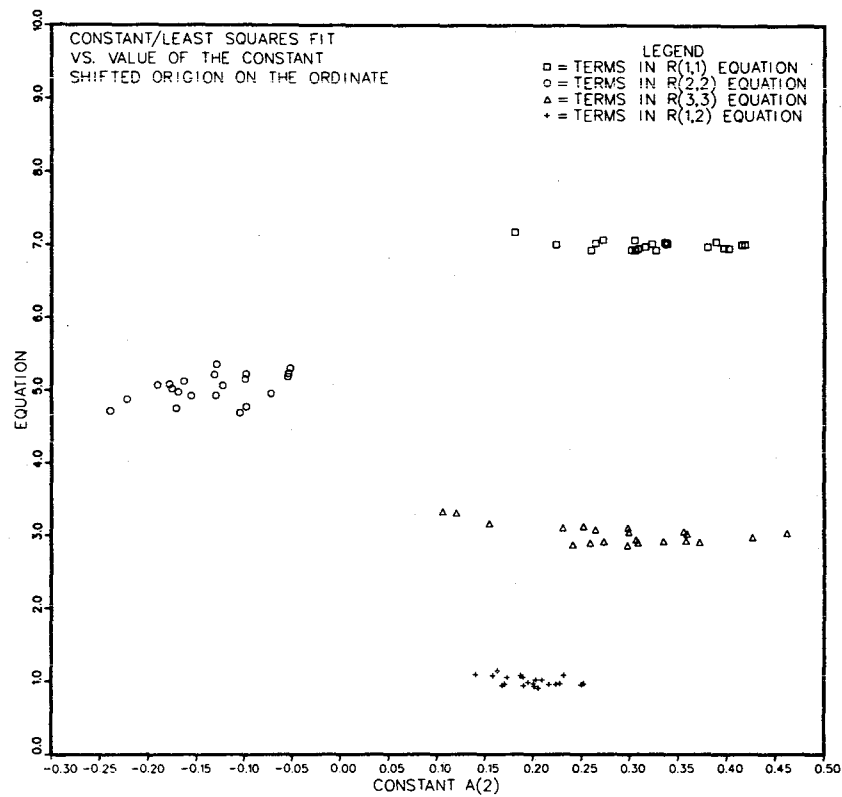
CONSTANT A(2)

Fig. 4.23. Constant A_1 in the fourth-rank tensor model for the Fast pressure-strain terms.

Fig. 4.24. Constant A_2 in the Gibson-Launder model for the Fast pressure-strain terms.

An estimate of A from the least-squares fitted function is divided by A and plotted on the ordinate (the origin of the results for each of the four nonzero equations is shifted by two for clarity). The value of A is plotted on the abscissa.

RATIO OF PHI(3)11/PHI(2)11 PSTRAIN VS. SL(11)/C

RATIO OF PHI(3)22/PHI(2)22 PSTRAIN VS. SL(11)/C
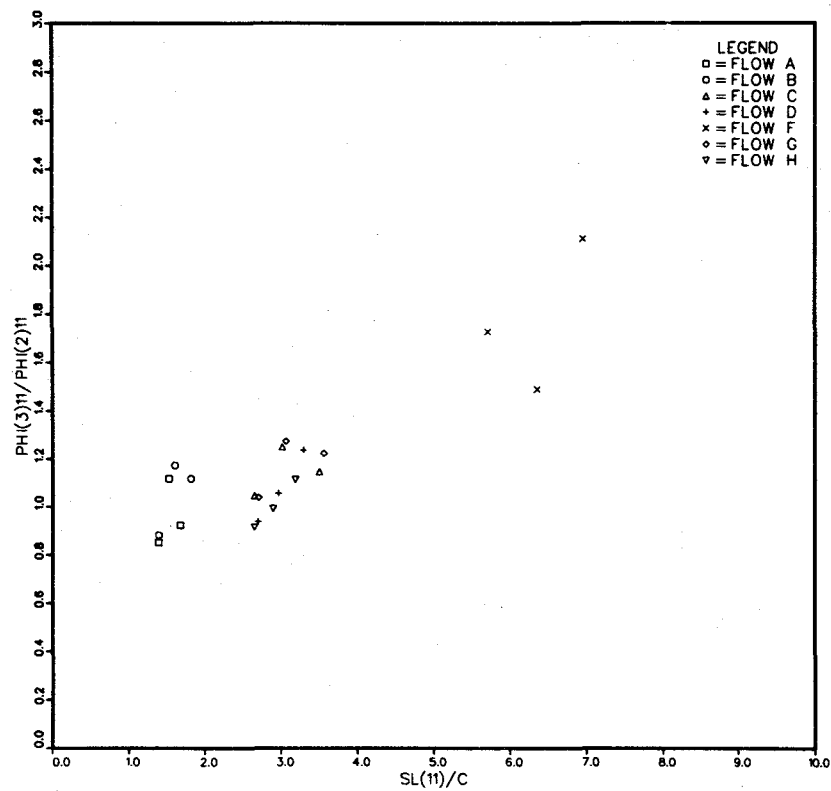
Fig. 4.25a. Ratio of compressible pressure-strain
terms to Fast pressure-strain terms,
$_3\phi_{11}/_2\phi_{11}$ vs. shear Mach number SL/c.

Fig. 4.25b. Ratio of compressible pressure-strain
terms to Fast pressure-strain terms,
$_3\phi_{22}/_2\phi_{22}$ vs. Shear Mach number SL/c.

RATIO OF PHI(3)33/PHI(2)33 PSTRAIN VS. SL(11)/C

RATIO OF PHI(3)12/PHI(2)12 PSTRAIN VS. SL(11)/C
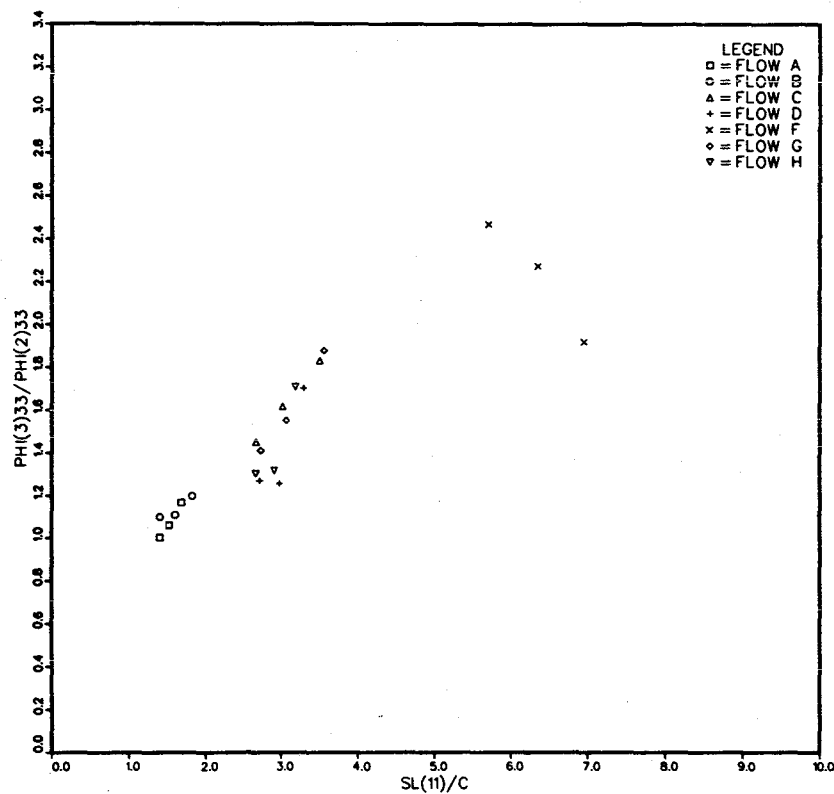
Fig. 4.25c. Ratio of compressible pressure-strain terms to Fast pressure-strain terms, $_3\phi_{33}/_2\phi_{33}$ vs. shear Mach number SL/c.
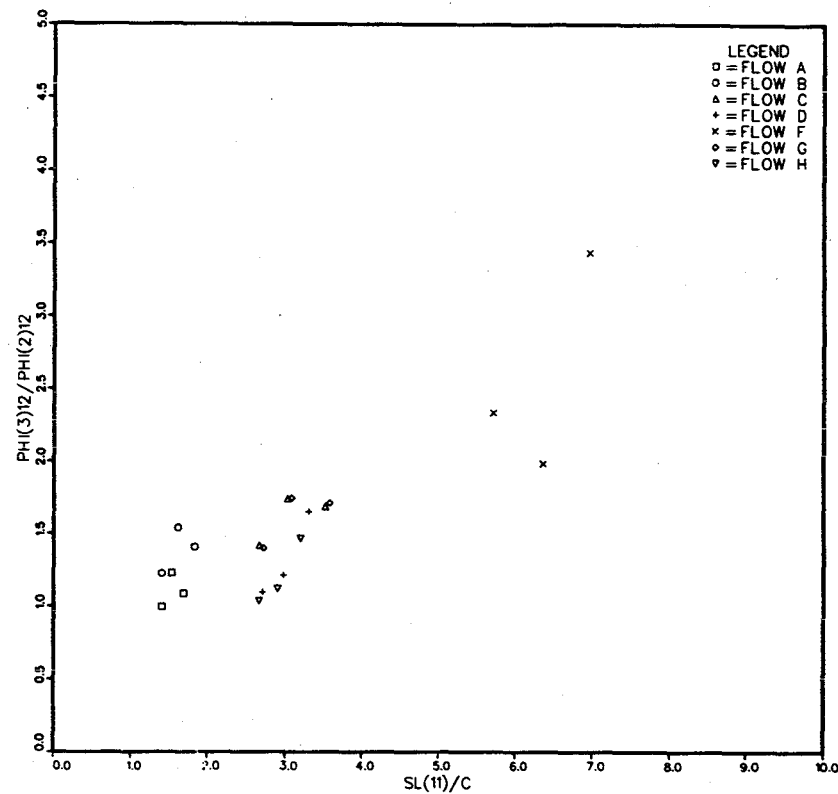
Fig. 4.25d. Ratio of compressible pressure-strain terms to Fast pressure-strain terms, $_3\phi_{12}/_2\phi_{11}$ vs. shear Mach number SL/c.

FOURTH RANK TENSOR MODEL ON COMPRESSIBLE TERMS
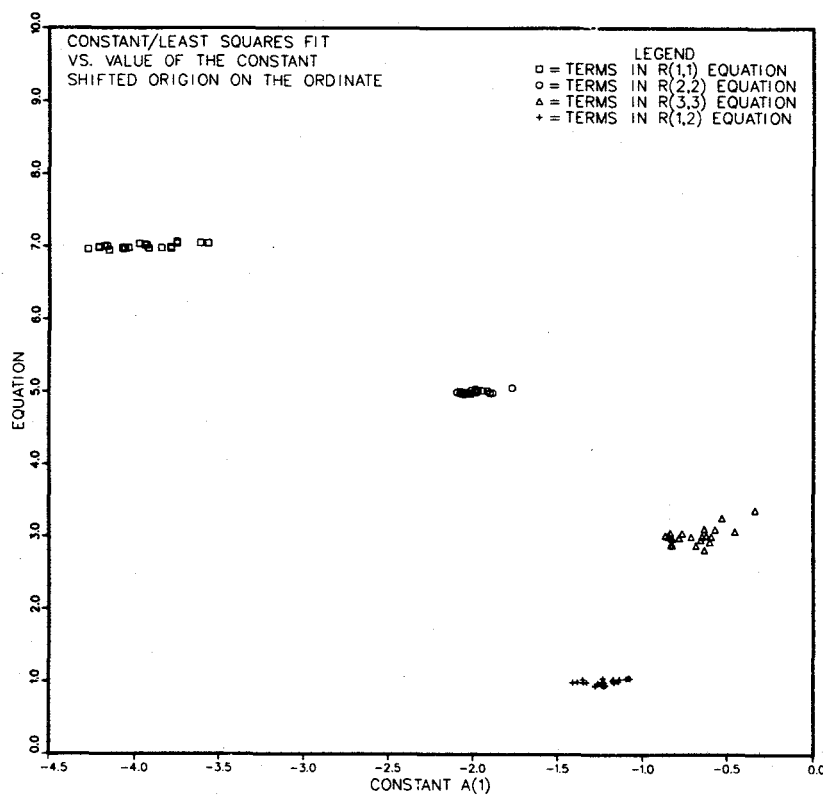
FOURTH RANK TENSOR MODEL ON FAST + COMP. TERMS
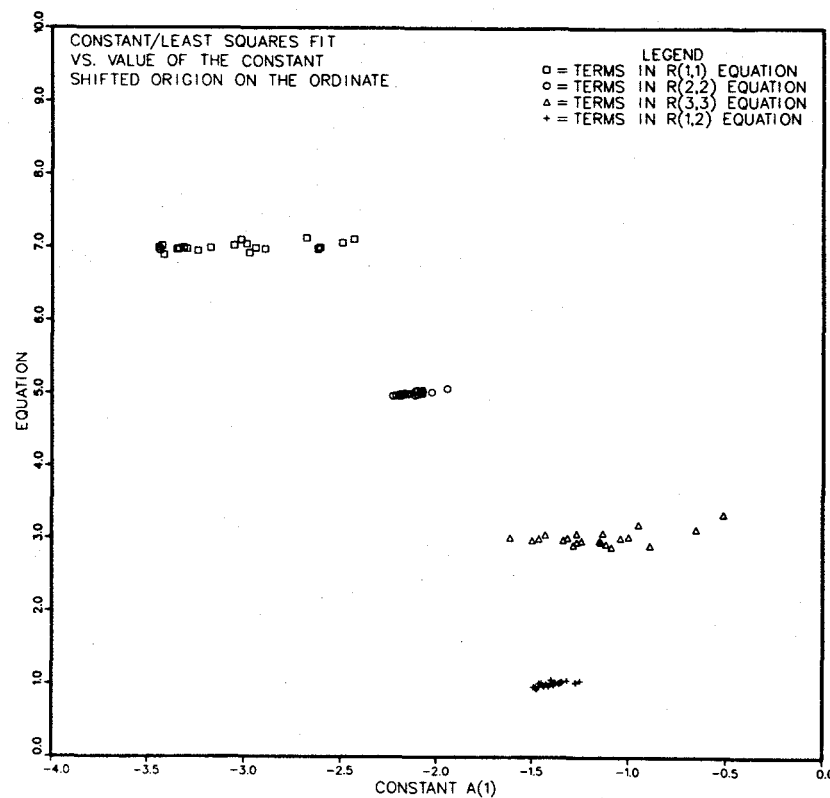
Fig. 4.26. Constant A_1 in the fourth-rank tensor model used for the compressible pressure-strain terms.

Fig. 4.27. Constant A_1 in the fourth-rank tensor model for the sum of the compressible and fast pressure-strain terms.

An estimate of A_1 from the least-squares fitted function is divided by A_1 and plotted on the ordinate (the origin of the results for each of the four nonzero equations is shifted by two for clarity). The value of A_1 is plotted on the abscissa.

165

RATIO OF PHI/(ALL TERMS IN (D/DT)BIJ) (D/DT)BIJ=0

CONSTANT/LEAST SQUARES FIT
VS. VALUE OF THE CONSTANT
SHIFTED ORIGION ON THE ORDINATE

RATIO

ORIGINAL TT MODEL FORMULATION

CONSTANT/LEAST SQUARES FIT
VS. VALUE OF THE CONSTANT
SHIFTED ORIGIN ON THE ORDINATE

CONSTANT C1

166
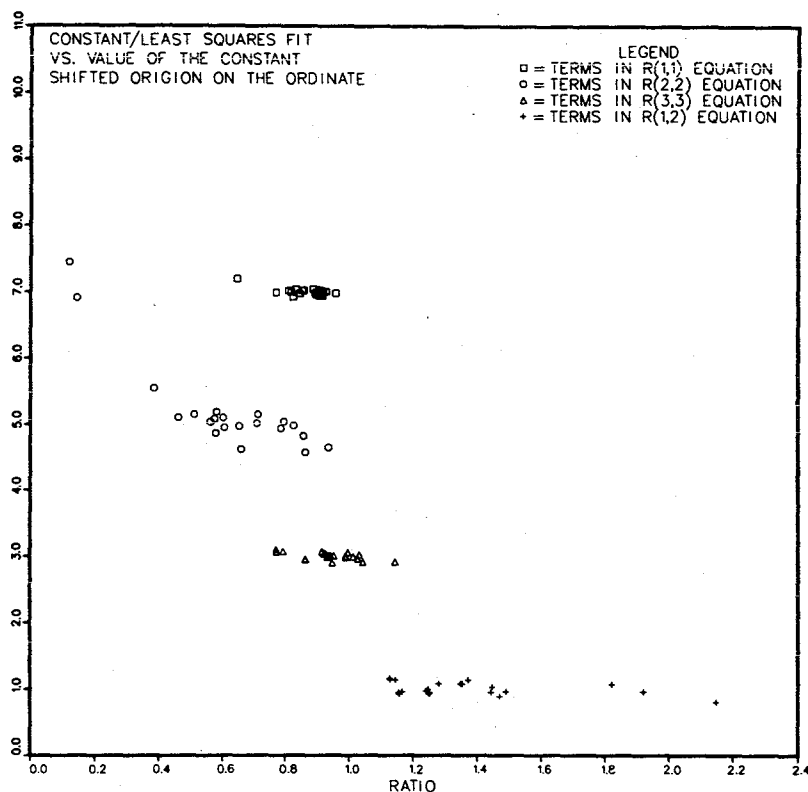
Fig. 4.28. Test of structural similarity. The
pressure-strain term is divided by the
sum of all other contributing terms in
the dynamic equations for b_{ij}, the
Reynolds stress anisotropy. This ratio
is fit by least squares. The least-
squares estimate is divided by the actual
ratio and plotted on the ordinate. The
ratio is plotted on the abscissa.

Fig. 4.29. Constant C_1 in the structural similar-
ity pressure-strain model, Eq. (4.12.5)
for the total pressure-strain tensor.
An estimate of C_1 from the least-squares
fitted function is divided by C_1 and
plotted on the ordinate (the origin of the
results for each of the four nonzero equa-
tions is shifted by two for clairty). The
value of C_1 is plotted on the abscissa.

APPENDIX

TABULATION OF REDUCED DATA FROM
THE SEVEN SHEAR FLOW SIMULATIONS

All quantities are nondimensionalized on four constants:

Density ρ_o

Sound Speed c_o

Reference length L_o = computational box side/2π

Molecular viscosity μ (constant)

For example, the pressure is nondimensionalized on

$$\rho_o c_o^2$$

Quantitative values for these dimensional quantities appear nowhere
in the simulation because we always work with the nondimensional
quantities. They have simply been used as guides to give the
simulations Reynolds, Mach, and Shear numbers that are similar to
those found in experiments. When these numbers are formed from the
following length scales, etc., the dimensional quantities ρ_o , c_o ,
L_o drop out entirely.

In this appendix, we use < > to indicate averages over the entire
mesh.

$$M = \left\langle \frac{(u_i u_i)^{1/2}}{c} \right\rangle \qquad S = \frac{dU}{dy}\frac{L_o}{c_o} \qquad Re_b^{-1} = \frac{\mu}{\rho_o c_o L_o}$$

Flow	St	M	S	Re_b^{-1}
A	4	6.40E-02	1.50E 00	1.50E-03
A	5	6.45E-02	1.50E 00	1.50E-03
A	6	6.54E-02	1.50E 00	1.50E-03
B	4	1.45E-01	1.50E 00	2.00E-03
B	5	1.45E-01	1.50E 00	2.00E-03
B	6	1.47E-01	1.50E 00	2.00E-03
C	4	3.12E-01	3.00E 00	3.00E-03
C	5	3.13E-01	3.00E 00	3.00E-03
C	6	3.16E-01	3.00E 00	3.00E-03
D	4	2.07E-01	3.00E 00	2.00E-03
D	5	2.15E-01	3.00E 00	2.00E-03
D	6	2.22E-01	3.00E 00	2.00E-03
F	4	2.38E-01	6.00E 00	2.00E-03
F	5	2.51E-01	6.00E 00	2.00E-03
F	6	2.62E-01	6.00E 00	2.00E-03
G	4	2.73E-01	3.00E 00	4.00E-03
G	5	2.70E-01	3.00E 00	4.00E-03
G	6	2.68E-01	3.00E 00	4.00E-03
H	4	2.50E-01	3.00E 00	1.00E-03
H	5	2.66E-01	3.00E 00	1.00E-03
H	6	2.81E-01	3.00E 00	1.00E-03

168

		Taylor Micro Scale	Integral Length Scale	Turbulent Velocity
Flow	St	$\dfrac{\lambda_{11}}{L_o}$	$\dfrac{L_{11}}{L_o}$	$\left[<\dfrac{u_i u_i}{c_o^2}>\right]^{(1/2)}$

****

Flow	St	$\dfrac{\lambda_{11}}{L_o}$	$\dfrac{L_{11}}{L_o}$	$\left[<\dfrac{u_i u_i}{c_o^2}>\right]^{(1/2)}$
A	4	3.24E-01	1.25E 00	8.50E-02
A	5	3.61E-01	1.37E 00	8.65E-02
A	6	3.98E-01	1.52E 00	8.80E-02
B	4	3.12E-01	1.25E 00	1.93E-01
B	5	3.53E-01	1.44E 00	1.94E-01
B	6	3.96E-01	1.64E 00	1.97E-01
C	4	2.85E-01	1.22E 00	4.28E-01
C	5	3.24E-01	1.40E 00	4.33E-01
C	6	3.64E-01	1.63E 00	4.39E-01
D	4	3.12E-01	1.22E 00	2.79E-01
D	5	3.45E-01	1.35E 00	2.91E-01
D	6	3.77E-01	1.50E 00	3.01E-01
F	4	3.38E-01	1.30E 00	3.25E-01
F	5	3.84E-01	1.46E 00	3.45E-01
F	6	4.27E-01	1.61E 00	3.64E-01
G	4	3.11E-01	1.25E 00	3.77E-01
G	5	3.55E-01	1.43E 00	3.76E-01
G	6	4.03E-01	1.67E 00	3.76E-01
H	4	2.81E-01	1.19E 00	3.34E-01
H	5	3.01E-01	1.30E 00	3.58E-01
H	6	3.18E-01	1.43E 00	3.79E-01

Flow	St	SL/q		Re_λ		$\langle \rho'^2/\rho_o^2 \rangle$
A	4	2.20E	01	1.84E	01	8.20E-05
A	5	2.38E	01	2.08E	01	1.11E-04
A	6	2.58E	01	2.33E	01	1.27E-04
B	4	9.71E	00	3.01E	01	7.21E-04
B	5	1.12E	01	3.41E	01	9.38E-04
B	6	1.25E	01	3.90E	01	9.57E-04
C	4	8.54E	00	4.07E	01	1.21E-02
C	5	9.66E	00	4.68E	01	1.16E-02
C	6	1.11E	01	5.33E	01	1.20E-02
D	4	1.31E	01	4.36E	01	3.17E-03
D	5	1.39E	01	5.03E	01	3.34E-03
D	6	1.49E	01	5.67E	01	4.16E-03
F	4	2.40E	01	5.49E	01	6.33E-03
F	5	2.53E	01	6.63E	01	5.87E-03
F	6	2.66E	01	7.77E	01	6.14E-03
G	4	9.97E	00	2.93E	01	8.89E-03
G	5	1.14E	01	3.34E	01	8.47E-03
G	6	1.33E	01	3.79E	01	8.85E-03
H	4	1.07E	01	9.38E	01	4.81E-03
H	5	1.09E	01	1.08E	02	5.53E-03
H	6	1.14E	01	1.21E	02	7.17E-03

Decomposed Pressure Strain Tensor.

Rotta Term.

$$_1\phi_{ij} = <P_1 (u_{i,j} + u_{j,i})> \frac{L_o}{\rho_o c_o^3}$$

$$_1\phi_{ij}$$

Flow	St	i=1,j=1	i=2,j=2	i=3,j=3	i=1,j=2
A	4	-1.71E-04	1.72E-04	2.09E-05	1.33E-04
A	5	-1.65E-04	1.69E-04	1.98E-05	1.41E-04
A	6	-1.51E-04	1.63E-04	1.86E-05	1.37E-04
B	4	-2.62E-03	2.40E-03	3.58E-04	1.86E-03
B	5	-2.49E-03	2.47E-03	2.83E-04	1.83E-03
B	6	-2.43E-03	2.40E-03	2.74E-04	1.83E-03
C	4	-2.55E-02	3.25E-02	3.32E-03	1.85E-02
C	5	-2.59E-02	3.38E-02	1.30E-03	2.00E-02
C	6	-2.63E-02	3.60E-02	2.42E-03	2.10E-02
D	4	-7.97E-03	8.20E-03	1.70E-03	6.37E-03
D	5	-8.96E-03	9.23E-03	1.91E-03	7.48E-03
D	6	-8.96E-03	1.01E-02	2.09E-03	8.43E-03
F	4	-7.63E-03	1.38E-02	1.34E-03	7.21E-03
F	5	-8.01E-03	1.28E-02	8.39E-04	8.54E-03
F	6	-9.08E-03	1.49E-02	2.17E-03	1.11E-02
G	4	-1.55E-02	2.19E-02	2.29E-03	1.07E-02
G	5	-1.50E-02	2.22E-02	9.80E-04	1.09E-02
G	6	-1.44E-02	2.32E-02	1.75E-03	1.10E-02
H	4	-1.67E-02	1.51E-02	3.52E-03	1.37E-02
H	5	-2.04E-02	1.82E-02	4.46E-03	1.75E-02
H	6	-2.27E-02	2.09E-02	5.61E-03	2.14E-02

Decomposed Pressure Strain Tensor.

Fast Term.

$$2\phi_{ij} = <P_2 (u_{i,j} + u_{j,i})> \frac{L_o}{\rho_o c_o^3}$$

$$2\phi_{ij}$$

Flow	St	i=1,j=1	i=2,j=2	i=3,j=3	i=1,j=2
A	4	-4.46E-04	-7.21E-05	4.84E-04	2.53E-04
A	5	-4.65E-04	-6.90E-05	4.23E-04	2.40E-04
A	6	-4.12E-04	-6.33E-05	3.71E-04	2.01E-04
B	4	-3.04E-03	-5.04E-04	3.21E-03	1.85E-03
B	5	-2.87E-03	-7.06E-04	2.86E-03	1.63E-03
B	6	-2.52E-03	-6.52E-04	2.38E-03	1.31E-03
C	4	-3.25E-02	-9.04E-03	2.49E-02	1.62E-02
C	5	-3.06E-02	-1.12E-02	2.10E-02	1.51E-02
C	6	-2.49E-02	-1.47E-02	1.80E-02	1.30E-02
D	4	-1.09E-02	-2.99E-03	8.96E-03	5.04E-03
D	5	-1.10E-02	-4.01E-03	7.74E-03	5.15E-03
D	6	-9.16E-03	-5.15E-03	6.94E-03	4.39E-03
F	4	-2.28E-02	-1.37E-02	1.21E-02	1.24E-02
F	5	-1.97E-02	-1.40E-02	9.38E-03	1.07E-02
F	6	-1.59E-02	-1.50E-02	8.24E-03	9.04E-03
G	4	-2.57E-02	-7.21E-03	1.94E-02	1.23E-02
G	5	-2.35E-02	-8.77E-03	1.54E-02	1.14E-02
G	6	-1.82E-02	-1.15E-02	1.27E-02	9.46E-03
H	4	-1.49E-02	-4.23E-03	1.27E-02	7.06E-03
H	5	-1.58E-02	-5.76E-03	1.21E-02	7.55E-03
H	6	-1.44E-02	-7.55E-03	1.17E-02	6.94E-03

Decomposed Pressure Strain Tensor.

Compressible Term.

$$_3\phi_{ij} = \ <P_3 \ (u_{i,j} + u_{j,i})> \ \frac{L_o}{\rho_o c_o^3}$$

$$_3\phi_{ij}$$

Flow	St	i=1,j=1	i=2,j=2	i=3,j=3	i=1,j=2
A	4	-3.81E-04	-5.57E-05	4.88E-04	2.53E-04
A	5	-5.23E-04	-7.29E-05	4.50E-04	2.95E-04
A	6	-3.81E-04	3.62E-05	4.31E-04	2.19E-04
B	4	-2.68E-03	-6.37E-04	3.52E-03	2.27E-03
B	5	-3.37E-03	-4.62E-04	3.17E-03	2.50E-03
B	6	-2.81E-03	1.15E-04	2.85E-03	1.85E-03
C	4	-3.40E-02	2.01E-03	3.62E-02	2.30E-02
C	5	-3.81E-02	-3.40E-03	3.40E-02	2.64E-02
C	6	-2.86E-02	1.71E-03	3.29E-02	2.19E-02
D	4	-1.02E-02	8.13E-04	1.14E-02	5.49E-03
D	5	-1.16E-02	-2.56E-04	9.73E-03	6.22E-03
D	6	-1.13E-02	-5.15E-04	1.18E-02	7.25E-03
F	4	-3.93E-02	8.01E-03	2.97E-02	2.89E-02
F	5	-2.93E-02	1.84E-02	2.14E-02	2.13E-02
F	6	-3.35E-02	9.16E-03	1.58E-02	3.11E-02
G	4	-2.66E-02	3.18E-03	2.74E-02	1.72E-02
G	5	-2.99E-02	-4.62E-04	2.40E-02	1.99E-02
G	6	-2.22E-02	4.20E-03	2.38E-02	1.63E-02
H	4	-1.36E-02	-4.39E-04	1.66E-02	7.32E-03
H	5	-1.57E-02	-2.87E-03	1.59E-02	8.47E-03
H	6	-1.60E-02	-3.57E-03	2.00E-02	1.02E-02

Decomposed Reynolds Stress Tensor.

Incompressible Part.

$$\frac{R^s_{ij}}{\rho_o c_o^2}$$

Flow	St	i=1,j=2	i=1,j=1	i=2,j=2	i=3,j=3
A	4	-1.30E-03	4.50E-03	7.59E-04	1.91E-03
A	5	-1.25E-03	4.96E-03	6.29E-04	1.83E-03
A	6	-1.17E-03	5.30E-03	5.38E-04	1.81E-03
B	4	-6.94E-03	2.05E-02	5.61E-03	1.09E-02
B	5	-6.60E-03	2.15E-02	4.81E-03	1.07E-02
B	6	-6.41E-03	2.29E-02	4.27E-03	1.08E-02
C	4	-3.33E-02	9.99E-02	2.57E-02	4.92E-02
C	5	-3.15E-02	1.06E-01	2.27E-02	4.84E-02
C	6	-3.10E-02	1.13E-01	2.04E-02	4.81E-02
D	4	-1.45E-02	4.84E-02	8.54E-03	1.90E-02
D	5	-1.45E-02	5.46E-02	7.86E-03	1.90E-02
D	6	-1.43E-02	6.03E-02	7.21E-03	1.94E-02
F	4	-1.82E-02	7.21E-02	7.74E-03	1.96E-02
F	5	-1.85E-02	8.66E-02	6.87E-03	1.88E-02
F	6	-1.83E-02	1.00E-01	6.22E-03	1.85E-02
G	4	-2.59E-02	7.90E-02	1.87E-02	3.77E-02
G	5	-2.37E-02	8.16E-02	1.54E-02	3.57E-02
G	6	-2.23E-02	8.54E-02	1.30E-02	3.42E-02
H	4	-2.09E-02	6.79E-02	1.34E-02	2.74E-02
H	5	-2.22E-02	8.01E-02	1.38E-02	2.93E-02
H	6	-2.34E-02	9.23E-02	1.43E-02	3.19E-02

Decomposed Reynolds Stress Tensor.

Compressible Part.

$$\frac{R_{ij}^{D}}{\rho_0 c_0^2}$$

Flow	St	i=1,j=2	i=1,j=1	i=2,j=2	i=3,j=3
A	4	-1.30E-06	4.65E-05	-3.08E-05	2.73E-05
A	5	-2.27E-05	4.69E-05	7.29E-06	6.52E-06
A	6	-3.18E-05	7.17E-05	-6.68E-07	3.79E-05
B	4	-2.40E-05	3.21E-04	-1.90E-04	1.52E-04
B	5	-1.14E-04	2.66E-04	4.54E-05	5.65E-05
B	6	-2.13E-04	3.93E-04	4.23E-05	2.88E-04
C	4	-1.57E-03	3.97E-03	1.13E-03	1.38E-03
C	5	-2.69E-03	4.69E-03	2.48E-03	1.80E-03
C	6	-2.02E-03	3.29E-03	4.65E-03	1.90E-03
D	4	-4.88E-04	1.21E-03	2.86E-04	4.73E-04
D	5	-9.65E-04	1.61E-03	9.38E-04	4.84E-04
D	6	-7.13E-04	1.05E-03	1.73E-03	5.42E-04
F	4	-1.36E-03	2.56E-03	2.27E-03	1.08E-03
F	5	-1.16E-03	2.54E-03	2.55E-03	1.44E-03
F	6	-1.25E-03	2.43E-03	3.32E-03	9.04E-04
G	4	-1.39E-03	3.38E-03	9.19E-04	1.22E-03
G	5	-2.30E-03	3.93E-03	2.08E-03	1.50E-03
G	6	-1.67E-03	2.52E-03	3.89E-03	1.50E-03
H	4	-5.57E-04	1.44E-03	3.97E-04	5.07E-04
H	5	-1.17E-03	2.01E-03	1.17E-03	5.53E-04
H	6	-8.89E-04	1.35E-03	2.23E-03	6.68E-04

Homogeneous Dissipation Tensor.

$$D_{ij}^{H} = Re_{b}^{-1} \langle u_{i,k} \, u_{j,k} \rangle \times \frac{L_{o}^{2}}{c_{o}^{2}}$$

Flow	St	i=1,j=1	i=2,j=2	i=3,j=3
A	4	2.09E-03	2.59E-04	1.16E-03
A	5	2.14E-03	2.05E-04	9.69E-04
A	6	2.14E-03	1.74E-04	8.39E-04
B	4	1.01E-02	2.45E-03	6.41E-03
B	5	9.42E-03	1.98E-03	5.53E-03
B	6	9.08E-03	1.74E-03	4.92E-03
C	4	8.47E-02	2.53E-02	5.26E-02
C	5	8.09E-02	2.19E-02	4.65E-02
C	6	7.86E-02	2.09E-02	4.20E-02
D	4	3.13E-02	5.68E-03	1.45E-02
D	5	3.34E-02	5.38E-03	1.32E-02
D	6	3.50E-02	5.46E-03	1.27E-02
F	4	5.26E-02	7.93E-03	1.84E-02
F	5	6.22E-02	7.13E-03	1.66E-02
F	6	7.02E-02	7.32E-03	1.54E-02
G	4	7.90E-02	2.06E-02	4.77E-02
G	5	7.32E-02	1.69E-02	4.04E-02
G	6	6.90E-02	1.57E-02	3.49E-02
H	4	2.59E-02	5.72E-03	1.20E-02
H	5	2.98E-02	6.10E-03	1.21E-02
H	6	3.33E-02	6.79E-03	1.27E-02

Homogeneous Dissipation Tensor.

$$D_{ij}^{H} = Re_{b}^{-1} \langle u_{i,k} \, u_{j,k} \rangle \times \frac{L_{o}^{2}}{c_{o}^{2}}$$

Flow	St	i=1,j=2	i=1,j=3	i=2,j=3
A	4	-4.54E-04	-1.67E-06	8.39E-06
A	5	-3.81E-04	-3.21E-06	2.70E-06
A	6	-3.22E-04	-5.15E-06	-1.66E-06
B	4	-2.63E-03	3.13E-05	3.20E-05
B	5	-2.12E-03	-8.28E-06	3.20E-05
B	6	-1.83E-03	-3.21E-05	6.52E-06
C	4	-2.28E-02	3.07E-04	4.88E-04
C	5	-1.90E-02	-1.26E-04	3.18E-04
C	6	-1.64E-02	-5.95E-04	4.77E-05
D	4	-7.82E-03	4.96E-06	9.38E-05
D	5	-7.25E-03	1.75E-04	-7.21E-06
D	6	-6.56E-03	5.49E-06	-1.82E-04
F	4	-1.21E-02	2.04E-05	1.40E-04
F	5	-1.19E-02	3.68E-04	-2.50E-05
F	6	-1.14E-02	2.07E-04	-1.83E-04
G	4	-2.12E-02	2.03E-04	5.00E-04
G	5	-1.71E-02	-1.77E-04	2.76E-04
G	6	-1.42E-02	-5.15E-04	-1.11E-04
H	4	-6.68E-03	9.38E-06	8.32E-05
H	5	-6.79E-03	1.87E-04	-1.50E-05
H	6	-6.64E-03	8.01E-05	-1.58E-04

Intensities of the decomposed pressure fields.

		Rotta	Fast	Compr.
		$\left\langle \dfrac{p'^2_1}{(\rho_o c^2_o)^2} \right\rangle$	$\left\langle \dfrac{p'^2_2}{(\rho_o c^2_o)^2} \right\rangle$	$\left\langle \dfrac{p'^2_3}{(\rho_o c^2_o)^2} \right\rangle$
Flow	St			

****

Flow	St	Rotta	Fast	Compr.
A	4	5.95E-06	2.04E-05	7.71E-05
A	5	5.53E-06	2.45E-05	1.21E-04
A	6	5.04E-06	2.24E-05	1.68E-04
B	4	1.75E-04	1.58E-04	6.33E-04
B	5	1.62E-04	1.82E-04	1.02E-03
B	6	1.57E-04	1.53E-04	1.22E-03
C	4	4.08E-03	1.80E-03	1.59E-02
C	5	3.97E-03	2.00E-03	1.67E-02
C	6	3.93E-03	1.78E-03	2.12E-02
D	4	7.10E-04	5.11E-04	4.16E-03
D	5	7.36E-04	6.18E-04	4.65E-03
D	6	7.59E-04	5.95E-04	6.83E-03
F	4	1.20E-03	1.17E-03	1.03E-02
F	5	1.24E-03	1.32E-03	1.05E-02
F	6	1.23E-03	1.16E-03	1.13E-02
G	4	2.55E-03	1.51E-03	1.29E-02
G	5	2.32E-03	1.63E-03	1.32E-02
G	6	2.20E-03	1.41E-03	1.69E-02
H	4	1.41E-03	6.33E-04	5.46E-03
H	5	1.64E-03	8.05E-04	6.29E-03
H	6	1.90E-03	8.13E-04	9.46E-03

End of Document